ÇUKUROVA UNIVERSITY
INSTITUTE OF NATURAL AND APPLIED SCIENCES

PhD THESIS

Mustafa AKYOL

CURRENT-DRIVEN SPIN-ORBIT-TORQUE PHENOMENA IN PERPENDICULARLY MAGNETIZED HEAVY METAL |FERROMAGNET |INSULATOR MULTILAYER STRUCTURES

DEPARTMENT OF PHYSICS

ADANA-2016

ÇUKUROVA UNIVERSITY
INSTITUTE OF NATURAL AND APPLIED SCIENCES

CURRENT-DRIVEN SPIN-ORBIT-TORQUE PHENOMENA IN PERPENDICULARLY MAGNETIZED HEAVY METAL|FERROMAGNET |INSULATOR MULTILAYER STRUCTURES

Mustafa AKYOL

PhD THESIS

DEPARTMENT OF PHYSICS

We certify that the thesis titled above was reviewed and approved for the award of degree of the Doctor of Philosophy by the board of jury on 25/11/2016.

……..	……..	……
Assoc. Prof. Dr. Ahmet EKİCİBİL	Prof. Dr. Bekir ÖZÇELİK	Prof. Dr. Metin ÖZDEMİR
SUPERVISOR	MEMBER	MEMBER

……	…… ……
Prof. Dr. Ebru ŞENADIM TÜZEMEN	Assoc. Prof. Dr. Mustafa GÜNEŞ
MEMBER	MEMBER

This PhD Thesis is written at the Department of Physics of Institute of Natural And Applied Sciences.
Registration Number:

Prof. Dr. Mustafa GÖK
Director
Institute of Natural and Applied Sciences

This study is supported by Çukurova University Scientific Research Fund.
Project Number: FEF2013D31

Not: The usage of the presented specific declarations, tables, figures, and photographs either in this thesis or in any other reference without citation is subject to "The law of Arts and Intellectual Products" number of 5846 of Turkish Republic.

ABSTRACT

PhD THESIS

CURRENT-DRIVEN SPIN-ORBIT-TORQUE PHENOMENA IN PERPENDICULARLY MAGNETIZED HEAVY METAL|FERROMAGNET |INSULATOR MULTILAYER STRUCTURES

Mustafa AKYOL

ÇUKUROVA UNIVERSITY
INSTITUTE OF NATURAL AND APPLIED SCIENCES
DEPARTMENT OF PHYSICS

Supervisor : Assoc. Prof. Dr. Ahmet EKİCİBİL
Year: 2016, Pages: 247
Jury : Assoc. Prof. Dr. Ahmet EKİCİBİL
: Prof. Dr. Bekir ÖZÇELİK
: Prof. Dr. Metin ÖZDEMİR
: Prof. Dr. Ebru ŞENADIM TÜZEMEN
: Assoc. Prof. Dr. Mustafa GÜNEŞ

In this thesis, we have systematically studied on the current-driven Spin-Orbit-Torque (SOT) phenomena in perpendicularly magnetized heavy-metal|ferromagnet|insulator multilayer structures to optimize the free-part of the magnetic tunnel junction. Firstly, we worked on the effect of heavy-metal layer thickness on the structural, magnetic, transport and spintronics properties in such a structure. A non-monotonic behavior in the Damping-Like (DL)-SOT is found as a function of the thickness of the heavy-metal layer. It is observed that the sign of the DL-SOT changes with increasing the thickness of the Hf layer in the multilayer structure. Secondly, we worked on the effect of oxide layer on magnetic, transport and spintronics properties in Hf|CoFeB|MgO and Hf|CoFeB|TaO_x multilayer structures. Both DL and Field-Like (FL)-torques are found to be significantly stronger in MgO-capped structures than those in TaO_x-capped structures. The difference in FL and DL SOTs in different structures may be attributed to the different Rashba-like Hamiltonian, arising from the difference in the electric potential profiles across the oxide|ferromagnet interfaces in the two cases. Finally, we worked on the engineering of structural asymmetry in multilayer structures to switch the magnetization without external field. The studied structures exhibit broken in-plane inversion symmetry due to a wedged CoFeB layer, resulting in a field-like spin-orbit torque, which can be quantified by a perpendicular effective magnetic field. In particular, while the current-driven deterministic perpendicular magnetic switching was observed at zero magnetic field in Hf|CoFeB|MgO, an external magnetic field is necessary to switch the CoFeB layer deterministically in Hf|CoFeB|TaO_x. Based on the experimental results, the SOT magnitude in Hf|CoFeB|MgO was found to be almost 13× larger than that in Hf|CoFeTaO_x. The CoFeB thickness dependence of the magnetic switching behavior, and the resulting effective magnetic field by in-plane currents are also investigated in this work. These findings could potentially be used to engineer SOT devices with enhanced current-driven switching efficiency.

Key Words: Perpendicular Magnetic Anisotropy, Magnetic Tunnel Junction, Spin-Orbit-Torque, Current-Driven Magnetization Switching, Magnetic Random Access Memory.

ÖZ

DOKTORA TEZİ

YÜZEYE DİK MANYETİZE OLMUŞ AĞIR METAL|FERROMANYETİK |YALITKAN KATMANLI YAPILARDAKİ AKIM SÜRÜMLÜ SPİN-YÖRÜNGE TORKU OLAYI

Mustafa AKYOL

ÇUKUROVA ÜNİVERSİTESİ
FEN BİLİMLERİ ENSTİTÜSÜ
FİZİK ANABİLİM DALI

Danışman : Doç Dr. Ahmet EKİCİBİL
Yıl: 2016, Sayfa: 247
Jüri : Doç. Dr. Ahmet EKİCİBİL
: Prof. Dr. Bekir ÖZÇELİK
: Prof. Dr. Metin ÖZDEMİR
: Prof. Dr. Ebru ŞENADIM TÜZEMEN
: Doç. Dr. Mustafa GÜNEŞ

Bu tezde, manyetik tünel eklemlerin serbest bölgesini optimize etmek için yüzeye dik olarak manyetize olmuş ağır-metal|ferromanyetik|yalıtkan katmanlı yapılarında akım sürümlü Spin-Yörünge Torku (SOT) olayı sistematik olarak çalışıldı. İlk olarak, ağır metal katman kalınlığının böylesi bir yapının yapısal, manyetik, taşıyıcı ve spintronik özellikleri üzerine etkisi çalışıldı. Sönümlü (DL)-SOT'da ağır metal katmanın kalınlığına bağlı, tek düze olmayan bir davranış bulundu. DL-SOT'un yönünün katmanlı yapıdaki Hf katman kalınlığının artması ile değiştiği gözlemlendi. İkinci olarak, yalıtkan katmanın Hf|CoFeB|MgO ve Hf|CoFeB|TaO_x katmanlı yapılarındaki manyetik, taşıyıcı ve spintronik özelliklere etkisi çalışıldı. DL ve Alan-Türü (FL)-SOT 'larının her ikisinin de MgO ile kaplanmış yapıda TaO_x ile kaplanmış yapıdakinden önemli ölçüde daha güçlü olduğu bulunmuştur. Farklı yapılardaki farklı FL ve DL SOT'lardaki fark, yalıtkan|ferromanyetik ara yüzeylerindeki elektriksel potansiyel farklılıklardan ortaya çıkan farklı Rashba-türü Hamiltonian'lara atfedilebilir. Son olarak, dış manyetik alan olmadan katmanlı yapıdaki manyetizasyonu kontrol edebilmek için yapının simetrisi üzerine mühendislik çalışması gerçekleştirildi. Kama şeklinde büyütülmüş ferromanyetik CoFeB katmandan dolayı çalışılan yapılarda yüzeye dik etkin manyetik alan üretilen alan türü spin-yörünge torku ile film düzleminde simetri bozukluluğu oluşturmaktadır. Özellikle, akım-sürümlü dik manyetizasyon kontrolü Hf|CoFeB|MgO yapısında sıfır alanda gözlenirken, Hf|CoFeB|TaO_x yapısındaki CoFeB katmanın kontrolü için bir dış manyetik alan gerekmektedir. Deneysel sonuçlarımıza göre, Hf|CoFeB|MgO yapısındaki SOT büyüklüğünün Hf|CoFeB|TaO_x yapısındakine kıyasla 13 kat daha büyük olduğu bulunmuştur. CoFeB kalınlığına bağlı manyetizasyon değişim davranışı ve düzlemsel akıma bağlı olarak sonuçlanan etkin manyetik alan da bu çalışmada araştırıldı. Bu çalışmadaki bulgular akım sürümlü manyetizasyon kontrol verimliliğini güçlendiren SOT aygıtlarında kullanılabileceğini göstermektedir.

Anahtar Kelimeler: Yüzeye Dik Manyetik Anizotropi, Manyetik Tünel Eklemi, Spin-Yörünge-Torku, Akım-Sürümlü Manyetizasyon Kontrolü, Manyetik Rasgele Erişimli Hafıza.

GENİŞLETİLMİŞ ÖZET

Hafıza aygıtlarının kapasitelerinin, her yıl bir önceki yıla kıyasla iki kat arttığı gözlenmiştir. Ancak son zamanlarda, kapasitelerinin arttırılmasında yaşanan güçlükler (örneğin bilginin manyetik katmanlara yatay olarak yazılması gibi) bu oranı %40'lar seviyesine geriletmiştir. Her bir datanın (0 veya 1) yazılması için oluşturulan aygıt boyutu çok küçültüldüğünde ve birbirlerine yaklaştırıldıklarında, termal enerjileri bir demanyetizasyon oluşturmaktadır. Bu zorluğun ve sınırlayıcı faktörlerin etkisini ortadan kaldırmak için, araştırmacılar yeni bir manyetik yazma tekniği geliştirdiler. Burada bilgi manyetik katmana yatay değil de dik bir şekilde yazılarak, aygıtın kapasitesini yaklaşık 10 kat daha arttırdığı ve yukarıda bahsedilen negatif etkinin ortadan kalktığı gözlenmiştir. Son yıllarda yeni nesil elektronik aygıtların geliştirilmesindeki potansiyelinden ötürü, ultra ince filmlerde yüzeye dik oluşturulan manyetik anizotropinin elde edilmesi ve araştırılması oldukça ilgi çekmiştir. Kapasiteye ek olarak, tasarlanan aygıtların enerji tüketimleri, bilgiyi yazma ve okuma hızları gibi bir çok teknolojik parametrenin geliştirilmesi için son yıllarda spin-tabanlı elektrik (Spintronik) konusu oldukça yoğun olarak çalışılmaktadır. Spintronik aygıtlarda elektronun yükünün yanı sıra spin açısal momentum değeri de kullanılmaktadır. Dolayısıyla, spin-tabanlı elektronik aygıtların kapasiteleri klasik elektronikteki aygıtlara göre daha hızlı, daha yoğun ve daha az enerji tüketimiyle çalışabilmektedirler.

Bu tez kapsamında, manyetik tünel eklemlerin serbest bölgesi; tampon katmanın kalınlığı, tünel katmanın materyali, ferromanyetik katmanın kalınlığı ve aygıt tasarım mühendisliği yapılarak optimize edilmeye çalışılmıştır. Üretilen katmanlı yapılar magnetron püskürtme sistemi ile termal olarak okside edilmiş Si/SiO_2 alttaşlar üzerine büyütülmüştür. Magnetron püskürtme sisteminde metal katmanlar DC güç kaynağı, yalıtkan katmanlar ise RF güç kaynağı ile plazma oluşturarak katmanlı filmler büyütülmüştür. Manyetik tünel eklemlerin serbest bölgesi aşağıda verilen araştırmalar yapılarak optimize edilmiştir.

İlk olarak, katmanlı yapılarda tampon katmanının kalınlığına (Hf) bağlı olarak yapının manyetik, taşınım ve spintronik özellikleri araştırılmıştır. Burada üretilen katmanlı ince filmler:

$Si/SiO_2/Hf(t)/Co_{20}Fe_{60}B_{20}(1.1)/MgO(2.0)/Ta(2.0)$ (burada t = 0.5, 0.75, 1.0, 1.5, 2.5, 3.5, 5.0, 7.0, 8.5 ve 10.0 nm'dir).

Üretilen katmanlı filmlerin yapısal özellikleri Atomik Kuvvet Mikroskobu (AFM) ve X-ışını Fotoelektron Spektroskopi (XPS) kullanılarak araştırılmıştır. Manyetik özellikleri Manyeto-Optik-Kerr-Etkisi (MOKE) ve Titreşimli Örnek Manyetometresi (VSM) kullanılarak araştırılmıştır. Taşınım ve spintronik özellikleri Probe İstasyonu ve Vektör ölçümleri ile gerçekleştirilmiştir. Tampon katmanın kalınlığı ile filmin yüzey pürüzlülüğünü araştırmak için gerçekleştirilen AFM analizlerinden, yüzey pürüzlülüğünün tampon katmanın kalınlığı ile arttığı gözlemlenmiştir. Tampon katman kalınlığının 5.0 nm'yi aştığı filmlerdeki AFM görüntülerinde yığılma şeklinde birikintiler ve öbekler gözlemlenmiştir. Bu öbeklerin kalınlığının yaklaşık 0.45 nm olması 1.1 nm kalınlığındaki ferromanyetik katmanın kristal yapısını da bozmuştur. Manyetik sonuçlardan da gözlemlendiği gibi manyetik anizotropi değeri tampon katmanın kalınlığının artması ile azalmıştır. XPS analizinden, Fe-O ve B-O hibritleşme miktarları tespit edilmiş ve manyetik anizotropi ile ilişkisi incelenmiştir. Yüzeye dik oluşan manyetik anizotropi (PMA) değerinin Hf tabakasının artışı (0.75 nm'den 3.5 nm'ye) ile güçlendiği ve bu durumun da Fe-O bağının artması ve B-O hibritleşmesinin azalması ile orantılı olduğu bulunmuştur. Bu sonuçların literatür ile uyumlu olduğu da gözlemlenmiştir. MOKE ve VSM analizlerinden katmanlı ince filmlerin manyetik özellikleri detaylı bir şekilde çalışılmıştır. Manyetik anizotropi alanının Hf katman kalınlığına bağlılığı tek düze olmayan bir şekilde değiştiği ve bu değişimin AFM ve XPS sonuçları ile uyumlu olduğu gözlemlenmiştir. Taşınım ve spintronik analizlerinden, çok ilginç olarak sönümleme spin-yörünge torkunun Hf katman kalınlığının artması ile işaret değiştirdiği gözlemlenmiştir. Bulk (yığın) formundaki elementlerin üreteceği spin akımları tek başlarına yön değiştirmezken,

büyüttüğümüz katmanlı ince filmlerde bu yön değişimini ara yüzeylerden geri saçılan elektronlara ve AFM görüntülerinden elde edilen öbek şeklindeki Hf birikimlerinden kaynaklandığını düşünmekteyiz. Ara yüzeydeki bu bozukluk bir iç elektrik potansiyeli oluşturacağından, Rashba ara yüzey alanının bulk formlarına göre daha baskın geleceğini düşünmekteyiz. Bu bölümde yapılan optimizasyon çalışmalarından, 3-6 nm aralığındaki Hf katman kalınlığının manyetik tünel eklemlerinin serbest bölgesinde uygun olacağı sonucuna varılmıştır.

İkinci olarak, yalıtkan (tünel) katmanda farklı malzemeler kullanılarak oluşturulan katmanlı ince filmlerin ve aygıtların manyetik, taşınım ve spintronik özellikleri araştırılmıştır. Burada üretilen katmanlı ince filmler:

$Si/SiO_2/Hf(5.0)/CoFeB(0.8)/MgO$ ve $Si/SiO_2/Hf(5.0)/CoFeB(0.8)/TaO_x$.

Üretilen katmanlı ince filmlerin manyetik, taşınım ve spintronik özellikleri MOKE, VSM ve Probe İstasyonu kullanılarak çalışılmıştır. Manyetik analizler, MgO kaplı katmanlı ince filmlerin PMA değerinin TaO_x kaplı olana göre daha büyük olduğunu göstermiştir. Bunun nedeninin CoFeB katmanın üzerine büyütülen seramik yapıdaki MgO (001) ve metal Ta'nın oksijen plazması ile oksitlendirilmesinden kaynaklanmış olabileceğini yorumladık. PMA değeri ferromanyetik katmanın kristal yapısıyla da ilgili olduğundan (001 yönelimi), MgO kaplı örnekte daha kaliteli bir ara yüzey olduğu sonucuna varılmıştır. Bu sonucu desteklemek için yaptığımız manyetik analizlerden ferromanyetik ölü tabaka kalınlığı tayinini gerçekleştirdik. Bu analize göre, 0.17 ve 0.24 nm ölü CoFeB tabakası elde edilmiştir. Buna ek olarak, her iki örnek için ara yüzey etkin manyetik anizotropi enerji yoğunluğu hesaplaması yapılmıştır. Bu hesaplama sonucunda MgO ve TaO_x kaplı ince filmlerin ara yüzey anizotropi enerji yoğunluğu sırasıyla 1.5 ± 0.3 erg/cm^2 ve 1.2 ± 0.3 erg/cm^2 olduğu bulunmuştur. Taşınım ve spintronik özelliklerinin incelenmesi için gerçekleştirilen probe istasyonu ve vector ölçümlerinden, MgO kaplı aygıtın FL-SOT değerinin TaO_x kaplı aygıta göre 13 kez daha büyük olduğu, DL-SOT değerinin ise 6 kez daha güçlü olduğu deneysel olarak bulunmuştur. Bu sonuçlardan, MgO kaplı katmanlı

ince filmlerin manyetik tünel eklemlerin serbest bölgesinde kullanılması MRAM aygıtların enerji ve yoğunluk performansı açısından kullanışlı olacağı sonucuna varılmıştır.

Son olarak, dış manyetik alana gerek kalmadan sadece akım sürerek manyetizasyonun kontrolünün sağlanması için ferromanyetik serbest katmanın kalınlık ve simetri düzeni bozularak katmanlı ince filmlerin ve aygıtların manyetik, taşınım ve spintronik özellikleri araştırılmıştır. Burada üretilen katmanlı ince filmler:

$Si/SiO_2/Hf(5.0)/Co_{20}Fe_{60}B_{20}$(*wedge*)$/MgO(2.0)/Ta(1.0)$ ve $Si/SiO_2/Hf(5.0)/Co_{20}Fe_{60}B_{20}$(*wedge*)$/TaO_x(2.0)$ (burada *wedge*=0.4-1.6 nm aralığındadır).

Üretilen katmanlı ince filmlerin manyetik, taşınım ve spintronik özellikleri MOKE, VSM ve probe istasyonu kullanılarak çalışılmıştır. Manyetik analiz sonuçları bir önceki film yapısına benzerliğinden dolayı benzer sonuçlar göstermiştir. Bu yapıdaki filmlerde ferromanyetik katmanın kalınlığına bağlı olarak PMA'da iki farklı yönelim gözlenmiştir. CoFeB katman kalınlığının 0.4 nm'den 1.0 nm'ye kadar ki artışında PMA'da bir artış gözlenirken, 1.0 nm'den 1.6 nm'ye kadar ki artışta PMA'da bir azalma gözlemlenmiştir. İlk bölgede PMA'nın artması ara yüzeydeki manyetik anizotropinin artması ile ilgiliyken, ikinci bölgede PMA'nın azalması artan CoFeB katmanının artık ince film formundan çıkıp bulk özellik göstermeye başlaması ile ilgili olduğu sonucuna varılmıştır. Taşınım ve spintronik özelliklerinin incelenmesi için gerçekleştirilen probe istasyonu ve vektör ölçümlerinden, MgO kaplı aygıtların DL-SOT ve FL-SOT değerlerinin TaOx kaplı aygıtlara göre daha büyük olduğu deneysel olarak bulunmuştur. DL ve FL-SOT'ların yanısıra filmlerin büyütme eksenine ek olarak düzlemsel olarakta simetrisi üzerine mühendislik yapılarak yeni bir dik FL-SOT oluşturulmuştur. Bu yeni tork MgO kaplı katmanlı yapıda sadece akım sürümü ile manyetizasyonun kontrolüne olanak sağladığı deneysel olarak gözlemlenmiştir. MgO kaplı katmanlı yapısındaki aygıtlarda dış manyetik alan olmadan akım sürerek gerçekleştirilen manyetizasyon kontrolü CoFeB katman kalınlığına bağlı olarak araştırıldı.

Ferromanyetik katmanın 0.4-1.0 nm kalınlık aralığında dış manyetik olmadan sadece akım sürerek manyetizasyon kontrolü sağlanabilirken, 1.0 nm'den daha kalın olan CoFeB katmanlı aygıtlarda bir dış manyetik alana gerek olduğu gözlemlenmiştir. Filmlerin büyütme yönündeki simetri bozukluluğunun yanı sıra düzlemsel olarak yapılan mühendislik ile bozulan simetri ile üretilen akım sürümlü dik spin-orbit torku manyetizasyonun kontrolünde dış manyetik alana bağlılığını ortadan kaldırmıştır. Dolayısıyla manyetizasyonun kontrolü sadece akım ile sağlanmış olup enerji tüketimini önemli ölçüde azaltmıştır. Bu sonuçlardan, MgO kaplı katmanlı ince filmlerin manyetik tünel eklemlerin serbest bölgesinde kullanılması MRAM aygıtların enerji ve yoğunluk performansı açısından kullanışlı olacağı sonucuna varılmıştır.

ACKNOWLEDGEMENTS

I would like to express my gratitude to all those people who have stand with me and contributed to my scientific and life experience during the completion of this thesis. I would like to many thanks all of those people.

In particular, I would like to express my deepest gratitude with my warmest regards to my supervisor, Assoc. Prof. Dr. Ahmet Ekicibil, for all his help, providing guidance, advice, encouragement and contribution through my PhD research. I must say that if Prof. Ekicibil did not encourage and support me on this subject in the beginning of my PhD study, I might not be complete successfully the dissertation. I would like to extent my sincerest thanks and appreciation to Prof. Ekicibil.

Secondly, I would like to thank to Prof. Kang L. Wang who opened the doors of Device Research Laboratories (DRLs) in University of California, Los Angeles (UCLA) during one and half year of my PhD research. His experience on the field of nanoelectronics and his guidance on my research projects helps me a lot during my dissertation research under his co-supervisor, not-officially. I would like to extent my appreciation to Prof. Wang for his care, guidance and encouragements.

Thirdly, I would like to thank to Prof. Pedram K. Amiri who is my co-supervisor in DRL group. He is not officially my supervisor but effectively guided me for all time during the research, even now. He always keeps open his door for discussions and his practical solutions. Whenever I face a problem and/or need a guidance, I just knock his door.

Fourthly, I would also like to thank people in the DRL spintronics group for helping me out on the way of my PhD research. Dr. Juan J. Alzate, Dr. Guoqiang Yu, Dr. Kin L. Wong, Dr. Qi Hu, Dr. Hochul Lee, Dr. Pramey Upadhyaya, Dr. Mohsen Yazdani, Dr. Mighua Li, Farbod Ebrahimi and Xue Qing Cai for their support.

Next, I would like to thank to my co-workers in Material Research Group. Assist. Prof. Dr. Ali Osman Ayaş, Dr. Selda Kılıç Çetin, Gönül Akça and İdris Adanur for their support.

I would like to thank to The Scientific and Technological Research Council of Turkey (TUBITAK) for supporting me during the visiting period in California University, Los Angeles, USA. Also, I want to thank a lot to the Research Funding Projects Unit and its members in Çukurova University for their support this PhD thesis under the project numbers FEF2013D31. I am also grateful to all staff of Institute of Natural and Applied Sciences for their valuable friendship and their support.

Last but not least, I would like to express my deepest thanks to my family for their supports and patience.

CONTENTS **PAGE**

ABSTRACT I
ÖZ II
GENİŞLETİLMİŞ ÖZET. III
ACKNOWLEDGEMENTS IX
CONTENTS X
LIST OF TABLES XIV
LIST OF FIGURES XVI
LIST OF ABREVIATIONS. XXX
1.INTRODUCTION 1
1.1. Motivation and Background of Spintronics 1
1.2. Towards Magnetic Random Access Memory (MRAM) 5
1.3. Nature of Spin 7
1.3.1. Spin Injection, Accumulation and Detection 9
1.3.2. Spin-Orbit Interaction 10
1.3.3. Spin-Orbit Torques 14
1.4. Origin of Magnetization 19
1.5. Hall Effects 25
1.5.1. Ordinary Hall Effect 25
1.5.2. Anomalous Hall Effect 27
1.5.3. Spin-Hall Effect 28
1.5.3.1. Intrinsic Mechanism of SHE 29
1.5.3.2. Extrinsic Mechanism of SHE 32
1.6. Magnetic Anisotropy in Multilayer Structures 38
1.6.1. Shape Anisotropy 40
1.6.2. Magneto-Crystalline Anisotropy 42
1.6.3. Magneto-Elastic Anisotropy 43
1.6.4. Interface Magnetic Anisotropy 44

1.7. Current-Induced Magnetization Switching Mechanism in Spin-Transfer Torque and Spin-Orbit-Torque based Devices....46
1.8. Objectives and Thesis Outlines....50
2. LITERATURE REVIEW....53
2.1. A Review on the Perpendicular Magnetic Anisotropy....54
2.2. A Review on the Controlling of Magnetic Layer in Heavy Metal/ Ferromagnet/Oxide Layer and MTJs....69
3. MATERIAL AND METHOD....81
3.1. Thin-Film Deposition Process....82
3.2. Device Fabrication....84
3.3. Sample Characterization Technique....92
3.3.1. Atomic Force Microscopy (AFM)....92
3.3.2. Magneto-Optical Kerr Effect (MOKE)....94
3.3.3. Transmission Electron Microscopy (TEM)....96
3.3.4. X-Ray Photoelectron Spectroscopy (XPS)....98
3.3.5. Transport Measurements....100
3.3.5.1. Probe Station....101
3.3.5.2. Vector Measurement System....102
3.3.6. Vibrating Sample Magnetometer (VSM)....107
4. RESULTS AND DISCUSSIONS....111
4.1. Heavy Metal Layer Thickness Dependence on Structural, Magnetic, Transport and Spintronic Properties in Hf(t)|CoFeB|MgO|Ta Multilayer Structures....112
4.1.1. Atomic Force Microscope Analysis of Hf(t)|CoFeB|MgO|Ta Multilayer StructuresAtomic Force Microscopy (AFM)....112
4.1.2. Transmission Electron Microscope Imaging in Hf|CoFeB|MgO Multilayer Structure....116
4.1.3. X-ray Photoelectron Spectroscopy Analysis of Hf(t)|CoFeB|MgO| Ta Multilayer Structures....122

4.1.4. Magnetic Analysis of Hf(t)|CoFeB|MgO|Ta Multilayer Structures .133
4.1.5. Transport Analysis of Hf(t)|CoFeB|MgO|Ta Multilayer Structures .145
4.1.6. Hf Layer Thickness Dependence on Damping-Like Spin-Orbit Torque in Hf(t)|CoFeB|MgO|Ta Multilayer Structures 161
4.1.7. Current-Driven Magnetization Switching by Spin-Orbit Torques in Hf(t)|CoFeB|MgO|Ta Multilayer Structures.....167
4.2. Oxide Layer Effect on Magnetic, Transport and Spintronic Properties in Hf|CoFeB|MgO and Hf|CoFeB|TaOx Multilayer Structures 171
4.2.1. Oxide Layer Effect on Magnetic Anisotropy and Transport Properties in Hf|CoFeB|MgO and Hf|CoFeB|TaOx Multilayer Structures.....172
4.2.2. Oxide Layer Effect on Spin-Orbit Torques in Hf|CoFeB|MgO and Hf|CoFeB|TaOx Multilayer Structures.....175
4.2.3. Current-Driven Magnetization Switching in Hf|CoFeB|MgO and Hf|CoFeB|TaOx Multilayer Structures.....185
4.3. New Spin-Orbit Torque Engineering via Lateral Symmetry Breaking in both Hf|CoFeB(wedge)|MgO and Hf|CoFeB(wedge)|TaOx Multilayer Structures 187
4.3.1. Wedge Shape Effect on Perpendicular Magnetic Anisotropy in Hf|CoFeB(wedge)|MgO and Hf|CoFeB(wedge)|TaOx Multilayer Structures.....190
4.3.2. Transport Analysis of Symmetry Breaked Hf|CoFeB(wedge)| MgO and Hf|CoFeB(wedge)|TaOx Multilayer Structures.....193
4.3.3. Current-Driven Magnetization Switching by Spin-Orbit Torques in Hf|CoFeB(wedge)|MgO and Hf|CoFeB(wedge)|TaOx Multilayer Structures.....213
4.3.4. CoFeB Layer Thickness Dependence on Field-Like Spin-Orbit Torque in Hf|CoFeB(wedge)|MgO and Hf|CoFeB(wedge)|TaOx Multilayer Structures 220

4.3.5. CoFeB Layer Thickness Dependence on Current-Driven Magnetization Switching in Hf|CoFeB(wedge)|MgO and Hf|CoFeB(wedge)|TaOx Multilayer Structures.....224
5. CONCLUSIONS 227
REFERENCES. 231
CURRICULUM VITAE 247

LIST OF TABLES **PAGE**

Table 1.1. Comparison of existing and emerging memory families in terms of technological requirements.....6
Table 1.2. Comparison of charge conductivities, spin-Hall conductivities and spin-Hall angles from experimental measurements.....36
Table 1.3. The demagnetization factors for simple shapes.....41
Table 4.1. The desired and actual thickness of each layer in Hf|CoFeB|MgO|Ta multilayer structure.....118
Table 4.2. Atomic percentage of each element in the selected points in TEM image for Hf|CoFeB|MgO|Ta multilayer structure.....122

LIST OF FIGURES **PAGE**

Figure 1.1. Magnetoresistance of Fe/Cr superlattices at 4.2 K temperature (Baibich, 1988).....2

Figure 1.2. A basis magnetic tunnel junction structure for parallel (Low Resistance) and antiparallel (High Resistance) magnetization states to each ferromagnetic layer. 3

Figure 1.3. Longitudinal (Standard) Recording (left-side), Perpendicular Recording (right-side) in the hard disc head. 5

Figure 1.4. Comparison of DRAM, SRAM, FLASH and MRAM families in terms of technological requirements. 7

Figure 1.5. Schematic illustration of spin injection, spin transfer and spin detection in a device composed of ferromagnet/non-magnet/ferromagnet trilayer structure. 9

Figure 1.6. a) An electron moves in a circular motion seen by the nucleus, b) the same motion but seen by the electron that the nucleus moves around the electron.....11

Figure 1.7. The estimated spin-orbit-coupling constant as a function of atomic number.....13

Figure 1.8. The motion of magnetization by precession and damping drawn by taken into account of LLG relation. 16

Figure 1.9. The motion of the magnetization by precession, damping and spin-transfer-torque damping drawn by taken into account of modified Slonczewski-LLG relation. 17

Figure 1.10. The magnetic moment generated from current loop. 19

Figure 1.11. Schematic illustrations of ferromagnetic, anti-ferromagnetic and ferrimagnetic materials.....24

Figure 1.12. A schematic illustration of ordinary Hall effect. 25

Figure 1.13. A schematic illustration of Anomalous Hall effect. 28

Figure 1.14. The spin-splitting under internal electric field due to the spin-orbit coupling. 30
Figure 1.15. The theoretically calculated intrinsic spin Hall conductivity for 4*d* and 5*d* transition metals (Tanaka et al., 2008).....31
Figure 1.16. Schematic illustration of spin-skew scattering effect a) before and b) after scattering when electrons are impressed by the local potential such as impurity or defect.....33
Figure 1.17. Schematic illustration of side-jump scattering effect a) before, after b) first and c) second scattering when electrons are impressed by the local potentials such as impurity or defect. 34
Figure 1.18. A review of Anomalous Hall conductivity as a function of longitudinal charge conductivity for various materials in the literature (Onoda et al., 2008). 35
Figure 1.19. Hysteresis of a ferromagnetic material.....38
Figure 1.20. Hysteresis of a ferromagnetic thin film having magnetic anisotropy. The blue (orange) color curve indicates the external magnetic field is perpendicular (paralel) to the film surface.....39
Figure 1.21. An ellipsoidal shape of a material. 41
Figure 1.22. Relative magnetization of single crystals of bcc-Fe, fcc-Ni and hcp-Co (Getzlaff, 2008). 42
Figure 1.23. Effective magnetic anisotropy energy density multiplied by the thickness of ferromagnetic Co film as a function of ferromagnetic Co layer thickness (Getzlaff, 2008). 46
Figure 1.24. Manipulation of free layer magnetization by Spin-Transfer-Torque (STT)-based device composed of free layer ferromagnet/tunnel barrier/fixed layer ferromagnet structure. 48
Figure 1.25. Manipulation of free layer magnetization by Spin-Orbit-Torque (SOT)-based device composed of heavy-metal/free layer ferromagnet/tunnel barrier/fixed layer ferromagnet structure. 49

Figure 2.1. Effective magnetic anisotropy energy times ferromagnetic layer thickness as a function of ferromagnetic layer thickness in Ta/CoFeB/MgO and Hf/CoFeB/MgO systems. 55
Figure 2.2. Effective magnetic anisotropy energy times ferromagnetic layer thickness as a function of ferromagnetic layer thickness for as-deposited and annealed stacks under magnetic field. 56
Figure 2.3. The moment as a function of applied magnetic field for a) CFB(15)/Ta and CFB(20)/Ru and b) CFB(20)/Ru(9) and CFB(20)/Ru(50) films. 57
Figure 2.4. Hall resistance as a function of applied magnetic field for a) SiO_2/Co(0.6)/Pt and b) SiO_2/Co(1.5)/Pt films annealed at various temperatures.....58
Figure 2.5. Anisotropy field as a function of annealing temperature. 59
Figure 2.6 a-d) Magnetic hysteresis of CoFeB/X (MgO, W, Ta and Ti) by sweeping both perpendicular and in-plane direction of magnetic field. e-f) schematically illustration of interfacial magnetic anisotropy. 60
Figure 2.7 a) Moment versus CoFeB layer thickness at various B concentration, b) Dead layer thickness as a function of B composition in ferromagnetic layer, c Saturation magnetization as a function of B composition in ferromagnetic layer. 62
Figure 2.8. Effective magnetic anisotropy energy density as a function of B composition in ferromagnetic layer.....63
Figure 2.9. Tunneling magnetoresistance as a function of B composition in ferromagnetic layer.....64
Figure 2.10. Multilayer film stacks a) before and b) after annealing process.....65
Figure 2.11. The x-ray photoelectron spectrum in Ta/CoFeB/MgO structure.....66
Figure 2.12. Moment versus external magnetic field in Ta/Co₁FeB/MgO stack annealed at a) 300°C, b) 325°C, c) 350°C and d) 375°C. 67

Figure 2.13 a) Multilayer structures of Sample A and Sample B, b) XPS depth profile of Co and Ta in such structure. 68
Figure 2.14. Transverse effective field as a function of applied voltage for various a) Ta and b) CoFeB thickness in Ta/CoFeB/MgO structure. The $\Delta HT/Vin$ versus a) Ta and b) CoFeB thickness in Ta/CoFeB/MgO structure.....70
Figure 2.15. Longitudinal effective field as a function of applied voltage for various a) Ta and b) CoFeB thickness in Ta/CoFeB/MgO structure. The $\Delta HL/Vin$ versus a) Ta and b) CoFeB thickness in Ta/CoFeB/MgO structure.....71
Figure 2.16. The relative magnitude of the transverse and longitudinal fields as a function of a) Ta and b) CoFeB thickness in Ta/CoFeB/MgO structure.....72
Figure 2.17 a) Multilayer film structure. FMR signal as a function of external magnetic field for b) CoFeB/Ta and c) CoFeB/Pt structure, d) effective field generated by SOT as a function of frequency.....73
Figure 2.18. Anomalous Hall resistance as a function of a) external magnetic field and b) dc electric current.....75
Figure 2.19. The film structure and device shape.....76
Figure 2.20 a) Diagrams representing Mz reversal regions, showing the intensity and orientation of the applied magnetic field, B, at constant current (I=3.3 mA), b)applied magnetic field as a function of angle between current and magnetic field, c) schematic illustration of current-induced effective fields on the magnetization. 77
Figure 2.21. Anomalous Hall resistance as a function of longitudinal magnetic field at various electric current. 78
Figure 2.22. Polar MOKE images at different H_x with I_x =−8 mA.....79

Figure 3.1. The schematic illustration of multilayer film structure. 82
Figure 3.2. Basic representation of sputtering process. 83
Figure 3.3. Physical Vapor Deposition System (AJA Sputtering System) at UCLA. 84
Figure 3.4. Photo-Resist coating by Spin-Coating equipment at UCLA NanoLab. 86
Figure 3.5. KARL SÜSS mask aligner to expose the films coated by photoresist at UCLA NanoLab. 87
Figure 3.6. Development Process. 88
Figure 3.7. Microscope to check whether the development process is performed successfully, or not (UCLA NanoLab). 88
Figure 3.8. Dry-etching equipment at UCLA NanoLab. 89
Figure 3.9. Metal deposition equipment at UCLA NanoLab.....90
Figure 3.10. Device Fabrication Process. 91
Figure 3.11. The microscope images of the fabricated Hall-bar device. 92
Figure 3.12. The working scheme of the atomic force microscope. 93
Figure 3.13. Park-System Atomic Force Microscope.....94
Figure 3.14. The schematic form of the Magneto-Optical Kerr Effect set-up (LIA1: Lock-in Amplifier-1, LIA2: Lock-in Amplifier-2, DVM: DC Voltmeter). 95
Figure 3.15. Magneto-Optical Kerr Effect (MOKE) measurement set-up at UCLA Device Research Laboratory. 95
Figure 3.16. The principle of Transmission Electron Microscope imaging technique. 97
Figure 3.17. Energy band diagram of a material. 99
Figure 3.18. A schematic illustration of x-ray photoelectron spectroscopy. 99
Figure 3.19. ESWCALAB 250Xi X-ray Photoelectron Spectroscopy (XPS). ...100
Figure 3.20. The set-up of probe station for out-of-plane transport measurements. 101

Figure 3.21. The screen capture of in-time measurement.....102
Figure 3.22. The coordinate system of a magnetization vector in a ferromagnetic layer.....103
Figure 3.23. The set-up of vector measurement in Lake-Shore Probe Station at UCLA Device Research Laboratory.....105
Figure 3.24. The first-order harmonic signal versus in-plane magnetic field as an example on the calculation of effective field. 106
Figure 3.25. The second-order harmonic signal versus in-plane magnetic field as an example on the calculation of effective field. 106
Figure 3.26. The screen capture of in-time measurement.....107
Figure 3.27. The schematic illustration of vibrating sample magnetometer.....108
Figure 3.28. Quantum Design DynaCool Physical Properties Measurement System (PPMS) with Vibrating Sample Magnetometer (VSM) module.....109
Figure 4.1 a-g (h-n) The 2D (3D) atomic force microscope images of the Hf(*t*)|CoFeB|MgO|Ta multilayer films for t_{Hf} = 1.0, 1.5, 2.5, 3.5, 5.0, 7.0 and 10 nm, respectively.....115
Figure 4.2. The roughness, R_q found from the atomic force microscope imaging technique versus Hf layer thickness in Hf(*t*)|CoFeB(1.1)|MgO(2.0) |Ta(2.0) multilayer film structure.....116
Figure 4.3. Transmission electron microscope images of Hf|CoFeB|MgO|Ta multilayer structures scaled at a)100 nm, b) 50 nm, c) 20 nm and d) 2nm. 117
Figure 4.4 a-e. The energy dispersive spectrums of P1, P2, P3, P4 and P5 points in SiO_2|Hf|CoFeB|MgO|Ta multilayer structure, respectively.....121
Figure 4.5. The x-ray photoelectron spectrum of Ta-4*f* in Hf(*t*)|CoFeB|MgO|Ta multilayer structure a) *t*=0.75 nm and b) *t*=3.5 nm. 124

Figure 4.6. The x-ray photoelectron spectrum of O-1*s* in Hf(*t*)|CoFeB|MgO|Ta multilayer structure a) *t*=0.75 nm and b) *t*=3.5 nm. 126
Figure 4.7. The x-ray photoelectron spectrum of Mg-1*s* in Hf(*t*)|CoFeB|MgO|Ta multilayer structure a) *t*=0.75 nm and b) *t*=3.5 nm. 127
Figure 4.8. The x-ray photoelectron spectrum of B-1*s* in Hf(*t*)|CoFeB|MgO|Ta multilayer structure a) *t*=0.75 nm and b) *t*=3.5 nm. 128
Figure 4.9. The x-ray photoelectron spectrum of Fe-3*p* in Hf(*t*)|CoFeB|MgO|Ta multilayer structure a) *t*=0.75 nm and b) *t*=3.5 nm. 130
Figure 4.10. The x-ray photoelectron spectrum of Hf-4*f* in Hf(*t*)|CoFeB|MgO|Ta multilayer structure a) *t*=0.75 nm and b) *t*=3.5 nm. 132
Figure 4.11. Magneto-Optical Kerr effect curves measured under out-of-plane magnetic field for a) t_{Hf}=0.5 nm, b) t_{Hf}=1.0 nm, c) t_{Hf}=1.5 nm, d) t_{Hf}=2.5 nm, e) t_{Hf}=3.5 nm, f) t_{Hf}=5.0 nm, g) t_{Hf}=7.0 nm, h) t_{Hf}=8.5 and i) t_{Hf}=10.0 nm in Hf(*t*)|CoFeB(1.1)|MgO(2.0)|Ta(2.0) multilayer films. 137
Figure 4.12. The coercive field, H_c as a function of Hf layer thickness in Hf(*t*)|CoFeB(1.1)|MgO(2.0)|Ta(2.0) multilayer films. 138
Figure 4.13. Magnetic hysteresis curves measured under both in-plane and out-of-plane magnetic field for a) t_{Hf}=0.5 nm, b) t_{Hf}=1.0 nm, c) t_{Hf}=1.5 nm, d) t_{Hf}=2.5 nm, e) t_{Hf}=3.5 nm, f) t_{Hf}=5.0 nm, g) t_{Hf}=7.0 nm, h) t_{Hf}=8.5 and i) t_{Hf}=10.0 nm in Hf(*t*)|CoFeB(1.1)|MgO(2.0)|Ta(2.0) multilayer films. 143
Figure 4.14. The anisotropy field, H_k as a function of Hf layer thickness in Hf(*t*)|CoFeB(1.1)|MgO(2.0)|Ta(2.0) multilayer films. 144

Figure 4.15. a) Optical photograph of one device and the dc transport experimental configuration, b) Schematic illustration of the film structure of Hf|CoFeB|MgO multilayer with electric current in the *x* direction. 145
Figure 4.16. The ΔR_{AHE} as a function of Hf layer thickness in the Hf(*t*)|CoFeB|MgO|Ta multilayer structure. 148
Figure 4.17. The anomalous Hall resistance as a function of out-of-plane magnetic field under several current density in Hf(1.5)|CoFeB(1.1)|MgO|Ta(2.0) multilayer structure. 150
Figure 4.18. The anomalous Hall resistance as a function of in-plane magnetic field under several current density in Hf(1.5)/CoFeB(1.1)/MgO/Ta(2.0) multilayer structure. 151
Figure 4.19. The anomalous Hall resistance as a function of out-of-plane magnetic field under several current density in Hf(2.5)|CoFeB(1.1)|MgO|Ta(2.0) multilayer structure. 152
Figure 4.20. The anomalous Hall resistance as a function of in-plane magnetic field under several current density in Hf(2.5)|CoFeB(1.1)|MgO|Ta(2.0) multilayer structure. 153
Figure 4.21. The anomalous Hall resistance as a function of out-of-plane magnetic field under several current density in Hf(3.5)|CoFeB(1.1)|MgO|Ta(2.0) multilayer structure. 154
Figure 4.22. The anomalous Hall resistance as a function of in-plane magnetic field under several current density in Hf(3.5)|CoFeB(1.1)|MgO|Ta(2.0) multilayer structure. 155
Figure 4.23. The anomalous Hall resistance as a function of out-of-plane magnetic field under several current density in Hf(5.0)|CoFeB(1.1)|MgO|Ta(2.0) multilayer structure. 156

Figure 4.24. The anomalous Hall resistance as a function of in-plane magnetic field under several current density in Hf(5.0)|CoFeB(1.1)|MgO|Ta(2.0) multilayer structure. 157
Figure 4.25. The anomalous Hall resistance as a function of out-of-plane magnetic field under several current density in Hf(7.0)|CoFeB(1.1)|MgO|Ta(2.0) multilayer structure. 158
Figure 4.26. The anomalous Hall resistance as a function of in-plane magnetic field under several current density in Hf(7.0)|CoFeB(1.1)|MgO|Ta(2.0) multilayer structure. 159
Figure 4.27. The anomalous Hall resistance as a function of out-of-plane magnetic field under several current density in Hf(10.0)|CoFeB(1.1)|MgO|Ta(2.0) multilayer structure. 160
Figure 4.28. The anomalous Hall resistance as a function of in-plane magnetic field under several current density in Hf(10.0)|CoFeB(1.1)|MgO|Ta(2.0) multilayer structure. 161
Figure 4.29. The schematic illustration of the multilayer structure and vector measurement configuration under sinusoidal bias current. 162
Figure 4.30. The first and second harmonic voltage as a function of in-plane longitudinal magnetic field for various Hf layer thickness in Hf(t)|CoFeB|MgO|Ta multilayer structure (t_{Hf} = 1.5, 2.5, 3.5, 5.0, 7.0, 8.5 and 10 nm).....163
Figure 4.31. The damping-like spin-orbit torque dependence Hf layer thickness for both $MzUp$ and $MzDown$ states in Hf(t)|CoFeB|MgO multilayer structure (t_{Hf} = 1.5, 2.5, 3.5, 5.0, 7.0, 8.5 and 10 nm).....164
Figure 4.32. The modelling of polarization of spin current as a function of heavy metal layer thickness.....165
Figure 4.33. The damping-like spin-orbit torque on magnetization a) without and b) with longitudinal external magnetic field.....167

Figure 4.34. The current-driven magnetization switching by spin-orbit torques in Hf(1.5)|CoFeB(1.1)|MgO|Ta(2.0) multilayer structure by applying a) positive and b) negative longitudinal external field to break the symmetry. 168
Figure 4.35. The current-driven magnetization switching by spin-orbit torques in Hf(2.5)|CoFeB(1.1)|MgO|Ta(2.0) multilayer structure by applying a) positive and b) negative longitudinal external field to break the symmetry. 169
Figure 4.36. The current-driven magnetization switching by spin-orbit torques in Hf(3.5)|CoFeB(1.1)|MgO|Ta(2.0) multilayer structure by applying a) positive and b) negative longitudinal external field to break the symmetry. 169
Figure 4.37. The current-driven magnetization switching by spin-orbit torques in Hf(5.0)|CoFeB(1.1)|MgO|Ta(2.0) multilayer structure by applying a) positive and b) negative longitudinal external field to break the symmetry. 170
Figure 4.38. The current-driven magnetization switching by spin-orbit torques in Hf(10.0)|CoFeB(1.1)|MgO|Ta(2.0) multilayer structure by applying a) positive and b) negative longitudinal external field to break the symmetry. 170
Figure 4.39. a) Optical graph of one device and the dc experimental configuration. b) The film structure of Hf|CoFeB|MgO(TaO_x) multilayer with ac electric current. H_R corresponds to the Rashba-field, H_{SHE} denotes the equivalent field due to the spin-Hall-effect, and M represents the magnetization direction of the CoFeB layer. 173
Figure 4.40. Anomalous Hall resistance, R_{AHE} as a function of the out-of-plane magnetic field, H_z in a) Hf|CoFeB|MgO and b) Hf|CoFeB|TaO_x multilayers. 174

Figure 4.41. Anomalous Hall resistance, R_{AHE} as a function of the in-plane (longitudinal) magnetic field, H_L in a) Hf|CoFeB|MgO and b) Hf|CoFeB|TaO_x multilayers. 175
Figure 4.42. First-harmonic signals, V^w as a function of in-plane magnetic field applied to the device in longitudinal, H_L (transverse, H_T) a) (c) Sample I and b) (d) Sample II and transverse direction, H_T. Inset of each figure corresponds to the second-harmonic signal, V^{2w} as a function of applied field for each sample. Solid red (solid black) and open red (open black) symbols represent the signal coming from the magnetization states of M_z>0, up and M_z<0, down, respectively. 178
Figure 4.43. Longitudinal (transverse) SOT-induced effective field generated by in-plane electric current depends on the amplitude of the alternating current for a) (c) Sample I and b) (d)Sample II. 181
Figure 4.44. The illustration of a, b) DL and c, d) FL effective fields on $MzUp$ and $MzDown$ in Hf|CoFeB|MgO and Hf|CoFeB|TaO_x structures. 182
Figure 4.45. The schematically illustration of the Hf|CoFeB|MgO (TaO_x) film stacks with each interface effect on ferromagnetic layer under in-plane electric current. Current is flowing in the +*x* direction a) (c) and –*x* direction b) (d) for MgO (TaO_x) cap layer. 184
Figure 4.46. Current-driven magnetization switching for a) MgO and b) TaO_x capped devices under positive (black) and negative (red) longitudinal magnetic fields. 186
Figure 4.47. Schematics of symmetry breaking in a) *z*-direction and b) both *y* and *z*-directions. 188
Figure 4.48. Moment per area as a function of CoFeB layer thickness in Hf|CoFeB(*wedge*)|MgO and Hf|CoFeB(*wedge*)|TaO_x structures. ..191

Figure 4.49. Effective magnetic anisotropy energy, K_{eff} multiplied by the thickness of the CoFeB film, t_{CoFeB}, as a function of the CoFeB thickness in Hf|CoFeB(*wedge*)|MgO and Hf|CoFeB(*wedge*)|TaO_x multilayer structures.....192
Figure 4.50. Anomalous Hall resistance as a function of out-of-plane magnetic field in a) Hf|CoFeB(wedge)|MgO and b) Hf|CoFeB(wedge)|TaO_x structures. The right axis indicates the thickness of CoFeB layer thickness in both multilayer structures. 194
Figure 4.51. The coercive field, H_c as a function of the CoFeB layer thickness in Hf|CoFeB(*wedge*)|MgO and Hf|CoFeB(*wedge*)|TaO_x multilayer structures.....195
Figure 4.52. Anisotropy field, H_k as a function of CoFeB layer thickness in Hf|CoFeB(*wedge*)|MgO and Hf|CoFeB(*wedge*)|TaO_x structures...196
Figure 4.53. Anomalous Hall resistance as a function of out-of-plane magnetic field at various bias currents for Device I.....197
Figure 4.54. The offset field as a function of current density for Device I.....198
Figure 4.55. Anomalous Hall resistance as a function of out-of-plane magnetic field at various bias currents for Device II. 199
Figure 4.56. The offset field as a function of current density for Device II. 200
Figure 4.57. Anomalous Hall resistance as a function of out-of-plane magnetic field at various bias currents for Device III. 201
Figure 4.58. The offset field as a function of current density for Device III.....202
Figure 4.59. Anomalous Hall resistance as a function of out-of-plane magnetic field at various bias currents for Device IV.....203
Figure 4.60. The offset field as a function of current density for Device IV.....204
Figure 4.61. Anomalous Hall resistance as a function of out-of-plane magnetic field at various bias currents for Device V. 205
Figure 4.62. The offset field as a function of current density for Device V.....206

Figure 4.63. Anomalous Hall resistance as a function of out-of-plane magnetic field at various bias currents for Device VI. 207
Figure 4.64. The offset field as a function of current density for Device VI.....208
Figure 4.65. Anomalous Hall resistance as a function of out-of-plane magnetic field at various bias currents for Device VII.....209
Figure 4.66. The offset field as a function of current density for Device VII. ...210
Figure 4.67. Anomalous Hall resistance as a function of out-of-plane magnetic field at various bias currents for Device VIII. 211
Figure 4.68. The offset field as a function of current density for Device VIII. ..212
Figure 4.69. Current-induced out-of-plane magnetization, M_z as a function of the current density for Device I. 214
Figure 4.70. Current-induced out-of-plane magnetization, M_z as a function of the current density for Device II.....214
Figure 4.71. Current-induced out-of-plane magnetization, M_z as a function of the current density for Device III. 215
Figure 4.72. Current-induced out-of-plane magnetization, M_z as a function of the current density for Device IV. 215
Figure 4.73. Current-induced out-of-plane magnetization, M_z as a function of the current density for Device V. 216
Figure 4.74. Current-induced out-of-plane magnetization, M_z as a function of the current density for Device VI. 216
Figure 4.75. The switching mechanism of magnetization under DL, FL and out-of-plane effective fields in Hf|CoFeB(wedge)|MgO structure. 217
Figure 4.76. The switching mechanism of magnetization under DL, FL and out-of-plane-FL effective fields in Hf|CoFeB(wedge)|TaO_x structure. 219
Figure 4.77. The βFL values as a function of the CoFeB thickness in Hf|CoFeB(*wedge*)|MgO multilayer structure. 221

Figure 4.78. The βFL values as a function of the CoFeB thickness in Hf|CoFeB(*wedge*)|TaO_x multilayer structure. 221
Figure 4.79. The βz values as a function of the CoFeB thickness in Hf|CoFeB(*wedge*)|MgO multilayer structure. 223
Figure 4.80. The βz values as a function of the CoFeB thickness in Hf|CoFeB(*wedge*)|TaO_x multilayer structure. 223
Figure 4.81. Current-induced perpendicular magnetic switching phase diagram in Hf|CoFeB(*wedge*)|MgO multilayer structure. 225
Figure 4.82. Current-induced perpendicular magnetic switching phase diagram in Hf|CoFeB(*wedge*)|TaO_x multilayer structure. 225

LIST OF ABREVIATONS

AFM : Atomic Force Microscope
AHE : Anomalous Hall Effect
ALD : Atomic Layer Deposition
AMR : Anisotropic Magneto-Resistance
Ar : Argon
$\vec{B}$: Strength of magnetic field
BE : Binding Energy
c : Velocity of light
CCD : Charge Coupled Device
CVD : Chemical Vapor Deposition
DI : De-Ionized
DL-SOT : Damping-Like Spin-Orbit Torque
DRAM : Dynamic Random Access Memory
e^- : Electron charge
$\vec{E}$: Strength of electric field
E_a : Anisotropy energy
E_B : Strength of Binding energy
E_{int} : Internal electric field
E_{kin} : Kinetic energy
EDS : Energy Dispersive Spectroscopy
EHE : Extraordinary Hall Effect
$\vec{F}$: Force vector
FL-SOT : Field-Like Spin-Orbit Torque
FM : Ferromagnetism
GMR : Giant Magneto-Resistance
g_s : Spin g factor

H_c : Coercive field

H_k : Anisotropy field

H^+ : Positive switching magnetic field

H^- : Negative switching magnetic field

H_L : Longitudinal magnetic field

H_R : Rashba field

H_T : Transverse magnetic field

H_z : Out-of-plane magnetic field

H_{offset} : Out-of-plane offset field

H_{SO} : Hamiltonian for Pauli Spin-Orbit term

$\vec{H}_{eff}$: Effective field vector

$\vec{H}_{ext}$: External field vector

$\vec{H}_{exch}$: Exchange field vector

$\vec{H}_{ani}$: Anisotropy field vector

$\vec{H}_{demag}$: Demagnetization field vector

$\vec{H}_{mc}$: Magnetostatic coupling field vector

$\vec{H}_{current}$: Ampere field vector

$\vec{H}_{th}$: Thermal field vector

$H_{y,z}^{FL}$: Strengths of the current-induced effective field-like field

$H_{y,z}^{DL}$: Strengths of the current-induced effective damping-like field

HM : Heavy-Metal

I : Electric current

IP : In-Plane

ISHE : Inverse Spin Hall Effect

$\vec{J}$: Total angular momentum vector

j : Quantum number of total angular momentum

J : Current density

J_s : Spin current density

J_c : Charge current density

J_x : Longitudinal current density

J_{sw} : Switching current density

J_{sw}^{+} : Positive switching current density

J_{sw}^{-} : Negative switching current density

K_{eff} : Effective magnetic anisotropy energy

K_b : Bulk magnetic anisotropy energy density

K_i : Interfacial magnetic anisotropy energy density

$\vec{L}$: Orbital angular momentum vector

l : Quantum number of orbital angular momentum

LIA : Lock-In Amplifier

m : Unit moment

m_{e^-} : Mass of a free electron

$\vec{M}$: Magnetization vector

M_r : Remanence magnetization

M_s : Saturation magnetization

M_z : Out-of-plane magnetization

M_z^{Up} : Up-state magnetization

M_z^{Down} : Down-state magnetization

MBE : Molecular Beam Epitaxy

MOKE : Magneto-Optical Kerr Effect

MR : Magneto-Resistance

MRAM : Magnetic Random Access Memory

MTJ : Magnetic Tunnel Junction

NAND-Flash : Negative-AND Flash Memory

OOP : Out-Of-Plane

OX : Oxide

$\vec{P}$	: Momentum vector
PMA	: Perpendicular Magnetic Anisotropy
PPMS	: Physical Property Measurement System
$\vec{r}$	: Position vector
R_0	: Anomalous Hall coefficient
R_{AHE}	: Anomalous Hall Effect Resistance
R_{AP}	: Anti-parallel Resistance
R_H	: Hall coefficient
R_P	: Parallel Resistance
$\vec{S}$	: Spin angular momentum vector
s	: Quantum number of spin angular momentum
SOC	: Spin-Orbit Coupling
SOI	: Spin-Orbit Interaction
SOT	: Spin-Orbit Torque
SRAM	: Static Random Access Memory
STT	: Spin Transfer Torque
STT-RAM	: Spin Transfer Torque Random Access Memory
SQUID	: Superconducting Quantum Interference Device
TEM	: Transmission Electron Microscope
TMR	: Tunneling Magneto-Resistance
t_c	: Critical thickness
t_{CoFeB}	: Thickness of CoFeB layer
t_{FM}	: Thickness of ferromagnetic layer
t_{HM}	: Thickness of heavy-metal layer
U	: Potential energy
UV	: Ultra-Violet
V	: Coulomb potential
$\vec{v}$	: Velocity vector

VSM : Vibrating Sample Magnetometer

VCMA : Voltage Controlled Magnetic Anisotropy

V^{1w} : First Harmonic Voltage

V^{2w} : Second Harmonic Voltage

Z : Atomic number

XPS : X-ray Photoelectron Spectroscopy

W_f : Work function

α : Damping factor

α_R : Strength of the Rashba effect

β_{DL} : Strength of Damping-Like torque

β_{FL} : Strength of Field-Like torque

β_z : Strength of out-of-plane torque

γ : Electron gyromagnetic ratio

σ : Stress

$\vec{\sigma}$: Vector of Pauli spin matrices

σ_{xx}^{c} : Charge conductivity

σ_{xy}^{s} : Spin-Hall conductivity

$\hat{\sigma}_{SHE}$: Spin-Hall spin matrices

δ_{SHE} : Spin-orbit torque spin-Hall effect coefficient

$\vec{\nabla}$: Vector of Delta operator

∇H^{DL} : Damping-like effective field

∇H^{FL} : Field-like effective field

∇H^{z} : Out-of-plane effective field

ε_0 : Vacuum electric permittivity

ε_{S0} : Spin-orbit coupling constant

$\hbar$: Planck constant

θ_{SHE} : Spin-Hall angle

λ : Damping parameter

λ_{sd} : Spin-diffusion length

λ_{hkl} : Magnetostriction constant

η : Damping parameter modified by Gilbert

μ_0 : Vacuum magnetic permittivity

μ_B : Bohr magneton

μ_l : Orbital magnetic dipole moment

μ_j : Total magnetic dipole moment

μ_s : Spin magnetic dipole moment

$\vec{\mu}$: Magnetic moment vector

$\vec{\tau}$: Torque vector

$\vec{\tau}_{SOT}$: Spin-Orbit Torque vector

$\tau_{\parallel}$: Parallel torque

$\tau_{\perp}$: Perpendicular torque

π : Pi number

ψ : Spacial wavefunction

χ : Spin wavefunction

1. INTRODUCTION

1.1. Motivation and Background of Spintronics

Over the last three decades, spin-based electronics called as “Spintronics” have become one of the most important research fields in the technology due to their new functionalities by using of electron’s spin as well as its charge. In conventional electronics, the electron’s spin is ignored because of the limitation of classical mechanics. However, in quantum mechanics, we must consider also electron’s spin angular momentum. Spin-based electronics have capability of new functionalities in terms of higher data processing speed, higher density, lower power consumption, higher reliability and non-volatility property than the conventional electronics (Wolf et al., 2001; Liu et al., 2012; Yu et al., 2014; Yu et al., 2014; Wang et al., 2013; Liu et al., 2012; Miron et al., 2011; Mihai Miron et al., 2010; Ryu et al., 2013; Emori et al., 2013). Since the electron’s spin is directly related to their magnetic moments that will be discussed in Section 1.4, the odd number of valence electrons can create a measurable intrinsic magnetic field. The spins of unpaired valance electrons can be aligned naturally parallel to each other without external magnetic field. This phenomena is known as “Ferromagnetism (FM)” and this type of materials are called ferromagnetic materials. Ferromagnetic materials play an important role in spintronics technology, because they provide spin-polarized currents. In addition, they can also exhibit the “Magnetoresistance (MR)” property which is defined as a change in the resistance of a material when external magnetic field is applied to the material. The MR ratio can be defined as

$$\frac{\Delta R}{R} = \frac{R_{AP} - R_P}{R_P} \tag{1.1}$$

where R_P and R_{AP} are the resistance of parallel and antiparallel alignment of the magnetization in two ferromagnetic layers. The first MR effect which is known as “Anisotropic Magnetoresistance (AMR)” was observed by Thomson in 1856

(Thomson, 1856). But, it was not pointed out due to its low resistance changing ~5% in that term. Almost one century later, a significant change in resistance was observed by applying external magnetic field in a multilayer structure where a non-magnetic layer is sandwiched between two ferromagnetic layers. After the discovery of the Giant Magnetoresistance (GMR) for the Fe/Cr nanostructure in 1988 by Albert Fert *et al*. (Binasch et al., 1989; Baibich et al., 1988), the scientists around the world have focused on this new promising area. Figure 1.1 shows the magnetoresistance of Fe/Cr superlattices for series repetation and various Cr thickness.

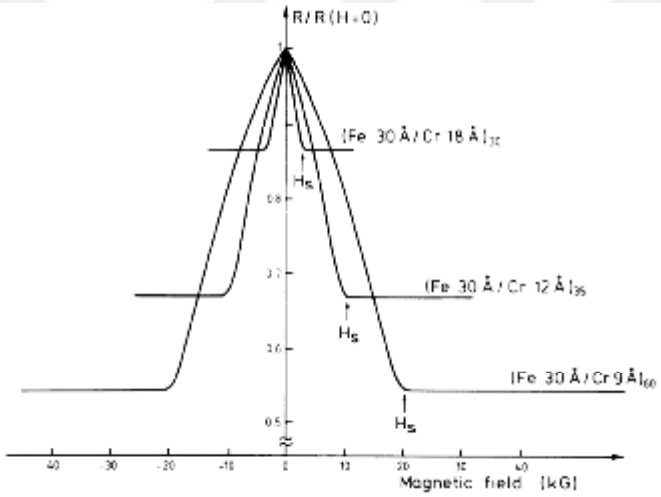


Figure 1.1. Magnetoresistance of Fe/Cr superlattices at 4.2 K temperature (Baibich, 1988).

After the discovery of GMR, a new mechanism similar with GMR was emerged as “Tunneling Magnetoresistance (TMR)” in the “Magnetic Tunnel Junction (MTJ)” structure where there is a tunneling barrier (insulator) sandwiched between two ferromagnetic layers (see Figure 1.2). The main difference between TMR and GMR is the material type of barrier whereas an insulator (non-magnetic material) is used for TMR (GMR). The basic mechanism of MTJ depends on these two ferromagnetic layers’ magnetic states mean alignment of them are parallel or

antiparallel to each other. In other words, it can be explained that when a bias voltage applied across the barrier, the current can flow across the tunneling barrier with quantum mechanical principle based on alignment of two ferromagnetic states. The motivation of using an insulating spacer layer is that extremely large values of TMR – potentially exceeding 1000% using crystalline MgO as a barrier (MgO based MTJ) – have been predicted from calculations of spin dependent tunneling probabilities (Butler et al., 2001; Mathon et al., 2001).

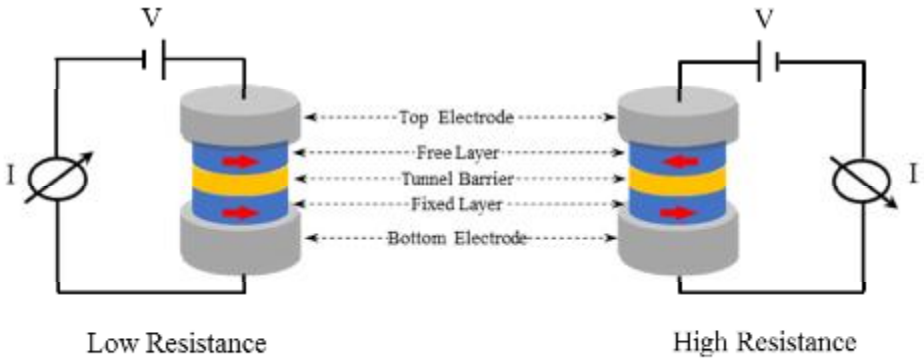


Figure 1.2. A basis magnetic tunnel junction structure for parallel (Low Resistance) and antiparallel (High Resistance) magnetization states to each ferromagnetic layer.

Until 2004, amorphous AlO_x was used as insulating barrier in the MTJs, and the resistance changes in AlO_x based MTJs was only up to 70% at room temperature (Dexin et al., 2004). Due to the theoretical prediction on the MR ratio up to 1000%, great attention has been attracted to reach this high value in experiment. Some experimental scientist showed that MgO based MTJ's resistance change (up to 200%) greater than using amorphous AlO_x as a barrier (Yuasa et al., 2004; Parkin et al., 2004). The highest MR ratio was reached up to 600% at room temperature using CoFeB material as free and fixed layer in the MTJ in 2008 (Lee et al., 2007; Ikeda et al., 2008) . This huge magneto-resistance change in the MgO

based MTJs has been used in hard-disk drives as a magnetic read head due to the having extremely sensitive resistance change under magnetic field.

The scientist and technologists in all around the world have made an effort to increase the scalability of the devices, due to increasing volume of data day by day. This demand in increasing recording density can be achieved by scaling. Historically, areal density has increased doubled every year, though, recently, this rate has dropped to ~ 40% because of growing challenges in increasing areal densities of longitudinal recording where the magnetization of the bits lies in the plane of the magnetic film. The data bits have to be minimized and packed more close to each other to increase areal densities in longitudinal recording devices. However, when the data bits are made too small, the magnetic energy on the each bit will be so small which means that thermal energy can cause it to demagnetize, a phenomenon known as superparamagnetism. To overcome this superparamagnetic effect, the scientist developed a new magnetic recording system called as perpendicular magnetic recording where magnetic moments are aligned perpendicular by upward or downward to the film plane (Iwasaki, 1980; Grundy, 1998; Kim et al., 2011). In perpendicular recording system, there is an additional layer which is soft magnetic under-layer that functions as part of the write field return path and effectively produces an image of the recording head that doubles the recording field, enabling higher recording density than with longitudinal recording system (see Figure 1.3). It is accepted that perpendicular magnetic recording is advantageous for a further increase in the areal density, and the scientist and recording industry have focused on transition to this technology.

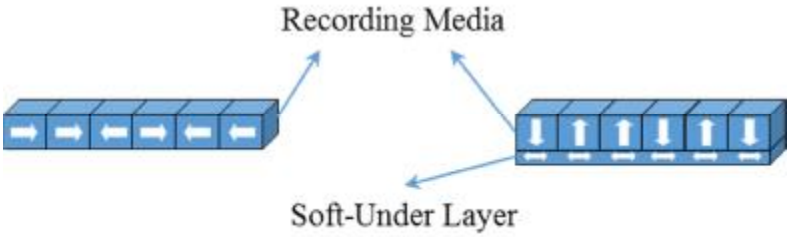


Figure 1.3. Longitudinal (Standard) Recording (left-side), Perpendicular Recording (right-side) in the hard disc head.

1.2. Towards Magnetic Random Access Memory (MRAM)

Recently, the development of magnetic tunnel junctions brings a new memory family called as Magnetic Random Access Memory (MRAM) that collects the best technological parameters, such as energy consumption, high write and read speed, density, *etc.* Table 1.1 shows the comparison of Static-Random Access Memory (SRAM), Dynamic-Random Access Memory (DRAM), Negative-AND Flash Memory (NAND Flash), Spin-Transfer-Torque Random Access Memory (STT-RAM) and Magnetoelectric-Random Access Memory (MRAM) in terms of application parameters. As seen from the Table 1.1, the MRAM can be a commercial memory products in the computer industry. However, the cost of MRAM device is still high for mass production. To overcome this big issue, the material and fabrication based researches are still going on to the standard production cost level.

For a high performance MRAM device application, there are three crucial technological requirements;

i) Scalability: The density of devices can be enhanced by creating perpendicular recording rather than the in-plane recording. The increment of data density can be achieved up to 10 times larger than the commercial in-plane geometry.

ii) Reading Process: For high performance MRAM device, the tunneling magneto-resistance ratio must be large enough to realize the correct data from the device. So far, the highest TMR value has been found in a material stack of CoFeB/MgO/CoFeB. The main part of this stack is MgO as a tunnel barrier crystallized in (001) direction.

iii) Writing Process: The data writing process can be done by field, spin-transfer-torque, Voltage-Control-Magnetic-Anisotropy (VCMA) and current-driven Spin-Orbit Torque (SOT) process. Among these writing processes, current-driven perpendicular magnetization switching for free layer in a magnetic tunnel junction has been worked in this dissertation.

Table 1.1. Comparison of existing and emerging memory families in terms of technological requirements.

Technology	SRAM	DRAM	NAND Flash	MRAM
Energy/bit (fJ)	100	1,000	10^6	<10
Write Speed (ns)	1	20	10^6	1-10
Read Speed (ns)	1	30	50	1-10
Density (area in F^2)	>30	6-10	4	4-8
Endurance (cycles)	Very High	Very High	Low	Very High
Non-volatility	No	No	Yes	Yes
Standby Power	Leakage Current	Leakage Current	None	None
Nonvolatile Logic Capability	No	No	No	Yes

In conclusion, the next-generation memory devices can be nano-magnetism based devices. In Figure 1.4, the MRAM collects the best technological requirements from existing memory families.

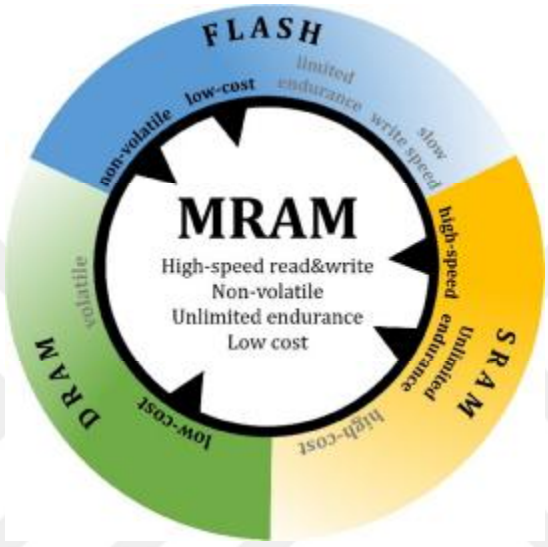


Figure 1.4. Comparison of DRAM, SRAM, FLASH and MRAM families in terms of technological requirements.

1.3. Nature of Spin

If the electrons are investigated in the quantum mechanical perspective, an internal degree of freedom which is known as ***spin***, can be seen in their nature. In quantum mechanics, the spin angular momentum operator is described as (Eisberg et al., 1974; Shankar, 1994);

$$\vec{S} = \frac{\hbar}{2}\vec{\sigma} \tag{1.2}$$

where $\hbar$ is Planck's constant (4.135×10^{-15} eV.s) and $\vec{\sigma}$ is the vector of the Pauli spin matrices which can be represented as;

$$\sigma_x = \begin{pmatrix} 0 & 1 \\ 1 & 0 \end{pmatrix} \tag{1.3}$$

$$\sigma_y = \begin{pmatrix} 0 & -i \\ i & 0 \end{pmatrix} \tag{1.4}$$

$$\sigma_z = \begin{pmatrix} 1 & 0 \\ 0 & -1 \end{pmatrix} \tag{1.5}$$

The eigenstates of spin-up (1/2) and spin-down (-1/2) states can be written as $|\uparrow>$ and $|\downarrow>$, respectively. The corresponding eigenstates of $\vec{S}$ to the eigenvalues of spin-up and spin-down are $+\hbar/2$ and $-\hbar/2$, respectively (Shankar, 1994).

$$|\uparrow> = \begin{pmatrix} 1 \\ 0 \end{pmatrix} \tag{1.6}$$

$$|\downarrow> = \begin{pmatrix} 0 \\ 1 \end{pmatrix} \tag{1.7}$$

If we assume that the relation between the spin magnetic dipole moment and the spin angular momentum is the same form as the relation for orbital magnetic dipole moment and orbital angular momentum, that is,

$$\overrightarrow{\mu_s} = -\frac{g_s \mu_B}{\hbar} \vec{S} \tag{1.8}$$

here, g_s is called the Landau spin g factor and μ_B is the Bohr magneton.

As we described above that the electrons have “intrinsic” angular momentum, called as ***spin***, which does not related to their orbital motion. Let’s summarize the basic concept of spin properties as following,

- An electron has an intrinsic angular momentum except for its mass and charge,
- Each spin has two orientations with the magnitude $\pm\hbar/2$,

- If an external magnetic field is applied to an electron, it has different energies depending on its spin's orientation with the external magnetic field.
- The motion of electron spin in directional and coherent creates a spin current which transport the information in spintronic devices.

1.3.1. Spin Injection, Accumulation and Detection

Since the heart of spintronics is spin-dependent transport in devices, we should emphasize a couple of physical phenomena which are spin generation, accumulation and detection which are demonstrated in the following figure.

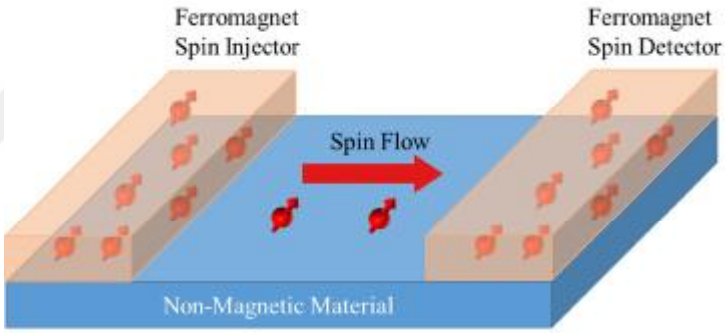


Figure 1.5. Schematic illustration of spin injection, spin transfer and spin detection in a device composed of ferromagnet/non-magnet/ferromagnet trilayer structure.

- Spin injection: It can be defined as the transferring of spin angular momentum from a ferromagnetic material where spins are polarized, to a non-ferromagnetic material. It is limited by the spin diffusion length, λ_{sd} of spin source materials.
- Spin accumulation: The spin polarized electrons can be accumulated at the edges of the device by spin-orbit interaction. The opposite spin polarization

at opposite device edges results in a measurable voltage referred as the spin Hall effect which will be discussed in Section 1.5.3. However, the spin accumulation decays with a scale of λ_{sd}, because of the spin relaxation processes in the nonmagnetic metal.

- Spin detection: The accumulate spins can be detected by the electrode which is connected to the voltmeter. The magnitude of spin detection directly proportional to the spin accumulation at the edges of the devices. More discussion will be given in Section 1.5.3.

1.3.2. Spin-Orbit Interaction

In traditional electronic devices, an electron carries just its charge ($\acute{e}$), since spin orientation of electrons are random. The information and energy can be transported by electric current which are created by scattering of electrons in a traditional materials. In spintronic devices, electrical signal can be formed by the spin of electrons. We assume a similar behavior like spin-dependent scattering in spintronic devices. Spin-dependent scattering can be phrased a physical phenomena known as *spin-orbit interaction (coupling) (SOI or SOC).* The interaction between an electron's spin magnetic dipole moment and the internal magnetic field which is related to the electron's orbital angular momentum. In other words, spin-orbit interaction can be defined as effect of an electron's orbital motion on its spin orientation.

The SOI goes into the Hamiltonian from a nonrelativistic approximation to the Dirac equation (Sakurai, 1967). This approach is able to the Pauli SO term;

$$H_S = \frac{e\hbar}{4m^2c^2}\vec{\sigma}.\left[\vec{\nabla}V(\vec{r})x\vec{p}\right] \tag{1.9}$$

where $\hbar$ is Planck's constant, m is the mass of a free electron, c is the velocity of light, V is the Coulomb potential, $\vec{p}$ is the electron momentum and $\vec{\sigma}$ is the vector of the Pauli spin matrices. It is well known that atomic spectra are strongly affected

by SO coupling (Slater, 1960). Thus, in order to understand the origin of the SOC, we should derivate an equation by using basic physics equations. If we consider the motion of the nucleus from the point of view of the electron in a frame of reference fixed on the electron, the charged nucleus moves around the electron and the electron is located inside a current loop which produces the magnetic field. Figure 1.6.a-b are showing a) the basic electron motion around the nucleus and b) a relativistic nucleus motion means that the nucleus moves around the electron.

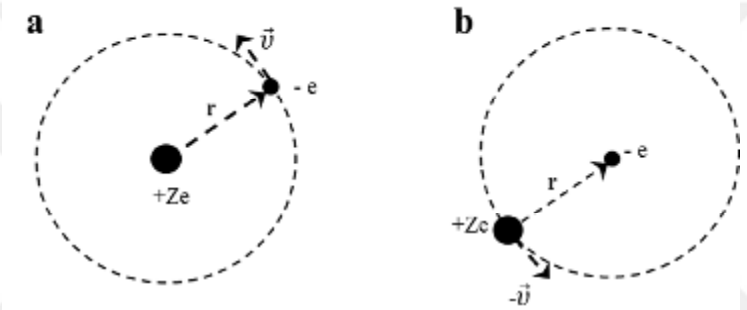


Figure 1.6. a) An electron moves in a circular motion seen by the nucleus, b) the same motion but seen by the electron that the nucleus moves around the electron.

The charged nucleus moving with velocity $-\vec{v}$ constitutes a current element $\vec{J}$;

$$\vec{J} = -Ze\vec{v} \tag{1.10}$$

According to the Ampere's law, this motion produces a magnetic field $\vec{B}$ on the electron which is;

$$\vec{B} = \frac{\mu_0}{4\pi}\frac{\vec{j}x\vec{r}}{r^3} = -\frac{Ze\mu_0}{4\pi}\frac{\vec{v}x\vec{r}}{r^3} \tag{1.11}$$

It is convenient to define this equation in terms of the electric field $\vec{E}$ acting on the electron. According to Coulomb's law;

$$\vec{E} = \frac{Ze}{4\pi\varepsilon_0}\frac{\vec{r}}{r^3} \tag{1.12}$$

From the last two equations, we obtain;

$$\vec{B} = -\varepsilon_0\mu_0\vec{v}x\vec{E} \tag{1.13}$$

The quantity of $\vec{B}$ is the magnetic field strength experienced by the electron when it is moving with velocity $\vec{v}$ relative to the nucleus, and therefore through the electric field of strength $\vec{E}$ which the nucleus exerts on it. The electron and its spin magnetic dipole moment can assume to be at different orientations in the internal magnetic field of the atom, and its potential energy is different for each of these orientations. If we evaluate the orientational potential energy, U of the magnetic dipole moment in this magnetic field, we can obtain;

$$\Delta U = -\vec{\mu}_s.\vec{B} \tag{1.14}$$

Using the relation of (1.8), the potential energy comes from the spin-orbit interaction can be written in terms of the electron's spin angular momentum $\vec{S}$;

$$\Delta U = \frac{g_s\mu_b}{2\hbar}\vec{S}.\vec{B} \tag{1.15}$$

The strength of magnetic field, $\vec{B}$ taking place from the electron motion which is proportional to the magnitude of $|\vec{L}|$, since it moves around the nucleus with orbital angular momentum, $\vec{L}$. The magnetic field vector is also in the same direction with angular momentum vector. Thus, we can express the spin-orbit interaction energy by modified with $\vec{B} = \left({}^{1}/_{mc^2er}\right)\frac{\partial U_{(r)}}{\partial r}\vec{L}$ and $U = eV$ as;

$$\Delta U = \frac{1}{2m^2c^2}\frac{1}{r}\frac{dV(r)}{dr}\vec{S}.\vec{L} \tag{1.16}$$

This SOI energy equation shows that the Hamiltonian of a system can be include SOC term, if the system's spin and angular momentum interactions are enough large to contribute other term of the Hamiltonian. Since the SOC constant, $\varepsilon_{SO} \sim (Ze^2/\hbar c)^2$ (without spin matrices contribution) in the Hamiltonian is proportional to the atomic number of elements, the magnitude of the SOC can be strong (weak) in heavy (light) elements. The trend of the ε_{SO} is shown in Figure 1.7.

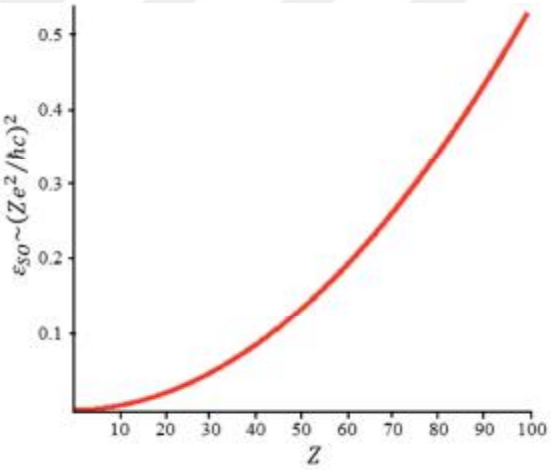


Figure 1.7. The estimated spin-orbit-coupling constant as a function of atomic number.

1.3.3. Spin-Orbit Torques

Before definition of spin-orbit torques, we would like to explain physics of the torque in classically. In classical physics, the torque or moment can be defined as a force to rotate an object on its axis by a general relation;

$$\vec{\tau} = \vec{r} \times \vec{F} \tag{1.17}$$

where $\vec{\tau}$ is the torque vector, $\vec{r}$ is the position vector and $\vec{F}$ is the force vector. Thus, an object can be rotated by applying a force within a distance of its axis.

Let's go to the torque in electromagnetism. In a microscopic scale, the torque on magnetic moment of a magnet can be occurred when a magnetic field is applied. The relation of the torque can be given as following;

$$\vec{\tau} = \vec{\mu} \times \vec{B} \tag{1.18}$$

where $\vec{\mu}$ is the magnetic moment and $\vec{B}$ is the external magnetic field. Therefore, the magnetic moment of a ferromagnet can be rotated by external field. The Landau-Lifshitz-Gilbert equation explains the rotation of the magnetization in response to torques. In 1935, the Landau-Lifshitz (Landau et al., 1935) equation first introduced the motion of magnetization by following relation;

$$\frac{d\vec{M}}{dt} = -\gamma \vec{M} \times \vec{H}_{eff} - \lambda \vec{M} \times (\vec{M} \times \vec{H}_{eff}) \tag{1.19}$$

where $\vec{M}$ is the magnetization vector, $\gamma = -{}^{e}/_{2m_e} = -{}^{\mu_B}/_{\hbar}$ is the electron gyromagnetic ratio, $\vec{H}_{eff} = \vec{H}_{ext} + \vec{H}_{exch} + \vec{H}_{ani} + \vec{H}_{demag} + \vec{H}_{mc} + \vec{H}_{current} + \vec{H}_{th}$ is the effective field by combination of the external magnetic field, exchange field, anisotropy field, demagnetization field, magnetostatic coupling between the reference layer and the free layer in magnetic tunnel junction, Ampere field, and the thermal field, respectively. And $\boldsymbol{\lambda}$ is a damping parameter which can be written as;

$$\lambda = \alpha \frac{\gamma}{M_s} \tag{1.20}$$

where α is a dimensionless constant named the damping factor. Its typical values are in the range of 0.001 to 0.1.

In 1955, Gilbert modified the damping term of the Landau-Lifshitz equation by adding time derivation of the magnetization (Gilbert, 1955);

$$\frac{d\vec{M}}{dt} = -\gamma\left(\vec{M} \times \vec{H}_{eff} - \eta\vec{M} \times \frac{d\vec{M}}{dt}\right) \tag{1.21}$$

This new equation is called the Landau-Lifshitz-Gilbert or commonly known as LLG equation. Here, η is the damping parameter which is a characteristic parameter of the material. The first term is known as precession motion of the magnetization in its motion axis (shown as red arrow in Figure 1.8), the second term is the damping case (shown as orange arrow in Figure 1.8). Due to the acting of both terms on the magnetization, the magnetic moment of a ferromagnet will be rotated by the torques.

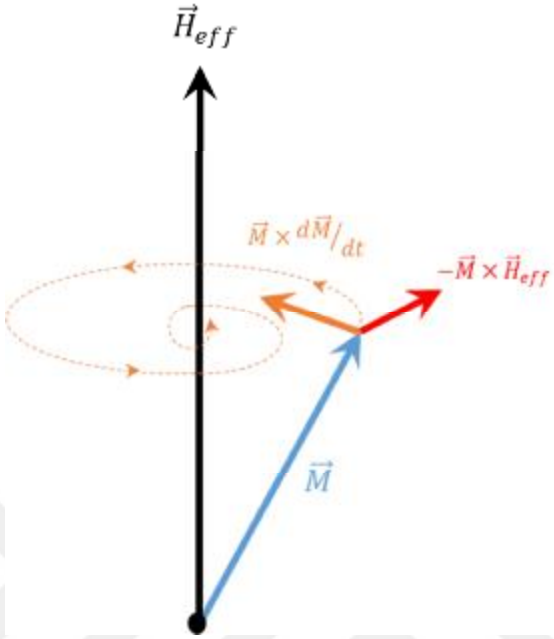


Figure 1.8. The motion of magnetization by precession and damping drawn by taken into account of LLG relation.

In 1996, Slonczewski (Slonczewski, 1996) added a new term to the LLG equation called as spin-transfer torque (STT). The STT on the magnetization can be formed by spin-polarized current passing through the ferromagnet. The domain wall motion with electric current can be done by transferring angular momentum from conduction electrons to the localized magnetic moments. This is the origin proposal of Slonczewski torque in magnetic multilayer systems. When the electrons move across the domain wall, they can bring their spin orientation to the direction of the local moments. The modified LLG equation by the Slonczewski is given as following;

$$\frac{d\vec{m}}{dt} = -\gamma\vec{m} \times \vec{H}_{eff} + \alpha\vec{m} \times \frac{d\vec{m}}{dt} + \tau_{\parallel}\frac{\vec{m} \times (\vec{m} \times \vec{r})}{|\vec{m} \times \vec{r}|} + \tau_{\perp}\frac{\vec{m} \times \vec{r}}{|\vec{m} \times \vec{r}|} \qquad (1.22)$$

where $m = M/M_s$ is the unit moment, $\tau_{\parallel}$ and $\tau_{\perp}$ are parallel and perpendicular torques and $\vec{r}$ is the unit vector along the polarization of the current.

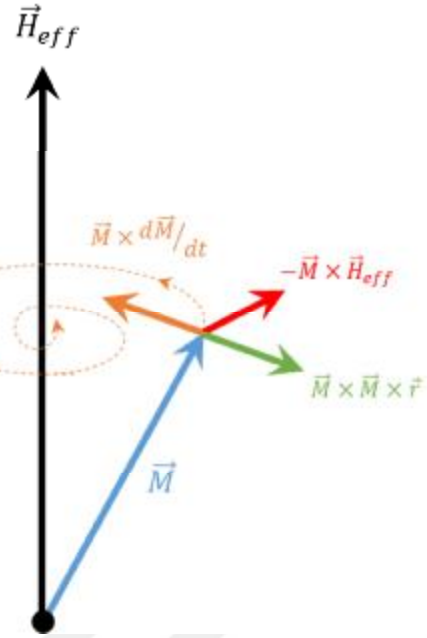


Figure 1.9. The motion of the magnetization by precession, damping and spin-transfer-torque damping drawn by taken into account of modified Slonczewski-LLG relation.

The sign of STT can be altered by changing electric current direction through the device. Therefore, the magnitude of damping-like torque can be enhanced or reduced by the passing electric current with different directions.

Recently, the spin-polarized electrons have been generated from the heavy-metal instead of ferromagnet. The current-driven (induced) spin-orbit torques by spin Hall effect (SOT-SHE) such as damping-like and field-like, come from the moving of polarized electrons through the devices. Although the physical mechanism looks like similar with the spin-transfer-torque, a big difference in current-driven spin-orbit torque is the moving of electric current direction. In STT,

the electric current passes through the devices. But, in SOT-SHE, the spin current passes through the devices, not electric current. As explained the detail of spin-orbit interactions in the previous section (1.2.5), the electric current can generate spin-current align through the device by spin-orbit coupling. Therefore, the spin-current as a source of torque can rotate the magnetization by field-like and/or damping-like torques. The magnetization dynamics can be modified by adding SOT-SHE terms into the LLG equation;

$$\frac{d\vec{m}}{dt} = -\gamma\vec{m} \times \vec{H}_{eff} + \alpha\vec{m} \times \frac{d\vec{m}}{dt} + \frac{\delta_{SHE}}{M_s}(\vec{m} \times \hat{\sigma}_{SHE} \times \vec{m}) \tag{1.23}$$

where M_s is the saturation magnetization, δ_{SHE} is SOT-SHE coefficient which can be written in the following form;

$$\delta_{SHE} = \frac{J_{SHE}\theta_{SHE}\hbar\gamma}{2et_{FM}} \tag{1.24}$$

where J_{SHE} is the current density flowing through the heavy-metal layer located underneath of the free layer, θ_{SHE} is the spin-Hall angle of the heavy-metal layer material, $\hbar$ is the reduced Plank constant, e is the charge of electron and t_{FM} is the free ferromagnetic layer thickness. The spin-Hall angle is defined as the ratio of spin current density (J_s) per charge current density (J_c) as; $\theta_{SHE} = {J_s}/{J_c}$. It might be more understandable if we can write it down by using conductivity terms as the charge conductivity, $\sigma_{xx}^{c} = ne\mu$ and the spin-Hall conductivity, $\sigma_{xy}^{s} = n\hbar\mu\theta_{SHE}$. Thus, the spin-Hall angle can be written as (Hoffmann, 2013);

$$\theta_{SHE} = {J_s}/{J_c} = \frac{\sigma_{xy}^{s}e}{\sigma_{xx}^{c}\hbar} \tag{1.25}$$

It is understood that the origin of spin-current in SOT-SHE based system is coming from the heavy-metal layer used as a spin generator. The spin-Hall conductivity is depending on the spin-Hall angle of the heavy-metal layer.

Therefore, high spin-current can be created by strong spin-orbit coupled materials. In addition to the materials, there are other effects on the SOT-SHE which will be discussed in Chapter 4. More discussions on the STT and SOT-based magnetization switching mechanism will be given in Section 1.5.

In this dissertation, the field-like and damping spin-orbit torques are determined by vector measurements. In addition to these traditional torques, a new perpendicular field-like torque has been created by engineering the symmetry of the devices. The calculation and measurement details will be discussed in Chapter 3.

1.4. Origin of Magnetization

A current loop can be created by moving electrons around the nucleus with a radius *R*. This current loop produces magnetic moment as simply $|\vec{\mu}| = |I\vec{A}|$, where $|\vec{A}|$ is the area of the current loop. A schematic illustration of one electron-nucleus system is shown in Figure 1.10.

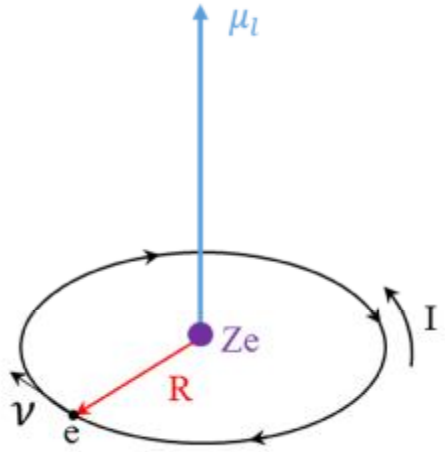


Figure 1.10. The magnetic moment generated from current loop.

In a simple example of Hydrogen atom, the current corresponding to the electron rotation around the nucleus can be written as;

$$I = \frac{ev}{2\pi R} \tag{1.26}$$

where, v is the velocity of electron, e is the charge of electron. The magnetic dipole is;

$$\vec{\mu} = I\vec{A} = \frac{ev}{2\pi R}\pi R^2\hat{A} = \frac{1}{2}evR\hat{A} \tag{1.27}$$

If we write the magnetic dipole down by the orbital angular momentum,

$$\vec{L} = m\vec{v} \times \vec{R} \tag{1.28}$$

$$|\vec{\mu}| = \left|\frac{1}{2}evR\hat{A}\right| = \frac{e}{2m_e}\left|\vec{L}\right| = \gamma\left|\vec{L}\right| \tag{1.29}$$

where γ is the gyromagnetic ratio. So far, we just consider that electrons have orbital angular momentum. Electrons, however, have also spin angular momentum which can be written by operator of $\hat{S}^2$,

$$\hat{S}^2\chi = \hbar^2 s(s+1)\chi \tag{1.30}$$

The length of spin angular momentum;

$$\left|\vec{S}\right| = \hbar\left|\sqrt{s(s+1)}\right| \tag{1.31}$$

Then, spin magnetic moment;

$$|\mu_s| = \gamma\left|\vec{S}\right| = \gamma\hbar\sqrt{s(s+1)} \tag{1.32}$$

Here $\gamma\hbar$ also written as $e\hbar/2m_e$ is known as Bohr magneton, μ_B. Therefore, the magnetic dipole coming from both orbital and spin angular momentum can be written as;

$$|\mu_l| = \gamma|\vec{L}| = \mu_B\sqrt{l(l+1)} \tag{1.33}$$

$$|\mu_s| = \gamma|\vec{S}| = \mu_B\sqrt{s(s+1)} \tag{1.34}$$

The total of both contribution to magnetic dipole;

$$|\mu_j| = \gamma|\vec{J}| = \mu_B\sqrt{j(j+1)} \tag{1.35}$$

Here, j is the quantum number of total angular momentum and $\vec{J} = \vec{L} + \vec{S}$.

After description of magnetic dipole inside a material, we can talk about the behavior of the material under magnetic field. In nature, there are five magnetic material groups which are known as paramagnetic, diamagnetic, ferromagnetic, ferrimagnetic and antiferromagnetic. The difference in magnetic phases is related to the magnetic interaction of each magnetic dipole in the material. Since the concept of this dissertation is directly related to the permanents magnetic properties, we will focus on the ferromagnetism as following.

In ferromagnetic materials, magnetic dipoles interact with each other. These interactions between magnetic diploes cause to orient of them in particular orientation to minimize the total energy of the material. These interactions are formed by neighboring magnetic diploes. The sign and magnitude of interaction between magnetic dipoles determine the alignment of magnetic moments, such as parallel or anti-parallel to each-other. To explain simply of these interactions, let's consider a system which has two Hydrogen atoms with a single electron. The wavefunction of two-electron system can be set by combination of the spacial and spin parts;

$$\Psi(1,2) = \psi(\overrightarrow{r_1},\overrightarrow{r_2})\chi(1,2) \tag{1.36}$$

where $\psi(\vec{r}_1,\vec{r}_2)$ is the spacial wavefunction and $\chi(1,2)$ is the spin wavefunction. Since electrons are fermions, an anti-symmetric wavefunction mode can be build when two electron bring together into a system ($\Psi(1,2) = -\Psi(2,1)$). To create an exchange between electrons, the spacial or spin wavefunction must be anti-symmetric. The symmetric and anti-symmetric spacial wavefunctions are;

$$\psi_s(\overrightarrow{r_1},\overrightarrow{r_2}) = \frac{1}{\sqrt{2}}[\varphi_1(\overrightarrow{r_1})\varphi_2(\overrightarrow{r_2}) + \varphi_1(\overrightarrow{r_2})\varphi_2(\overrightarrow{r_1})] \tag{1.37}$$

$$\psi_a(\overrightarrow{r_1},\overrightarrow{r_2}) = \frac{1}{\sqrt{2}}[\varphi_1(\overrightarrow{r_1})\varphi_2(\overrightarrow{r_2}) - \varphi_1(\overrightarrow{r_2})\varphi_2(\overrightarrow{r_1})] \tag{1.38}$$

where $\varphi(\vec{r}_1)$ and $\varphi(\vec{r}_2)$ are the single electron wavefunctions. The spin wavefunctions are responsible for their spin direction "*up*" or "*down*". Two-electron spin wavefunctions can be formed as;

$$\chi_s(1,2) = \begin{cases} \chi_\uparrow(1)\chi_\uparrow(2) \\ \chi_\downarrow(1)\chi_\downarrow(2) \\ \frac{1}{\sqrt{2}}[\chi_\uparrow(1)\chi_\downarrow(2) + \chi_\downarrow(1)\chi_\uparrow(2)] \end{cases} \tag{1.39}$$

$$\chi_a(1,2) = \frac{1}{\sqrt{2}}[\chi_\uparrow(1)\chi_\downarrow(2) - \chi_\downarrow(1)\chi_\uparrow(2)] \tag{1.40}$$

Thus, the total two-electron wavefunction can be written as;

$$\Psi(1,2) = \begin{cases} \psi_s(\overrightarrow{r_1},\overrightarrow{r_2})\chi_a(1,2) \\ \psi_a(\overrightarrow{r_1},\overrightarrow{r_2})\chi_s(1,2) \end{cases} \tag{1.41}$$

The total Hamiltonian of the two-electron system;

$$\hat{H} = \hat{H}_1 + \hat{H}_2 + \hat{H}_{ex} \tag{1.42}$$

where $\hat{H}_1$ and $\hat{H}_2$ are single electron Hamiltonians, $\hat{H}_{ex}$ is the Hamiltonian for the exchange interaction. The Hamiltonian for the exchange interaction can be written as;

$$\hat{H}_{ex} = -2J_{ex}\hat{S}_1\hat{S}_2 \tag{1.43}$$

where $\hat{S}_1$ and $\hat{S}_2$ are the spin operators for the electrons 1 and 2, respectively. J_{ex} is the exchange integral or overlap integral. For our simple example, the exchange integral is**;**

$$J_{12} = \iint \varphi_1(\overrightarrow{r_1})\varphi_2(\overrightarrow{r_2})\hat{H}_{ex}\varphi_1(\overrightarrow{r_2})\varphi_2(\overrightarrow{r_1})d^3\overrightarrow{r_1}d^3\overrightarrow{r_2} \tag{1.44}$$

So far, we did not add any term for external magnetic field. Let's apply an external magnetic field to our simple example. The total Hamiltonian is;

$$\begin{aligned}\hat{H} &= \hat{H}_1 + \hat{H}_2 + \hat{H}_{ex} + \hat{H}_{1,field} + \hat{H}_{2,field} \\ &= \hat{H}_1 + \hat{H}_2 - J_{12}\hat{S}_1\hat{S}_2 + \vec{B}.\vec{\mu}_1 + \vec{B}.\vec{\mu}_2\end{aligned} \tag{1.45}$$

The magnetic part of the Hamiltonian can be written as;

$$\hat{H}_{mag} = -J_{12}\hat{S}_1\hat{S}_2 + \frac{\mu_B}{\hbar}\vec{B}.\vec{S}_1 + \frac{\mu_B}{\hbar}\vec{B}.\vec{S}_2 \tag{1.46}$$

Here, the moment is written as $\vec{\mu}_{1,2} = \gamma\vec{S}_{1,2} = \frac{\mu_B}{\hbar}\vec{S}_{1,2}$. The magnetic Hamiltonian can be shown in a general formation;

$$\hat{H}_{mag} = -\sum_{i,j} J_{ij}\hat{S}_i\hat{S}_j + \frac{\mu_B}{\hbar}\sum_i \vec{B}.\vec{S}_i = \sum_i \left[\sum_j J_{ij}\hat{S}_j + \frac{\mu_B}{\hbar}\vec{B}\right].\vec{S}_i \tag{1.47}$$

The mean magnetic field coming from the collecting of neighboring magnetic dipoles (exchange interaction between each pair of magnetic dipoles) and individual magnetic dipole;

$$\sum_j J_{ij}\hat{S}_j + \frac{\mu_B}{\hbar}\vec{B} \longrightarrow \frac{\mu_B}{\hbar}\vec{B}_{ex} \tag{1.48}$$

where $\vec{B}_{ex}$ is the molecular exchange field. Thus, the magnetic Hamiltonian can be written as a combination of exchange and applied magnetic field;

$$\hat{H}_{mag} = \frac{\mu_B}{\hbar} \sum_i \left[\vec{B}_{ex} + \vec{B}_{applied}\right] \hat{S}_i \tag{1.49}$$

Therefore, the spontaneous ordering of magnetic dipoles in the absence of the applied magnetic field can show field which is called as mean exchange field (Anikeeva et al., 2013).

The sign and magnitude of exchange integral can classify the type of magnetic interaction of materials. In the following illustrations, we show the ferromagnetic ($J_{ex} > 0$), antiferromagnetic ($J_{ex} < 0$) and ferrimagnetic ($J_{ex} < 0$) materials' typical magnetic moments' ordering.

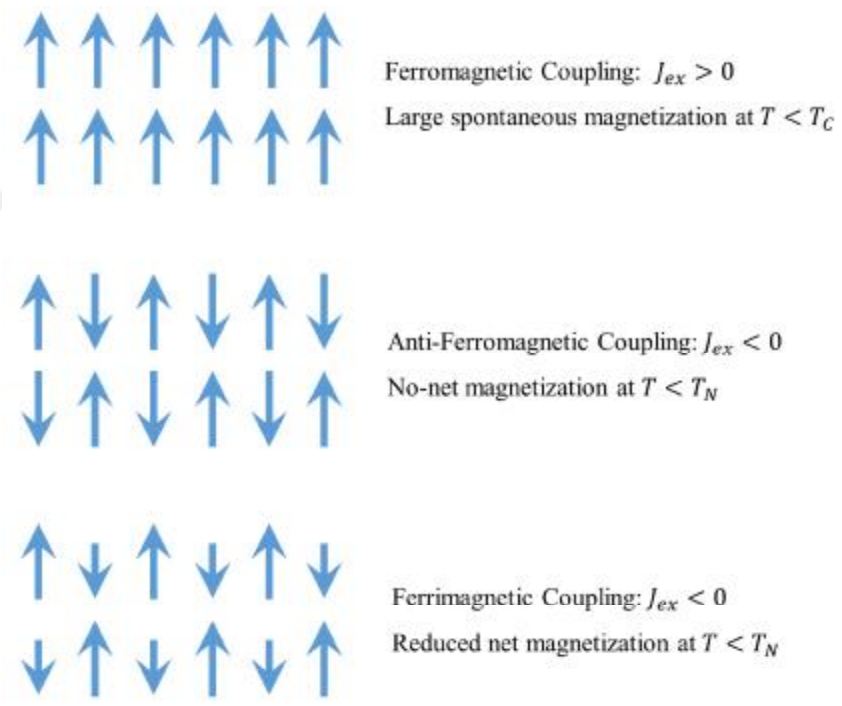


Figure 1.11. Schematic illustrations of ferromagnetic, anti-ferromagnetic and ferrimagnetic materials.

1.5. Hall Effects

1.5.1. Ordinary-Hall Effect

In ordinary Hall effect, a conductor can create a transverse voltage due to the Lorentz force when electric current passes through the conductor or semiconductor, and an external magnetic field is applied perpendicular to the current direction. This physical phenomena was first discovered by Edwin H. Hall in 1879 (Hall, 1879). Figure 1.12 presents a simple illustration of ordinary Hall effect.

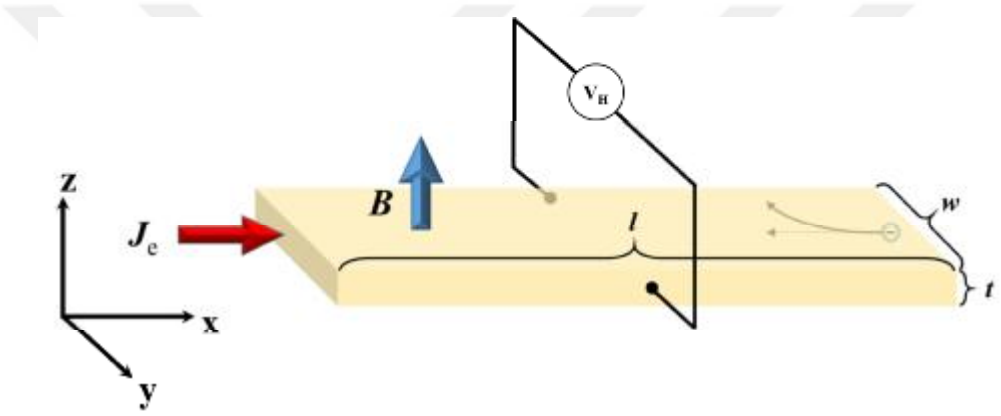


Figure 1.12. A schematic illustration of ordinary Hall effect.

Although the current composes of movement of charge carriers, such as electrons, holes, ions or all three, in a simple conductor, there is only one type of charge carrier which is electron. The current density, J_x is the current, I_x per cross-sectional area of conductor, *wt*. It can be written as;

$$J_x = \frac{I_x}{wt} \tag{1.50}$$

In other definition of current density is the amount of charge carrier, *nq* times the drift velocity, v_x.

$$J_x = nqv_x \tag{1.51}$$

So, the current is,

$$I_x = nqv_x wt \tag{1.52}$$

Since the charge current produce an electric field along the length of conductor, E_x, the charge density can be written as;

$$J_x = \sigma E_x \tag{1.53}$$

where σ is the conductivity of material. If we apply an external magnetic field along the *z*-direction, B_z as shown in Figure 1.12, the charge carrier will feel a Lorentz force as $q(\vec{v} \times \vec{B})$. Due to the cross product of drift velocity and external magnetic field, the charge carrier will move transverse side in the material. This deflection causes charge accumulation in the edge of material which generates an electric field in the *y*-direction, E_y which is also called Hall field. If the system is reached its equilibrium state, this charge flow will be stop and the net Lorentz force will be zero. Thus, it can be written as;

$$E_y = v_x B_z \tag{1.54}$$

The potential difference in the *y*-direction, known as Hall voltage, V_H has a relation with Hall field as;

$$V_H = -\int_0^w E_y d_y = -E_y w \tag{1.55}$$

If we combine equations of (1.52), (1.54) and (1.55), we can get;

$$V_H = -\left(\frac{1}{nq}\right)\frac{I_x B_z}{t} \tag{1.56}$$

where, the $(1/nq)$ term is known as Hall coefficient, R_H. The type of charge carrier can be detected by the sign of R_H.

When Edwin H. Hall used a ferromagnetic material instead of non-magnetic conductor, this transverse voltage also observed without external magnetic field. This new discovery of Edwin H. Hall is nowadays known as anomalous-Hall effect (AHE) or extraordinary-Hall effect (EHE) (Hall, 1881). Since charge currents in ferromagnetic materials have already polarized which depends on the magnetization direction, the transverse voltage drops spin-dependently. Therefore, we can now refer spin Hall effect (SHE) as a spin accumulation with opposite spin polarity at two edges of the material. In the following section, we will discuss detail of AHE and SHE.

1.5.2. Anomalous-Hall Effect

The origin of anomalous-Hall effect has been worked theoretically more than a century. But, first acceptable study on the understanding of AHE was done by Karplus and Luittinger in 1954 (Karplus et al., 1954). When a ferromagnetic conductor is used as a metal instead of simple conductor, the internal magnetization of the ferromagnetic material can create a new term in the Hall voltage. The effective Hall voltage in a ferromagnetic metal can be written as following;

$$V_H = -\frac{R_H I_x}{t} B_z + \frac{R_0 \mu_0 I_x}{t} M_z \tag{1.57}$$

The first term is coming from the ordinary-Hall effect, as explained in the previous section. The second term is corresponding to the Anomalous-Hall effect. Here, R_0 is a coefficient of AHE. It is much larger than the ordinary constant, R_H. The AHE term is proportional to the perpendicular component of the magnetization of ferromagnetic material. Therefore, a similar physics like OHE, a perpendicular electric field to the magnetization and charge current can be created by passing charge carrier through the device. The schematic illustration is given in the Figure 1.13.

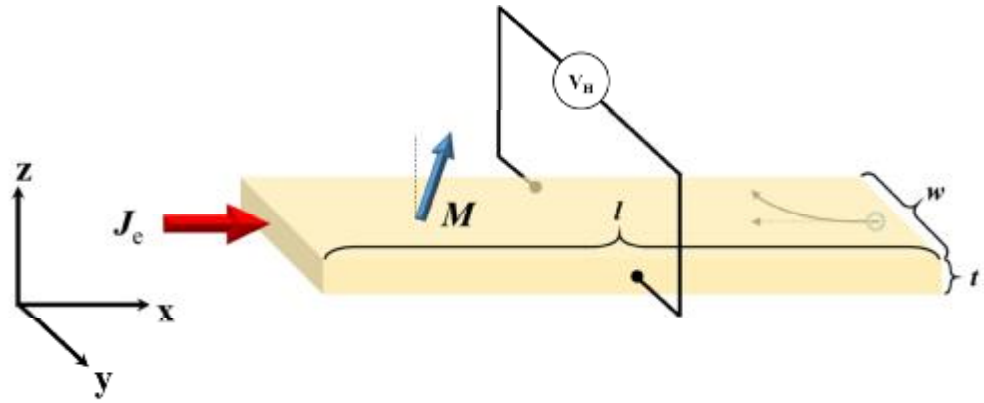


Figure 1.13. A schematic illustration of Anomalous Hall effect.

Karplus and Luittinger explained that the physical mechanism of AHE is related to the spin-orbit coupling referred intrinsic spin-Hall effect. Due to the spin-orbit coupling, a transverse velocity in electrons can be generated between scatterings. The intrinsic property of spin-Hall effect is directly related to the material property used as a spin-generator. After that, Smit (1958) and Berger (1970) come up with new mechanisms which are spin-skew and side-jump scattering (Smit, 1958; Berger, 1970) where transverse velocity can be generated during the scatterings. These mechanisms are nowadays referred as extrinsic spin-Hall effects. It would be much easy to understand, if we write the contributions of Hall effects down in term of the conductivity in *xx* and *xy* direction.

$$\rho_{xy} = R_H B_z + R_0 4\pi M = R_H\big(H + 4\pi M(1-N)\big) + R_0 4\pi M \qquad (1.58)$$

The detail of these mechanisms will be discussed in the next section.

1.5.3. Spin-Hall Effect

The generation, manipulation and detection of spin currents are crucial points in spintronic devices. Although the spin-dependent transport is first predicted by D'yakonov and Perel in 1971 (D'yakonov et al., 1971) where the idea was based on the asymmetric Mott scattering (Mott, 1929), it is referred as spin-Hall effect (SHE) by Hirsch from theoretical work in 1999 (Hirsch, 1999). Due to

the interesting results of SHE from theoretical works, optical and electrical detection of spin currents from the charge currents were observed in a short time (Kato et al., 2004; Wunderlich et al., 2005; Day, 2005). The discovering of SHE leads the way to explain physical mechanism behind of the relation of transported spin and charge currents. A basic definition of SHE is that if an electric current passes through a material which must have spin-orbit coupling, it can create a transverse pure spin current. The polarization of spin current is always perpendicular to the plane composed of charge and spin current (Hoffmann, 2013; Sinova et al., 2015). In vice case, a pure spin current can generate a transverse charge current which is known as Inverse Spin Hall Effect (ISHE).

Recently, experimental results show that the spin-Hall effect can be used to switch magnetization or excite magnetization dynamics due to the sufficiently large effect of SHE for practical usage (Liu et al., 2012; Pai et al., 2012; Niimi et al., 2012). Although the SHE can be observed in all conductivity phases, means in insulating, semiconductor or metallic materials, the strongest SHE has been observed in conducting material systems (Hoffmann, 2013). The spin-dependent Hall effects (AHE, SHE and ISHE) coming from three mechanisms which are the skew-scattering, the side-jump effect and the intrinsic effect. Either all of these effects can be found in the system or one of them. The coherent band mixing effects induced by the external electric field and the disorder potential cause these mechanisms (Sinova et al., 2015). Because of the mixing mechanisms, the system would be more complex that the simpler single-band transport. The intrinsic and extrinsic mechanisms (the skew scattering and side-jump effects) will be discussed in the following sub-sections.

1.5.3.1. Intrinsic Mechanism of SHE

The spin-dependent transverse velocity of spin-polarized electrons is coming from the effect of spin-orbit coupling on the band structure in intrinsic spin-Hall effect. In contrast to the extrinsic effects, the transverse spin currents is

generated in between scattering events, instead of during scattering (Hoffmann, 2013). Because of the direct relation of the intrinsic spin Hall conductivity (σ_{xy}^{int}) and the spin polarization at the Fermi level $< \vec{l}.\vec{s} >_{FS}$, the spin Hall conductivity is expected to be positive for more than half-filling and negative for less than half-filling of the *d*-bands in transition metals (Hoffmann, 2013; Kontani et al., 2009).

$$\sigma_{xy}^{int} \approx \frac{e}{4a} \frac{< \vec{l}.\vec{s} >_{FS}}{\hbar^2} \tag{1.59}$$

The schematic illustration of intrinsic deflection is shown in Figure 1.14. As seen that the electrons deflect to the *up* or *down* as they are accelerated by an electric field only because of the spin-orbit coupling in the periodic potential.

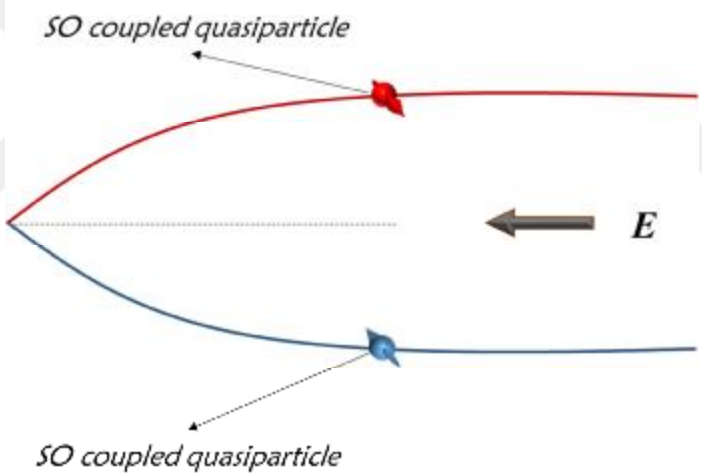


Figure 1.14. The spin-splitting under internal electric field due to the spin-orbit coupling.

The intrinsic spin-Hall contribution can be evaluated by using microscopic *ab-initio* theory calculations even for materials having complex electronic band structure. In heavy-metals which have strong spin-orbit-coupled bands, the intrinsic contribution might be dominant means the SHE and AHE. *Tanaka and Kontani et al.* have theoretically calculated some of 4*d* and 5*d* metals' spin Hall conductivities

based on a tight binding model by using for all elements for comparison the same quasiparticle relaxation rate which is proportional to the charge resistivity (Kontani et al., 2009; Tanaka et al., 2008). As seen in Figure 1.15, the sign of spin Hall conductivity changes from negative to positive when the atomic number is increased, for example from Ta to Pt. This sign change is expected from the equation (1.59). Some experimental results have already shown the sign reversal for these materials. To compare the charge conductivity, spin Hall conductivity and spin-Hall angles determined from the experimental measurements, a basic review is tabulated in Table 1.2.

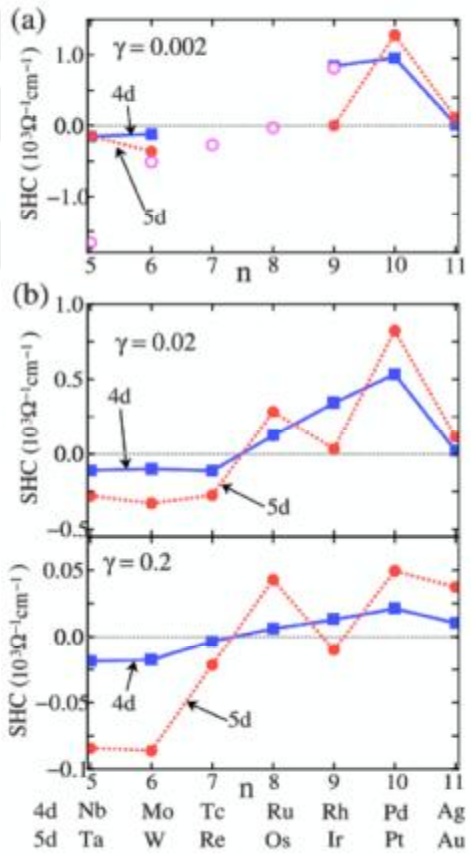


Figure 1.15. The theoretically calculated intrinsic spin Hall conductivity for 4*d* and 5*d* transition metals (Tanaka et al., 2008).

In addition to intrinsic spin Hall effect coming from the bulk band structure, there might be another possible spin Hall effects coming from the symmetry breaking at surface and interfaces, such as Rashba-type spin-orbit coupling. The presence of Rashba spin-orbit coupling might result in current-induced spin accumulations. It is difficult to distinguish of spin accumulation based spin Hall effect in the experiments. The current induced domain wall motion in a very thin ferromagnetic layer sandwiched between heavy metal and tunnel barrier creates spin-transfer torque comes from the spin accumulations at the interfaces due to Rashba-type spin-orbit coupling. In some materials, the interface or surface Rashba-type spin-orbit coupling might be overcome the bulk band coupling, and thus the intrinsic band model might be recessive.

1.5.3.2. Extrinsic Mechanisms of SHE

The extrinsic effects on spin-Hall effect can be referred as spin acquires a transverse velocity due to the spin-orbit coupling during the scattering of electrons. In addition to the intrinsic origin of scattering (e.g., phonons) as explained in the previous section, the source of the scattering can be also extrinsic such as impurities and grain boundaries. In the extrinsic effects, there are two scattering mechanisms which are spin-skew scattering and side-jump scattering. The spin-skew scattering can be defined as the direction of the electron momentum after scattering becomes spin-dependent. On the other hand, the side-jump scattering can be occurred a spin-dependent displacement during each scattering.

The mechanism of skew-scattering is that spin-orbit coupling comes out an effective magnetic field gradient within the scattering plane. This field gradient results in a net force toward or away from the scattering center which is depending on the direction of spin. Therefore, spin-skew scattering creates spin-Hall conductivity in the presence of spin-orbit interactions. Figure 1.16a-b indicate the schematic illustration of skew-scattering mechanism a) before and b) after

scattering of electrons when they are impressed by the local potential such as impurity or defect. It is also known as Mott scattering (Mott et al., 1965; Landau et al., 1965) that asymmetric scattering has been formed due to the spin-orbit coupling of the electron under potential of the impurity. The spin-Hall conductivity from spin-skew scattering is directly proportional to the longitudinal charge conductivity, such as $\sigma_{xy}^{ext} \propto \sigma_{xx}$. The spin-skew scattering is disposed to dominate the spin-Hall conductivity in high-purity samples. The magnitude of the extrinsic spin-Hall effect originated from the spin-skew scattering depends on the contrast between the spin-orbit coupling of the impurity and the host. Therefore, one can deduce that either heavy elements impurities in light element hosts or light elements impurities in heavy elements hosts can end up large spin-Hall conductivities (Gradhand et al., 2010).

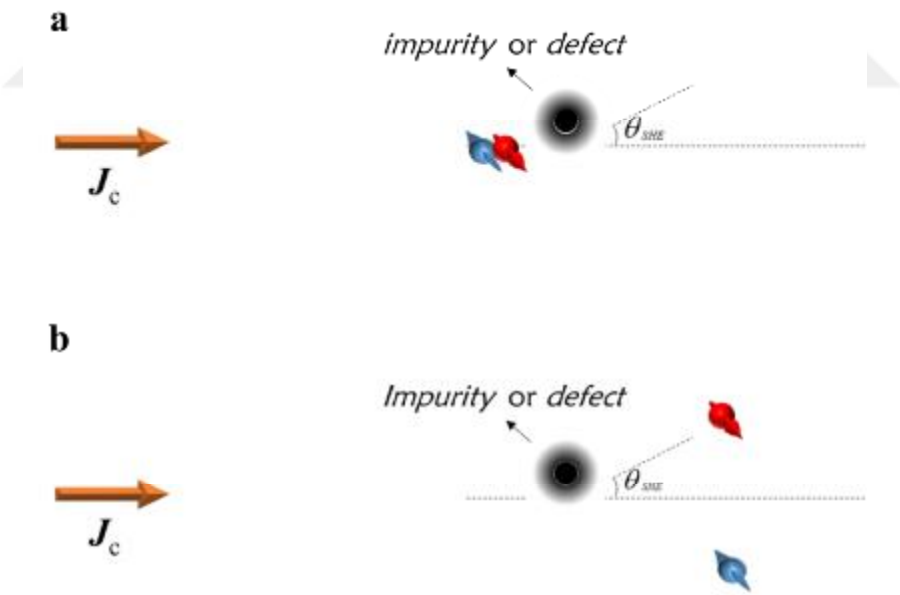


Figure 1.16. Schematic illustration of spin-skew scattering effect a) before and b) after scattering when electrons are impressed by the local potential such as impurity or defect.

For side-jump scattering, spin-dependent scattering can be accelerated or decelerated during the scattering which ends up an effective transverse displacement of electron upon repeated scattering. Figure 1.17a-c indicate schematic illustration of side-jump scattering when electrons are impressed by the potential of the impurities or defects. Although the side-jump scattering contribution is smaller than both spin-skew scattering and intrinsic contributions, the spin-Hall conductivity due to the side-jump scattering can result in a spin-Hall angle which is proportional to the impurity concentration..

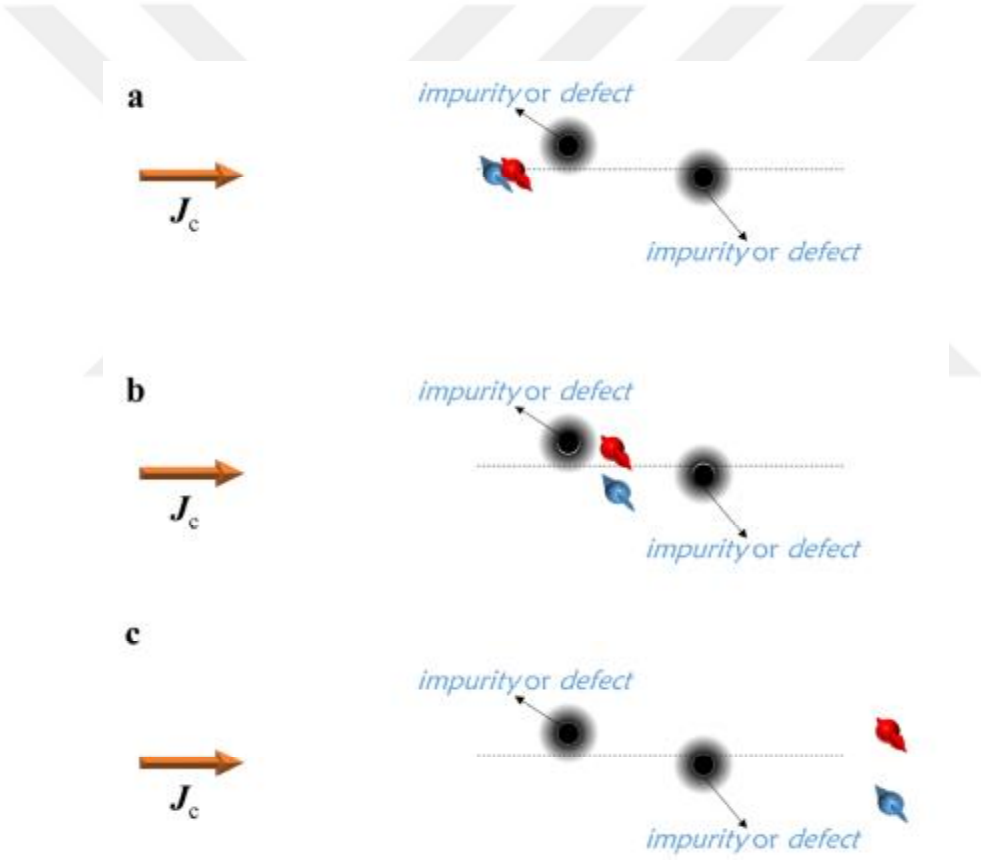


Figure 1.17. Schematic illustration of side-jump scattering effect a) before, after b) first and c) second scattering when electrons are impressed by the local potentials such as impurity or defect.

In other words, the spin-jump contribution might be dominant if the sample is dirty that means if the materials have enough impurity inside the host. In addition, the contribution to the spin-Hall conductivity due to the side-jump scattering can show stronger anisotropy property compared to the other possible mechanisms (Weischenberg et al., 2011)

Figure 1.18 shows that a review of Anomalous Hall conductivity as a function of longitudinal charge conductivity for various materials in the literature (Onoda et al., 2008). Because of the different dependencies of intrinsic and extrinsic mechanisms on the momentum relaxation time, the spin-skew scattering is expected to be dominant mechanism for very clean conductors with low scattering rates, here Anomalous Hall conductivity is proportional to the charge conductivity. In contrast, intrinsic or side-jump scattering mechanisms can be dominant for dirty conductors as shown in Figure 1.18.

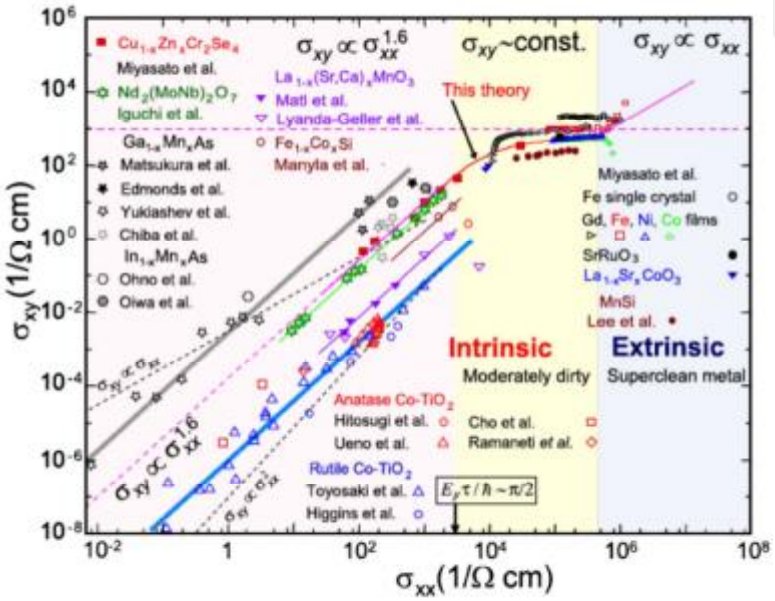


Figure 1.18. A review of Anomalous Hall conductivity as a function of longitudinal charge conductivity for various materials in the literature (Onoda et al., 2008).

Table 1.2. Comparison of charge conductivities, spin-Hall conductivities and spin-Hall angles from experimental measurements (Hoffmann, 2013).

Material	T (K)	σ_{xx}^{c} $\left(10^6/_{\Omega m}\right)$	$\sigma_{xy}^{S_z}$ $\left(\hbar 10^6/_{e\Omega m}\right)$	θ_{SH} (%)	Ref.
Al	4.2	17	2.7±0.6	0.02±0.01	(Valenzuela et al., 2006)
Au	293	48.3	< 1110	< 2.3	(Mihajlović et al., 2009)
	293	25.2	88±8	0.35±0.03	(Mosendz et al., 2010)
	293	5.3	84±5	1.6±0.1	(Hung et al., 2013)
	293	7.0	23.4±0.4	0.335±0.006	
	293	20	50±10	0.25±0.05	(Vlaminck et al., 2013)
	295	37	~ 4200	~ 11	(Seki et al., 2008)
	295	25.7	< 694	< 2.7	(Mihajlović et al., 2009)
Bi	3	0.0247	> 0.198	> 0.8	(Fan et al., 2008)
$Cu_{99.5}Bi_{0.5}$	10	8.8	~ -970	-11±4	(Niimi et al., 2012)
$Cu_{88}Ir_{12}$	10	2	~ 43	2.1±0.6	(Niimi et al., 2011)
Mo	10	2.8	-23±5	-0.8±0.18	(Morota et al., 2011)
	293	4.66	-2.3±0.5	-0.05±0.0	(Mosendz et al., 2010)
Nb	10	1.1	-10±2	-0.87±0.2	(Morota et al., 2011)
Pd	10	2.2	27±9	1.2±0.4	
	293	4.0	26±4	0.64±0.1	(Mosendz et al., 2010)
	293	1.97	~ 20	~ 1	(Ando et al., 2010)

Table 1.2. Continue.

	293	3.7	30±7	0.8±0.2	(Kondou et al., 2012)
	293	2.4	29±5	1.2±0.2	(Vlaminck et al., 2013)
Pt	10	8.1	170±40	2.1±0.5	(Morota et al., 2011)
	293	6.4	~ 510	~ 8	(Ando et al., 2008)
	293	2.4	31±5	1.3±0.2	(Mosendz et al., 2010)
	293	2.0	~ 80	~ 4	(Ando et al., 2011)
	293	5	340±30	6.8±0.5	(Liu et al., 2011)
	293	2.42	97±12	4.0±0.5	(Azevedo et al., 2011)
	293	4.3	51.6±3	1.2±0.2	(Feng et al., 2012)
	293	3.6	76±14	2.2±0.4	(Kondou et al., 2012)
	293	1.02	20.51±0.03	2.012±0.003	(Hung et al., 2013)
	293	1.2	~ 47	~ 4	(Nakayama et al., 2013)
	293	2.45	74±10	3.±4.	(Hahn et al., 2013)
	293	4	110±10	2.7±0.3	(Vlaminck et al., 2013)
	300	3.05	330±24	11.±8.	(Althammer et al., 2013)
Ta	10	0.3	-1.1±0.3	-0.37±0.11	(Morota et al., 2011)
	293	0.53	~ -63	-12.±4.	(Liu et al., 2012)
	293	0.08	-1.6±1.2	-2.±1.5	(Hahn et al., 2013)
W	293	0.38	-127±23	-33.±6.	(Pai et al., 2012)

1.6. Magnetic Anisotropy in Multilayer Structures

Magnetic property of a ferromagnetic material is generally explained by its magnetic hysteresis loops as shown in Figure 1.19 where coercive, H_c and remenance, H_r fields and saturation, M_s and remanence magnetization, M_r give characteristic properties of the material. The term of "magnetic anisotropy" can be basically described as the energy requirement of magnetization switching from up to down (or vice versa) that means its non-volatility property. The magnetization direction can be considered as *"easy-axis"* and *"hard-axis"* in the ferromagnetic single crystals. These terms are related to the energy requirements of the magnetization of a crystal depends on the direction of the applied magnetic field. Although, note that in the absence of magnetic field, magnetically isotropic materials have no favored direction, magnetically anisotropic materials have aligned magnetic moment with the easy-axis direction. Based on the magnitude of the anisotropy, the materials are classified as soft and hard magnets in nature.

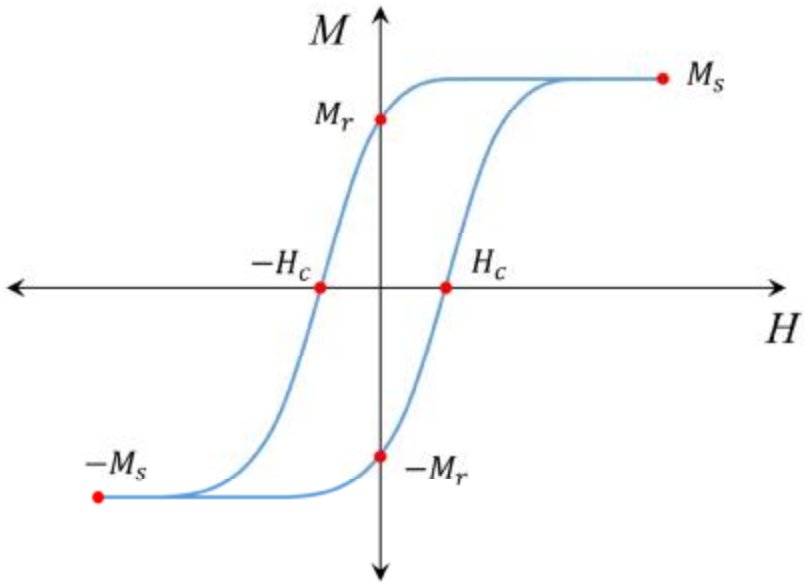


Figure 1.19. Hysteresis of a ferromagnetic material.

The magnetic anisotropy can be classified by in-plane (parallel to the film plane) and out-of-plane (perpendicular to the film plane) in ultrathin magnetic films and multilayers. The tendency of magnetization can form in its easy-axis direction by the anisotropy energy, E_a;

$$E_a = K_1 sin^2\theta \tag{1.60}$$

where θ is an angle between magnetization and the anisotropy axis. K_1 is anisotropy constant.

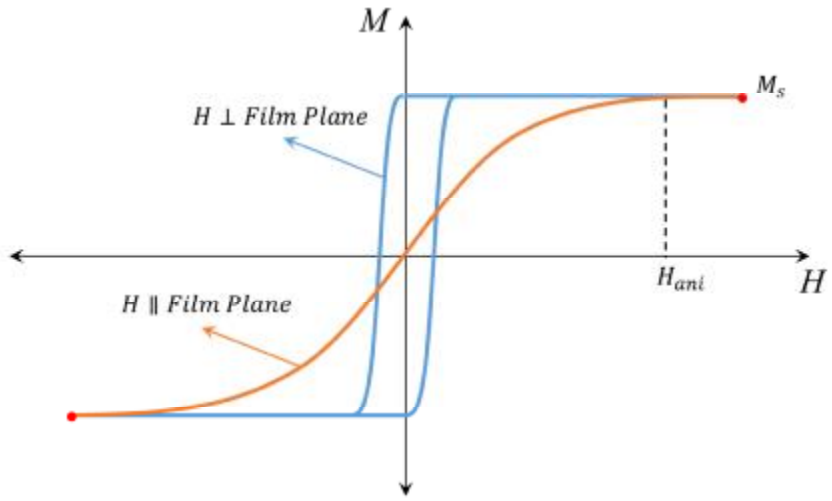


Figure 1.20. Hysteresis of a ferromagnetic thin film having magnetic anisotropy. The blue (orange) color curve indicates the external magnetic field is perpendicular (paralel) to the film surface.

The perpendicular magnetic anisotropy (PMA) is particularly important for information technology in terms of creating high density devices. However, it is so difficult to fabricate PMA rather than in-plane orientation of magnetization to the film plane. The origin of the PMA has come from the interface of the magnetic film, and so it is called interface or surface anisotropy. It is important to understand

the source of magnetic anisotropy to explain the magnetic behavior of a material. The sources of magnetic anisotropy are given below;

- Shape anisotropy,
- Magneto-crystalline anisotropy,
- Bulk and interface anisotropy,
- Magneto-elastic anisotropy,
- Exchange anisotropy,
- Stress anisotropy.

Since, in this dissertation study, some of these anisotropy sources do not include, we will just introduce shape, magneto-crystalline, magneto-elastic and bulk-interface anisotropy terms as following sub-sections.

1.6.1. Shape Anisotropy

The shape anisotropy is directly related to the demagnetization field in the system. Since the demagnetization field, H_d reduces the total energy of the system, the shape of sample becomes important to enhance effective energy of the system. The relation between demagnetization field and the magnetization can be written as;

$$\vec{H}_{di} = -N_{ij}\vec{M}_j \qquad i,j = x,y,z \tag{1.61}$$

where N_{ij} is the demagnetization tensor. In the ellipsoid shape, for an example, H_d and M are collinear and the component of N in diagonal form. Let's call the axes in an ellipsoid shape as (a, a, c).

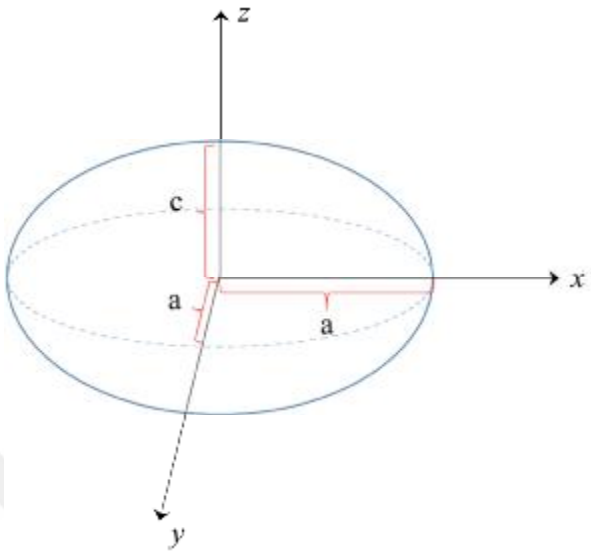


Figure 1.21. An ellipsoidal shape of a material.

The total of each component of demagnetization tensor is “1”, means;

$$N_x + N_y + N_z = 1 \tag{1.62}$$

The other basic shapes’ demagnetization tensors are given in Table 1.2.

Table 1.3. The demagnetization factors for simple shapes (Coey, 2010).

Shape	Magnetization Direction	N
Long Needle	Parallel to axis	0
	Perpendicular to axis	1/2
Sphere	And direction	1/3
This Film	Parallel to axis	0
	Perpendicular to axis	1
General Ellipsoid of Revolution	$N_c = (1 - 2N_a)$	

1.6.2. Magneto-Crystalline Anisotropy

Magneto-crystalline anisotropy is related to the crystal lattice of the ferro/ferri-magnetic materials. In other words, it is an intrinsic property of ferro/ferri-magnetic materials. Since the origin of magneto-crystalline anisotropy energy is coming from the crystal lattice, the grain size and shape have not affected the magneto-crystalline anisotropy. Figure 1.22 shows single crystal iron, cobalt and nickel elements hysteresis curves under different magnetized directions. As can be seen from the figure, the magnetization curves of single crystals ferromagnetic elements indicate different approach to the saturation when they are magnetized in different directions.

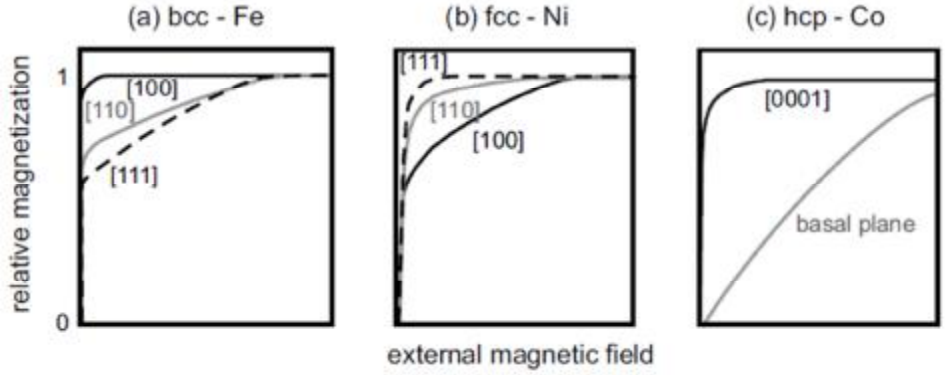


Figure 1.22. Relative magnetization of single crystals of bcc-Fe, fcc-Ni and hcp-Co (Getzlaff, 2008).

The magneto-crystalline anisotropy energy in hexagonal and cubic symmetries are given in the following relations.

For hexagonal symmetry;

$$E_a = K_1 \sin^2\theta + K_2 \sin^4\theta + K_3 \sin^6\theta + K_4 \sin^8\theta + \cdots \quad (1.63)$$

For cubic symmetry;

$$E_a = K_{1c}(\alpha_1^2\alpha_2^2 + \alpha_2^2\alpha_3^2 + \alpha_3^2\alpha_1^2) + K_{2c}(\alpha_1^2\alpha_2^2\alpha_3^2) \quad (1.64)$$

where α_i are the direction cosines of the magnetization (Coey, 2010). The K_{1c} term is equivalent to the $K_{1c}(\sin^4\theta\cos^2\phi\sin^2\phi + \cos^2\theta\sin^2\theta)$. When $\theta \approx 0, \phi \approx 0$, this reduces to $K_{1c}\sin^2\theta$. Thus, this term in every case is of the form equation (1.56).

The anisotropy field, H_{ani} can be defined as the field needed to saturate the magnetization of a uniaxial crystal in a hard direction. The energy of a system can be written as following;

$$E = K_u\sin^2\theta - \mu_0 M_s H cos(\frac{\pi}{2} - \theta) \quad (1.65)$$

Minimizing energy, $\partial E/\partial\theta = 0$ and setting $\theta = \pi/2$,

$$H_{ani} = 2K_u/\mu_0 M_s \quad (1.66)$$

The magnitude of anisotropy field give an information of the anisotropy degree of ferro/ferri-magnetic materials. In recent spintronic memory devices, the perpendicular magnetic anisotropy is used to make high density memories. In this dissertation, the anisotropy field is found both magnetization and transport measurements.

1.6.3. Magneto-Elastic Anisotropy

The magneto-elastic anisotropy comes from the spin-orbit interactions. Magnetostriction can be created from the strain which is dependence of anisotropy constants. A magnetic material can change the lattice dimensions when the material is under magnetic field. The inverse effect can also be seen that the stress/strain can change the magnetization of the materials. It is well known that the spin moments are coupled to the lattice by electrons in the conduction orbitals. If the lattice is

changed by strain/stress, the distance between the magnetic atoms is also changed. Thus, the interaction energy has been reformed under this kind of strain/stress. This enhancement or worsting in the interaction energy brings the magneto-elastic anisotropy.

The magneto-elastic energy per unit volume is given as following relation;

$$E = -\frac{3}{2}\lambda_{hkl}\sigma\cos^2\theta \tag{1.67}$$

where σ is the stress, θ is the angle between the magnetization and stress direction, λ_{hkl} is a magnetostriction constant which is depending on the crystal directions (Coey, 2010).

The sign of λ_{hkl} assigns the magnetization alignment. For positive λ_{hkl}, the easy magnetization direction will be along the tensile direction or perpendicular to a compressive stress direction.

In thin films and multilayers, the magneto-elastic anisotropy has crucial role for designing devices. The strain can be produced by growing parameters. For example, lattice mismatch between the layers can create a strain at the interfaces. In some applications, the stress can be used for enhancement of the performance of the device. However, in some cases, the stress can overcome the whole capabilities of the devices itself. Therefore, researchers first select the suitable substrate to make worsting or enhancement of mismatch between the layers for their applications.

1.6.4. Interface Magnetic Anisotropy

In contrast to the bulk (volume) systems, the multilayer or heterostructure films have another anisotropy term called as interface anisotropy. The interfacial magnetic anisotropy can only be observed at low dimensional systems. In a

multilayer film structure, the symmetry along the growing direction has been broken due to the each layer's different physical property. So, the order of bulk anisotropy energy will be reduced than the interfaces for ultra-thin film structures. The effective magnetic anisotropy energy density, K_{eff} can be written by combination of the bulk and interface contributions;

$$K_{eff} = K_b + {}^{K_i}/_{t} \tag{1.68}$$

where $K_b$is the bulk anisotropy energy density which depends on the magneto crystalline anisotropy, K_i is the interfacial magnetic anisotropy energy density and t is the thickness of ferromagnetic layer in the multilayer structure.

In order to investigate the thickness of ferromagnetic layer dependence on the effective magnetic anisotropy energy density, the relation of (1.64) transforms to the following form;

$$K_{eff}.t = K_b.t + K_i \tag{1.69}$$

The thickness of ferromagnetic layer dependence effective magnetic anisotropy can be drawn to determine the interfacial magnetic anisotropy energy density by sloping of this relation. Figure 1.23 shows the $K_{eff}.t$ versus t_{Co} in Co/Pd multilayer structure. Since the sign of $K_{eff}.t$ gives information about the magnetization direction, the critical thickness of ferromagnetic layer can be found by this figure. The critical thickness of ferromagnetic layer is that when the bulk and interfacial energy terms are equal means the effective anisotropy energy is zero. Therefore, the critical thickness of ferromagnetic layer is written as;

$$t_c = -{}^{K_i}/_{K_b} \tag{1.70}$$

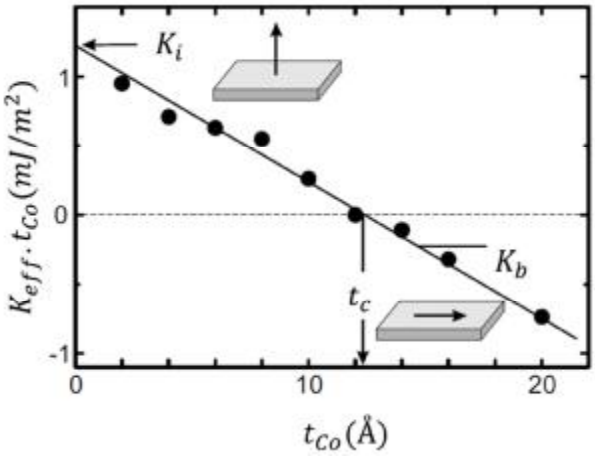


Figure 1.23. Effective magnetic anisotropy energy density multiplied by the thickness of ferromagnetic Co film as a function of ferromagnetic Co layer thickness (Getzlaff, 2008).

If the thickness of ferromagnetic layer is thinner than the critical thickness, the film will show perpendicular easy-axis magnetization. In other case, if the thickness of ferromagnetic layer is thicker than the critical thickness, the film will show in-plane easy-axis magnetization. This shows that the bulk contribution always dominants for thick films where the magnetization being within the film plane.

1.7. Current-Induced Magnetization Switching Mechanism in Spin-Transfer-Torque and Spin-Orbit-Torque based Devices

The controlling of magnetization in memory and logic devices is crucial part in spintronics. Although there are several method to control of the magnetization, such as magnetic-field induced, electric-field induced *etc*, the energy consumption is still high for those of the methods. Recently, a new switching mechanism has been emerged in spintronics called as current-induced magnetization switching. Spin angular momentum transferred between two ferromagnetic layer separated by a non-magnetic barrier (or tunnel barrier) might

excite the magnetization in one of the ferromagnetic layers. If this excitation is large enough to rotate the magnetization of ferromagnetic layer, the magnetization could be controlled by electric current. This physical mechanism was first proposed by Slonczewski and Berger in 1996 (Slonczewski, 1996; Berger, 1996). The first experiment on this switching mechanism was done in 1998 by Tsoi et al (Tsoi et al., 1998). They used a typical multilayer structure as fixed-ferromagnet (Co-10.0 nm)/spacer (Cu-6.0 nm)/free-ferromagnet (Co-2.5 nm) in their devices. The reason of the different thickness of ferromagnetic layers is due to the creating fixed and free layer in their experiment.

As explained in Section 1.3.3, while the spin polarized current (the electric current is passing through the device) is created by ferromagnetic layer in spin-transfer-torque devices, the spin current is generated by heavy-metal by driven in-plane electric current in spin-orbit-torque devices. Let's compare both switching mechanisms as following illustrations.

The spin-transfer-torque mechanism is illustrated in Figure 1.24. In the phenomena of STT, the electrons generally un-polarized are first passed through the fixed layer (FM_1) which has strong ferromagnetism. The majority of electron spins align with the fixed layer's magnetization ($\boldsymbol{M}_1$). Thus, the transferring electric current becomes spin-polarized current called as spin current. The moving of spin current can tunnel through the non-magnetic layer which is a barrier between two ferromagnets. After that the tunneled spin-currents can reach and hit the free layer's (FM_2) magnetization ($\boldsymbol{M}_2$). Here, the spin-current can be detected from the free layer. If these two ferromagnetic layers are not collinear with each other, the detected spin-currents can rotate the $\boldsymbol{M}_1$. In other words, the injected spin polarized electric current from the fixed layer creates a torque on the magnetization of free layer because of the non-collinear alignment of them. If the current density and spin current are large enough to excite the magnetization in the free layer, the direction of free layer magnetization could be switched by this method. This

physical phenomena is known as spin-transfer-torque which is recently started to use in magnetic random access memory devices as a data writing method.

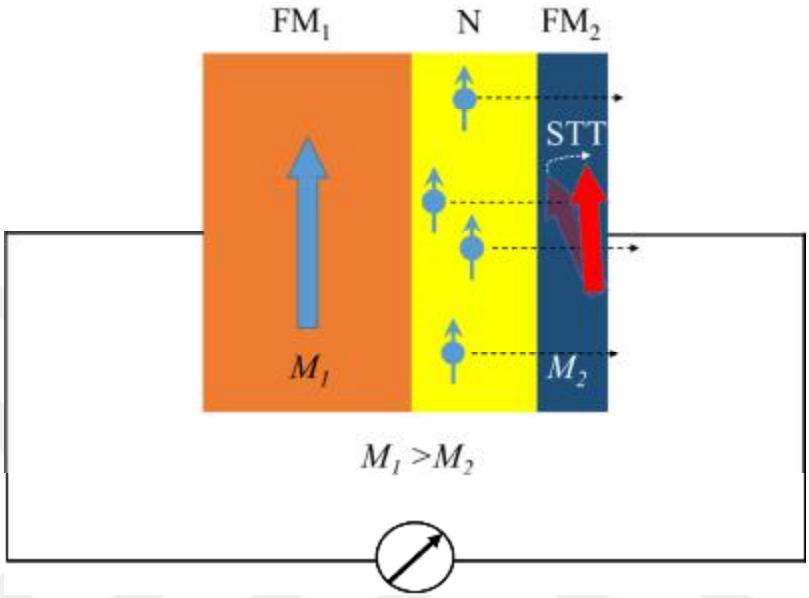


Figure 1.24. Manipulation of free layer magnetization by Spin-Transfer-Torque (STT)-based device composed of free layer ferromagnet/tunnel barrier/fixed layer ferromagnet structure.

In contrast to the STT mechanism, the spin-polarized electric current in spin-orbit-torque based devices is generated from the heavy-metal, instead of ferromagnet. A schematic illustration for spin-orbit-torque based device is given in Figure 1.25. The structure is composed of that heavy-metal (HM)/Ferromagnet (Free Layer, FM_2)/non-magnetic layer (N)/Ferromagnet (Fixed Layer, FM_1).

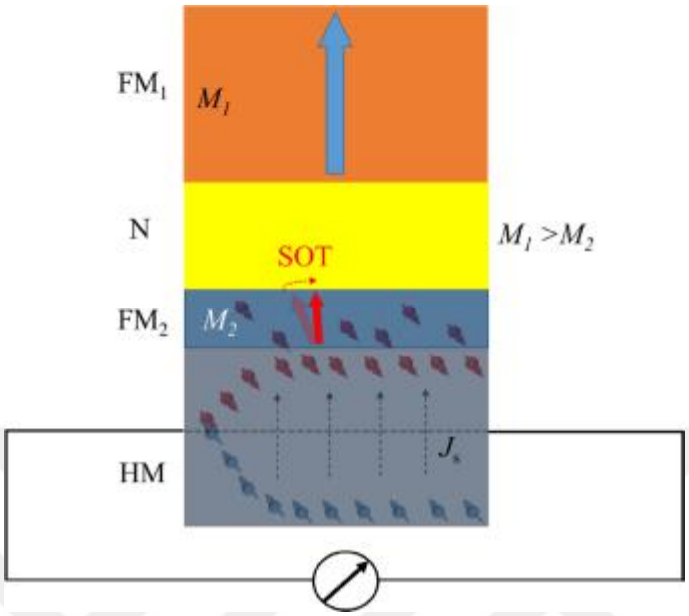


Figure 1.25. Manipulation of free layer magnetization by Spin-Orbit-Torque (SOT)-based device composed of heavy-metal/free layer ferromagnet/tunnel barrier/fixed layer ferromagnet structure.

Current-induced SOTs are generally observed in structures lacking inversion symmetry along the growth direction. They exhibit both field-like and damping-like torque terms, which each term has been attributed to contributions from different intrinsic and extrinsic mechanisms, including Rashba and spin Hall effects (Liu et al., 2012; Miron et al., 2011; Kim et al., 2013). In particular, structures with broken inversion symmetry along the growth direction may exhibit an internal electric field (E_{int}) at the interfaces along the direction of symmetry breaking (Mihai Miron et al., 2010), which results in a field-like SOT often associated with the Rashba magnetic field (H_R) that is given by $H_R = \alpha_R(\hat{z} \times \vec{J}_x)$. Here, α_R is a constant quantifying the strength of the Rashba effect, $\hat{z}$ is a unit vector along the perpendicular axis (i.e. along which symmetry is broken), and $\vec{J}_x$ is the current density vector. In another scenario, a spin current can be generated directly in the heavy metal due to the spin-Hall effect. The spin current which is

transverse to the charge current can cause a damping-like SOT which is often quantified as the spin-Hall effective field H_{SHE} that is given by $H_{SHE} = -\tau_{SHE}(\hat{m} \times (\hat{z} \times \vec{J}_x)$ (Khvalkovskiy et al., 2013). Here, τ_{SHE} is the spin-Hall effect spin-torque and $\hat{m}$ is the unit vector along the direction of magnetization. If the spin-current density is large enough to excite the free layer magnetization, the direction of it could be controlled by SOT-based method. Several works have addressed the effect of the heavy metal layer, ferromagnetic layer, and their interface on the resulting SOTs in such structures. This includes experiments with different heavy metal materials such as Ta, Pt, and W,(Liu et al., 2012; Liu et al., 2012; Miron et al., 2011; Mihai Miron et al., 2010; Emori et al., 2013; Pai et al., 2012; Garello et al., 2013; Pai et al., 2014) and their thickness dependence, as well as ferromagnetic layers such as Co and CoFeB (Pai et al., 2012; Kim et al., 2013) or the effect of the interface between the heavy metal and the ferromagnetic layer (Liu et al., 2012; Fan et al., 2013).

1.8. Objectives and Thesis Outlines

As discussed in Section 1.2 that there are three crucial technological requirements for high performance magnetic tunnel junction devices in application markets. One of them is the density of devices that can be increased almost 10 times by designing perpendicular magnetic anisotropy rather than in-plane recording media. Another one is data reading process from the MRAM devices. The tunneling magnetoresistance ratio must be large for high sensitive MRAM devices in terms of reading data. The last one is the writing data into the MRAM devices. The most important requirement might be the writing process due to energy consumption. Although there are couple of methods to write the data into the recording media in the MRAM devices, a new method has been emerged in spintronic. This new writing process is performed by driving electric current to create torque on magnetization.

In this dissertation, the perpendicular magnetic anisotropy in metallic multilayer structures and controlling of the magnetization by electric current-driven spin-orbit torques have been worked in ultra-thin ferromagnetic free layer. The introduction part of this dissertation gives a motivation and basic background of the spintronics.

In the second chapter, we summarize the literature previews of the perpendicular magnetic anisotropy and magnetization controlling mechanism in such structures.

In the third chapter, ultra-thin magnetic multilayer film deposition, fabrication process of devices and their characterization methods in terms of structural, electrical and magnetic properties have been explained.

In the fourth chapter, the various experimental results on the structural, transport and magnetic characteristics are presented. Experimental studies have also been performed to understand the physical origin of the designed structures. This chapter covers following sub-sections;

- A study on the heavy-metal layer thickness dependence surface roughness, perpendicular magnetic anisotropy, x-ray photo electron spectroscopy, electrical transport, current-driven spin-orbit torques and current-driven magnetization switching mechanism.
- A study on the oxide layer effect on perpendicular magnetic anisotropy, electrical transport, current-driven spin-orbit torques and current-driven magnetization switching mechanism.
- A study on the engineering the structural inversion symmetry to switch the magnetization without external magnetic field. This sub-section has been investigated by performing perpendicular magnetic anisotropy, electrical transport, current-driven spin-orbit torques and current-driven magnetization switching mechanism. In addition, a study on the free-layer

ferromagnetic layer thickness dependence perpendicular magnetic anisotropy, electrical transport, current-driven spin-orbit torques and current-driven magnetization switching mechanism in both Hf|CoFeB(*wedge*)|TaO_x and Hf|CoFeB(*wedge*)|MgO multilayer structures.

In the final chapter, the dissertation has been concluded and suggested a couple of recommendation for the future research efforts in the spintronic devices.

2. LITERATURE REVIEW

Computing technology consists of the writing, storing and retrieving information encoded as magnetic bits. The main issues in traditional information technology can be listed as high energy consumption, low endurance, volatile property, stand-by power consumption, low density and low write/read speed. After the discovery of spin electronics, the modern computing technology is getting better day by day. However, there are still some challenges in terms of the magnetic writing process of a high-coercivity single layer ferromagnet, such as density. The high-density non-volatile memory with high thermal stability can be achieved using perpendicular magnetic anisotropy. Thus, the large coercivity and perpendicular magnetic anisotropy signify high performance data storage media. At that time, the magnetic switching of the PMA with large coercive ferromagnetic layer brings another issue which is the energy consumption. Therefore, different research group in all around the world have working on overcome these challenges of the magnetic recording medias.

So far, many material and/or materials group have been worked in terms of obtaining perpendicular magnetic anisotropy to integrate into the magnetic tunnel junctions. Although there are many materials capable of demonstrating PMA property, the origin of PMA comes from different mechanisms for each material and structure. In addition to the PMA property of MTJs, the controlling of magnetization in meanwhile writing process of data into the MTJs is also crucial phenomena in memory-based devices. An overview of the main research on different material based PMA mechanisms and switching of perpendicular magnetic layer by spin-orbit torques have been summarized as following sections.

2.1. A Review on the Perpendicular Magnetic Anisotropy

The most available materials as an electrode by creating perpendicular magnetic anisotropy in magnetic tunnel junctions are the rare earth/transition metal alloys (Kay et al., 2010; Nishimura et al., 2002; Ohmori et al., 2008), $L1_0$-ordered (Co, Fe)- (Pt, Pd) alloys (Yoshikawa et al., 2008; Kim et al., 2008) and Co/(Pt, Pd, Ni) multilayers (Yakushiji et al., 2010; Carvello et al., 2008; Park et al., 2008). In addition to these materials, Co, Co_xFe_{1-x} and $Co_xFe_{1-x}B_y$ layer sandwiched by Pt, Pd, Ta, Mo, Hf, W and AlO_x, TaO_x and MgO have been explored in term of showing strong PMA (Jung et al., 2010; Nistor et al., 2009).

Liu et al. (2012) experimentally worked on the PMA in CoFeB/MgO system with Ta as a seed layer by replacing Hf layer. Although the origin of PMA is coming from the interfaces between CoFeB and MgO layers, they observed that the buffer layer material affects PMA significantly. The enhancement in PMA by replacing Ta with Hf material is around 35%. In addition to the PMA enhancement, they observed the thickness of CoFeB can be increased further due to the larger thermal stability of Hf than Ta. Figure 2.1 shows the effective magnetic anisotropy energy dependence ferromagnetic CoFeB layer thickness in Ta/CoFeB/MgO and Hf/CoFeB/MgO multilayer structures (Liu et al., 2012).

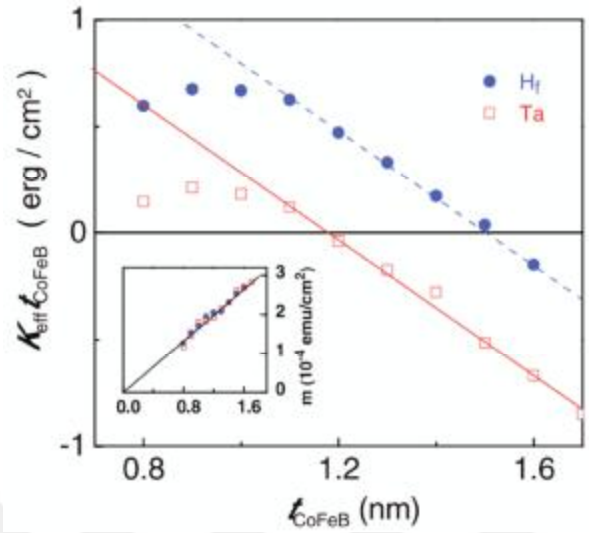


Figure 2.1. Effective magnetic anisotropy energy times ferromagnetic layer thickness as a function of ferromagnetic layer thickness in Ta/CoFeB/MgO and Hf/CoFeB/MgO systems.

The theory proposed by Yang et al. suggested that CoFeB/MgO interfacial PMA comes from the overlap between the O-p_z and transition metal d_{z2} orbits with larger spin-orbit coupling induced splitting around the Fermi level for the perpendicular magnetization orientation. The SOC of the CoFeB layer can be strengthened by the adding heavy elements. Therefore, a heavier element dusting layer can enhance the interfacial magnetic anisotropy, i.e., Hf>Ta>W by sequence. From the light of theory as explained above, the Hf insertion layer enhances the CoFeB/MgO interfacial anisotropy (Yang et al., 2011). Therefore, the author observed stronger PMA in Hf-based structure than that of Ta-based structure.

Lee et al. (2011) worked on the effect of annealing and crystallization of MgO (100) on magnetic anisotropy of CoFeB. The thickness of CoFeB was studied in a range of 1.5 to 5.0 nm. The films were grown by magnetron sputtering system and annealed at 300°C for 2h under 1.5T magnetic field. They measured magnetization as a function of external magnetic field directed to the in-plane and out-of-plane to the films by vibrating sample magnetometer. First of all, they

determined the magnetic dead layer thickness (4.1Å) for annealed films. The saturation magnetization, M_s was obtained as ~830 emu/cc and ~1130 emu/cc with and without-annealing process, respectively. The increase in M_s is explained due to the crystallization of CoFeB during annealing process. The graph of effective magnetic anisotropy energy, K_{eff} as a function of effective magnetic layer thickness is shown in Figure 2.2.

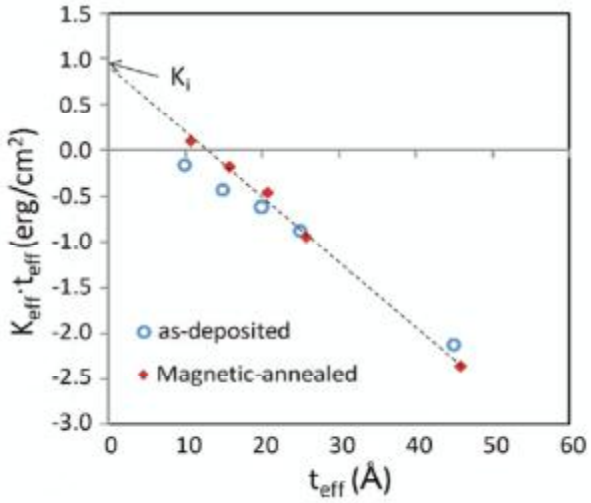


Figure 2.2. Effective magnetic anisotropy energy times ferromagnetic layer thickness as a function of ferromagnetic layer thickness for as-deposited and annealed stacks under magnetic field.

Since the negative K_{eff} value means the in-plane magnetic anisotropy in film structure, the films have in-plane magnetic anisotropy, except the film of CoFeB (1.5nm) annealed under magnetic field. The interfacial magnetic anisotropy energy, K_i was extracted ~0.94 erg/cm^2 which is comparable to the literature in such a film structure. In addition to the annealing and CoFeB layer thickness effect on the magnetic anisotropy, they studied a very thin Ru layer insertion effect on the PMA property. For that, they inserted a very thin Ru (0.9 nm) layer between CoFeB and Ta as a capped layer. They observed that the insertion of Ru (0.9 nm)

enhances the PMA when the CoFeB thickness is 2.0 nm. Although they did not calculate the effective magnetic anisotropy energy, the out-of-plane magnetization was observed (see Figure 2.3) in CoFeB(2.0nm)/Ru(0.9nm)/Ta while they couldn't see it without Ru layer.

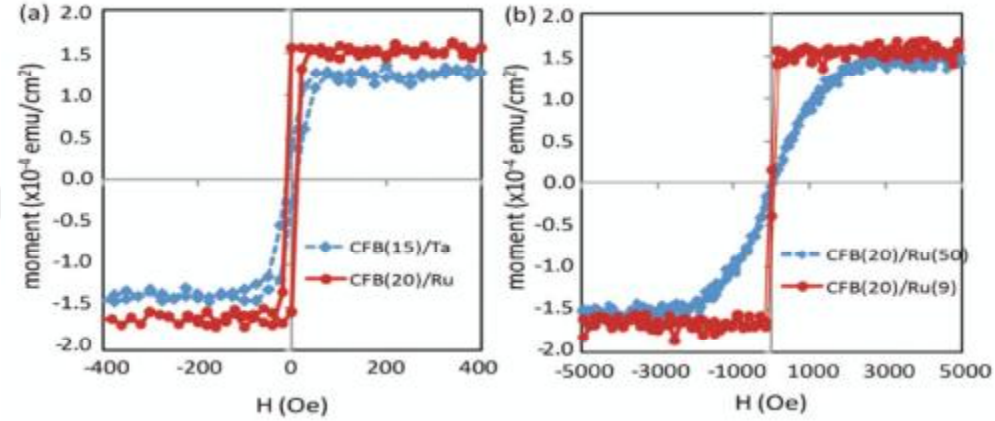


Figure 2.3. The moment as a function of applied magnetic field for a) CFB(15)/Ta and CFB(20)/Ru and b) CFB(20)/Ru(9) and CFB(20)/Ru(50) films.

They also worked on the effect of MgO crystallinity on the PMA by performing single-crystal MgO (100) and rf-sputtered MgO. The crystallinity of MgO and in parallel with CoFeB crystallinity have crucial role to create strong interfacial PMA in such multilayer structures.

Nistor et al. (2009) worked on the perpendicular magnetic anisotropy in Pt/Co/oxide and oxide/Co/Pt structures as an electrode in magnetic tunnel junctions. They grew multilayer films on thermally oxidized Si/SiO_2 substrate by sputtering system. Co layer thickness was selected 0.6 and 1.5 nm in main structure. The magnetic properties of the films were studied by doing extra-ordinary Hall effect (EHE) measurement, since the EHE voltage is proportional to the out-of-plane magnetization, M_z. When the thickness of Co is 0.6 nm, the film has superparamagnetic phase. However, the film became perpendicular magnetic

anisotropy for 1.5 nm Co thickness. Figure 2.4a-b show the EHE resistance as a function of out-of-plane magnetic field in SiO_2/Co(0.6)/Pt and SiO_2/Co(1.5)/Pt structures (Nistor et al., 2009).

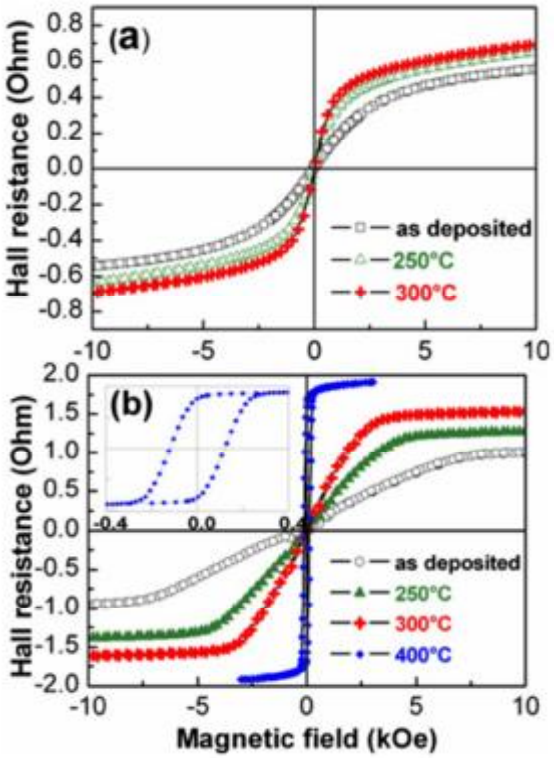


Figure 2.4. Hall resistance as a function of applied magnetic field for a) SiO_2/Co(0.6)/Pt and b) SiO_2/Co(1.5)/Pt films annealed at various temperatures

They observed the magnetization is in-plane direction for all samples in the as-deposited form of films. But, the PMA increases with the annealing temperature as shown in Figure 2.5. They showed that all the films which are oxidized by different oxide materials such as MgO, AlO_x and SiO_2, exhibit perpendicular magnetic anisotropy after the annealing 325°C. The largest anisotropy field (H_{an}) value was found for Co deposited on the plasma oxidized Al. The anisotropy is directly related to the enthalpy of formation of different oxides. Therefore, the

hybridization of Co and O orbitals at the interface is different for natural and plasma oxidation of Mg, Al and Si materials.

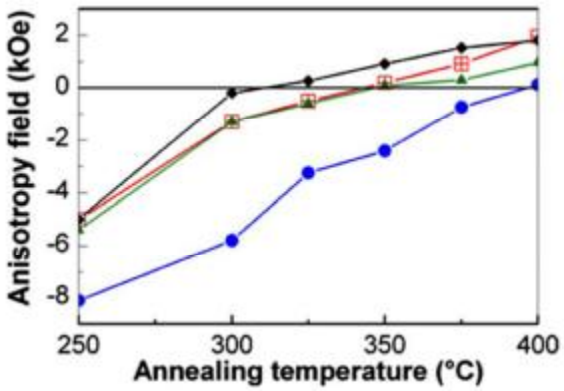


Figure 2.5. Anisotropy field as a function of annealing temperature.

Nister et al. (2009) experimentally showed that the magnetic anisotropy of the top electrode oxide/Co/Pt is smaller, by a factor of 10, than that for the bottom electrode Pt/Co/oxide. They concluded that the growing of Co is more difficult on an oxide than on Pt.

Cui et al. (2013) experimentally studied on the perpendicular magnetic anisotropy in CoFeB(1.0 and 0.5 nm)/X (X=MgO, Ta, W, Ti and Pt) multilayers deposited by magnetron sputtering system. To investigate the magnetic property of the multilayer films, they used a superconducting quantum interference device (SQUID). The CoFeB/MgO multilayer films showed strong PMA property coming from the Co-O and/or Fe-O bonding, whereas CoFeB/metal multilayers have weak perpendicular magnetic anisotropy properties. Figure 2.6a-d show magnetic hysteresis of CoFeB/X (MgO, W, Ta and Ti) by sweeping both perpendicular and in-plane direction of magnetic field. The saturation magnetization of CoFeB/MgO multilayer film is the highest value (~1400 emu/cm^3), while others are below than ~400 emu/cm^3. The authors explained that this remarkably high M_s value in CoFeB/MgO structure is coming from the interfacial PMA property which is

schematically illustrated in Figure 2.6e. The hybridization of Co-O and/or Fe-O align the same direction of magnetic moments, thus perpendicular magnetic anisotropy might increase the magnetic moment of Co and/or Fe (Cui et al., 2013).

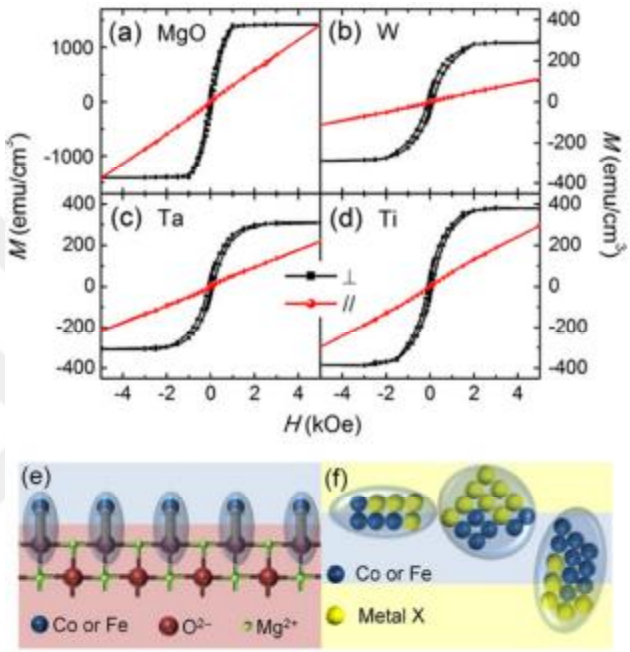


Figure 2.6 a-d) Magnetic hysteresis of CoFeB/X (MgO, W, Ta and Ti) by sweeping both perpendicular and in-plane direction of magnetic field. e-f) schematically illustration of interfacial magnetic anisotropy.

For other multilayer structures, CoFeB/W, CoFeB/Ta and CoFeB/Ti as shown in Figure 2.6b-d, respectively, the magnetization curves indicate a relatively large coercive field and low saturation magnetization when H is perpendicular to the film plane. The decrease of M_s value in CoFeB/metallic multilayers could be mainly due to the paramagnetic contributions coming from the forming of interfacial alloying. A schematic illustration is shown in Figure 2.6f. In contrast to the uniform bonding of Co-O and/or Fe-O in CoFeB/MgO interface, the interfacial

alloying during non-equilibrium sputtering process could pin the turn of magnetic domain.

Cui et al. summarized that while the perpendicular magnetic anisotropy in CoFeB/MgO can be observed by bonding of Co-O and/or Fe-O, the CoFeB/metallic multilayers' magnetic anisotropy is very weak due to the formation of interfacial alloying caused paramagnetic phase. As a result, the magnetic property and formation enthalpy of interfacial alloy plays an important role in PMA property.

Ikeda et al. (2012) published a work on the effect of Boron composition on the magnetic anisotropy and tunnel magnetoresistance in MgO/CoFe(B) based stack structure. They deposited the films stacks on thermally oxidized Si (001) substrate by magnetron sputtering system at room temperature. The film stacks are; SiO_2/Ta(5.0)/MgO(1.0)/$(Co_{0.25}Fe_{0.75})_{100-x}B_x$ (t_{CoFeB}=1.5-3.0)/Ta(5.0)Ru(5.0). The numbers in parenthesis are nominal thickness in nanometers. This stack is composed of the top electrode structure in MTJs. The *x* values of Boron are 0, 15, 20 and 25 (in at %). The full stack of MTJ is composed of SiO_2/Ta(5.0)Ru(10.0)/Ta(5.0)/$Co_{20}Fe_{60}B_{20}$(0.9)/MgO(0.9)/$(Co_{0.25}Fe_{0.75})_{100x}B_x$(1.5)/ Ta(5.0)/Ru(5.0). The magnetic properties of the films were investigated by vibrating sample magnetometer. Firstly, they determined saturation magnetization, M_s and magnetically dead layer thickness, t_d as a function of Boron composition in $(CoFe)_{100-x}B_x$ (see Figure 2.7a-c). The Boron composition dependence of the M_s in MgO/$(CoFe)_{100-x}B_x$ stack shows that the M_s decreases with increasing B composition. On the other hand, the M_s increases with increasing annealing temperature from as-deposited to 350°C (Ikeda et al., 2012).

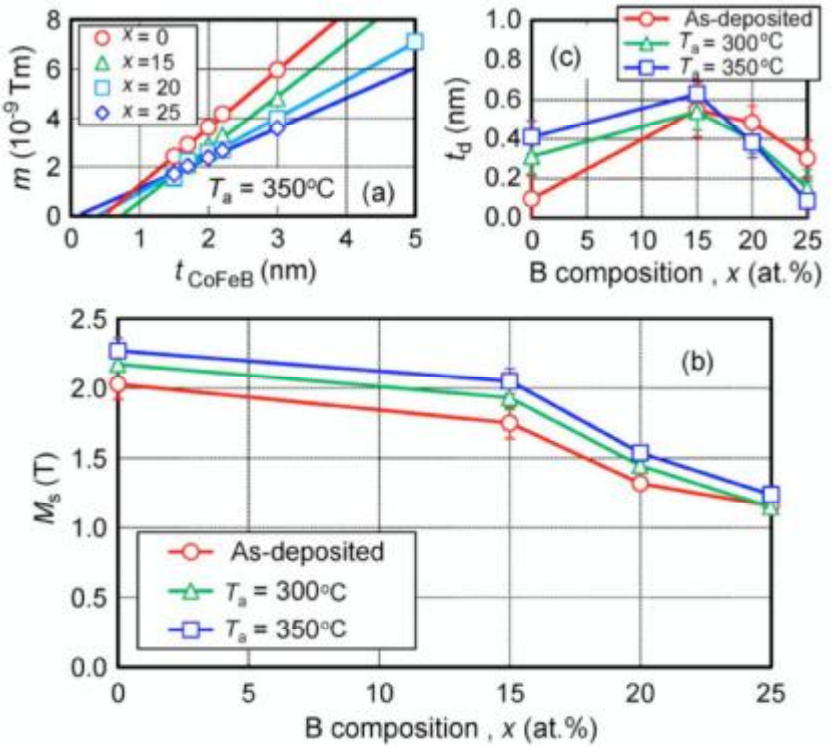


Figure 2.7 a) Moment versus CoFeB layer thickness at various B concentration, b) Dead layer thickness as a function of B composition in ferromagnetic layer, c Saturation magnetization as a function of B composition in ferromagnetic layer.

Authors explained that the increasing of M_s with annealing temperature could be attributed to the reduction of B composition in CoFeB layer by means that B is absorbed by Ta layer. In addition, a non-monotonic behavior was observed in t_d dependence B composition. The B composition dependence of effective magnetic anisotropy energy density, K_{eff} of the stack with t_{CoFeB}=1.5 nm was determined by $K_{eff}=M_sH_k/2$. It is interestingly observed from the authors that the magnetic anisotropy of the films is in-plane magnetic easy-axis for x=0 and 15, whereas it exhibits perpendicular easy-axis for x=20 and 25. The increase of K_{eff} by annealing temperature is coming from the enhancement of interface anisotropy energy, K_i. In contrast, the K_i decreases with increasing B composition.

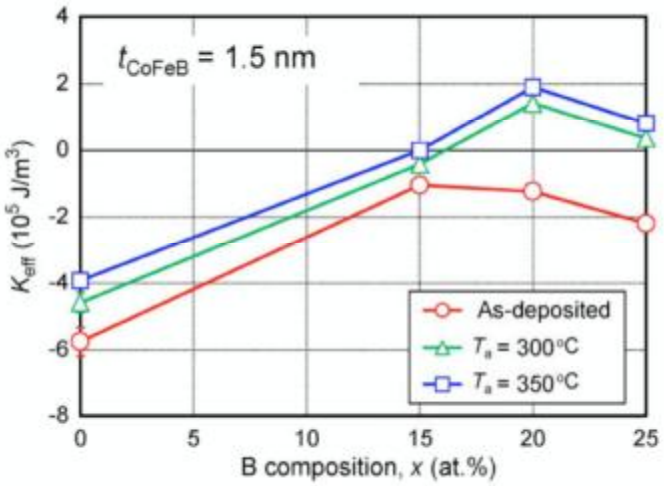


Figure 2.8. Effective magnetic anisotropy energy density as a function of B composition in ferromagnetic layer.

The authors finally worked on the B composition dependence of tunneling magnetoresistance (TMR) property of the fully magnetic tunnel junction. The TMR value increases with increasing B composition for annealed films, except as-deposited one. At higher annealing temperature, the Boron diffusion from the CoFeB to the electrode will be higher. Thus, the crystallization of CoFe will be improved and TMR enhances.

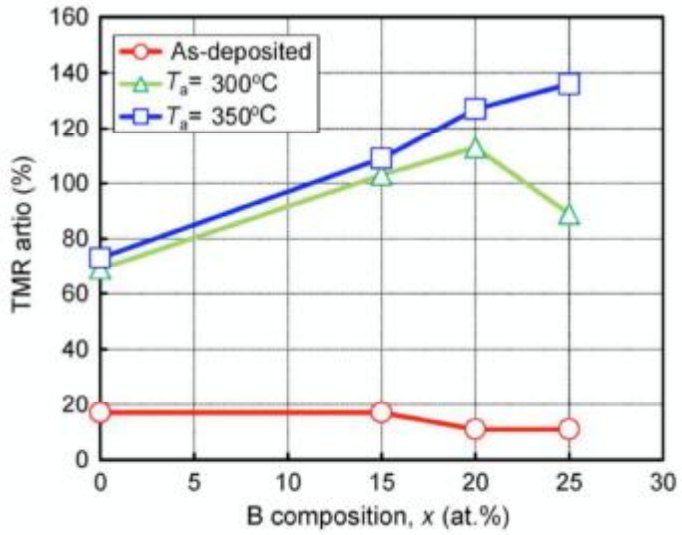


Figure 2.9. Tunneling magnetoresistance as a function of B composition in ferromagnetic layer.

Greer et al. (2012) worked on the Boron distribution in Ta/$Co_{20}Fe_{60}B_{20}$/MgO multilayer structure. The film was annealed at 300°C for 1 h to crystal CoFe. They used a standing-wave (SW) excited hard x-ray photoemission spectroscopy (HXPS, HAXPES) which is an effective material characterization measurement for magnetic multilayer films. The film stack is shown in Figure 2.10a-b for as-deposited and after annealing process, respectively (Greer et al., 2012).

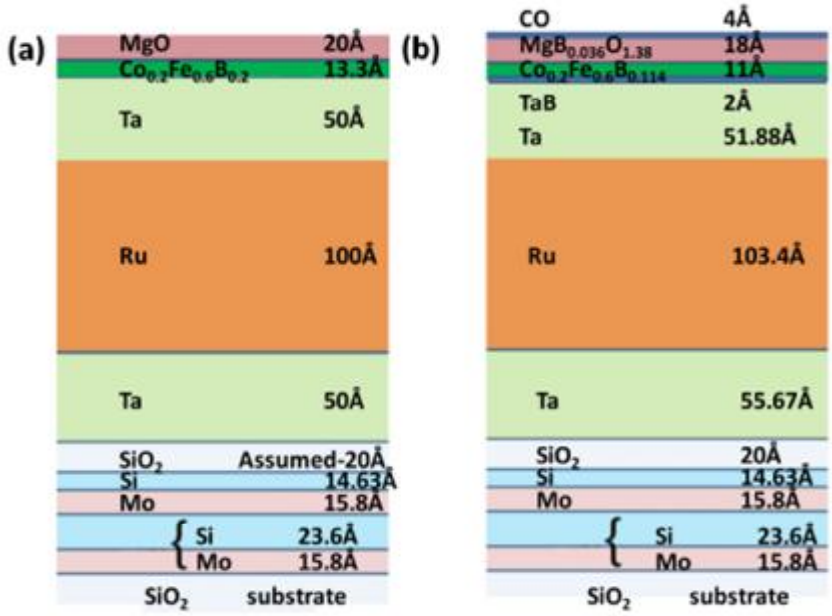


Figure 2.10. Multilayer film stacks a) before and b) after annealing process.

The x-ray photoelectron spectra of all elements in Ta/CoFeB/MgO structure is shown in Figure 2.11. It has been observed from the XPS spectrum that the Boron has three formation in the structure after annealing process. They are *i*) remaining B inside the CoFeB layer, *ii*) formation of BO_x at the interface between CoFeB and MgO layers, and *iii*) formation of TaB_x at the interface between CoFeB and Ta layers (see Figure 2.11c, f). The authors determined the diffusion of Boron around 19.5% uniformly into the MgO and 23.5% into the TaB interface layer by SW-HXPS analysis.

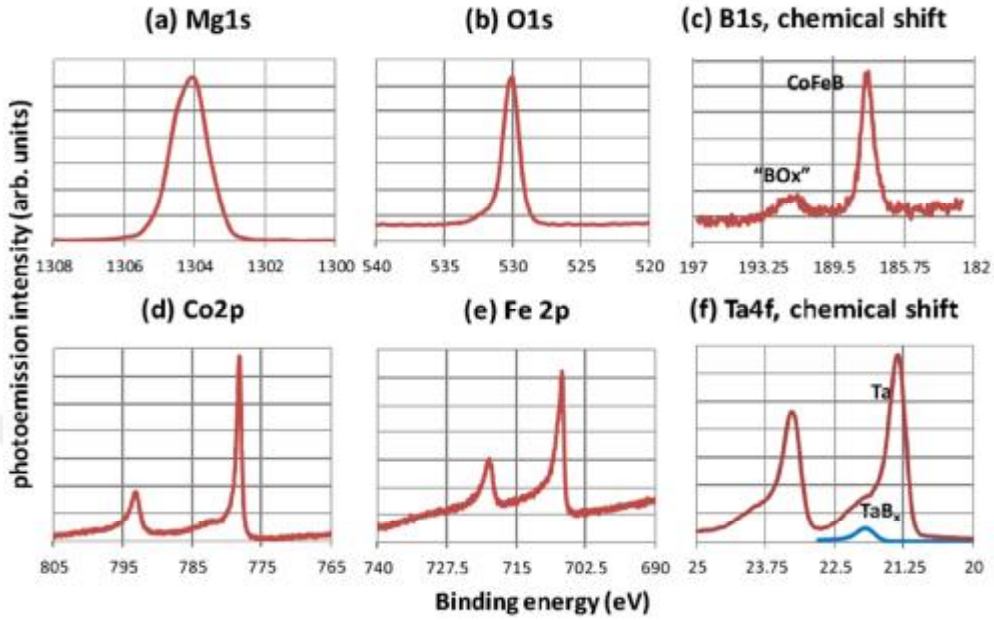


Figure 2.11. The x-ray photoelectron spectrum in Ta/CoFeB/MgO structure.

Yang et al. (2015) worked on the Ta thickness dependence perpendicular magnetic anisotropy in Ta(t_{Ta})/$Co_{20}Fe_{60}B_{20}$(t_{CoFeB})/MgO(2)/W(3) multilayer structure. They grew the multilayer films by magnetron sputtering system. The Ta layer thickness varied from 0.75 nm to 4.5 nm with a 0.75 nm step and CoFeB layer thickness varied from 1.02 nm to 2.22 nm. The W as a cap layer was deposited to prevent oxidation by atmosphere during analysis. The multilayer films were annealed at 300, 325, 350 and 375°C for 1h under vacuum condition with a 3 T perpendicular magnetic field. The magnetic hysteresis of Ta(1.2)/CoFeB(1.2)/MgO(2)/W(3) multilayer films annealed at 300, 325, 350 and 375°C were performed to investigate the effect of annealing temperature on PMA feature (Yang et al., 2015). Figure 2.12a-d show in-plane and out-of-plane M-H curves in such structure annealed at various temperatures. The M-H curves of the films annealed at 300 and 325°C indicate PMA feature in Ta/CoFeB/MgO stack. However, the PMA properties decrease with increasing annealing temperature. The

results clearly show that the destroying PMA feature after high temperature thermal treatment could originate from the thermally activated Ta atom diffusion toward the CoFeB and MgO layers. The diffusion of the Ta atoms could destroy the hybridization of Co-O and/or Fe-O which are required to create PMA feature in such structures. Therefore, the PMA property is getting weaker when annealing temperature is increased.

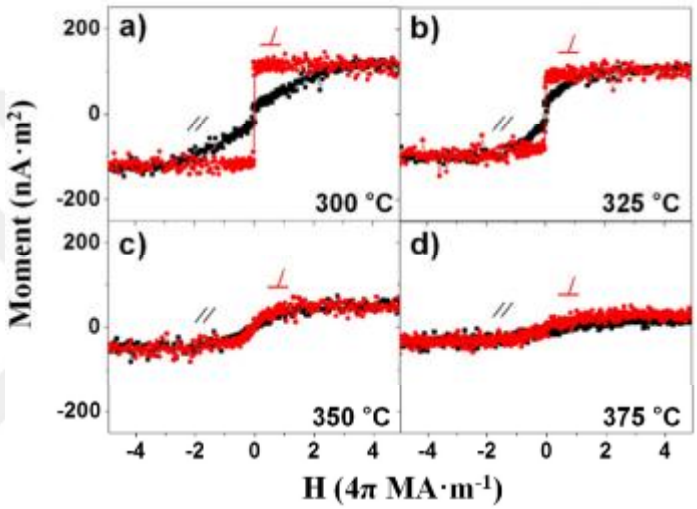


Figure 2.12. Moment versus external magnetic field in Ta/Co₁FeB/MgO stack annealed at a) 300°C, b) 325°C, c) 350°C and d) 375°C.

The authors performed XPS depth profile analysis of Co and Ta atoms to clarify Ta thickness dependent diffusion behavior during thermal treatment. The XPS data was taken in low vacuum pressure (10^{-6} Pa) by etching with a time step of 3s up to 51s. They used Ar ion etching process to analyze atomic property at the interfaces. Figure 2.13a shows the multilayer film stack of Sample A and Sample B which are stacked as Ta(1.5)/CoFeB(1.2)/MgO(2)/W(3) and Ta(4.5)/CoFeB(1.2)/ MgO(2)/W(3), respectively. Figure 2.13b shows typical depth profile analyses for Ta and Co atoms in Sample A and B annealed at 350°C. The Co atoms diffusion seems almost same in both samples since the distribution of Co atoms at the

interface between CoFeB and MgO layers are similar. However, the Ta 4*f* depth profile measurement showed a clear difference in Ta atom distributions. At the CoFeB/MgO interface region, a large amount of Ta atoms in Sample B is appeared. This result confims that the weaking of effective magnetic anisotropy by increasing annealing temperature could be explained the diffusion of Ta atoms at thye interface between CoFeB and MgO layers. Thus, the hybridization of Co-O and/or Fe-O become weaker when the annealing temperature is higher than 350°C in Ta-based structure.

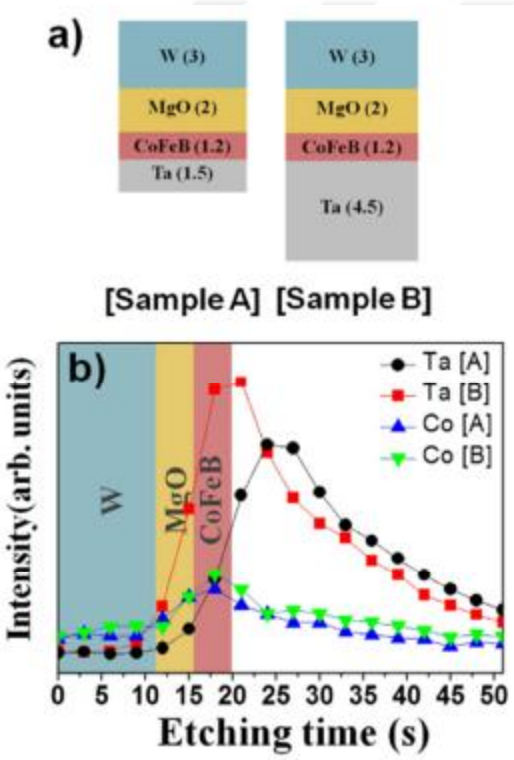


Figure 2.13 a) Multilayer structures of Sample A and Sample B, b) XPS depth profile of Co and Ta in such structure.

All these materials (or the combination of materials systems) suffer from many difficulties when they are integrated into the MTJs. Some of these difficulties can be listed as low magnetoresistance ratio, low chemical and/or thermal

stabilities, large energy requirement for current-induced magnetization switching due to their large Gilbert damping constant. Therefore, research groups in all around the world have worked intensely to find out optimum parameters as explained above.

2.2. A Review on the Controlling of Magnetic Layer in Heavy Metal/ Ferromagnet/Oxide Layer and MTJs.

Kim et al. (2013) worked the vector measurements of the current-induced effective field in Ta(t_{Ta})/$Co_{20}Fe_{60}B_{20}$(1.0)/MgO(2.0)/Ta(1.0) and Ta(1.0)/$Co_{20}Fe_{60}B_{20}$(t_{CFB})/MgO(2.0)/Ta(1.0) multilayer structures where the thickness of each layer, t_{Ta} and t_{CFB} is varied from 0 to 2.0 nm. They grew the multilayer films on Si/SiO_2 substrate by magnetron sputtering system. After growing process, they fabricated the devices to pattern Hall bars by photolithography and Ar ion etching process. The magnetic property of multilayer films are perpendicularly magnetized to the films surface (Kim et al., 2013).

The vector measurement was used to determine effective fields generated from the spin Hall and Rashba effects. The similar experimental set-up will be discussed detail in Chapter 3. The longitudinal (ΔH_L) and transverse (ΔH_T) effective fields were affected significantly by Ta and CoFeB layer thickness in such multilayer structures. The results showed that the size and sign of the longitudinal, and transverse effective fields varied with the Ta and CoFeB layer thickness. The effective fields, ΔH_T and ΔH_L dependence applied voltage to the device and effective fields per voltage dependence Ta and CoFeB thickness are given in the Figure 2.14 a-d and Figure 2.15a-d, respectively. The sign of effective field for longitudinal case are the same for both magnetic states pointing along +Z and –Z, whereas their sign reverses for the transverse field. It can be deduced that the transverse effective field is independent of the magnetization direction from the Figure 2.14a-b. The magnitude of the transverse effective field per applied voltage,

$\Delta H_T / V_{in}$ increases with the Ta thickness, whereas it monotonically decreases with increasing CofeB thickness. A similar plotting for longitudinal case is given in Figure 2.15a-d. The sign of longitudinal field depends on the magnetization states. Due to the magnetization dependence, the longitudinal effective field, orthogonal to the transverse effective field, takes the form of $m \times \Delta H_T$ where m is a unit vector of magnetization direction and ΔH_T is transverse effective field.

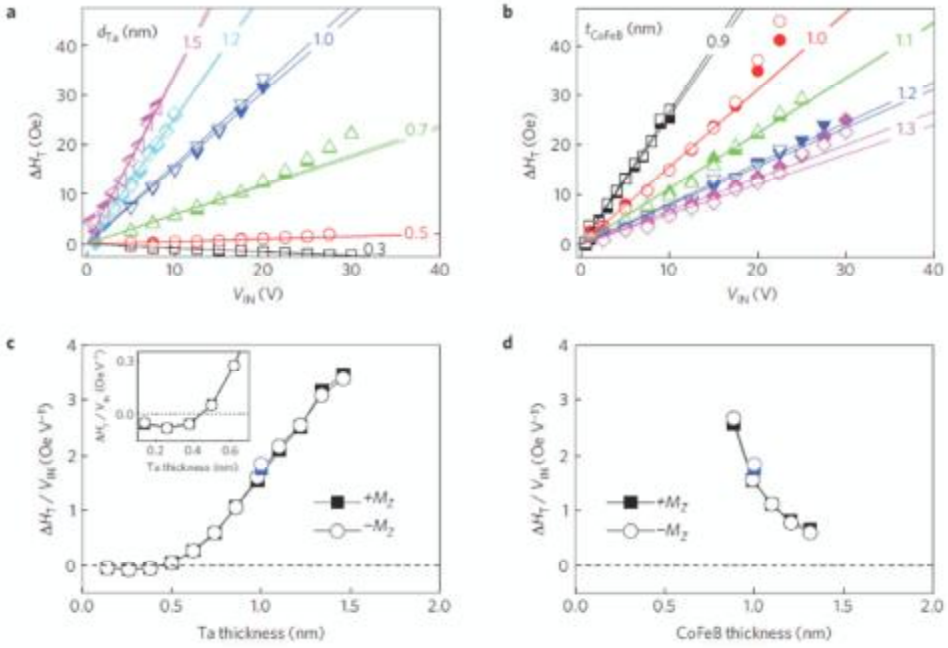


Figure 2.14. Transverse effective field as a function of applied voltage for various a) Ta and b) CoFeB thickness in Ta/CoFeB/MgO structure. The $\Delta H_T / V_{in}$ versus a) Ta and b) CoFeB thickness in Ta/CoFeB/MgO structure.

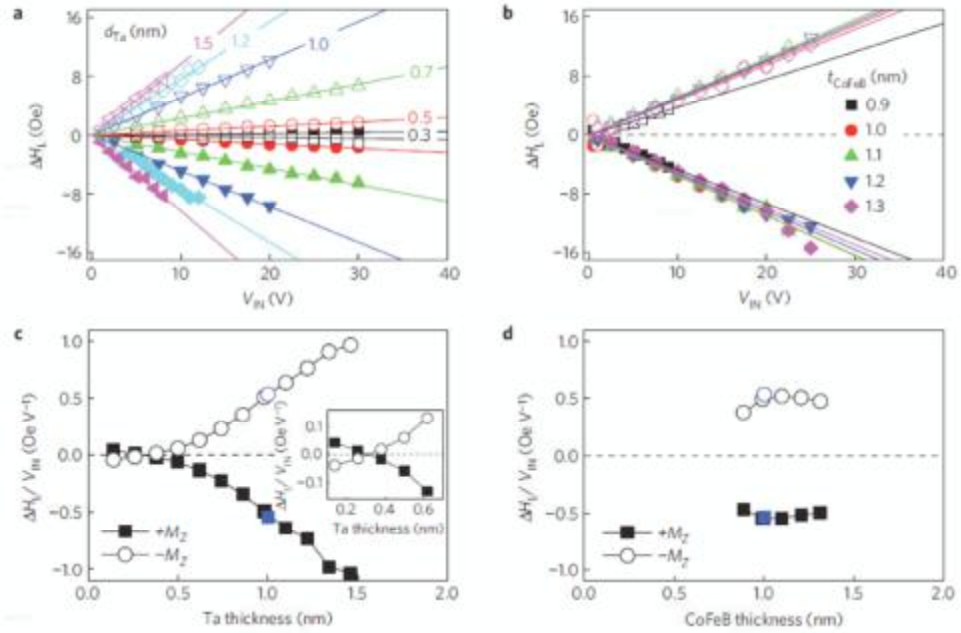


Figure 2.15. Longitudinal effective field as a function of applied voltage for various a) Ta and b) CoFeB thickness in Ta/CoFeB/MgO structure. The $\Delta H_L / V_{in}$ versus a) Ta and b) CoFeB thickness in Ta/CoFeB/MgO structure.

The relative magnitude of the transverse and longitudinal fields has been shown by plotting the ratio of these two with the relation of $R = (\Delta H_L \times sgn(-M_z))/\Delta H_T$. Figure 2.16a-b) show that R dependence Ta and CoFeB layer thickness in wedge shape films. The authors have been explained qualitatively their experimental results on spin-orbit torques which is combination of two effects coming from spin-Hall spin torque and Rashba-like Hamiltonian. The spin-Hall effective field increases with increasing Ta layer thickness since the spin current density increases with Ta thickness within the spin diffusion length of Ta. In addition to the spin-Hall effective field, the transverse effective field also scales with Ta thickness. While the transverse effective field dependence CoFeB layer thickness is different from the longitudinal case, the R dependence CoFeB thickness indicates a linear trend.

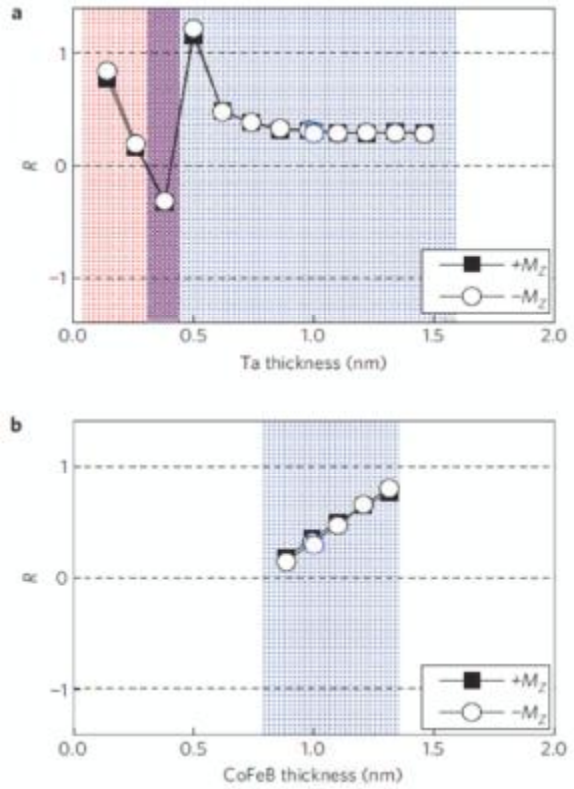


Figure 2.16. The relative magnitude of the transverse and longitudinal fields as a function of a) Ta and b) CoFeB thickness in Ta/CoFeB/MgO structure.

For thinner Ta layer thickness, a sign-reversal has been explained that the large fraction of the total current flows into the CoFeB layer and therefore the contribution of spin-Hall effect on the effective field decreases. Due to the inverse sign, it can be attributed to the presence of a second effect.

Liu et al. (2012) worked on the spin-torque switching with giant spin-Hall effect of Tantalum. They reported the discovery of a giant spin-Hall effect of Tantalum formed as high-resistive β-Ta. The giant SHE creates enough spin-torque to manipulate magnetization for both perpendicular-to-plane and in-plane magnetized samples at room temperature. The high-resistive β-Ta was grown by sputtering Ta onto the amorphous surface, such as Si. The theoretical calculations

have predicted that high-resistive β-Ta form have larger spin-Hall angle than its normal form and/or greater than that of Pt with opposite sign. Since the generating of spin-current has a crucial role in such structure, the authors quantified the magnitude of SHE in β-Ta by using three different methods. The first one is spin-torque-induced ferromagnetic resonance (ST-FMR) technique. This measurement technique is used in in-plane magnetized samples due to the ineligibility of the vector measurement. The film structures in their studies are $Co_{40}Fe_{40}B_{20}(4)/Ta(8)$ and $Co_{40}Fe_{40}B_{20}(3)/Pt(6)$ (the numbers in parentheses represent layer thickness in nanometers) bilayers sputter-deposited onto oxidized Si substrates and then patterned into 10μm wide strips. The film structure and ST-FMR measurement configuration is shown in Figure 2.17a. Here, an external magnetic field, B_{ext} is applied to the film-plane at a 45° angle with respect to the current direction, I_{RF} which is an oscillating radio frequency current.

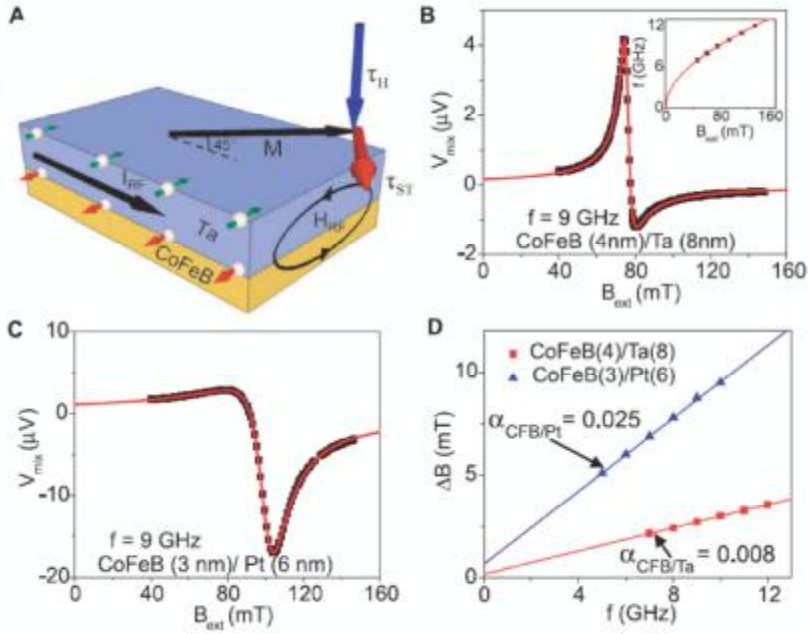


Figure 2.17 a) Multilayer film structure. FMR signal as a function of external magnetic field for b) CoFeB/Ta and c) CoFeB/Pt structure, d) effective field generated by SOT as a function of frequency.

Due to the spin-Hall effect, the oscillating electric current in Ta under layer can generate an oscillating spin current through the ferromagnetic layer. Thus, this oscillating spin currents exert an oscillating spin-torque on the magnetic moment of CoFeB layer. The mixing of radio-frequency electric current and the oscillating anisotropic magnetoresistance of the ferromagnetic layer can result in a dc voltage. The authors performed ST-FMR measurement for CoFeB/Ta and CoFeB/Pt bilayer structures (see Figure 2.17b and c). Due to the inverse spin-Hall angle of Pt and Ta, the shape of FMR of Ta and Pt is asymmetric. The Gilbert damping coefficients, α of these two samples were calculated by using the relation $\alpha = (\gamma/2\pi f)\Delta B$ where B is an external magnetic field, f is frequency of applied current and γ is gyromagnetic ratio (1.76×10^{11} Hz T^{-1}). As shown in Figure 2.17d, the $\alpha_{CoFeB/Pt}$ and $\alpha_{CoFeB/Ta}$ are found as 0.008 and 0.025, respectively. The results indicate that the damping caused by spin-pumping is much stronger in CoFeB/Ta bilayer than that of CoFeB/Pt.

The authors also worked on the switching a perpendicularly magnetized ferromagnetic layer by the spin-Hall effect. For experiment, they deposited a thin film stack with the structure of substrate/Ta(4)/$Co_{40}Fe_{40}B_{20}$(1)/MgO(1.6)/Ta(1) and then patterned it into the Hall bars 2.5 to 20μm wide and 3 to 200μm long. Since the Anomalous Hall resistance, R_H is proportional to the vertical component of magnetization of the CoFeB layer, i.e. $R_H \sim M_z = M_s.sin\theta$ where θ is the angle between the magnetic moment and film plane, M_z is the vertical component of magnetization and M_s is the saturation magnetization, the spin-torque switching measurement was done by applying a dc current through the device and measuring anomalous Hall resistance. Figure 2.18a shows anomalous Hall resistance as a function of magnetic field at an angle of β=90° means out-of-plane magnetic field. Figure 2.18b represents current-induced switching caused by the spin-Hall effect spin-torque under fixed external magnetic fields which is required to break the symmetry for full switching.

The authors finally experimentally demonstrated current-driven magnetization switching in in-plane magnetized magnetic tunnel junction. Therefore, they showed the initial of three terminal SHE device. Due to the limitation of in-plane geometry, researchers have worked on the make a similar device in perpendicularly magnetized MTJ stack.

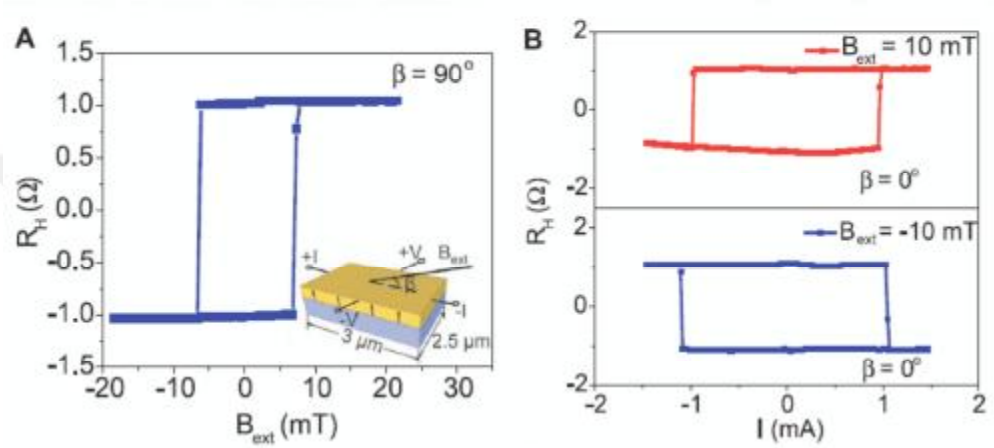


Figure 2.18. Anomalous Hall resistance as a function of a) external magnetic field and b) dc electric current.

Miron et al. (2011) worked on the perpendicular single ferromagnetic switching in Pt/Co/AlO_x by in-plane current injection. They grew the multilayer film on thermally oxidized Si wafer by magnetron sputtering system. Due to the presence of two dissimilar interfaces in the structure, an electric potential gradient has been created across the Co layer. This type of structure inversion asymmetry generates a Rashba magnetic field which is parallel to the *y*-direction when the electric current flows along the *x*-direction. After the growing multilayer film, they fabricate square magnetic dots by patterning Hall cross. Figure 2.19 shows the multilayer structure, device shape and transport measurement configuration. The magnetic field switching is also shown in the same figure.

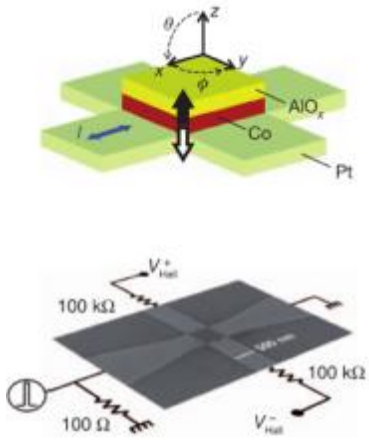


Figure 2.19. The film structure and device shape.

The authors demonstrated a systematic study of current-induced magnetization reversal as function of applied magnetic field direction. Figure 2.20a-c show the applied magnetic field direction dependence switching in Pt/Co/AlO_x structure. The switching torque is maximum when B and J are parallel to each other, and decreases away from this orientation by a $\sin(\phi - \frac{\pi}{2})$ function. The authors observed that the action of the current on the magnetization is equivalent to the $\vec{B}_{Sz} \approx \vec{B}_R \times \vec{B} \approx (\hat{z} \times \hat{j}) \times \vec{B}$. Thus, the $\vec{B}_{Sz}$ is considered the perpendicular component of an effective magnetic field proportional to $\vec{B}_R \times \vec{M}$.

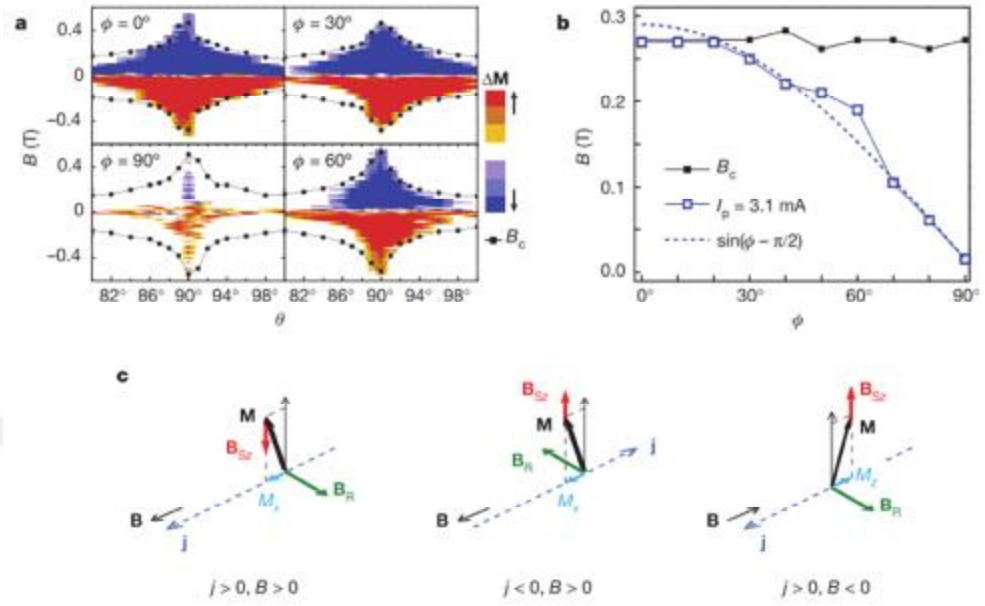


Figure 2.20 a) Diagrams representing M_z reversal regions, showing the intensity and orientation of the applied magnetic field, B, at constant current (I=3.3 mA), b)applied magnetic field as a function of angle between current and magnetic field, c) schematic illustration of current-induced effective fields on the magnetization.

Yu et al. (2014) reported that the influence of the spin-Hall effect spin torque (SHE-ST) induced by in-plane charge current on switching and domain wall motion in Ta/CoFeB/TaO_x perpendicularly magnetized trilayer structure. The authors performed the switching-phase diagram to explain the reason of the SHE-ST for using an applied magnetic field in the *xz* plane with a very small tilted away from the *x* axis. In addition, they also worked on the domain wall motion using MOKE imaging and electrical transport measurement (Yu et al., 2014).

The authors grew multilayer film by magnetron sputtering system. Figure 2.21 shows Anomalous Hall resistance as a function of longitudinal magnetic field under various dc electric current. When enough electric current (≈15 mA) flows into the Ta layer, the SHE-ST dominates the favored magnetization direction. The

interesting point was observed from the authors that multiple switching occur for the intermediate currents (-8 mA < I < -6 mA) as shown in Figure 2.21.f and g.

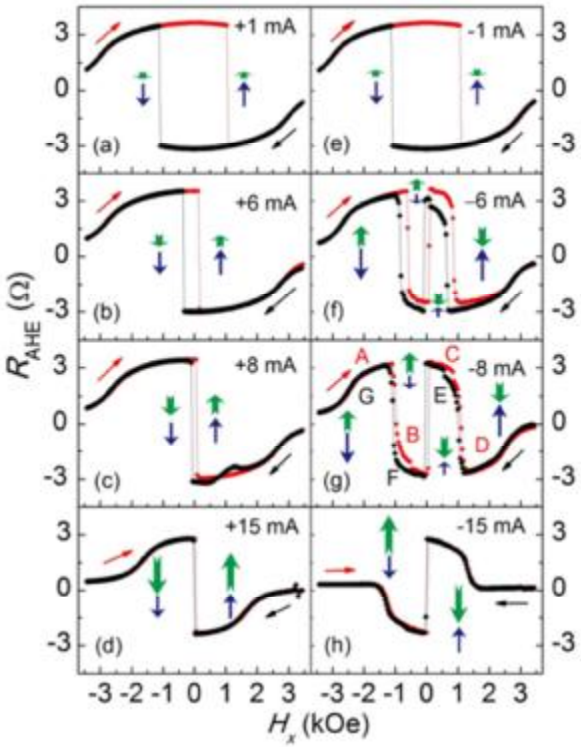


Figure 2.21. Anomalous Hall resistance as a function of longitudinal magnetic field at various electric current.

To understand of this unexpected multiple switching, the authors performed polar MOKE imaging on the Hall bar device. Figure 2.22 indicate the magnetization configuration at different external magnetic fields. The red (blue) color represents $M_z>0$ ($M_z<0$) direction. The authors explained that the switching has been occurred through domain wall propagation.

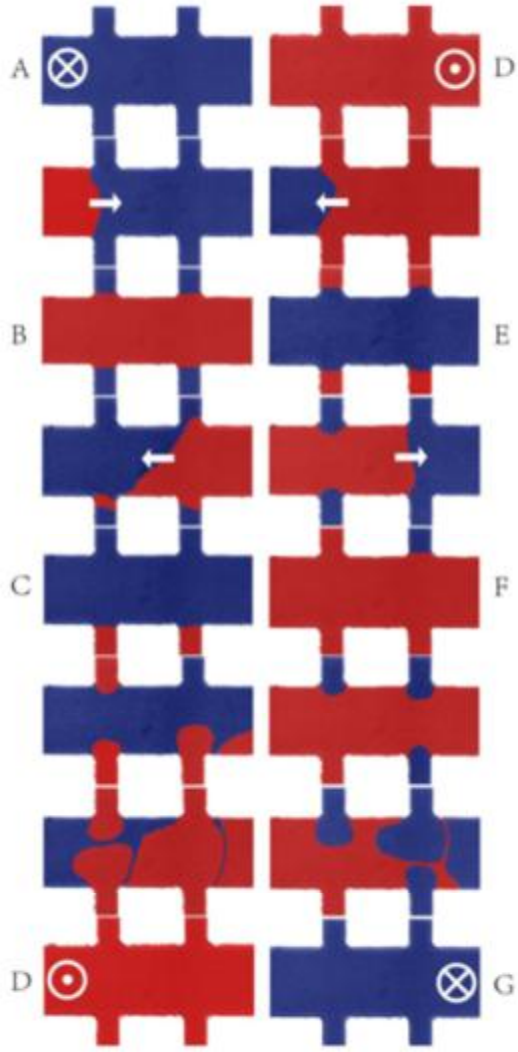


Figure 2.22. Polar MOKE images at different H_x with I_x =−8 mA.

3. MATERIAL AND METHOD

The reproducibility is a main principle in scientific studies, as well as device fabrication for applications. Although the reproduce depends on “how” and “who” are producing scientific material, it is generally expected the same scientific results by doing same process can be achieved independently. For that, in this chapter, we give an overview of all experimental techniques used in this dissertation to provide all experimental process to other researchers. We divide three main part of this chapter: (1) deposition of ultra-thin multilayer films, (2) fabrication process of devices and (3) characterization methods in terms of structural, transport and magnetic properties of multilayer films and devices. In general, we have tried to explain each experiment in terms of how it works and what the physical principle of them is. By all means, we cannot give all the details which are deep physics of each experimental process, but lacking information can be found in the literature, if needed.

The deposition of ultra-thin films, especially for multilayer structures, is an important process to obtain high quality spintronic devices. Although there are a lot of systems to grow thin films, such as Molecular Beam Epitaxy (MBE), Chemical Vapor Deposition (CVD), Atomic Layer Deposition (ALD), Pulsed Laser Deposition (PLD) and *etc*, the sputtering system among them fits well with our desired multilayer film structure. In this dissertation, we used magnetron sputtering system to grow ultra-thin multilayer structures. The details on the growing technique will be given in Section 3.1.

In this dissertation, we deposited the free-part of magnetic tunnel junctions. It means that the multilayer films are composing of substrate|seed layer|ferromagnetic free layer|tunnel barrier|cap layer. The schematic illustration of our multilayers is shown in Figure 3.1.

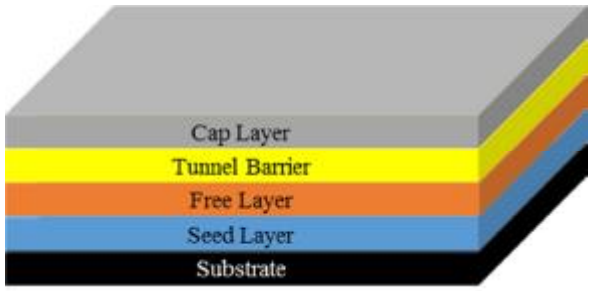


Figure 3.1. The schematic illustration of multilayer film structure.

After the growing multilayer films, devices are fabricated to make transport measurement and determine the device's spintronic properties. The fabrication process will be discussed in the second part of this chapter (Section 3.2). Finally, the multilayer films and their devices' characterization techniques from micro-structural analysis to magnetic characterization as well as transport measurements will be discussed in Section 3.3.

3.1. Thin-Film Deposition Process

A DC/RF magnetron sputtering system (AJA Sputtering System) has been used to deposit for the some trilayer and MgO-based *p*-MTJ structures. Sputtering is one of the physical vapor deposition methods of depositing thin film materials on wafers, such as SiO_2. The main process of bombarding atoms out of the target material onto the wafer is conducted by ions with large energy, typically Ar^+, which is a crucial component of the matter state called plasma. The typical sputtering process can be represented in Figure.2.1.

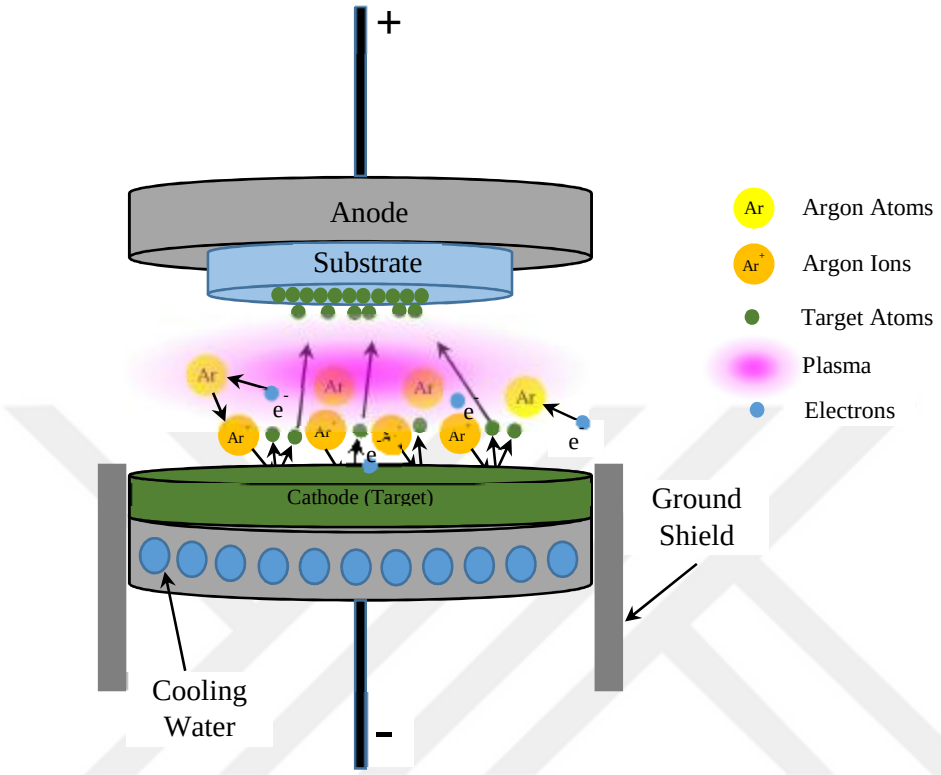


Figure 3.2. Basic representation of sputtering process.

The process can be basically explained that firstly, deposition chamber is injected with inert gas (such as Ar), and kept to vacuum (around ~10^{-3} mTorr). Then we can apply a high potential difference (DC or RF) between cathode and anode which are both in the vacuum atmosphere. In this way, part of the Argon atoms will be excited into ions and electrons, and Argon will be ionized. These Argon ions carrying large momentum are accelerated to the target. After impact between Argon ions and target, the target atoms will be released and travel to the substrate. Therefore, target atoms are being deposited on the wafer as a thin film.

In this dissertation, we used a magnetron sputtering system (AJA Company) to grow ultra-thin multilayer films that the system is in Device Research Laboratory, University of California, Los Angeles (UCLA). The system has a load-

lock and a main chamber as shown in Figure 3.2. While the load-lock chamber is vacuumed by a rotary and a turbo molecular pump, a cryopump is used in the main chamber to reach the base-pressure level at around 1×10^{-9} Torr. The metallic and insulator layers were grown by a dc and rf power source, respectively under Argon (Ar) as an inert gas. The system is capable of growing up to 4 inch size of wafer. To grow a high quality multilayer film and make a high performance device, the substrate's roughness and resistivity are quite important. Here, we used Si (500μm) substrate with thermally oxidized SiO_2 (100nm).

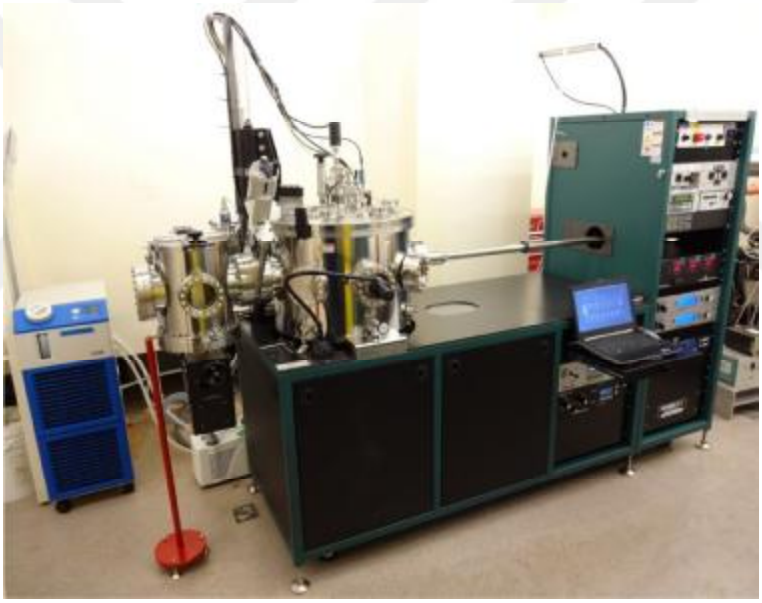


Figure 3.3. Physical Vapor Deposition System (AJA Sputtering System) at UCLA.

3.2. Device Fabrication

The micron-scale devices were fabricated by a standard optical (photo) lithography process. The thin films composed of semiconducting and/or metallic materials are generally patterned by photolithography. The ultraviolet (UV)

radiation is used to expose the geometric pattern from a photomask to a UV-sensitive chemical resist on the films. There are two process in optical lithography;

i) Positive process that the exposed area is removed during the development,

ii) Negative process that the exposed area is remained during development.

Here, we used positive photo-resist named as AZ-5214. The process of photolithography is explained as following;

- *Cleaning:* If the film does not have clean surface, it can be cleaned by using acetone and then dried by blowing N_2 gas. In addition, the HMDS (HP-Primer) can be used to enhance the bonding of photo-resist to the film surface.
- *Mask cleaning:* Before using the mask, it must be cleaned in chemical bath with ALEG 335 for 10 minutes. And then the mask was washed inside the DI water. After the cleaning of mask, it is dried via N_2 blowing.
- *Photo-Resist Coating:* The photo-resist was coated by a conventional spin-coating equipment shown in Figure 3.4. Before the coating process, all parts of the spin-coating system must be cleaned by acetone. The coating process was done by following steps;
  - *0 to 500 rpm for 5sec*
  - *500 to 4000 rpm for 30sec.*
  - *4000 to 0 rpm in a 0 seconds. The thickness of photo-resist is around 1.2-1.4 μm.*

After coating resist on top of the film, it was prebaked by hot-plate at 100ºC for 1 min.

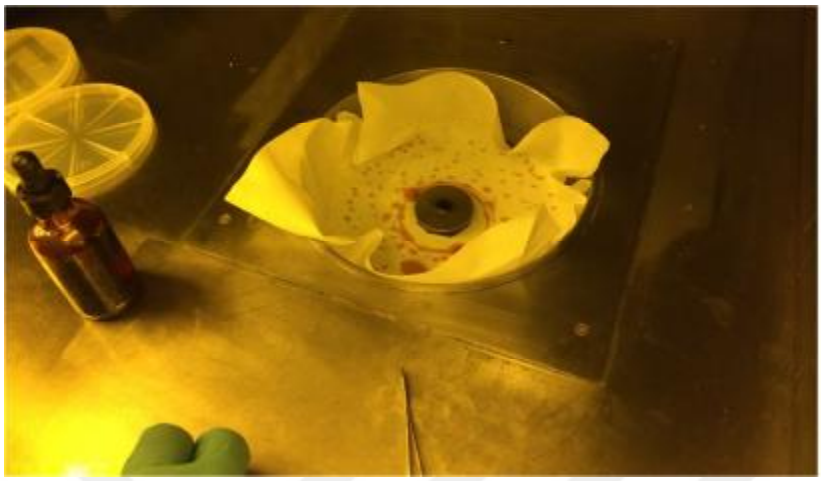


Figure 3.4. Photo-Resist coating by Spin-Coating equipment at UCLA NanoLab.

- *Exposure:* The films coated photo-resist were exposed to desired pattern by KARL SÜSS mask aligner as shown in Figure 3.5 for exposure time of 10±1 s. The exposure of UV radiation causes a chemical change in photo-resist which results of removing exposed part of the photo-resist by chemical solutions known as developer.



Figure 3.5. KARL SÜSS mask aligner to expose the films coated by photoresist at UCLA NanoLab.

- *Development:* The exposed photo-resist can be removed by special solutions that is composed of 100 mL deionized (DI) water and 20 mL AZ-400K developer. The exposed film was kept inside this special solution for 1 min and then inside the DI water for 20 s. After the development process, the film must be dried by N_2 gas and checked the development process by using microscope.

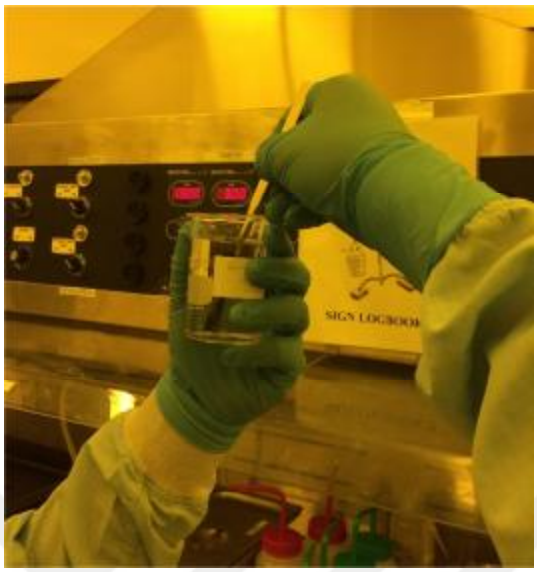


Figure 3.6. Development Process.

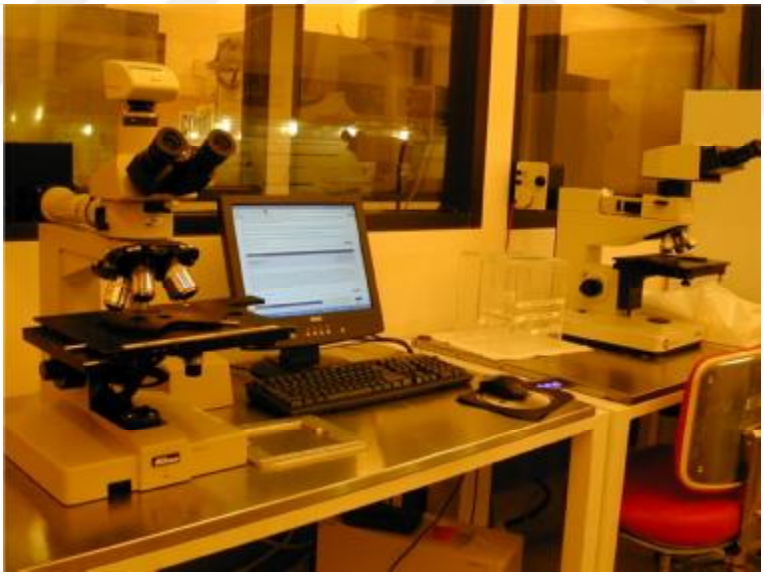


Figure 3.7. Microscope to check whether the development process is performed successfully, or not (UCLA NanoLab).

- *Etching:* The developed films were etched by plasma reactive ion etching with Chlorine gas.



Figure 3.8. Dry-etching equipment at UCLA NanoLab.

- *Lift off:* To lift off photo-resist on top of the film, the films kept inside the Acetone until the photo-resist is gone. If photo-resist cannot completely remove by acetone, O_2 plasma can be used for around 2 mins. After the photo-resist cleaning process, the films keep in the HDMS container for next photo-resist coating process.
- *Photo-Resist Coating:* The same photo-resist coating process is used as explained above.
- *Alignment and expose:* The same alignment and exposure process (~4 s) were used as explained above. But the pattern has contacts. After exposure process, the films were baked to make negative resist at 110°C for 45 seconds.

- *Flat Expose:* The films were exposed without mask.
- *Development:* The same process (~50 s) is used as explained above.
- *Metal Deposition:* The Au/Cr deposited on the films to create contact for transport measurement.



Figure 3.9. Metal deposition equipment at UCLA NanoLab.

- *Lift off:* The same lift off process is used as explained above.

Therefore, the Hall-bar shape devices have been fabricated by photolithography process. The size of Hall-bar shape devices is 20 µm×130 µm which is kept the same size for all devices to perform transport experiments in this dissertation. The whole device fabrication process is shown in Figure 3.10. And the microscope images of the device is given in Figure 3.11.

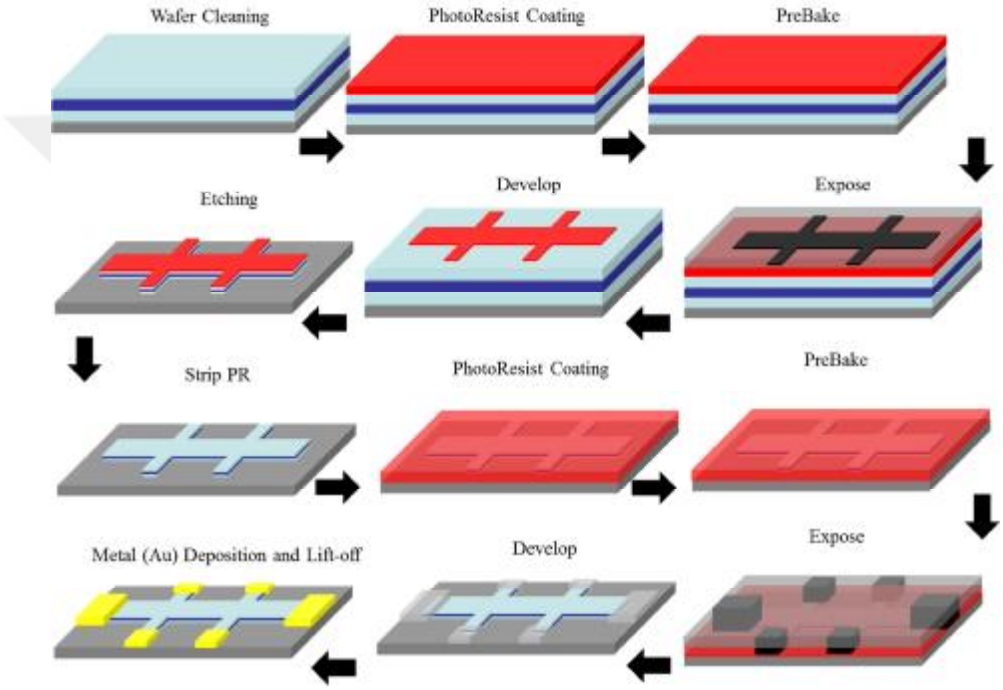


Figure 3.10. Device Fabrication Process.

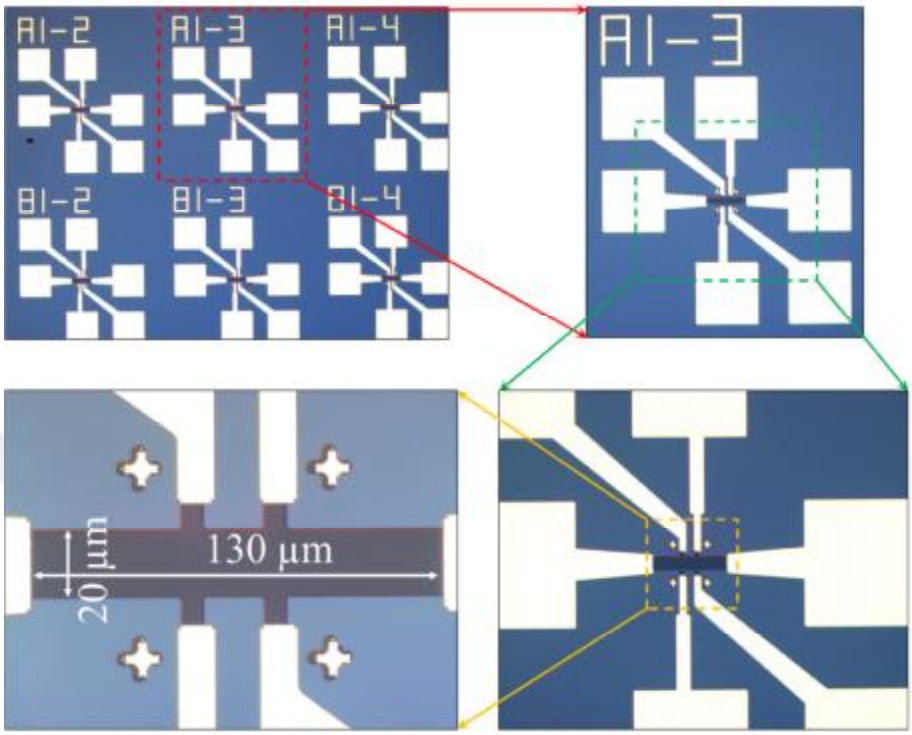


Figure 3.11. The microscope images of the fabricated Hall-bar device.

3.3. Sample Characterization Technique

3.3.1. Atomic Force Microscopy (AFM)

Uniform and smooth forms of the films are desired to obtain high quality crystallinity in thin films and high performance devices. Atomic Force Microscopy (AFM) is a useful technique to find out the surface morphology features of the films. In AFM topographic technique, a tip located in the edge of a cantilever oscillated with its resonant frequency in free air scans the surface. Due to the forces between film and tip, the cantilever can be bent or deflected. The data is collected by the detection of cantilever's bending/deflection amount. Thus, the bending of cantilever is transformed to the topology map of the films by a computer software. There are three modes in AFM topographic technique which are contact, non-contact and tapping modes. In the tapping mode, the cantilever is driven to oscillate

up and down at its resonance frequency. Thus, the surface morphology does not affected during the tapping mode.

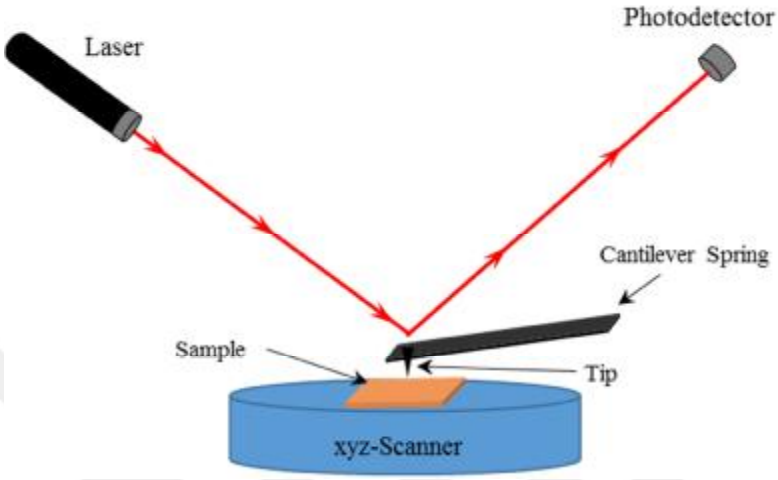


Figure 3.12. The working scheme of the atomic force microscope.

In this dissertation, we used a XE-100 Park Systems brand Atomic Force Microscope shown in Figure 3.13. The AFM system can be supported to scan area up to 50µm×50µm with 0.02 µm sensitivity in *xy* plane. While it is capable of working in non-contact and contact mode, we used tapping mode due to the advantage of tapping mode as explained above.



Figure 3.13. Park-System Atomic Force Microscope.

3.3.2. Magneto-Optical Kerr Effect (MOKE)

Magneto-Optical Kerr Effect (MOKE) has been used for the fast testing of magnetic characterization of grown films. MOKE can be described that the light that is reflected from a magnetized surface can change in terms of its polarization and reflection intensity. This effect is similar to Faraday effect that can be basicly described the changing of the light transmitted through a magnetic material. Otherwise, the Kerr effect can be described that the changing of the light reflected from a magnetic surface. This reflection can also produce some effects that are rotation of the direction of polarization of the light, ellipticity and changing the intensity of the reflected beam. MOKE can be used particularly to characterization of magnetization of ferromagnetic and ferrimagnetic films.

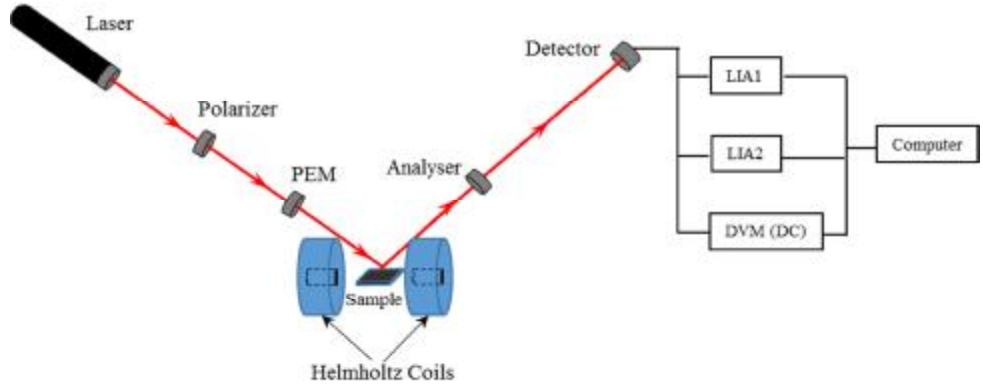


Figure 3.14. The schematic form of the Magneto-Optical Kerr Effect set-up (LIA1: Lock-in Amplifier-1, LIA2: Lock-in Amplifier-2, DVM: DC Voltmeter).

In this dissertation, we used a home-made MOKE system as shown in Figure 3.15. Longitudinal and transverse MOKE geometry can be supported by this system. Magnetic field sweep range +/- 1 Tesla by Helmholtz coils. While the system is capable of low temperature measurement via liquid He, we just use the system at room temperature since the samples show room temperature magnetic behavior.



Figure 3.15. Magneto-Optical Kerr Effect (MOKE) measurement set-up at UCLA Device Research Laboratory.

3.3.3. Transmission Electron Microscopy (TEM)

Human eyes can resolve two points which are so close each other in a distance order of millimeter. Although this distance is depending on how large the resolution power of eyes, it cannot be lower than 0.1 mm. Since the limit of our eyes is not comparable with the atomic size, we have to use some instruments to see in the atomic range. This kind of instrument is called as microscope. In a typical light microscope, the resolution can be found as following relation;

$$\delta = \frac{0.61\lambda}{\beta sin\theta} \tag{3.1}$$

where λ is wavelength of the light, β is refractive index of the view medium and θ is the semi-angle of collection of magnifying lens. Due to the above relation, the magnitude of the resolution of light microscope is mainly depending on the wavelength of the light. Even if we use a green light as a source of radiation, the resolution of microscope would be around a couple of hundred nanometers which is still not enough to distinguish two nearby atoms in the solid form. Thus, we cannot see the whole picture of a solid material in an atomic picture by light microscope since the distance of two atoms in the solid is around 0.2 nm.

The TEM imaging technique has the same basic principle as a light microscope, but it uses electrons instead of light. In TEM, the limitation of light microscope by the wavelength of light goes away due to the lower wavelength of electrons. Therefore, it is possible to get a resolution in TEM 1000 times better than a light microscope. The order of a few angstrom (10^{-10} m) can be observed via TEM. Since the images can be taken in the order of near atomic levels, the TEM imaging technique is used widely in medical, biological, chemistry, material and physical sciences.

In the TEM technique, the beam of electrons bombarded from the electron gun is focused into a thin beam by a magnetic lens. After that the beam strikes the sample and transmitted to the other side of the sample. The concentration of transmitted electron beam depends on the thickness and electron transparency of

the sample. The transmitted electron beam is focused by the projection lens on phosphor screen or charge coupled device (CCD) camera. There might be optional objective apertures and lens to enhance the contrast of electrons. In a TEM image, the dark (light) areas indicate the areas of sample that fewer (more) electrons are transmitted through the sample. Figure 3.16 shows the principle of transmission electron microscope imaging technique.

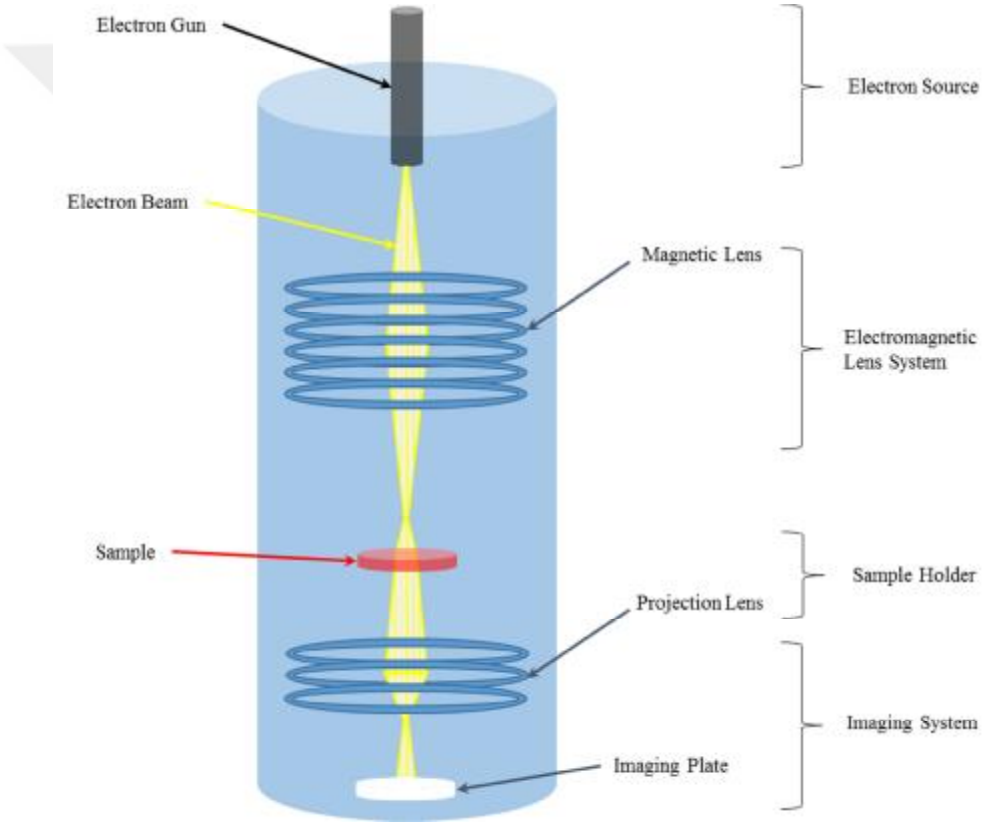


Figure 3.16. The principle of Transmission Electron Microscope imaging technique.

3.3.4. X-Ray Photoelectron Spectroscopy (XPS)

X-ray Photoelectron Spectroscopy (XPS) measures sensitively the chemical and electronic states of the surface of elements. In this spectroscopic technique, materials like conductors or insulator can be easily analyzed in surface areas from a few microns to a few millimeters across. When materials are exposed to a beam of x-ray in an ultra-high vacuum, the incident x-rays cause the ejection of core-level electrons from the materials' atoms. The kinetic energy of a photoemitted core electron is measured as a function of its binding energy, E_B which is characteristic of elements, $E_B = h\upsilon - E_{kin} - W_f$ where h is Planck constant, υ is the frequency of x-ray, E_{kin} is the kinetic energy and W_f is the work function. The energy analysis of the emitted photoelectrons is the primary data for the XPS measurements. When the core electron is ejected by the incident x-ray, an outer electron fills the core hole. The energy of this transition is balanced by the emission of an Auger electron (see Figure 3.17). The penetration depth of escaped electrons is in a range of 0 to 10 nm. But, it depends on the material property. The photoemitted and Auger electrons are detected by an electron energy analyzer (see Figure 3.18). Therefore, a spectrum made of the surface composition can be obtained from the number of photoemitted and Auger electrons as a function of their energy. In the XPS spectrum, the peaks indicate the corresponding energy of an element's characteristic. The area under a peak in the spectrum is a measure of the relative amount of the element represented by that peak. The peak shape and precise position indicates the chemical state for the element.

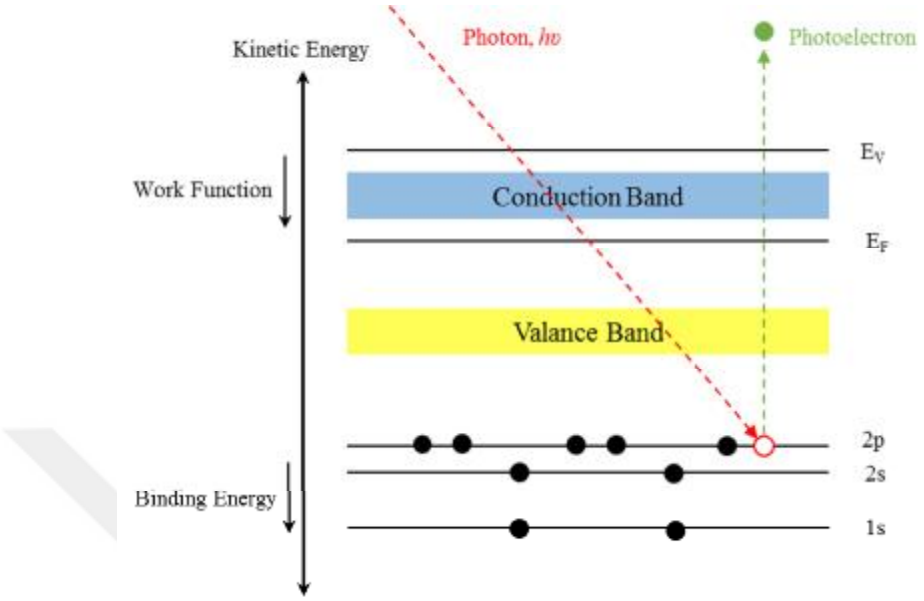


Figure 3.17. Energy band diagram of a material.

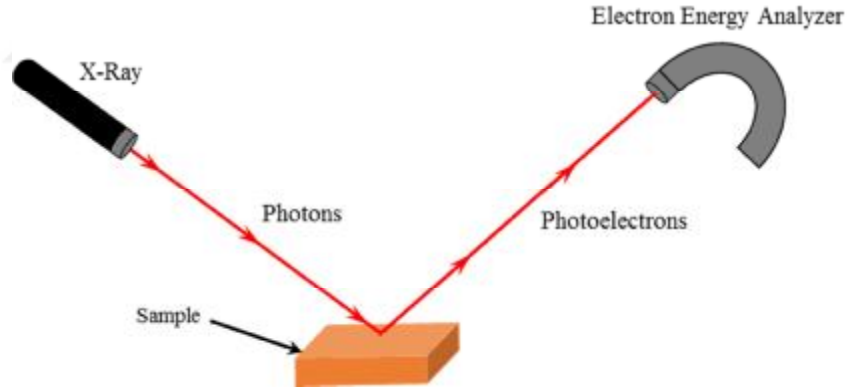


Figure 3.18. A schematic illustration of x-ray photoelectron spectroscopy.

In this dissertation, we used ESWCALAB 250Xi brand XPS system shown in Figure 3.19. The chamber vacuum before XPS analysis was better than 3×10^{-9} Torr. All binding energies were adjusted with reference to the C 1*s* line at 284.6 eV to eliminate the surface charging effect.



Figure 3.19. ESWCALAB 250Xi X-ray Photoelectron Spectroscopy (XPS).

3.3.5. Transport Measurements

In transport measurements, we used couple of measurement systems where the systems are modified by depending on our needed. All experiments have been done at room temperature. During the transport measurements, we only used Hall-bar shape devices. In our laboratory, we have two probe-station for transport measurements. Although one of them is capable of applying in both direction (in-plane and out-of-plane) of magnetic field, the other one has only in-plane direction magnetic field source. In the first probe station, anomalous Hall measurements have been done by applying out-of-plane to the devices. In the second probe station, the hard-axis transport and vector measurements have been done due to the having larger magnetic field than the first probe station. We will give more detail about the transport measurements in Section 3.3.5.1 and 3.3.5.2.

3.3.5.1. Probe Station

In anomalous Hall measurements, a probe station which has an electromagnet in both direction (in-plane and out-of-plane) were used. The maximum magnetic field of electromagnet in out-of-plane and in-plane directions are 2.1 kOe and 3.5 kOe, respectively. The probe station only support room temperature measurement. Keithley 2612A (having two channels) brand source and volt-meter was used in all transport experiments in this probe station. In the case of applying out-of-plane magnetic field, we set the following measurement set-up (see Figure 3.20).

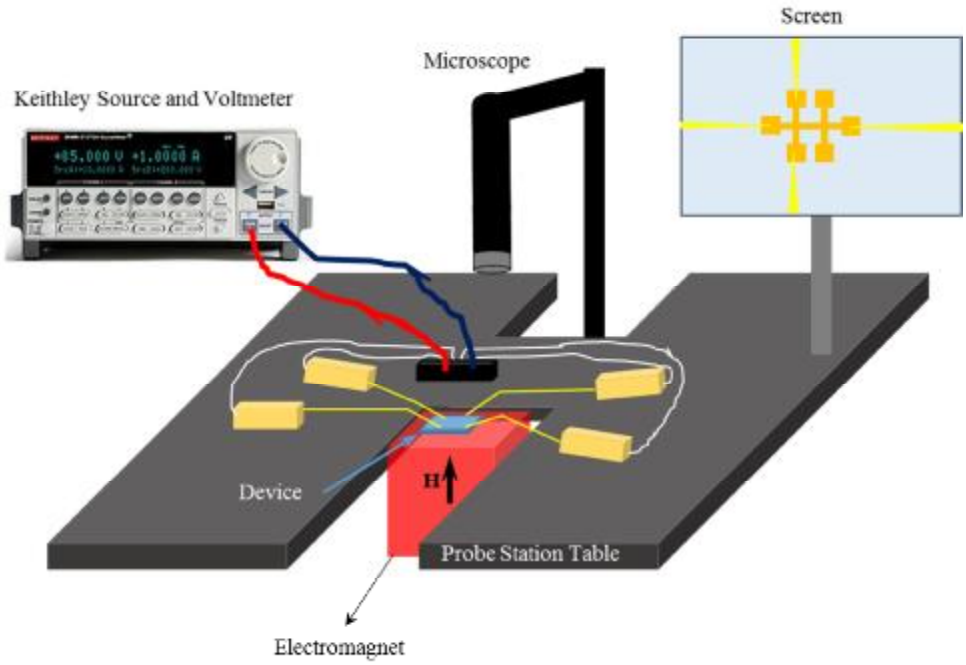


Figure 3.20. The set-up of probe station for out-of-plane transport measurements.

The transport measurements were controlled by computer software which is created by Labview language. A screenshot can be seen in Figure 3.21. The main concept of AHE measurements is that the voltage drop is measured under a dc bias

current by sweeping external out-of-plane magnetic field. This measurements have been done at different bias currents.

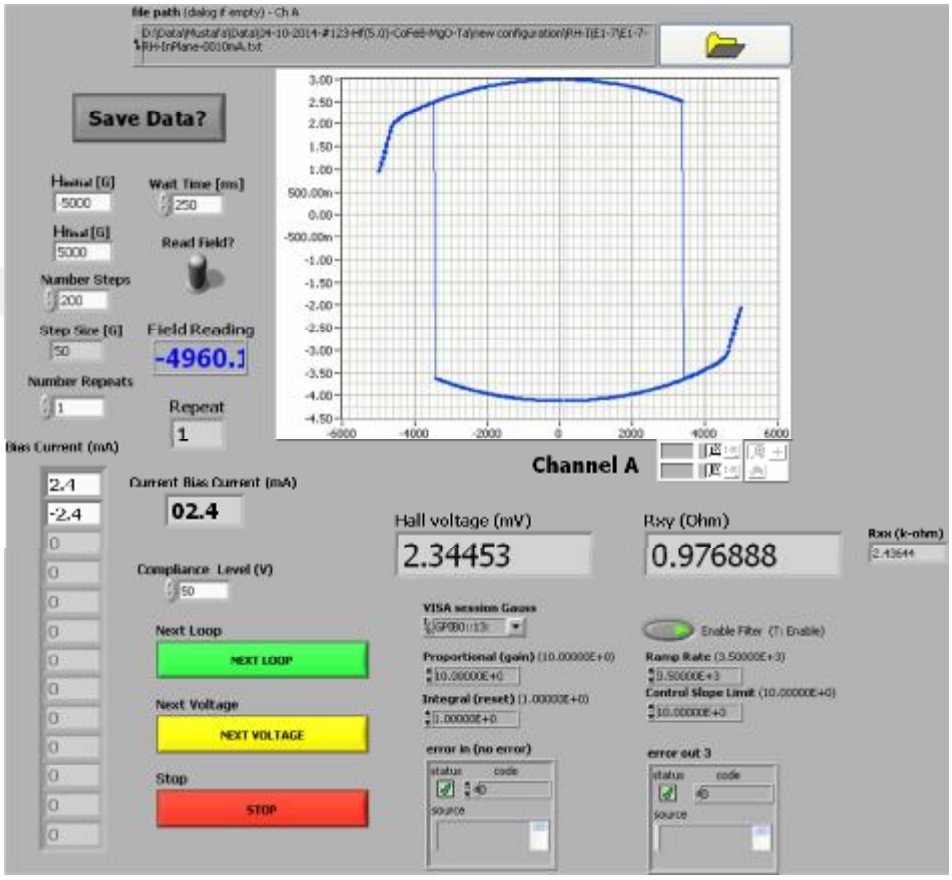


Figure 3.21. The screen capture of in-time measurement.

3.3.5.2. Vector Measurement System

The vector measurement technique can be used to quantify the current-induced effective fields corresponding to the damping-like (DL) and field-like (FL) SOTs. Let's consider that our system is in following form;

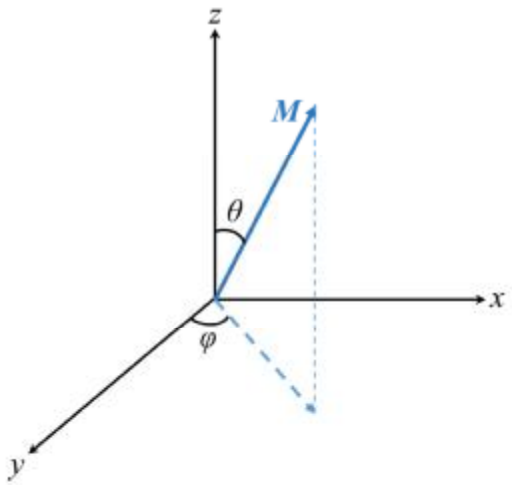


Figure 3.22. The coordinate system of a magnetization vector in a ferromagnetic layer.

The magnetization is selected as perpendicular magnetic easy-axis with an angle of θ to the *z*-axis. The φ is the azimuthal angle of magnetization with respect to the *y*-axis. The magnetization can be written in Cartesian coordinate system as following;

$$\vec{M} = |\vec{M}|sin\theta sin\varphi\hat{\imath} + |\vec{M}|sin\theta cos\varphi.\hat{\jmath} + |\vec{M}|cos\theta\hat{k} \tag{3.2}$$

The magnetic energy of the system can be expressed as;

$$E = K_{eff} - \vec{M}.\vec{H}(L,T,z) \tag{3.3}$$

$$\begin{aligned} E = {} & (-K_u + 2\pi M_s^2)cos^2\theta \\ & - \left[|\vec{M}|sin\theta sin\varphi|\overrightarrow{H_L}| + |\vec{M}|sin\theta cos\varphi|\overrightarrow{H_T}|\right. \\ & \left. + |\vec{M}|cos\theta|\overrightarrow{H_z}|\right] \end{aligned} \tag{3.4}$$

where K_u is magnetic anisotropy constant (positive (negative) indicates out-of-plane (in-plane) easy-axis), M_s is saturation magnetization, H_L, H_T, H_z are external magnetic fields corresponding the applied direction in longitudinal (along the *x*-

axis which is the same with current flow), in transverse (along the *y*-axis which is the transverse with current flow) and out-of-plane field, respectively.

During the vector experiments, a small amplitude of ac signal is applied to the device due to performing sensitive measurement of effective current-induced field. The derivation of current-induced longitudinal and transverse effective fields is shown as following;

$$V_H = R_H I \tag{3.5}$$

$$R_H(H) = \Delta R_H cos\theta \tag{3.6}$$

If an in-plane field (H_L or H_T) with an ac electric current are applied to the device, and measured the first and second harmonic signal;

$$I = \Delta I sinwt \tag{3.7}$$

$$\theta = \theta\left(H_{L,T} + \Delta H_{L,T} sinwt\right) \sim \theta\left(H_{L,T}\right) + \frac{\partial\theta}{\partial H_{L,T}} \Delta H_{L,T} sinwt \tag{3.8}$$

$$R_H(H) = \Delta R_H cos\theta \sim \Delta R_H \left[cos\theta_0 - sin\theta_0 \frac{\partial\theta}{\partial H_{L,T}} \Delta H_{L,T} sinwt\right] \tag{3.9}$$

$$V_H \approx \Delta R_H \Delta I \left[cos\theta_0 sinwt - \frac{\partial cos\theta_0}{\partial H_{L,T}} \frac{1}{2} \Delta H_{L,T} cos2wt\right] \tag{3.10}$$

$$\theta_0 \sim \frac{H_{L,T}}{2\,{K_u}/{M_s} - 4\pi M_s + H_z} = \frac{H_{L,T}}{D} \tag{3.11}$$

$$V_H \approx \Delta R_H \Delta I \left[\left(1 - \frac{1}{2}\frac{H_{L,T}^2}{D^2}\right) sinwt + \left(\frac{H_{L,T}}{D^2}\right) \frac{1}{2} \Delta H_{L,T} cos2wt\right] \tag{3.12}$$

$$\theta \ll 1 \qquad D = D(K, M_s) \tag{3.13}$$

The first term is related to the first harmonic signal and the second one is the second harmonic signal.

$$\frac{\partial^2 V_H^{1w}}{\partial H_{L,T}^2} \sim -\frac{\Delta R_H \Delta I}{D^2} \tag{3.14}$$

$$\frac{\partial^2 V_H^{2w}}{\partial H_{L,T}} \sim -\frac{\Delta R_H \Delta I}{D^2}\frac{\Delta H_{L,T}}{2} \tag{3.15}$$

$$\Delta H_{L,T} = -2\left[\frac{\partial^2 V_H^{2w}}{\partial H_{L,T}}\right] \Big/ \left[\frac{\partial^2 V_H^{1w}}{\partial H_{L,T}^2}\right] \tag{3.16}$$

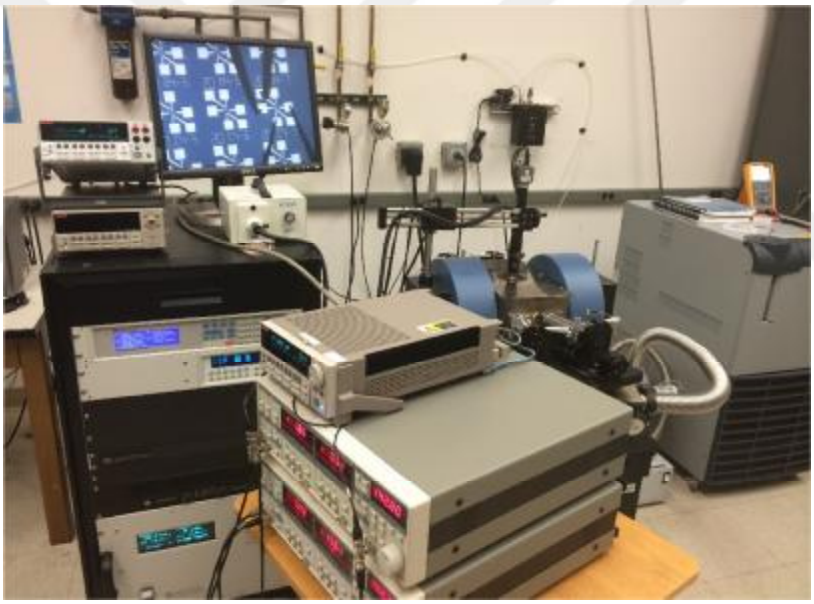


Figure 3.23. The set-up of vector measurement in Lake-Shore Probe Station at UCLA Device Research Laboratory.

Since the main theme of this work is related to the effective fields, in other words effective torques, it would be much easier to give the direct calculated effective field from experimental results if we can give a calculation example on it. Figure 3.26 shows a screen capture of the computer during the vector

measurement. The software written by LabView measures the first and second harmonic signals at the same time.

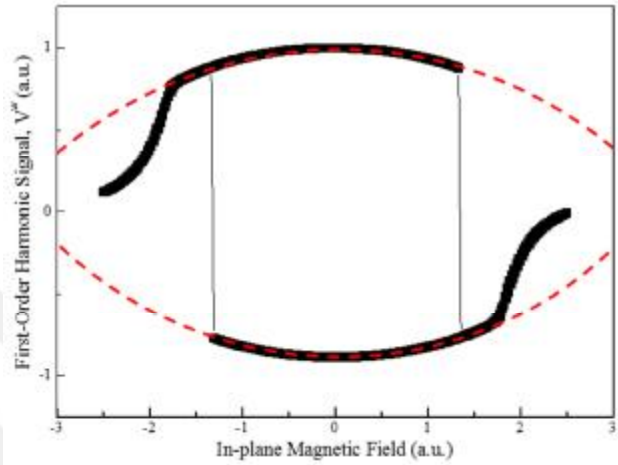


Figure 3.24. The first-order harmonic signal versus in-plane magnetic field as an example on the calculation of effective field.

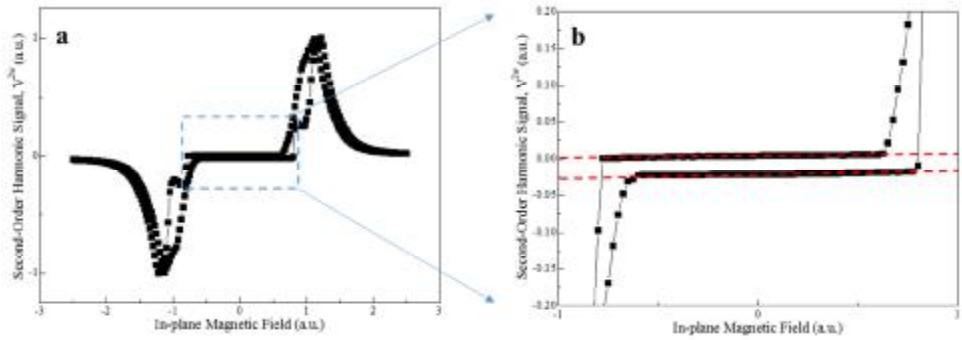


Figure 3.25. The second-order harmonic signal versus in-plane magnetic field as an example on the calculation of effective field.

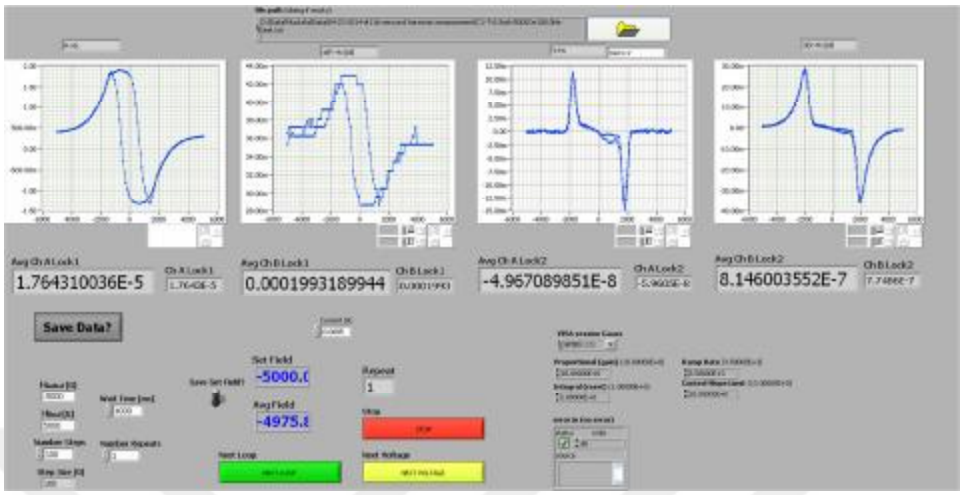


Figure 3.26. The screen capture of in-time measurement.

3.3.6. Vibrating Sample Magnetometer (VSM)

All materials in nature have a magnetization response when an external magnetic field, H_{ext} is applied to them. This external magnetic field can indirectly induce an internal magnetization, M inside the materials. There is a relation between the external magnetic field and susceptibility of the materials which is called magnetic susceptibility can be written by dM/dH. The magnetization of materials can be sensitively found by Vibrating Sample Magnetometer (VSM) and Superconducting Quantum Interference Device (SQUID). Although the Magneto-Optical Kerr Effect (MOKE) can give information of the magnetization, it suffers the magnitude of the magnetization. Physical Properties Measurement System (PPMS) produced by Quantum Design Company is capable of multi physical measurements in one system. One of them is the VSM module with the sensitivity around 1.6×10^{-6} emu. The system is capable of working temperature and magnetic field in range of 1.6 to 400 K and ±9 T, respectively. Due to the having friendly software of the PPMS system, it is easy to control and modify the measurement configuration from the computer of the system. Figure 3.27 shows the schematic illustration of the VSM system.

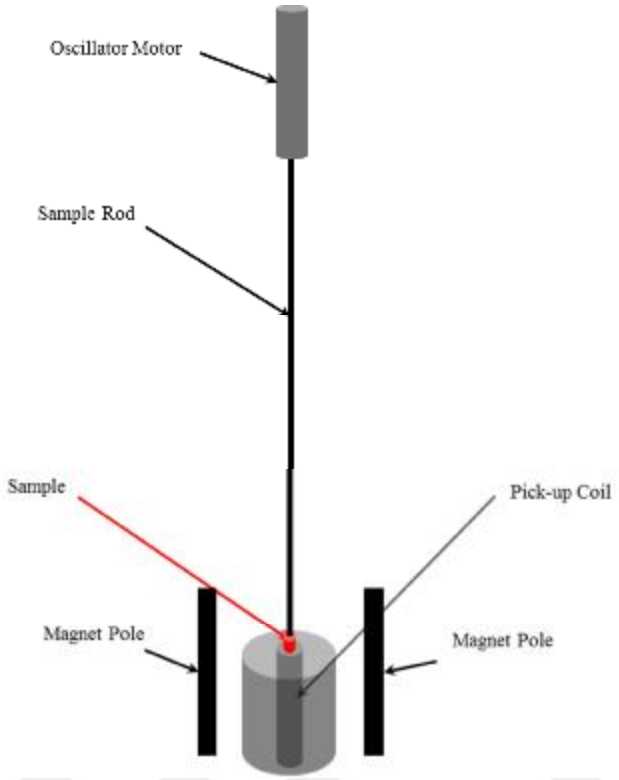


Figure 3.27. The schematic illustration of vibrating sample magnetometer.

In this dissertation, we used Physical Property Measurement System (PPMS) - Quantum Design with a module of VSM head (see Figure 3.28). Specifically, we measured the hysteresis loop to determine anisotropy field, H_k of multilayer films at room temperature. The system's sensitivity is around 1.6×10^{-6} emu.



Figure 3.28. Quantum Design DynaCool Physical Properties Measurement System (PPMS) with Vibrating Sample Magnetometer (VSM) module.

4. RESULTS AND DISCUSSIONS

In Magnetic Random Access Memory (MRAM), there are crucial parameters to get a well-designed and powerful devices in terms of reading, writing and scalability as explained in Chapter 1. Some of them can be listed as film growing parameters, device size and shape, thickness of insulating layer as a tunnel barrier and ferromagnetic free and fixed layers, *etc*. In addition, the electrodes in magnetic tunnel junctions have also important roles to reach high tunneling magnetoresistance ratio for sensitive reading, low writing energy and perpendicular magnetic anisotropy for high density devices. Since the main challenge is the writing process in spin-based devices, the effects of seed layer thickness, oxide-layer, ferromagnetic free layer thickness and symmetry breaking on structure, magnetic and spintronics properties have been worked in this thesis. Therefore, this chapter is divided into three sections as follows:

- The thickness of heavy metal layer as a seed layer in the MTJs has been studied in terms of structural, magnetic, transport and spintronics properties in Section 4.1.
- The effect of oxide layer as a tunnel barrier in MTJs has been studied in terms of magnetic, transport and spintronics properties in Section 4.2.
- The symmetry property has been studied by engineering the multilayer structure and device formation, as well as breaking the growth direction, in the Section 4.3. In addition, the effect of ferromagnetic free layer thickness in MTJs has been studied in terms of transport and spintronic properties in the same section.

4.1. Heavy Metal Layer Thickness Dependence on Structural, Magnetic, Transport and Spintronics Properties in Hf(*t*)|CoFeB|MgO|Ta Multilayer Structures

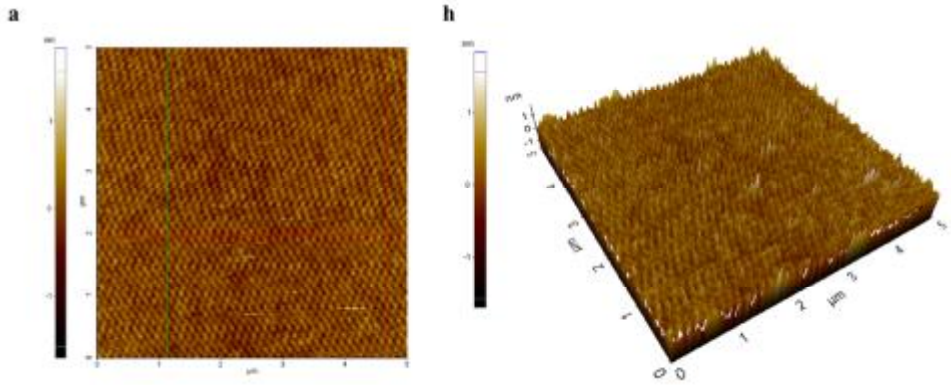
In this section, we have worked on the heavy metal layer thickness dependence on structural, magnetic, transport and spintronics properties in Hf(*t*)|CoFeB(1.1)|MgO(2.0)|Ta(2.0) multilayer structures (*t*=0.5, 0.75, 1.0, 1.5, 2.5, 3.5, 5.0, 7.0, 8.5 and 10.0 nm). The structural properties of the films have been studied by performing Atomic Force Microscope (AFM) imaging, Transmission Electron Microscope (TEM) imaging and X-ray Photoelectron Spectroscopy (XPS) techniques. The magnetic property of the multilayer films have been studied by Magneto-Optical Kerr Effect (MOKE) and Vibrating Sample Magnetometer (VSM) techniques. The transport properties of the devices have been studied by performing probe station measurements under out-of-plane and in-plane magnetic fields. The vector measurements have been performed for torque-calculations in probe station set-up. The detail of each measurement set-up was given in Chapter 3. The deposition of multilayer films worked in this section was explained in Section 3.1.

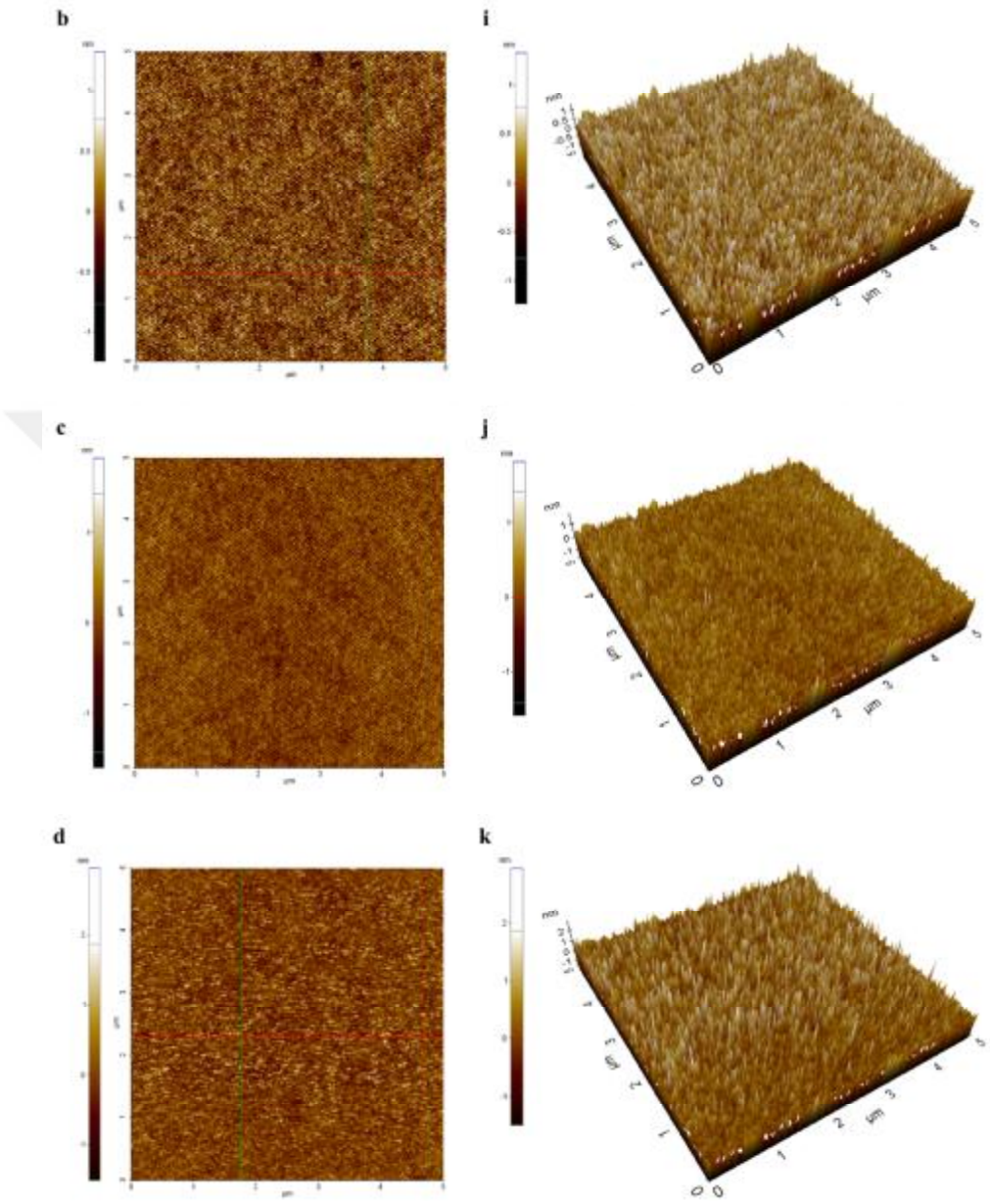
4.1.1. Atomic Force Microscope Analysis of Hf(*t*)|CoFeB|MgO|Ta Multilayer Structures

Atomic force microscope imaging technique has been performed to investigate the surface roughness of the Hf(*t*)|CoFeB|MgO|Ta multilayer films. The AFM images were taken by scanning 5μm×5μm area on the multilayer films. In order to explore the homogeneity of the film growing process, we took the AFM images at two areas on the multilayer films. The seed layer thickness dependence roughness was studied before the device fabrication.

Figure 4.1a-g (h-n) show the 2D (3D) AFM images of the Hf(*t*)|CoFeB|MgO|Ta multilayer films for t_{Hf} = 1.0, 1.5, 2.5, 3.5, 5.0, 7.0 and 10

nm, respectively. As seen from the Figure 4.1, the surface morphologies of the films are quiet smooth, and they show the uniform deposition of the films up to 5.0 nm. However, the morphology and the quality of the films is getting worse above t_{Hf} = 5.0 nm. In order to see the Hf layer thickness dependence of roughness in Hf(t)|CoFeB(1.1)|MgO(2.0)|Ta(2.0) multilayer film structure, Figure 4.2 is plotted which indictes roughness, R_q versus Hf layer thickness. The roughness almost linearly increases with the Hf layer thickness in the multilayer structure, and it was found in a range of 0.12 nm to 0.45 nm. In addition to the roughness, we observed some island formation above t_{Hf} = 5.0 nm. Since the thickness of ferromagnetic layer is around 1.1 nm, the roughness of the films above 5.0 nm is almost half of the CoFeB layer thickness. Therefore, it is expected that the crystal quality of the CoFe layer is reduced as the thickness of Hf is increased, and the effective perpendicular magnetic anisotropy might be reduced as well. The magnetic property dependence on the roughness will be discussed in Section 4.1.4.




b
i
c
j
d
k

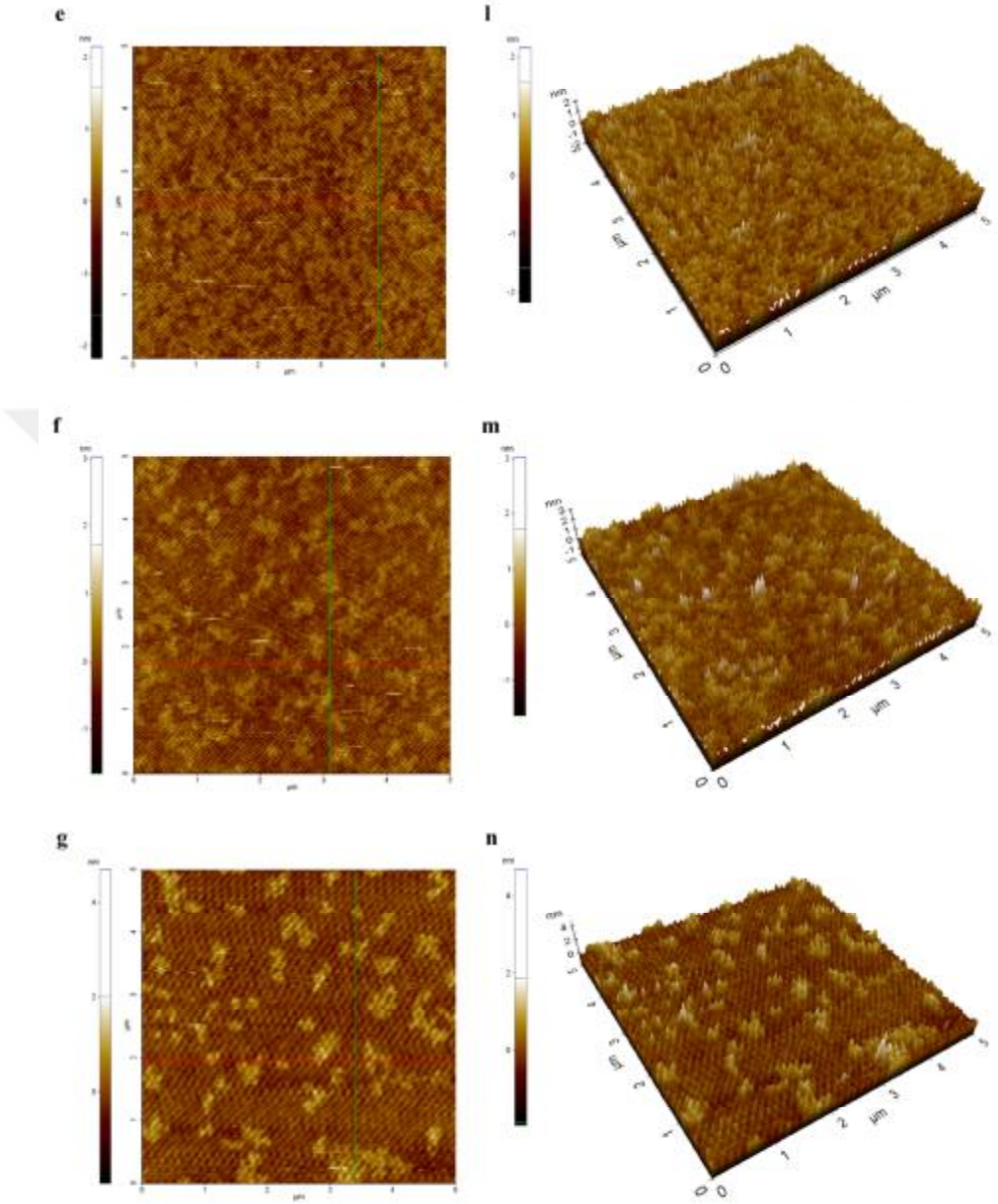


Figure 4.1a-g (h-n) The 2D (3D) atomic force microscope images of the Hf(*t*)|CoFeB|MgO|Ta multilayer films for t_{Hf} = 1.0, 1.5, 2.5, 3.5, 5.0, 7.0 and 10 nm, respectively.

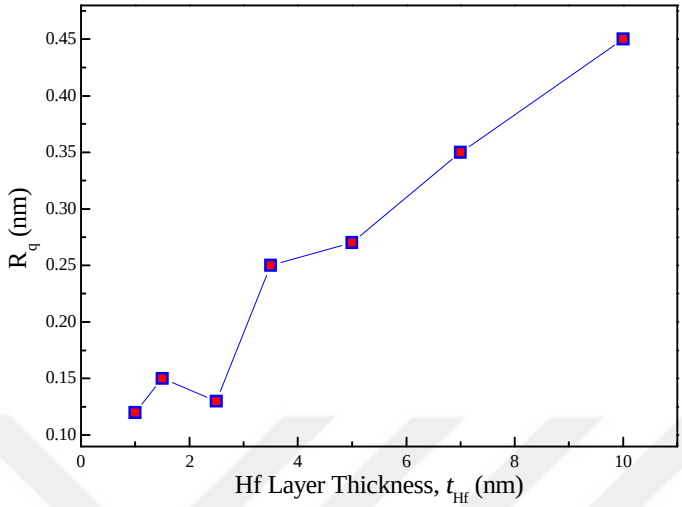


Figure 4.2. The roughness, R_q found from the atomic force microscope imaging technique versus Hf layer thickness in Hf(*t*)|CoFeB(1.1)|MgO(2.0) |Ta(2.0) multilayer film structure.

4.1.2. Transmission Electron Microscope Imaging in Hf|CoFeB|MgO Multilayer Structures

The theoretical calculations predicted that when the crystalline of free and fixed ferromagnetic layers are in same with tunnel barrier (MgO is crystallized in 001 direction), the TMR ratio is over than 1000% in in-plane geometry (Butler et al., 2001). Because of the huge TMR value of theoretical predictions, experimental scientists have focused on fabricate highly crystalline of ferromagnetic layers with tunnel barrier. Here, we studied the crystalline property of layers in our multilayer structure by transmission electron microscope imaging technique. In addition to the crystal property of the film, we are able to determine and compare the thickness of each layer in the multilayer structure between desired and actual ones. We only measured the thickest sample (t_{Hf}=10.0 nm) due to the limitation of measured TEM system. Figure 4.3a-d show the cross-section TEM images of Hf|CoFeB|MgO|Ta multilayer structure at various magnifications. As seen from high-resolution TEM image of the film (see Figure 4.3d), the

crystalline of Hf layer is found as (002) direction. The CoFeB layer sandwiched between Hf (002) and crystal MgO (001) has also the same crystal direction with (002). The results of TEM experiment indicates that the crystallinity is well formed at the interface between seed layer and tunnel barrier.

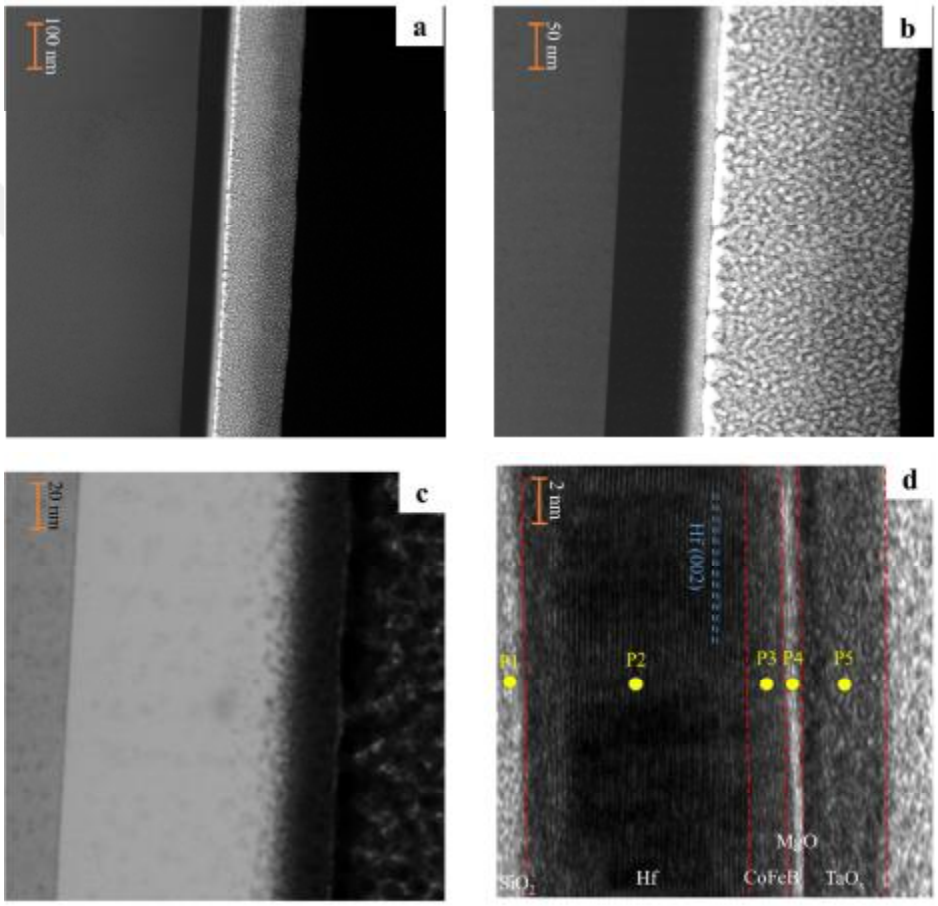


Figure 4.3. Transmission electron microscope images of Hf|CoFeB|MgO|Ta multilayer structures scaled at a)100 nm, b) 50 nm, c) 20 nm and d) 2nm.

In addition, we determined the actual thickness of each layer from the high-resolution transmission electron microscope image. The thickness of each layer is given in Table 4.1. The thickness of layers found from TEM experiment

are consisted with our desired thickness, except MgO layer which is found almost half of the desired thickness.

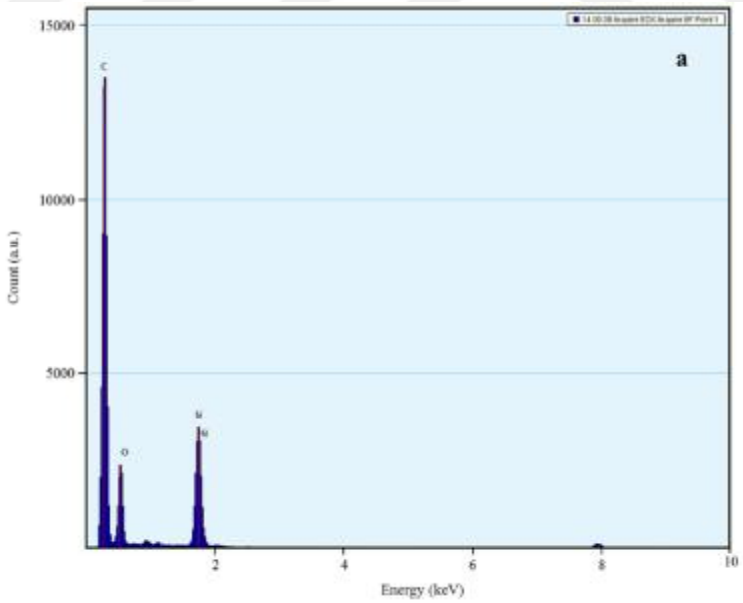
Table 4.1. The desired and actual thickness of each layer in Hf|CoFeB|MgO|Ta multilayer structure.

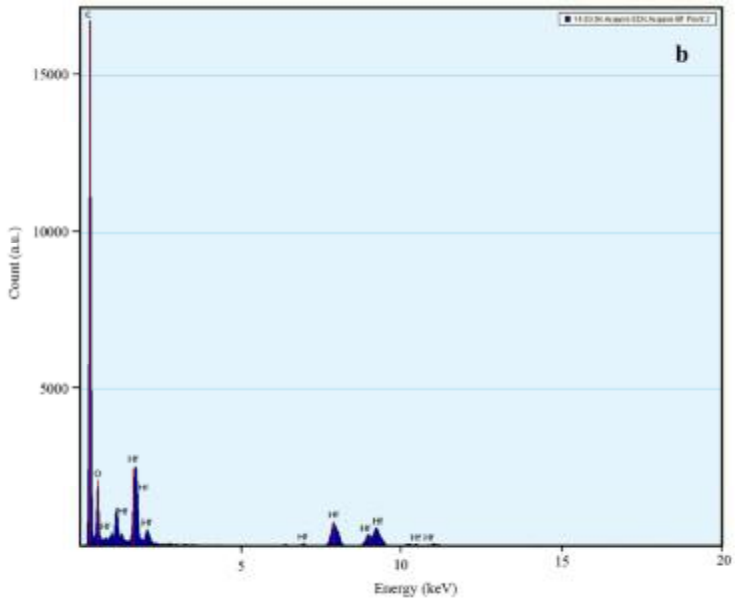
Multilayer Structure	Seed Layer (nm)	Ferromagnetic Layer (nm)	Tunnel Barrier (nm)	Capped Layer (nm)
	Hf	CoFeB	MgO	Ta
Desired	10.0	1.1	2.0	2.0
Measured	10.5	1.3	1.4	1.8

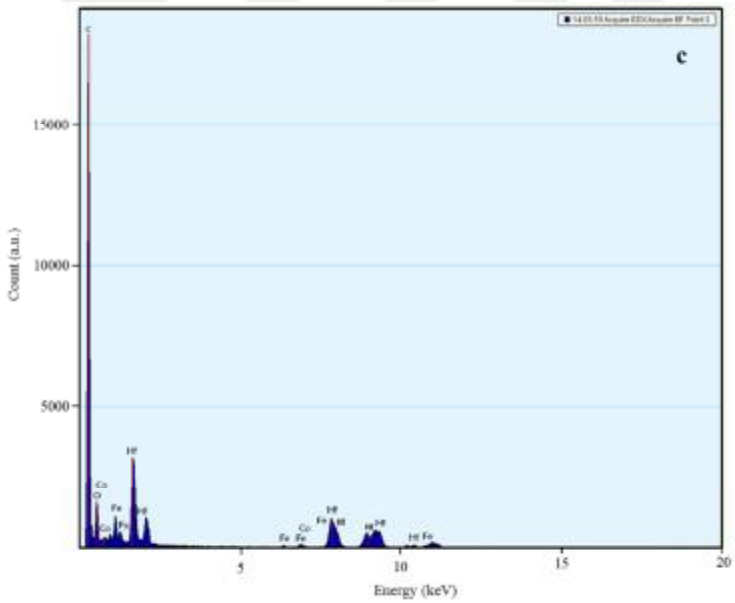
Although the desired thickness of CoFeB layer is 1.1 nm, it was found as 1.3 nm from the HR-TEM image. The reason of this increment in the thickness is due to the diffusion of Hf layer into the CoFeB layer as observed from the elemental analysis which will be discussed below. In addition, the thickness of MgO layer is found as 1.4 nm which is lower than the desired thickness (2.0 nm).

To find out the elemental analysis, we performed Energy Dispersive Spectroscopy (EDS) technique in our multilayer structure. The points taken the EDS data are indicated by yellow circles and labelled as P1, P2, P3, P4 and P5 located SiO_2, Hf, CoFeB, MgO and Ta layers, respectively, in Figure 4.3d. The each layer's EDS spectrums are shown in Figure 4.4a-e for SiO_2, Hf, CoFeB, MgO and Ta layers, respectively. The atomic percentage of elements in each point is tabulated in Table 4.2. In the first point which is corresponding to the SiO_2 as a substrate, we observed Si and O spectrum peaks in the EDS (see Figure 4.4a), as expected. In the second point which is corresponding to the Hf layer, we observed couple of Hf peaks and a weak O spectrum peak in the EDS (see Figure 4.4b). The elemental analysis shows the amount of Hf and O atoms in this layer are found as 75.4% and 24.6%, respectively. The reason of O in this layer is related to the oxidation of the bottom part of the Hf layer from the SiO_2 during the annealing

process. In the third point which is corresponding to the CoFeB layer, we observed couple of Hf, Co and Fe peaks and a weak O spectrum peak in the EDS (see Figure 4.4c). The amount of Hf, Fe, Co and O atoms in this layer are found as 52.6%, 15.8%, 10.5% and 21.1%, respectively. Due to being light of B, we couldn't recognize in the EDS spectrum. In the fourth point which is corresponding to the MgO layer, we observed couple of Hf, Mg and O peaks in the EDS (see Figure 4.4d). The amount of Hf, Mg and O atoms in this layer are found as 71.3%, 13.3% and 15.4%, respectively. The Hf atoms are also diffused into the MgO layer. However, the measured thickness of MgO layer is amost half of the desired thickness. Because of the ceramic form of MgO, it might not be easy control the growing of MgO in our system. In the final point which is corresponding to the capped Ta layer, we observed couple of Ta, Fe and O peaks in the EDS (see Figure 4.4e). The amount of Ta, Fe and O atoms in this layer are found as 93.6%, 2.1% and 4.3%, respectively.




b
15000
10000
5000
Count (a.u.)
5
10
15
20
Energy (keV)


c
15000
10000
5000
Count (a.u.)
5
10
15
20
Energy (keV)

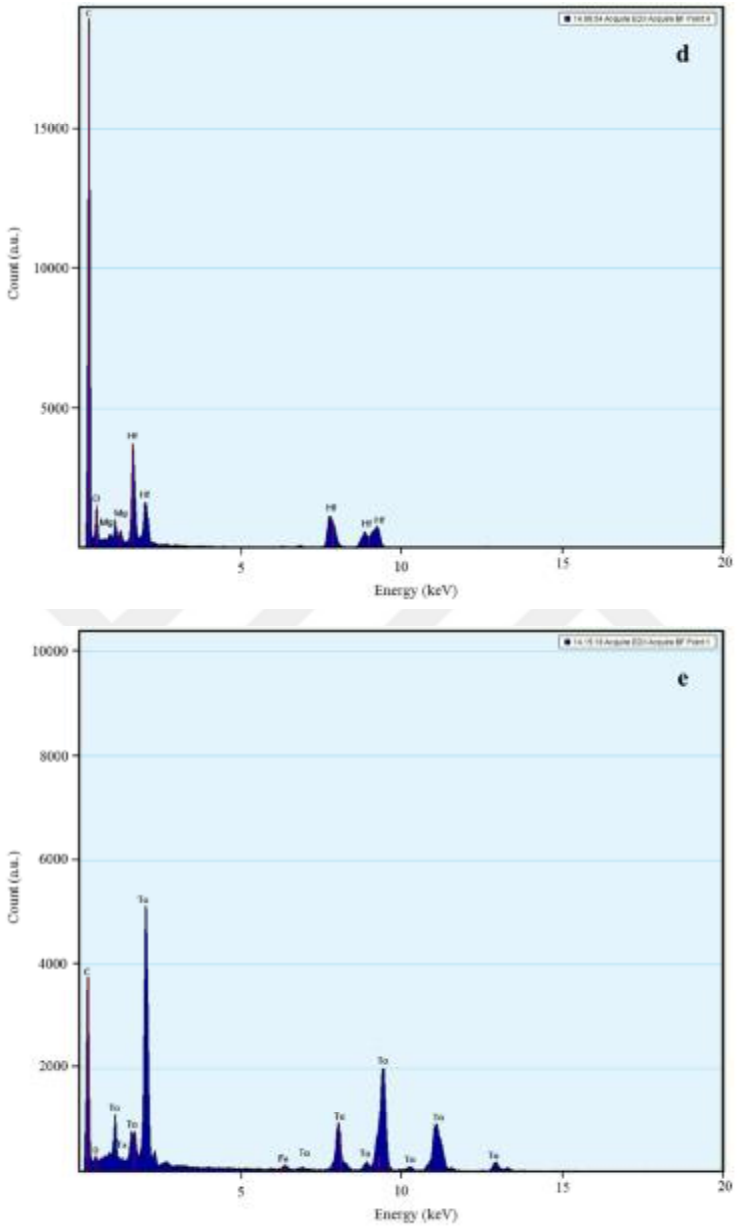


Figure 4.4a-e. The energy dispersive spectrums of P1, P2, P3, P4 and P5 points in SiO_2|Hf|CoFeB|MgO|Ta multilayer structure, respectively.

Table 4.2. Atomic percentage of each element in the selected points in TEM image for Hf|CoFeB|MgO|Ta multilayer structure.

Elements \ Points	P1	P2	P3	P4	P5
Si	57.1	-	-	-	-
O	42.9	24.6	21.1	15.4	4.3
Hf	-	75.4	52.6	71.3	-
Co	-	-	10.5	-	-
Fe	-	-	15.8	-	2.1
Mg	-	-	-	13.3	-
Ta	-	-	-	-	93.6

4.1.3. X-ray Photoelectron Spectroscopy Analysis of Hf(*t*)|CoFeB|MgO|Ta Multilayer Structures

X-ray photoelectron spectroscopy technique is one of the most widely used tools for investigation on the chemical bonding and oxidation states of the materials. Since the magnetic anisotropy is related to the chemical bonding and oxidation state of Fe in ferromagnetic layer in Hf(*t*)|CoFeB|MgO|Ta multilayer structures, we performed an etching and reading XPS data for the multilayer thin film samples using a time step varying between 0 and 45 s. Based on the XPS spectra of Ta, Mg, Fe, and Hf, we have worked on the chemical information near CoFeB|MgO interface during Ar ion etching process. For XPS measurement, the multilayer films for t_{Hf}=0.75 nm and t_{Hf}=3.5 nm in Hf(*t*)|CoFeB|MgO|Ta have been selected to compare their magnetic property because of having in-plane and out-of-plane magnetic anisotropy, respectively. Magnetic properties of the films will be discussed in Section 4.1.4.

The XPS data was collected from top to bottom of the multilayer films during Ar ion etching process. Figure 4.5a-b show the XPS spectra of Ta 4*f* for the

films of t_{Hf}=0.75 nm and t_{Hf}=3.5 nm at various etching time, respectively. The XPS spectrums exhibit strong spin-orbit splitting with metallic Ta and Ta oxide peaks. The peaks at~ 21.5 eV and at~ 23.1 eV are characteristics of the metallic Ta $4f_{7/2}$ and Ta $4f_{5/2}$, respectively. The peaks at ~ 26.2 eV and at ~ 28.1 eV are corresponding to the Ta^{+5} $4f_{7/2}$ and Ta^{+5} $4f_{5/2}$ phase in Ta_2O_5, respectively. The XPS results show that both Ta and Ta^{5+} were present in the surface of the film. Ta_2O_5 might be formed in the air atmosphere while the samples were transferred from the deposition system to the XPS system. At an etching time of 0 s, Ta^{5+} became dominant over Ta and the intensity of the Ta^{+5} peak became much higher than that of Ta, as expected. When the etching time is increased from 0 to 15 s, the Ta peak is much enhanced and the Ta^{+5} peak is weakened. At an etching time of 30 s, only Ta was present in the films. The XPS results show that the Ta surface was most oxidized and that only Ta was present in the films.

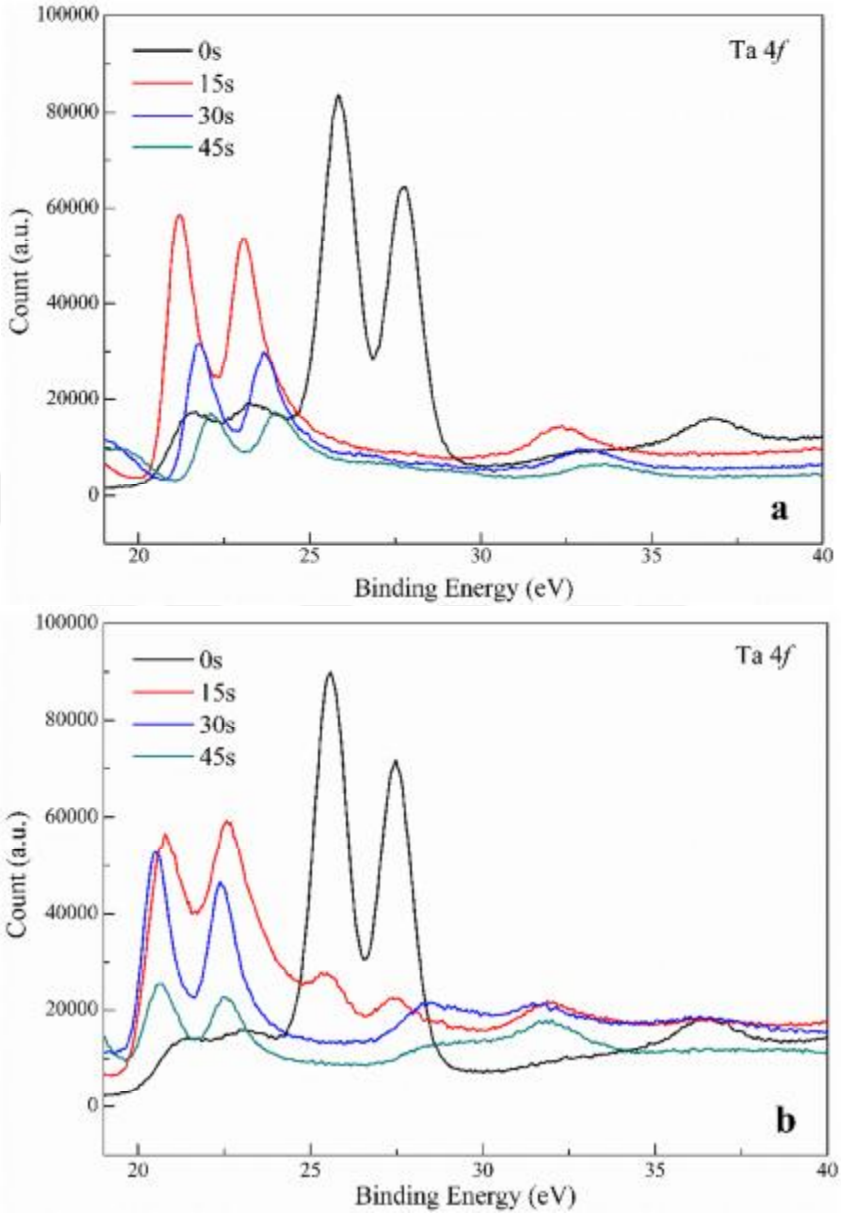


Figure 4.5. The x-ray photoelectron spectrum of Ta-4*f* in Hf(*t*)|CoFeB|MgO|Ta multilayer structure a) *t*=0.75 nm and b) *t*=3.5 nm.

Figure 4.6a-b show the high resolution XPS spectra of O 1*s* for t_{Hf}=0.75 and 3.5 nm at an etching time of 0, 15, 30 and 45 seconds, respectively. At the

initial time, the XPS will measure the O 1*s* on the surface of the films. Once the film was started to the etching from 0 to 15 seconds, a new spectrum peak in the sample of t_{Hf} = 0.75 nm has been observed at ~ 532 eV as well as observing a dominant peak at ~ 530 eV which can be attributed to the O atom in the MgO layer. For the sample with t_{Hf} = 3.5 nm, XPS spectra displays a weak one at ~532 eV and a strong one O 1*s* peak at ~530 eV. Based on the previous research in the literature that the peak at ~532 eV is corresponding to the BO_x (Meng et al., 2011; Read et al., 2007). Thus, we attribute the higher BE peak at ~532 eV to BO_x. However, calculated from the area of these curves, the ratio of O atom in the BO_x to O atom in the MgO is 0.61:1 for t_{Hf}=0.75 nm and 0.18:1 for t_{Hf}=3.5 nm. It means more BO_x was formed at the CoFeB|MgO interface for the sample with 0.75 nm thickness of Hf in the multilayer structure. The clear appearance of BO_x peaks indicates that B atoms diffused toward either the CoFeB|MgO interface or the MgO layer. The CoFeB|MgO heterostructures show strong interface perpendicular magnetic anisotropy features that can be attributed to the hybridization of Fe and O orbitals at the CoFeB|MgO interface that will be discussed as followings.

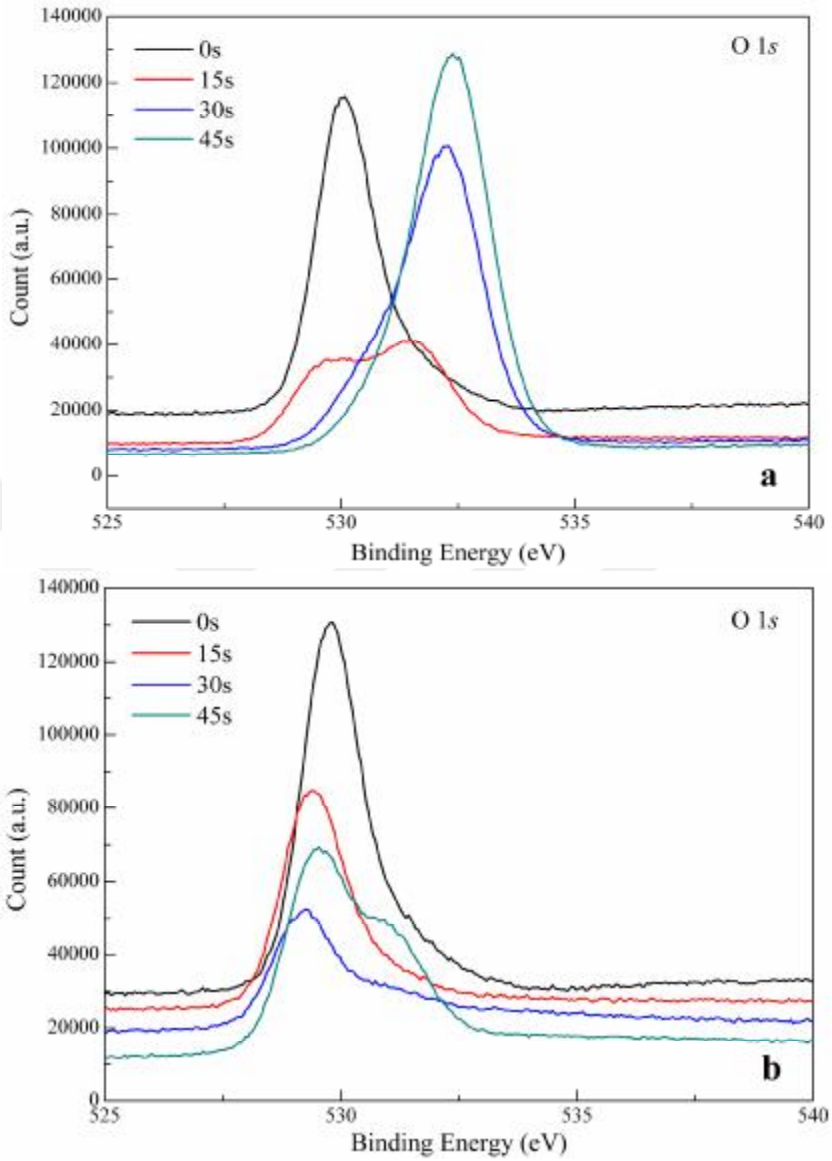


Figure 4.6. The x-ray photoelectron spectrum of O-1*s* in Hf(*t*)|CoFeB|MgO|Ta multilayer structure a) *t*=0.75 nm and b) *t*=3.5 nm.

Figure 4.7a-b show the XPS spectra of Mg-1*s* for t_{Hf}=0.75 nm and t_{Hf}=3.5 nm at various etching time, respectively. As seen from the figures that once the etching time is reached at 15 s, one peak at ~1303 eV which is characteristic Mg-

1*s*, is observed. When the etching time is increased above 15 s, the peak amplitude is getting lower and the position shifts to the higher binding energy.

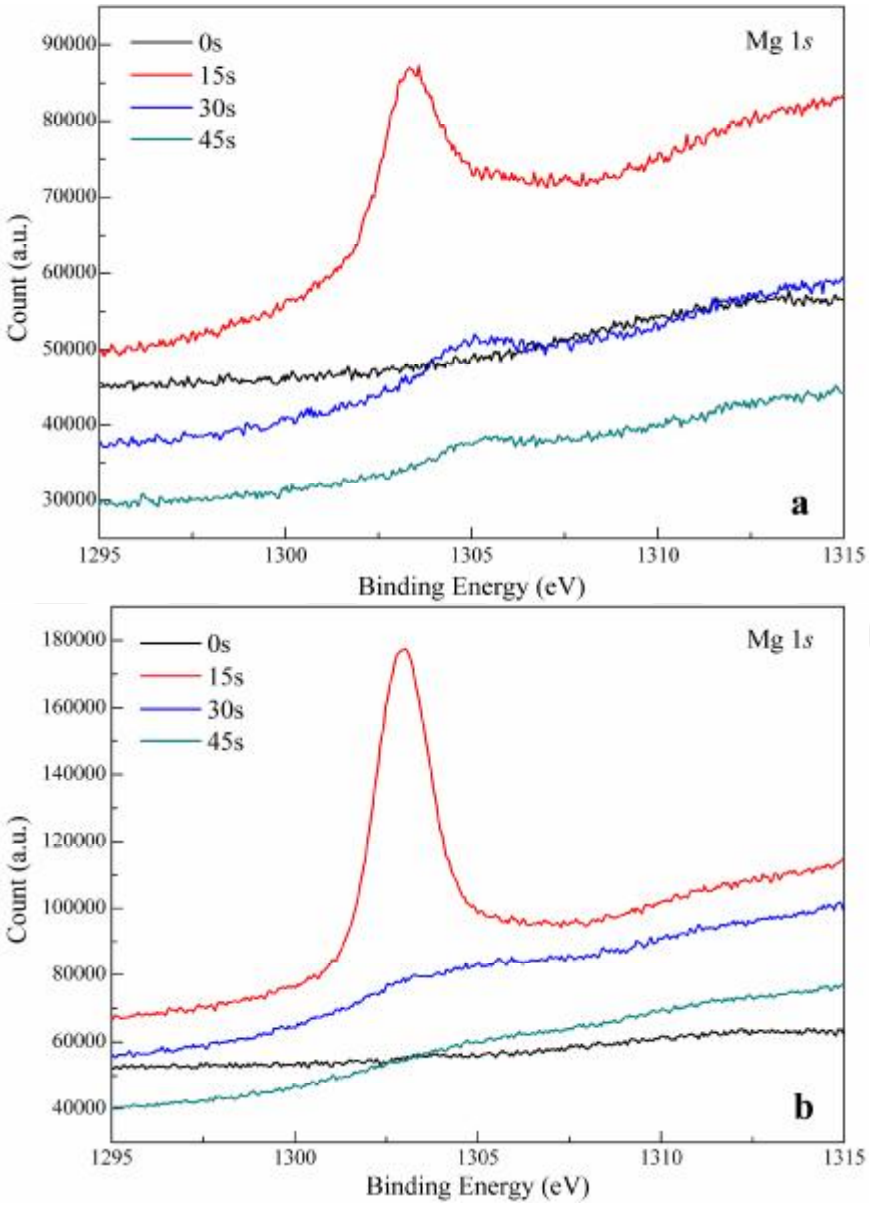


Figure 4.7. The x-ray photoelectron spectrum of Mg-1*s* in Hf(*t*)|CoFeB|MgO|Ta multilayer structure a) *t*=0.75 nm and b) *t*=3.5 nm.

Figure 4.8a-b show the XPS spectra of B 1*s* for t_{Hf}=0.75 and 3.5 nm at various etching time, respectively. Once the etching time is reached to 15 s, an XPS peak at ~186 eV has emerged for both samples. From the literature, the peak at 186 eV binding energy is labelled as B-1*s*.

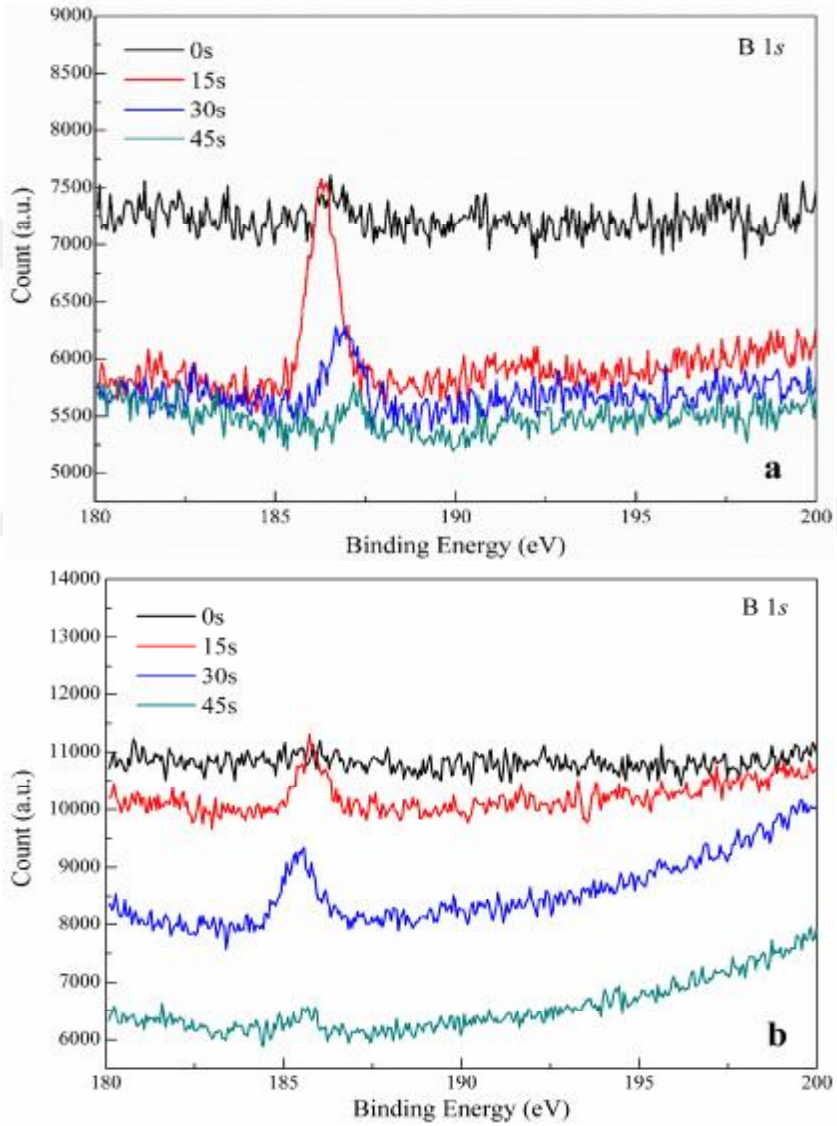


Figure 4.8. The x-ray photoelectron spectrum of B-1*s* in Hf(*t*)|CoFeB|MgO|Ta multilayer structure a) *t*=0.75 nm and b) *t*=3.5 nm.

Figure 4.9a-b show high resolution XPS spectra of Fe 3*p* for the samples with t_{Hf}= 0.75 nm and t_{Hf}= 3.5 nm for an etching time of 0, 15, 30 and 45 seconds, respectively. According to the XPS handbook (Wanger et al., 1979), the peaks located at ~52.7 eV and ~54.7 eV correspond to the metallic Fe 3*p* and Fe oxide 3*p* states, respectively. It indicates that the interfacial Fe atoms are partially oxidized. However, the ratio of Fe oxide to metallic Fe is 0.30:1 for t_{Hf}=0.75 nm and 0.53:1 for t_{Hf}=3.5 nm are found from the calculated area of the XPS curves. It means that the oxidation of Fe for t_{Hf}=3.5 nm was formed larger than the film for t_{Hf}=0.75 nm.

XPS measurements show that the Fe oxide peaks are very weak for t_{Hf} = 0.75 nm films. Based on the B atom diffusion and the presence of the BO_x peaks in the t_{Hf} = 0.75 nm films, we attribute the very weak Fe oxide for t_{Hf} = 0.75 nm films to the consumption of the O liberated by the reduction of Fe oxides by the diffusing B atoms. This indicates that Fe oxide was reduced through the formation of B oxide (Bae et al., 2006).

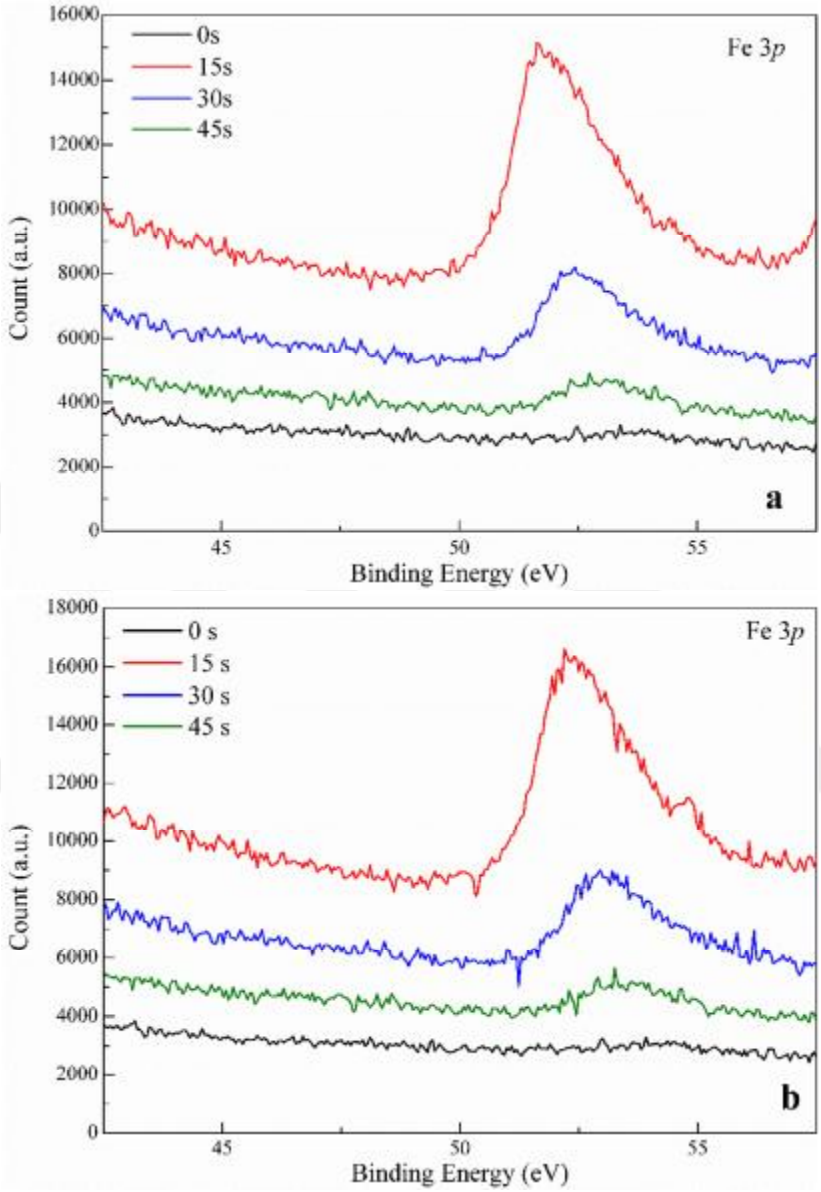


Figure 4.9. The x-ray photoelectron spectrum of Fe-3*p* in Hf(*t*)|CoFeB|MgO|Ta multilayer structure a) *t*=0.75 nm and b) *t*=3.5 nm.

The XPS peaks at ~14. 3 eV and ~16.1 eV in Figure 4.10a-b are characteristic of metallic Hf $4f_{7/2}$ and $4f_{5/2}$ peaks, respectively. The peaks at ~18.2 eV and ~ 19.5 eV correspond to the Hf oxide $4f_{7/2}$ and $4f_{5/2}$ peaks, respectively.

Figure 4.10a shows that Hf oxide is formed in t_{Hf} = 0.75 nm due to the oxidation of the Hf adjacent to the Si/SiO_2 substrate on the bottom of the sample by SiO_2.

Figure 4.10b shows that Hf atoms did not remain at the bottom of the film, but rather migrated to the film surface. At an etching time of 0 s, only small Hf signals can be distinguished and the two Hf peaks are weak, demonstrating that only metallic Hf was present in the film surface. The intensity of the Hf peak is enhanced with increasing etching time. It is important to note that at the etching times of 15 s and 30 s, the corresponding Hf 4*f* XPS spectra displays not only the peaks due to metallic Hf, but also the peaks arising from the Hf oxide present in the films. When the etching time is increased to 45 s, the corresponding Hf 4*f* spectrum only exhibits oxide Hf components, without no detectable trace of metallic Hf peaks. The Hf oxide was formed in film by oxidation of the Hf by the adjacent SiO_2. Determination of the origins and the mechanism of the Hf migration to the surface of the film requires further research and discussion.

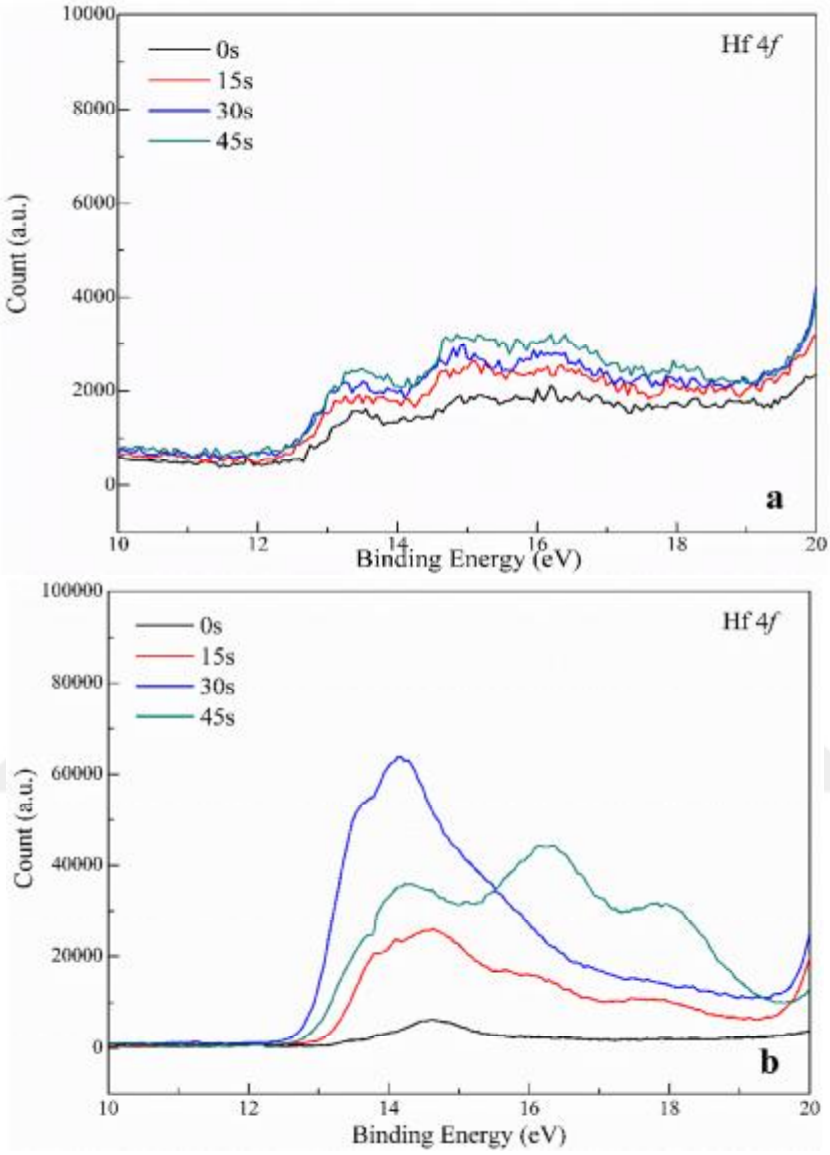


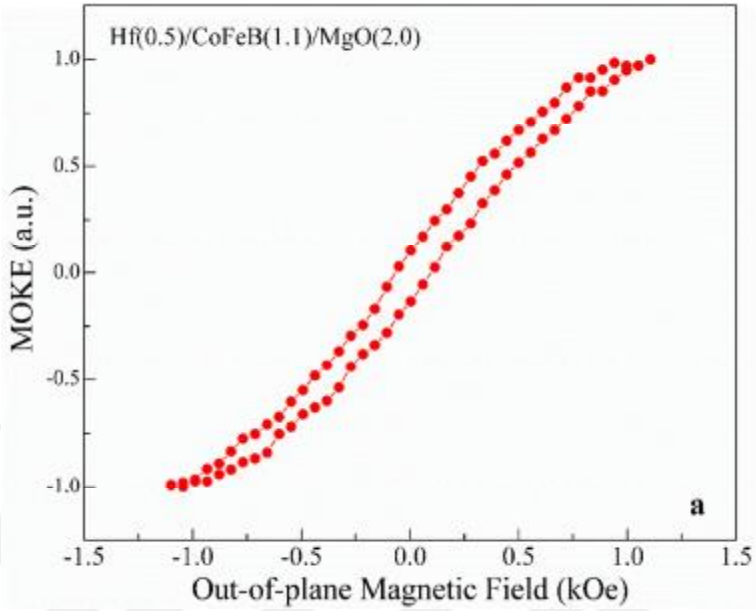
Figure 4.10. The x-ray photoelectron spectrum of Hf-4*f* in Hf(*t*)|CoFeB|MgO|Ta multilayer structure a) *t*=0.75 nm and b) *t*=3.5 nm.

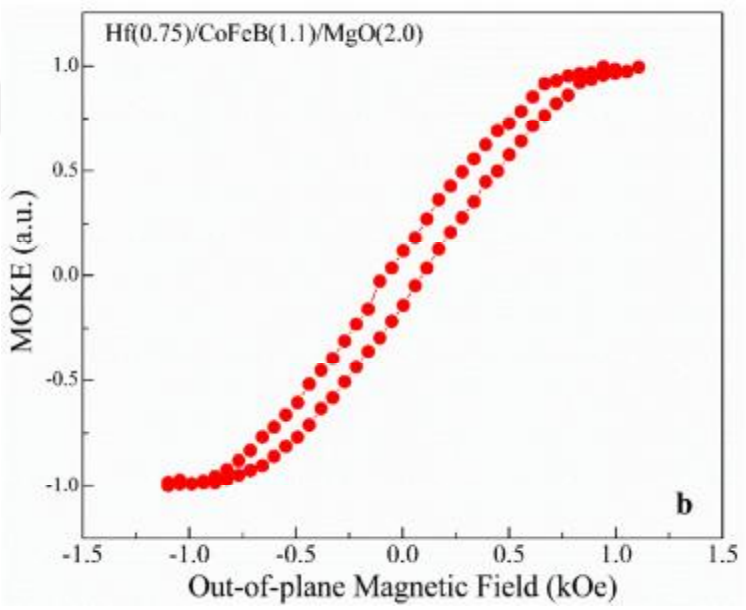
The above analysis shows that formation of more effective Fe–O orbital hybridization at the CoFeB|MgO interface is the critical factor for generation of PMA in Hf(*t*)|CoFeB(1.1 nm)|MgO(2 nm)|Ta(2 nm) films. The formation of B

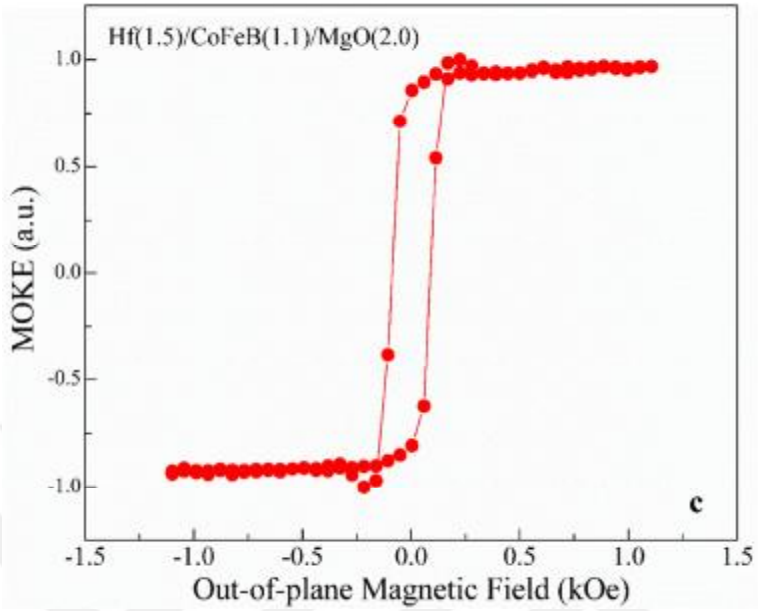
oxide and the simultaneous reduction of Fe oxide at the bottom interface suggest that B oxide formation has a negative impact on PMA of the interface under thermal annealing. The BO_x formed in t_{Hf} = 0.75 nm implies the reduction of Fe oxides, which is detrimental for PMA. The formation of Fe oxide at the CoFeB|MgO interface was found to be critical for the large enhancement of the PMA ratio for Hf|CoFeB|MgO|Ta film with t_{Hf} = 3.5 nm after thermal annealing. In the next section, the magnetic properties of the films will be discussed in detail.

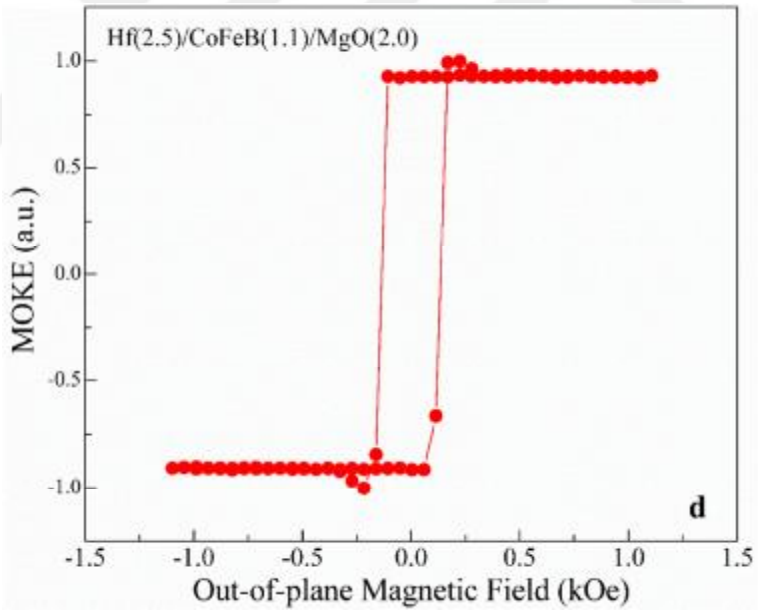
4.1.4. Magnetic Analysis of Hf(*t*)|CoFeB|MgO|Ta Multilayer Structures

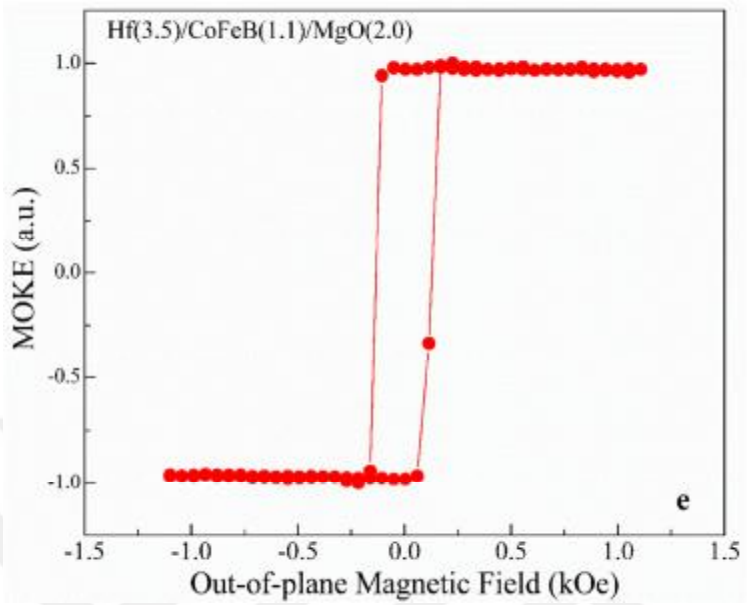
To determine the magnetic anisotropy, we used both magneto-optical-Kerr effect and vibrating sample magnetometer measurements. First, MOKE was performed under an out-of-plane magnetic field, H_z. Figure 4.11a-h show hysteresis loops of the MOKE signal as a function of H_z for the films at various Hf thickness from 0.5 to 10.0 nm. PMA is observed in the range of 1.0 to 10.0 nm of Hf layer thickness in main structure. Since the sharp switching of MOKE signal under out-of-plane magnetic field indicates the perpendicular magnetic anisotropy, it is observed that the magnetic anisotropy changes from perpendicular to in-plane below the thickness of Hf layer ~1.5 nm. The coercive field, H_c of the multilayer films is determined from MOKE experiment. It is found that the H_c increases with increasing Hf layer thickness (see Figure 4.12). But, the increment of H_c value is getting lower above t_{Hf} =5.0 nm. The first increment in H_c, *i.e.* increasing Hf layer thickness as well, is related to the enhancement of perpendicular magnetic anisotropy because of the better interface between seed and ferromagnetic layer.

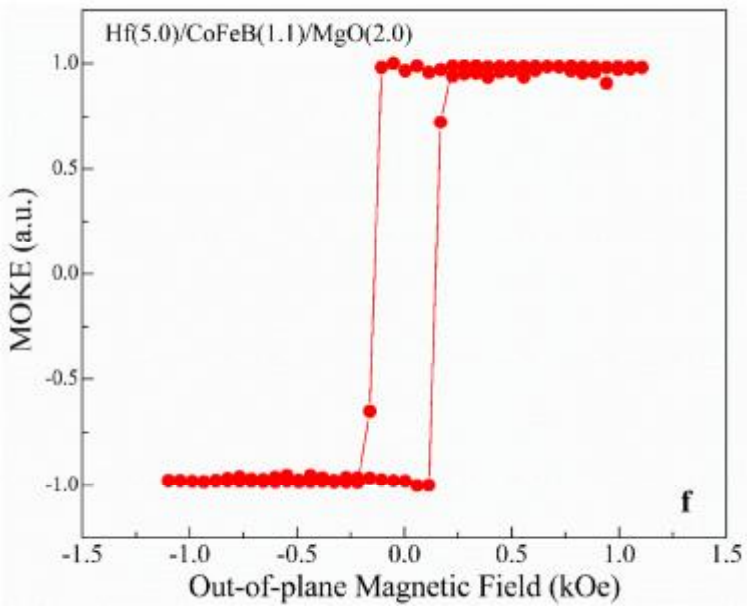

Hf(0.5)/CoFeB(1.1)/MgO(2.0)
MOKE (a.u.)
1.0
0.5
0.0
-0.5
-1.0
-1.5
-1.0
-0.5
0.0
0.5
1.0
1.5
Out-of-plane Magnetic Field (kOe)
a


Hf(0.75)/CoFeB(1.1)/MgO(2.0)
MOKE (a.u.)
1.0
0.5
0.0
-0.5
-1.0
-1.5
-1.0
-0.5
0.0
0.5
1.0
1.5
Out-of-plane Magnetic Field (kOe)
b


Hf(1.5)/CoFeB(1.1)/MgO(2.0)
MOKE (a.u.)
1.0
0.5
0.0
-0.5
-1.0
-1.5
-1.0
-0.5
0.0
0.5
1.0
1.5
Out-of-plane Magnetic Field (kOe)
c


Hf(2.5)/CoFeB(1.1)/MgO(2.0)
MOKE (a.u.)
1.0
0.5
0.0
-0.5
-1.0
-1.5
-1.0
-0.5
0.0
0.5
1.0
1.5
Out-of-plane Magnetic Field (kOe)
d


Hf(3.5)/CoFeB(1.1)/MgO(2.0)
MOKE (a.u.)
1.0
0.5
0.0
-0.5
-1.0
-1.5
-1.0
-0.5
0.0
0.5
1.0
1.5
Out-of-plane Magnetic Field (kOe)
e


Hf(5.0)/CoFeB(1.1)/MgO(2.0)
MOKE (a.u.)
1.0
0.5
0.0
-0.5
-1.0
-1.5
-1.0
-0.5
0.0
0.5
1.0
1.5
Out-of-plane Magnetic Field (kOe)
f

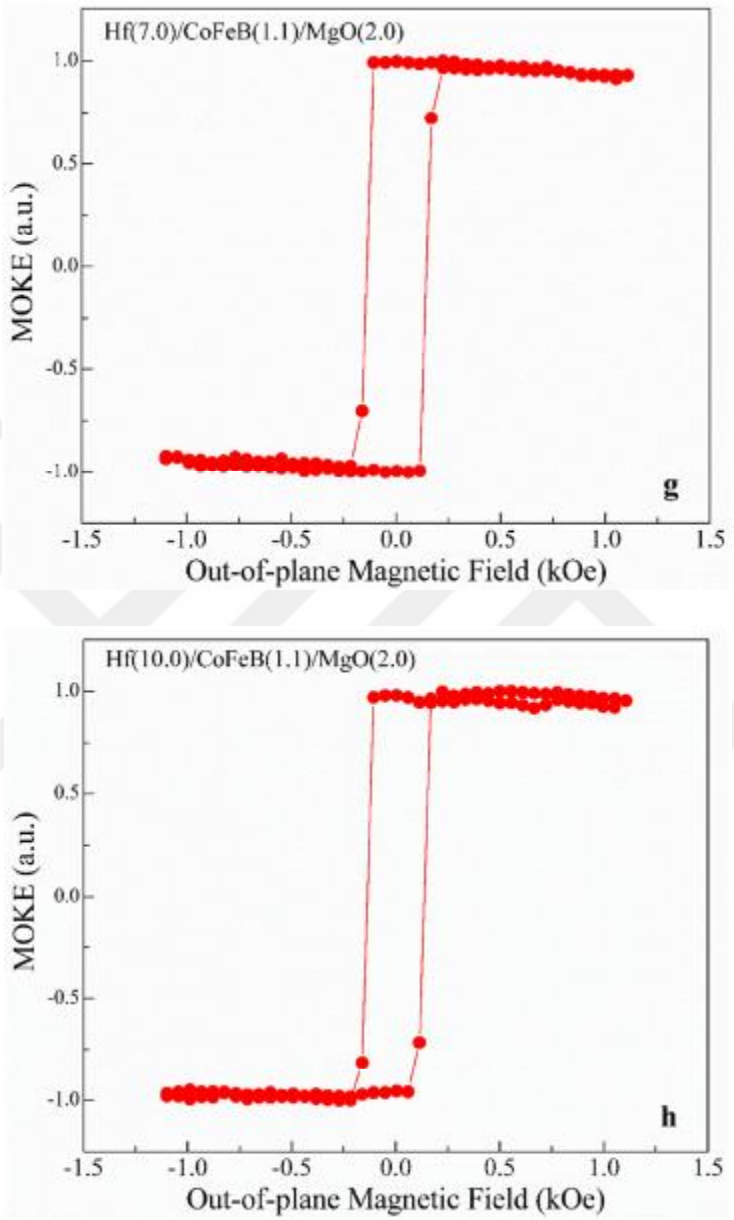


Figure 4.11. Magneto-Optical Kerr effect curves measured under out-of-plane magnetic field for a) t_{Hf}=0.5 nm, b) t_{Hf}=1.0 nm, c) t_{Hf}=1.5 nm, d) t_{Hf}=2.5 nm, e) t_{Hf}=3.5 nm, f) t_{Hf}=5.0 nm, g) t_{Hf}=7.0 nm, h) t_{Hf}=8.5 and i) t_{Hf}=10.0 nm in Hf(t)|CoFeB(1.1)|MgO(2.0)|Ta(2.0) multilayer films.

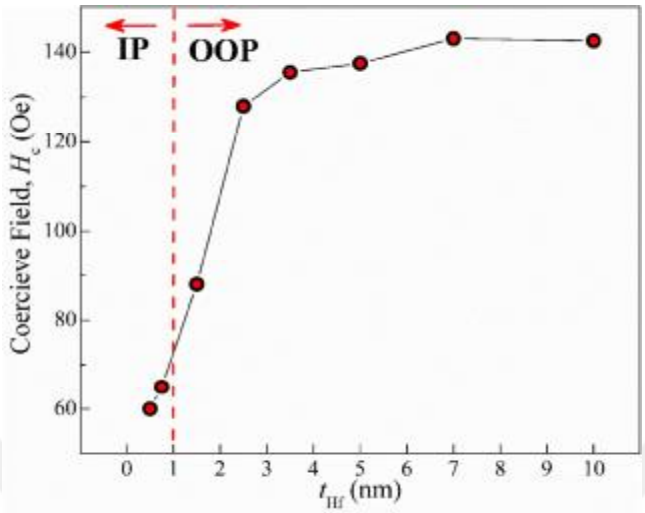
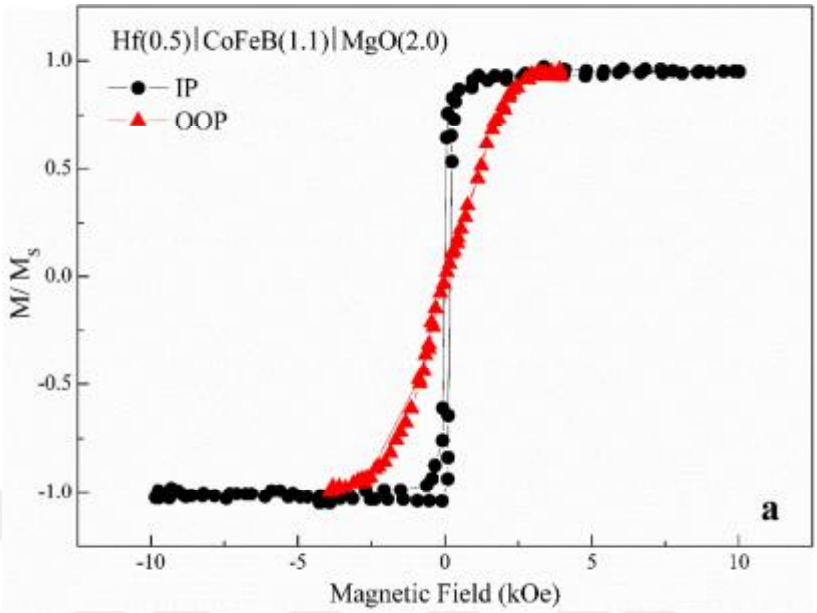
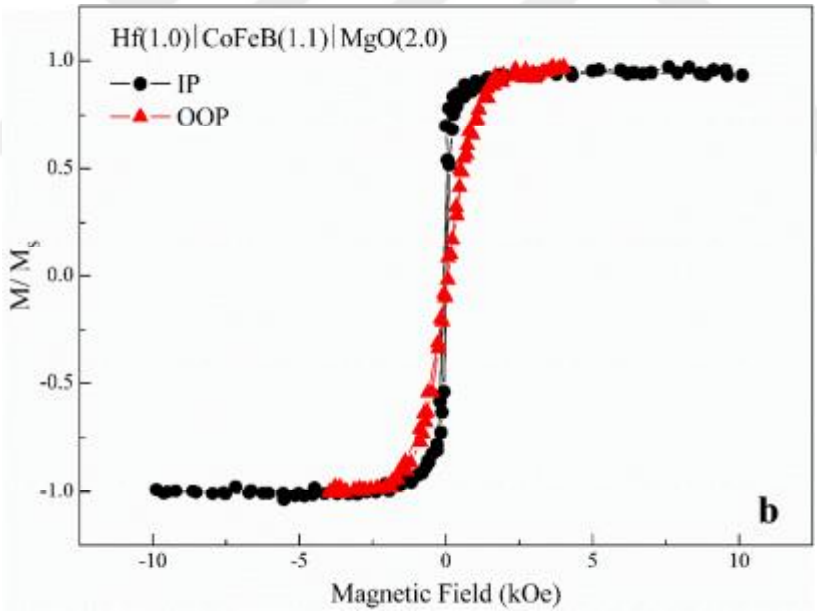
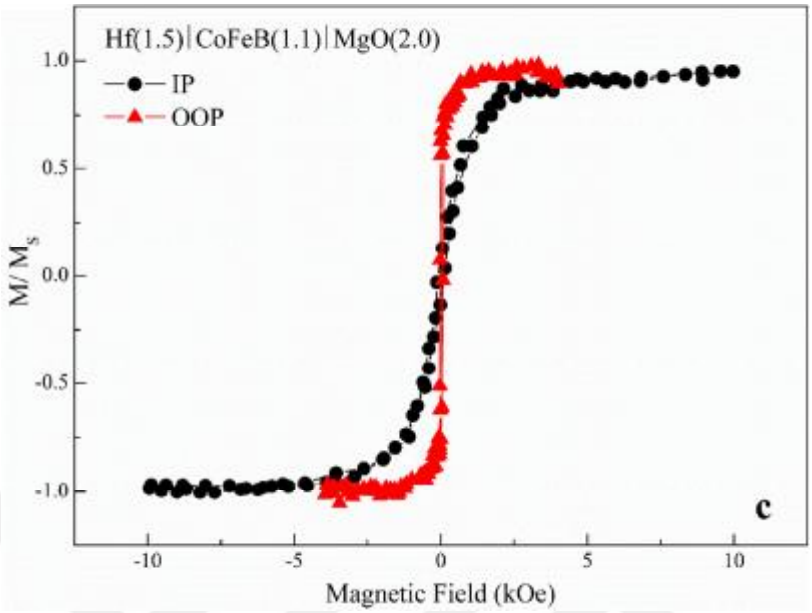


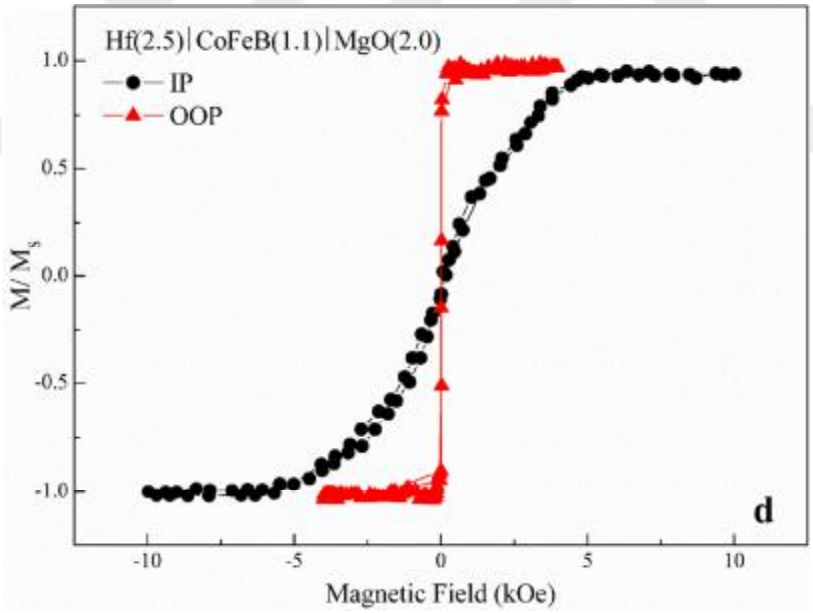
Figure 4.12. The coercive field, H_c as a function of Hf layer thickness in Hf(t)|CoFeB(1.1)|MgO(2.0)|Ta(2.0) multilayer films.

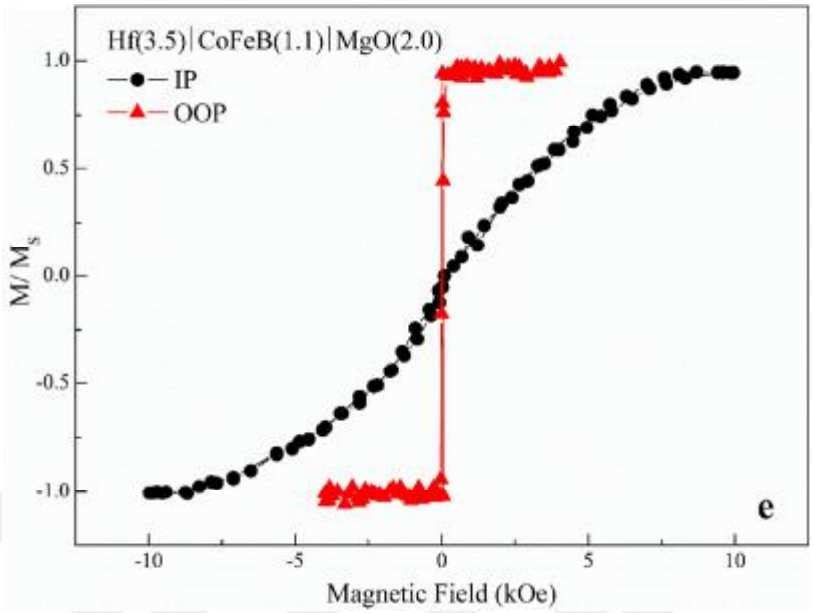
Since the MOKE experiment is used to determine qualitatively the magnetic property of the films, the magnetic property of the multilayer films were further studied by vibrating sample magnetometer measurements in Physical Property Measurement System (PPMS). It is expected that the magnetic moments of our multilayer films where the thickness of ferromagnetic layer is constant while the heavy metal layer thickness is in a range of 0.5 to 10 nm, should not change, if the ferromagnetic layer is not disturbed at low thickness of Hf due to the lacking of buffer layer. In addition to the magnetic moment of our multilayer films, we investigate the anisotropy field dependence Hf layer thickness. Thus, we performed both in-plane and out-of-plane magnetization measurements for all multilayer films. Figure 4.13a-i show the magnetization which is normalized by saturation magnetization as a function of in-plane and out-of-plane magnetic field for Hf(t)|CoFeB|MgO|Ta multilayer structures.

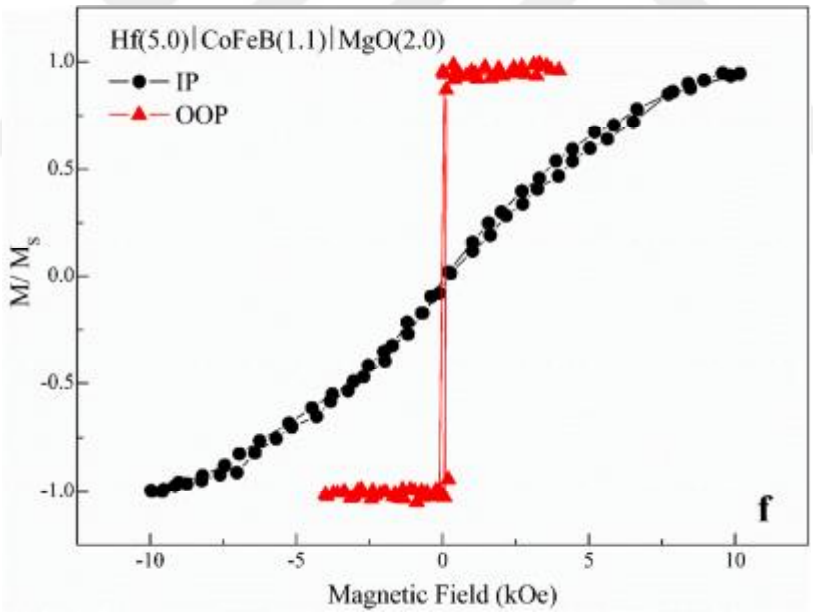

Hf(0.5)|CoFeB(1.1)|MgO(2.0)
IP
OOP
M/ M_s
Magnetic Field (kOe)
a

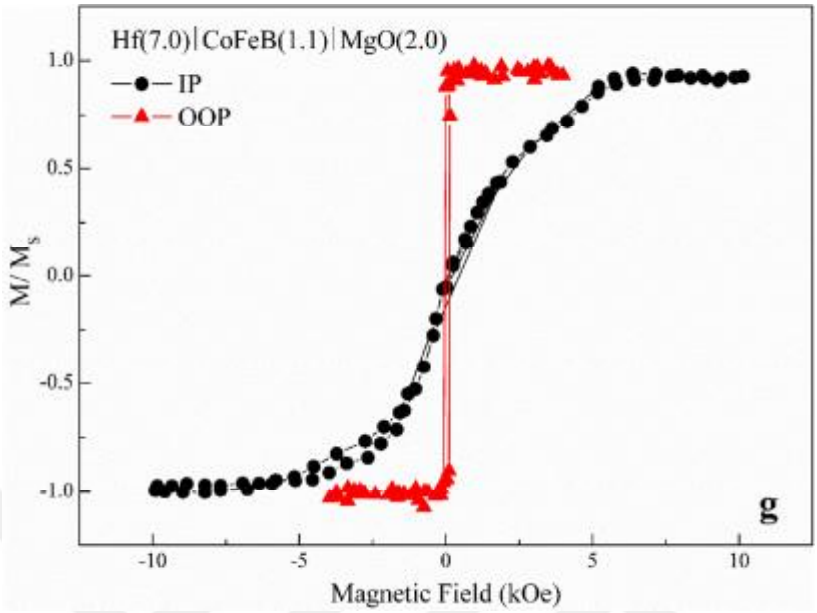

Hf(1.0)|CoFeB(1.1)|MgO(2.0)
IP
OOP
M/ M_s
Magnetic Field (kOe)
b

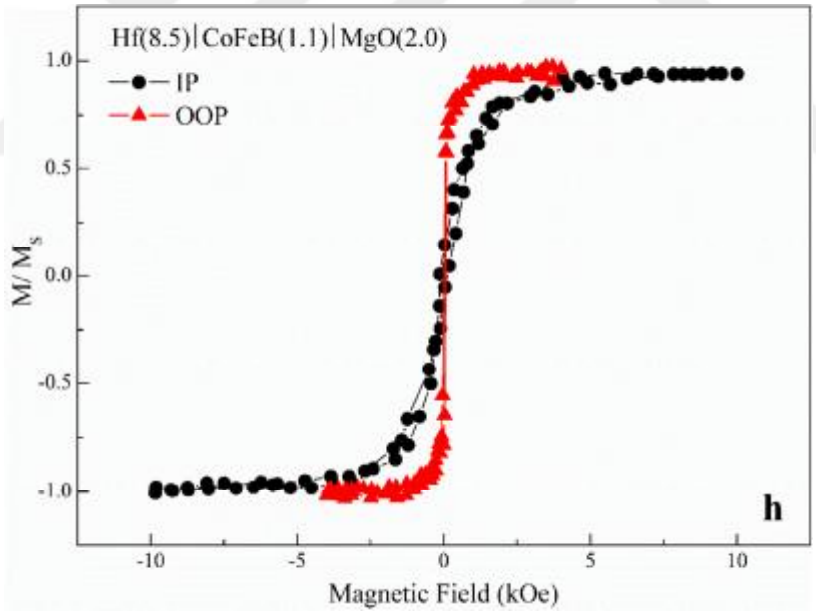

Hf(1.5)|CoFeB(1.1)|MgO(2.0)
IP
OOP
M/ M_S
Magnetic Field (kOe)
c


Hf(2.5)|CoFeB(1.1)|MgO(2.0)
IP
OOP
M/ M_S
Magnetic Field (kOe)
d


Hf(3.5)|CoFeB(1.1)|MgO(2.0)
IP
OOP
M/ M_S
Magnetic Field (kOe)
e


Hf(5.0)|CoFeB(1.1)|MgO(2.0)
IP
OOP
M/ M_S
Magnetic Field (kOe)
f


Hf(7.0)|CoFeB(1.1)|MgO(2.0)
IP
OOP
M/ M_s
Magnetic Field (kOe)
g


Hf(8.5)|CoFeB(1.1)|MgO(2.0)
IP
OOP
M/ M_s
Magnetic Field (kOe)
h

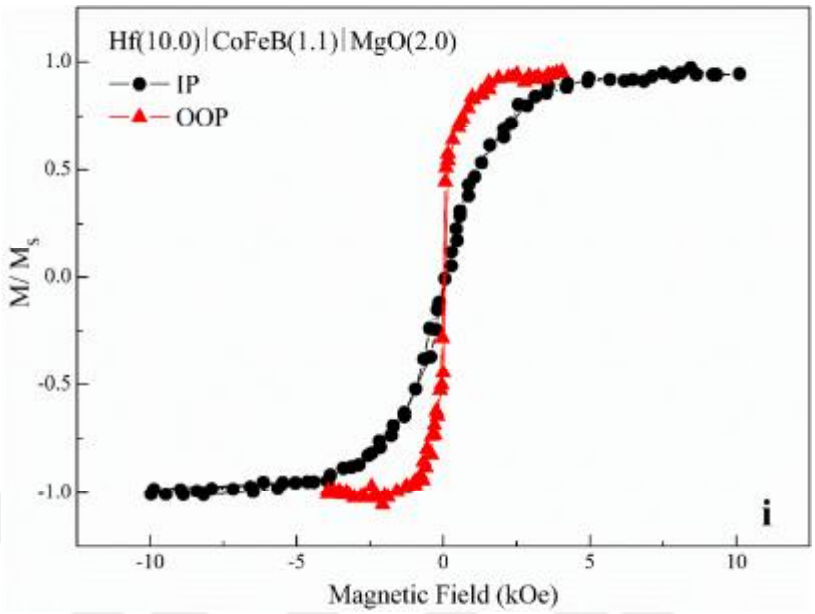


Figure 4.13. Magnetic hysteresis curves measured under both in-plane and out-of-plane magnetic field for a) t_{Hf}=0.5 nm, b) t_{Hf}=1.0 nm, c) t_{Hf}=1.5 nm, d) t_{Hf}=2.5 nm, e) t_{Hf}=3.5 nm, f) t_{Hf}=5.0 nm, g) t_{Hf}=7.0 nm, h) t_{Hf}=8.5 and i) t_{Hf}=10.0 nm in Hf(*t*)|CoFeB(1.1)|MgO(2.0)|Ta(2.0) multilayer films.

The perpendicular magnetic anisotropy fields, H_k of the various heavy-metal layer thickness films were determined from the hard-axis magnetization curves by performing VSM with an in-plane field. The determination of H_k is explained in Section 1.6. Figure 4.14 shows that the H_k as a function of Hf layer thickness in Hf(*t*)|CoFeB(1.1)|MgO(2.0)|Ta(2.0) multilayer films. As seen from the Figure 4.14 that a non-monotonic PMA behavior as a function of Hf layer thickness was observed in a range of 1.5 to 10.0 nm in Hf(*t*)|CoFeB(1.1)|MgO(2.0)|Ta(2.0) multilayer film structure. Here, there are two regions of PMA behavior: (*i*) the PMA increases with t_{Hf} up to 5.0 nm, and then (*ii*) once the thickness of Hf goes above 5.0 nm, it gets weaker up to 10.0 nm in this work. The origin of PMA is partly attributed to the Fe-O hybridization at the interface between CoFeB|MgO and partly to the interface between buffer-layer|CoFeB, as observed in previous works (Pai et al., 2014; Liu et al., 2012;

Kaidatzis et al., 2015; Peng et al., 2015). In the first region (below t_{Hf}=5.0 nm), the interface magnetic anisotropy enhances due to the increment buffer layer of CoFeB. Thus, the crystal quality of CoFeB layer can be enhanced by thicker Hf layer. In addition to the interface effect, the XPS experiment indicates that the Fe-3*p* oxidation level increases with Hf thickness from 0.75 nm to 3.5 nm (see Section 4.1.3). As it is known that the hybridization of Fe-O creates out-of-plane magnetic coupling at the interface between FM and OX layers. Thus, we observed enhancement in the PMA with Hf layer thickness. In the second region (above t_{Hf}=5.0 nm), the reason for observing a weaker PMA at thicker Hf layers may be attributed to the film roughness. As discussed in Section 4.1.1, the roughness of the films determined from the AFM measurements increases with increasing Hf layer thickness in the multilayer structure (see Figure 4.2). The roughness is found almost half of the ferromagnetic layer thickness in t_{Hf}=10.0 nm. Thus, it would be possible explanation in the trend of H_k versus Hf thickness above 5.0 nm. Therefore, we can conclude that the AFM results of the films consistent with the PMA behavior above the thickness of Hf ~5.0 nm.

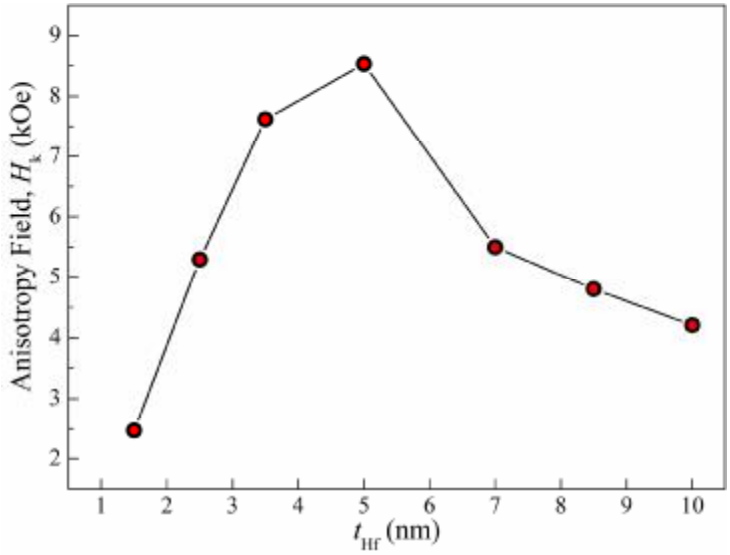


Figure 4.14. The anisotropy field, H_k as a function of Hf layer thickness in Hf(*t*)|CoFeB(1.1)|MgO(2.0)|Ta(2.0) multilayer films.

4.1.5. Transport Analysis of Hf(*t*)|CoFeB|MgO|Ta Multilayer Structures

The current-induced spin–orbit torque effect on the magnetization is first investigated by measuring anomalous Hall effect resistance, R_{AHE} as a function of sweeping out-of-plane, H_z and longitudinal, H_L magnetic field at various in-plane dc electric currents. Because of the direct proportionality between anomalous Hall resistance and the perpendicular component of the magnetization in the CoFeB layer (the detail of this relation has been discussed in Section 1.5.2), the out-of-plane measurements give information on the anisotropy property of the device. Since the under-layer thickness is different for each sample, the electric current density, J_x (or J_e) was used instead of electric current, I_x (or I_e) to compare all the results. The same current density was arranged in the devices as low (± ~1.9×10^6 A/cm^2), medium (± ~9.6×10^6 A/cm^2) and high (± ~15.4×10^6 A/cm^2) current density levels. Figure 4.15a shows the measurement configuration (also showing the Hall-bar device structure) where the bias current is applied along the *x*-axis and the voltage is measured along the *y*-axis. The same experimental configuration was used for all samples. The transport experiments were performed at room temperature.

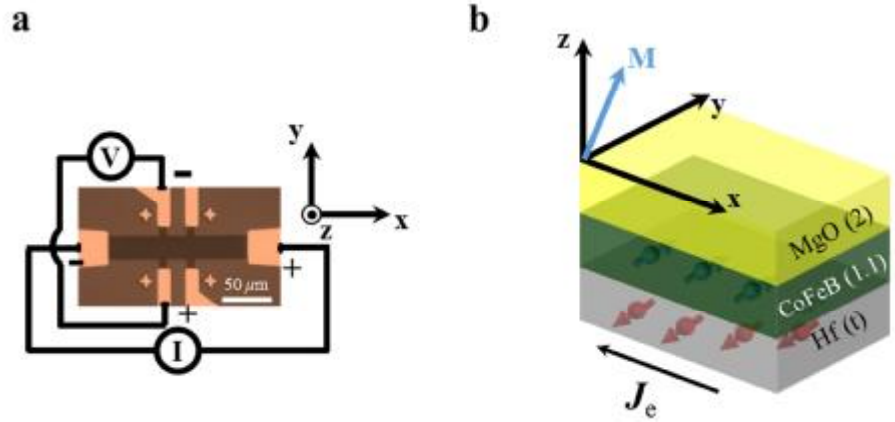


Figure 4.15. a) Optical photograph of one device and the dc transport experimental configuration, b) Schematic illustration of the film structure of Hf|CoFeB|MgO multilayer with electric current in the *x* direction.

Figure 4.17 shows R_{AHE} as a function of H_z under low (± ~1.9×10^6 A/cm^2), medium (± ~9.6×10^6 A/cm^2) and high (± ~15.4×10^6 A/cm^2) current density levels in Hf(1.5)|CoFeB(1.1)|MgO(2)|Ta(2) multilayer structure. The magnetization direction is M_z^{Up} (M_z^{Down}) for $R_{AHE} < 0$ ($R_{AHE} > 0$) case. Since the square shape in out-of-plane magnetization (R_{AHE}) versus out-of-plane magnetic field curve indicates the perpendicular magnetic anisotropy property, the magnetic anisotropy of device for 1.5 nm thickness of Hf in Hf(*t*)|CoFeB(1.1)|MgO(2)|Ta(2) multilayer structure shows a typical PMA effect. As seen from the Figure 4.17, the field sweeping characteristics for both current directions looks like same for all current density levels. However, the coercive field decreases when the current density is increased from ±1.9×10^6 A/cm^2 to ±15.4×10^6 A/cm^2. This decrement in the coercive field might be related to the heat effect, because the Joule heating can decrease the magnetic anisotropy property. In addition to the out-of-plane magnetic field sweeping measurements, the anomalous Hall resistance was also measured by sweeping in-plane magnetic field under low (± ~1.9×10^6 A/cm^2), medium (± ~9.7×10^6 A/cm^2) and high (± ~15.4×10^6 A/cm^2) current density levels for Hf(1.5)|CoFeB(1.1)|MgO(2)|Ta(2) multilayer structure. Figure 4.18 show the R_{AHE} as a function of H_L measurement results for t_{Hf}=1.5 nm. As seen from the figure that there is no clear difference between R_{AHE}~H_L loops at low positive (black) and negative (red) electric current density (here the current density is around 1.9×10^6 A/cm^2). When the J_x is increased to +9.7×10^6 A/cm^2, the switching field is reduced significantly. On the other hand, the hysteresis behavior for the negative current (−9.7×10^6 A/cm^2) is slightly changed. At higher J_x values (±15.4×10^6 A/cm^2), the direction of current determines the trend of the R_{AHE}~H_L loop, which means that the current-induced spin-orbit torque controls the magnetization direction in the Hf(1.5)|CoFeB(1.1)|MgO(2)|Ta(2) structure.

The qualitatively similar R_{AHE}~H_z behaviors for t_{Hf}= 2.5, 3.5, 5.0, 7.0 and 10.0 nm in the Hf(*t*)|CoFeB(1.1)|MgO(2)|Ta(2) structure with t_{Hf}=1.5 nm as

discussed above have been observed in our transport experiments. The difference between these devices' transport measurement under out-of-plane magnetic fields is quantitatively different coercive field and Hall resistance values. Figure 4.19, Figure 4.21, Figure 4.23, Figure 4.25 and Figure 4.27 show the quantitatively differences between the devices. It is found that the coercive fields found by MOKE results (detail is given in Section 4.1.4) are much lower than the transport measurements. The reason of this difference might be related to the sensitive measurements of the transport experiment than the MOKE where the laser point is much larger than the device size. Therefore, we observed a difference in coercive field between the film and device form of the materials. Other difference is the anomalous Hall resistance, $\Delta R_{AHE} = \Delta V_{AHE}/I_x$ defined as the difference in the AHE resistance when the magnetization of the CoFeB layer is along the up and down. To compare the results of each device, we used low electric current density for all devices. The ΔR_{AHE} decreases with the increasing Hf layer thickness in the multilayer structure (see Figure 4.16). As we discussed before that the direct relation between anomalous Hall resistance and magnetization, the decrement of R_{AHE} is due to the change in the amount of current which flows in the CoFeB layer. It can be concluded that the larger current flow in the CoFeB layer results in the larger R_{AHE}.

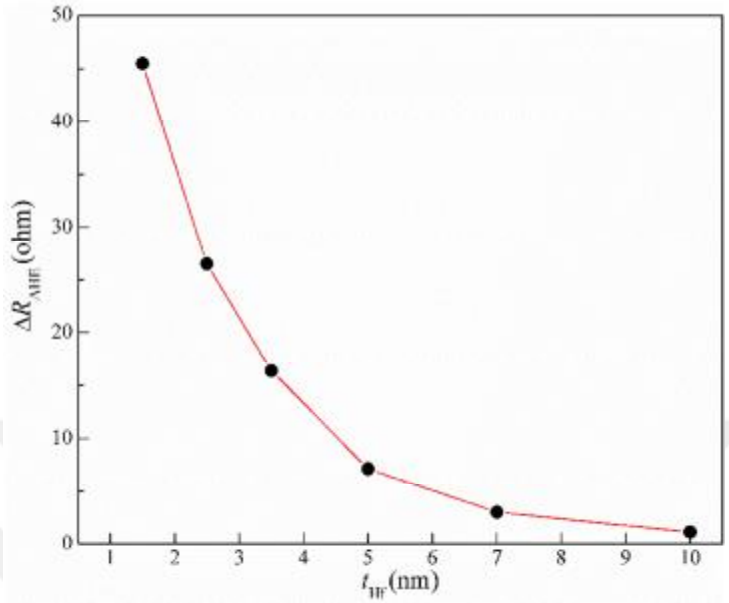


Figure 4.16. The ΔR_{AHE} as a function of Hf layer thickness in the Hf(t)|CoFeB|MgO|Ta multilayer structure.

On the other hand, although the similar behavior has also seen in the in-plane measurement for t_{Hf}= 2.5 (see Figure 4.20), 3.5 (see Figure 4.22) and 5.0 (see Figure 4.24) in the Hf(t)|CoFeB(1.1)|MgO(2)|Ta(2) structure with t_{Hf}=1.5 nm as discussed above, an un-expected behavior for t_{Hf}= 7.0 and 10.0 has been observed (see Figure 4.26 and Figure 4.28). Due to the unexpected behavior of these devices, we would like to explain them by comparing the data for t_{Hf}= 2.5, 7.0 and 10.0 nm as following.

Figure 4.20, Figure 4.26 and Figure 4.28 show the R_{AHE} as a function of in-plane magnetic field measurement results for t_{Hf}=2.5, 7.0 and 10.0 nm, respectively.

As can be seen from Figure 4.20, Figure 4.26 and Figure 4.28 at low current density, there is no clear difference between the R_{AHE}~H_L loops at low positive (black) and negative (red) electric currents (here the current density is ≈1.9×10^6 A/cm^2). When the J_x≈9.7×10^6 A/cm^2, the switching field is reduced

significantly, and in the negative electric current curve, the hysteresis behavior for t_{Hf}=2.5nm is slightly changed (see Figure 4.20). For t_{Hf}=7.0nm and 10.0 nm, however, there is still no clear difference at ±9.6×10^6 A/cm^2 (see Figure 4.26 and Figure 4.28). At higher J_x values (≈15.3×10^6 A/cm^2), the direction of current determines the trend of the R_{AHE}~H_L loop, which means that the current-induced spin-orbit torque controls the magnetization direction in the Hf(t)|CoFeB(1.1)|MgO(2)|Ta(2) structure for t_{Hf}=2.5 nm (see Figure 4.20). However, there is no clear difference in the R_{AHE}~H_L loop for t_{Hf}=7.0 nm even at a large current value (see Figure 4.26). Interestingly, a reverse sign R_{AHE}~H_L loop compared to t_{Hf}=2.5 nm was observed in t_{Hf}=10.0 nm at high current level (see Figure 4.28). Given that the sign of damping-like bulk spin-orbit-torque (DL-bulk SOT) cannot be changed by just increasing the heavy-metal layer thickness, this may indicate an additional mechanism in the present system to affect the DL-SOT sign. The detail of the DL-SOT will be discussed in the next section.

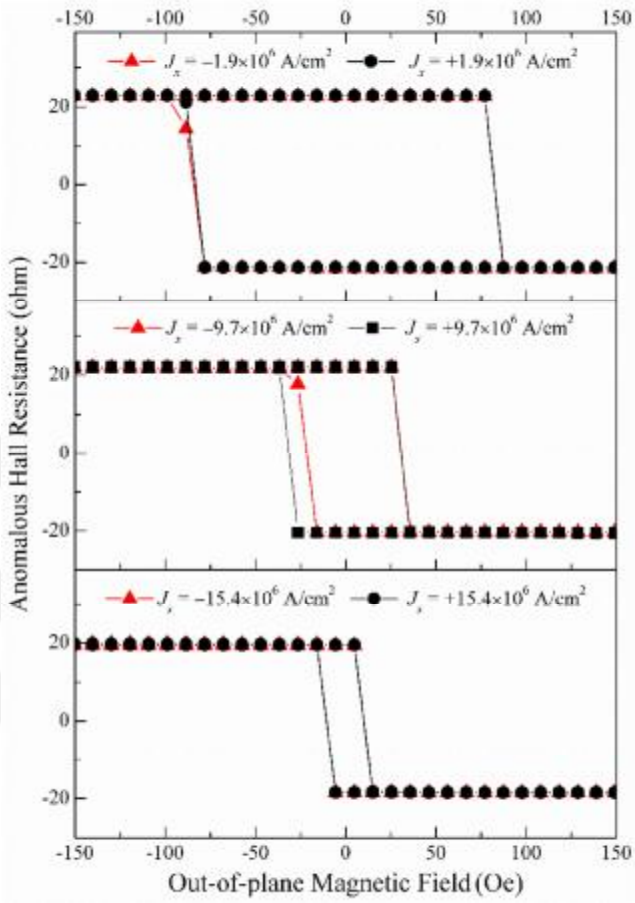


Figure 4.17. The anomalous Hall resistance as a function of out-of-plane magnetic field under several current density in Hf(1.5)|CoFeB(1.1)|MgO|Ta(2.0) multilayer structure.

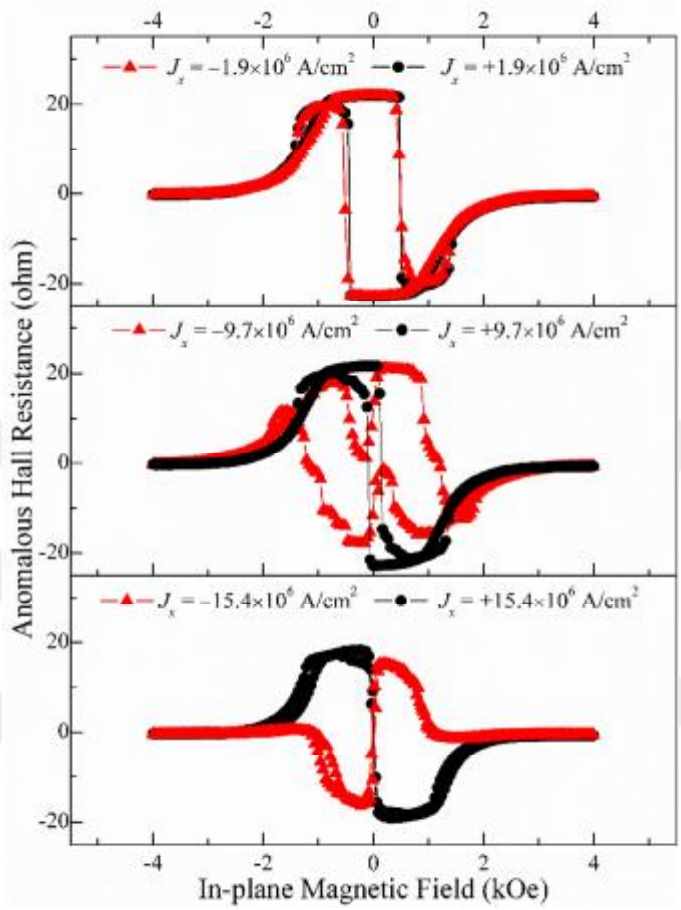


Figure 4.18. The anomalous Hall resistance as a function of in-plane magnetic field under several current density in Hf(1.5)/CoFeB(1.1)/MgO/Ta(2.0) multilayer structure.

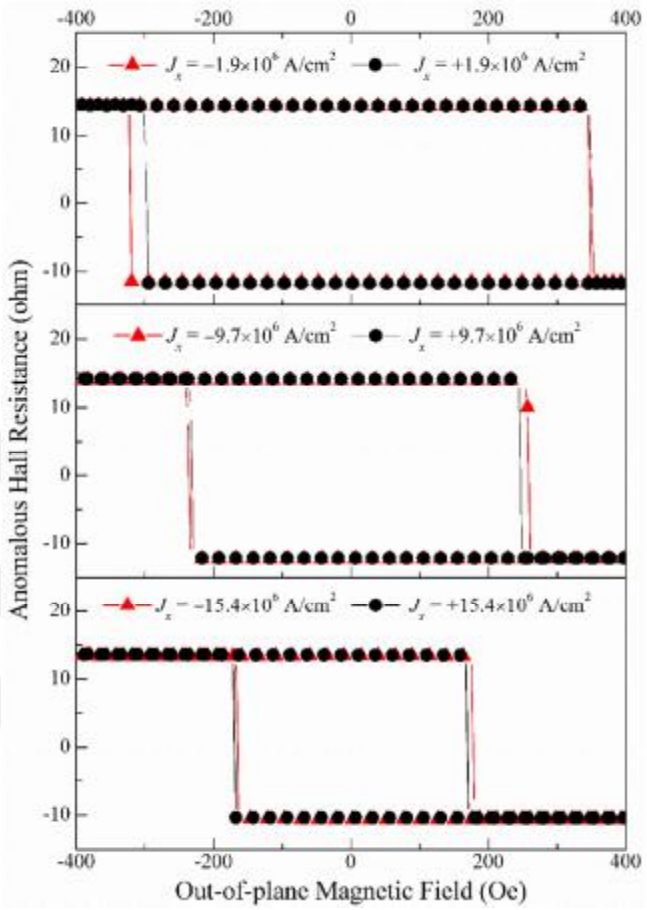


Figure 4.19. The anomalous Hall resistance as a function of out-of-plane magnetic field under several current density in Hf(2.5)|CoFeB(1.1)|MgO|Ta(2.0) multilayer structure.

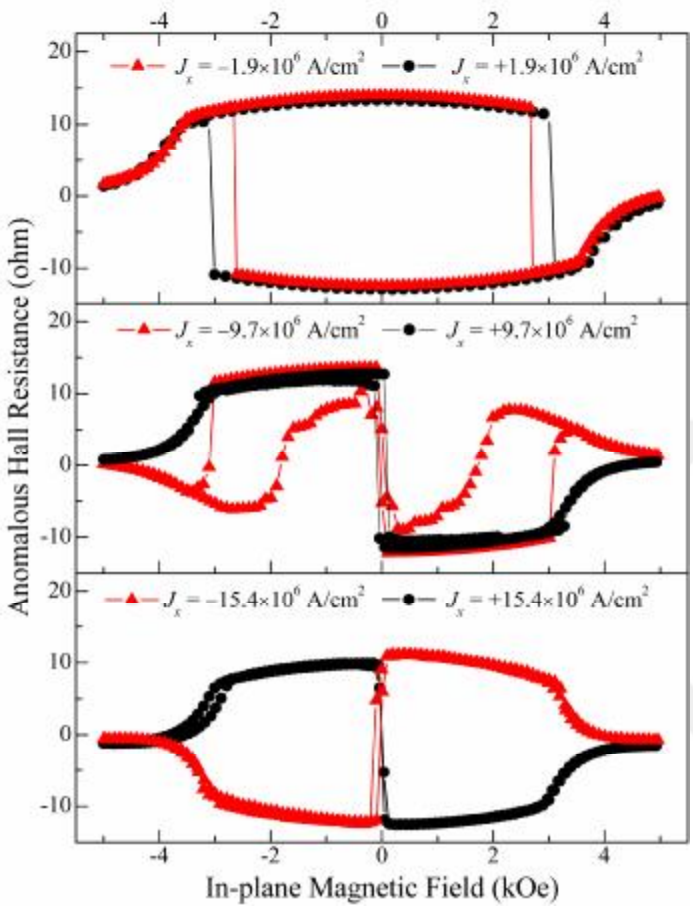


Figure 4.20. The anomalous Hall resistance as a function of in-plane magnetic field under several current density in Hf(2.5)|CoFeB(1.1)|MgO|Ta(2.0) multilayer structure.

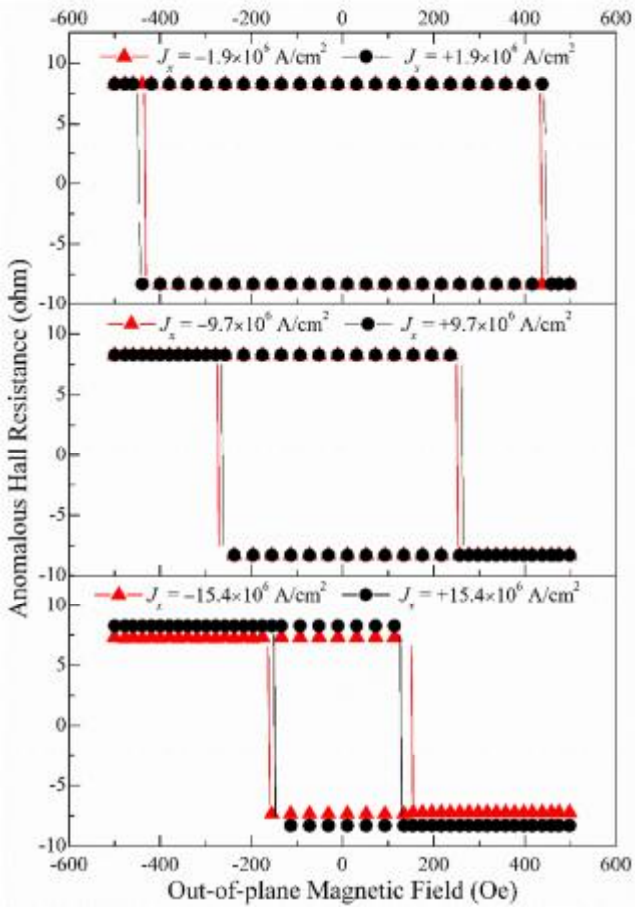


Figure 4.21. The anomalous Hall resistance as a function of out-of-plane magnetic field under several current density in Hf(3.5)|CoFeB(1.1)|MgO|Ta(2.0) multilayer structure.

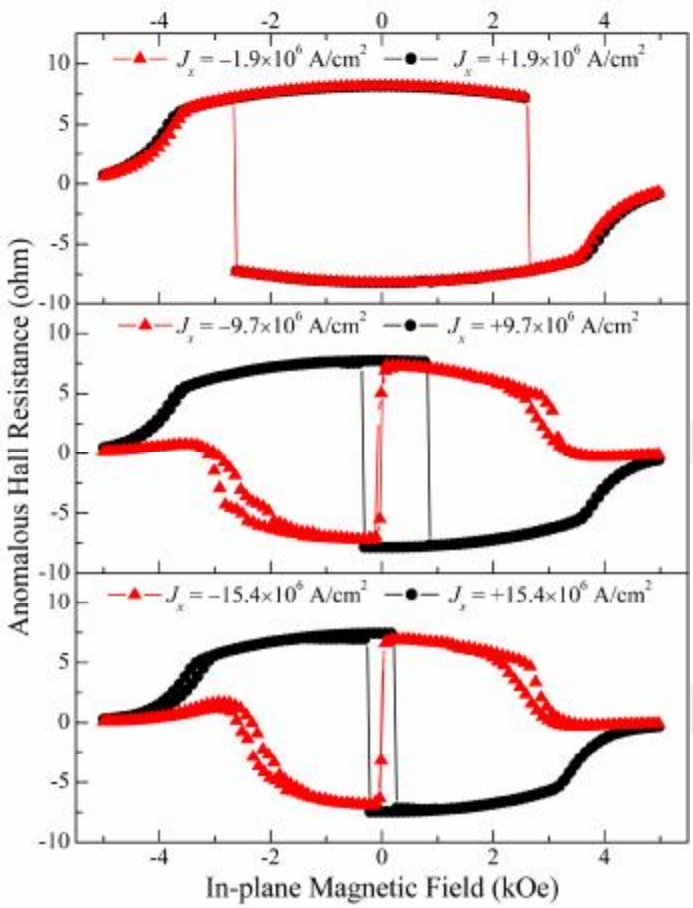


Figure 4.22. The anomalous Hall resistance as a function of in-plane magnetic field under several current density in Hf(3.5)|CoFeB(1.1)|MgO|Ta(2.0) multilayer structure.

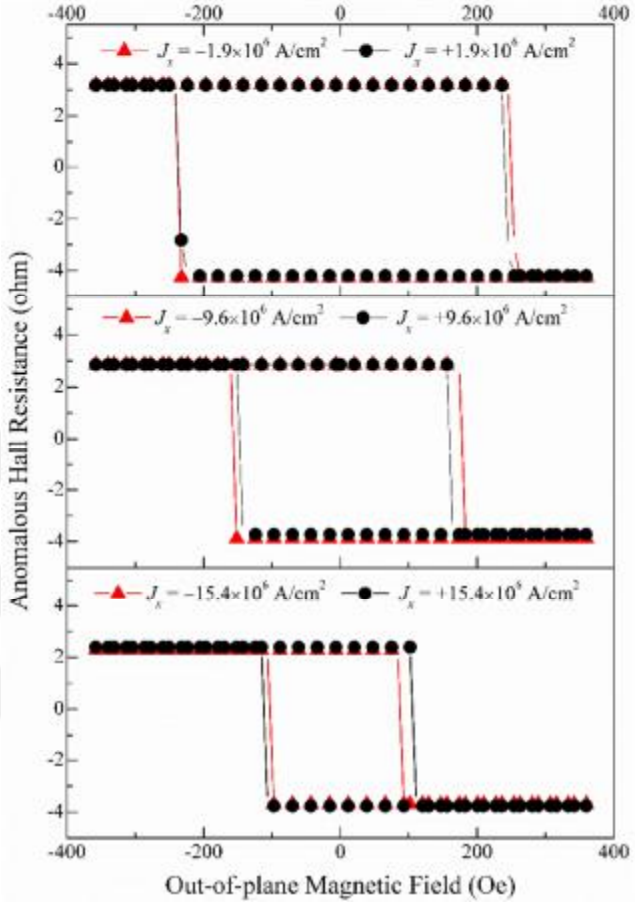


Figure 4.23. The anomalous Hall resistance as a function of out-of-plane magnetic field under several current density in Hf(5.0)|CoFeB(1.1)|MgO|Ta(2.0) multilayer structure.

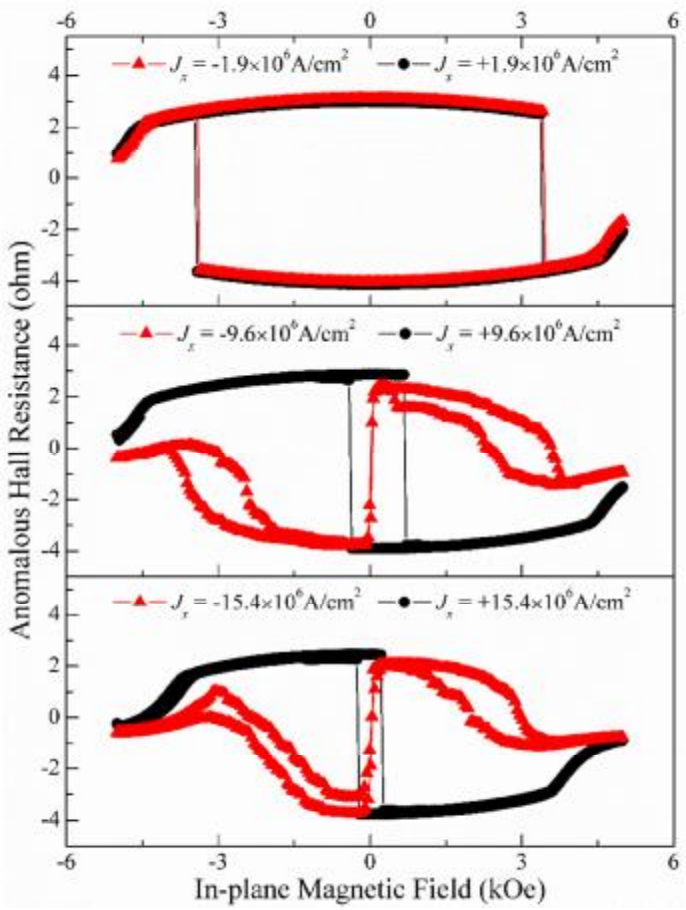


Figure 4.24. The anomalous Hall resistance as a function of in-plane magnetic field under several current density in Hf(5.0)|CoFeB(1.1)|MgO|Ta(2.0) multilayer structure.

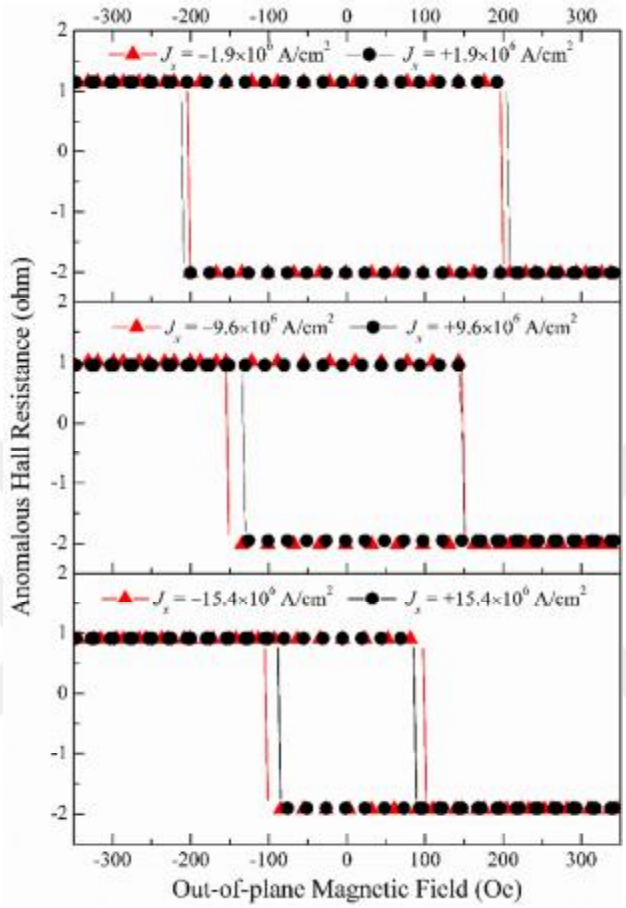


Figure 4.25. The anomalous Hall resistance as a function of out-of-plane magnetic field under several current density in Hf(7.0)|CoFeB(1.1)|MgO|Ta(2.0) multilayer structure.

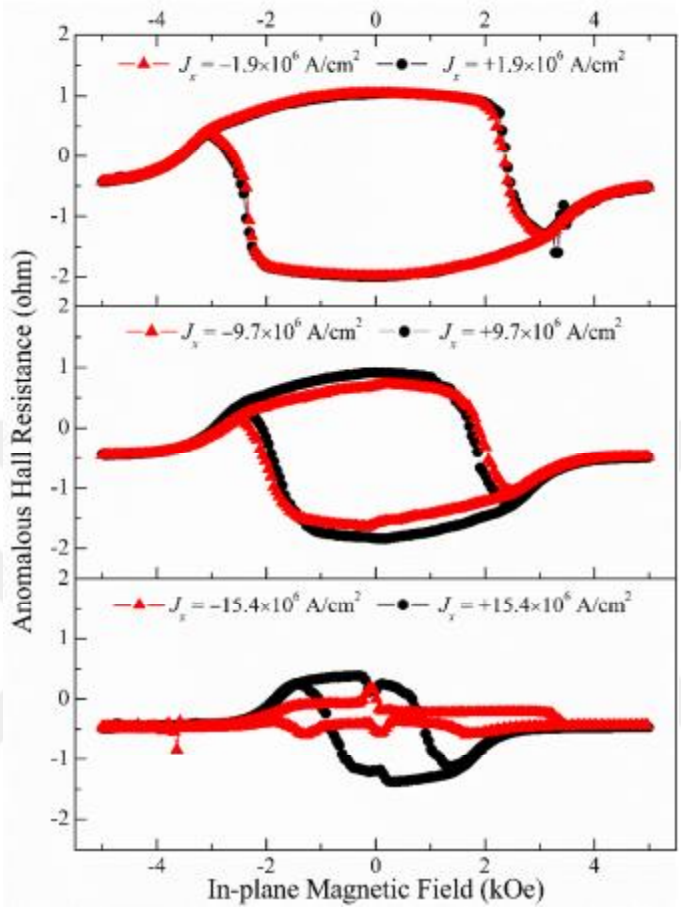


Figure 4.26. The anomalous Hall resistance as a function of in-plane magnetic field under several current density in Hf(7.0)|CoFeB(1.1)|MgO|Ta(2.0) multilayer structure.

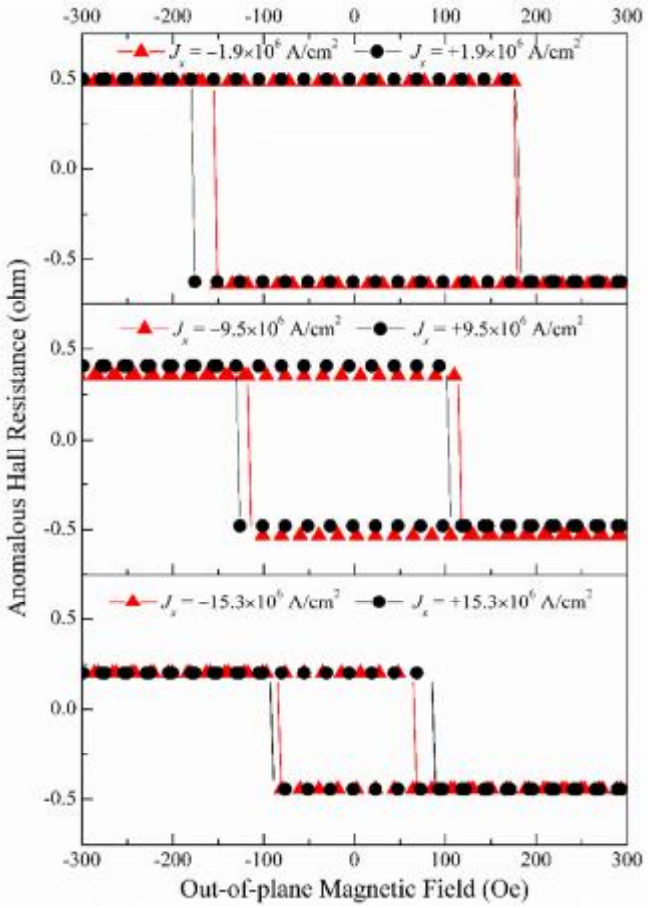


Figure 4.27. The anomalous Hall resistance as a function of out-of-plane magnetic field under several current density in Hf(10.0)|CoFeB(1.1)|MgO|Ta(2.0) multilayer structure.

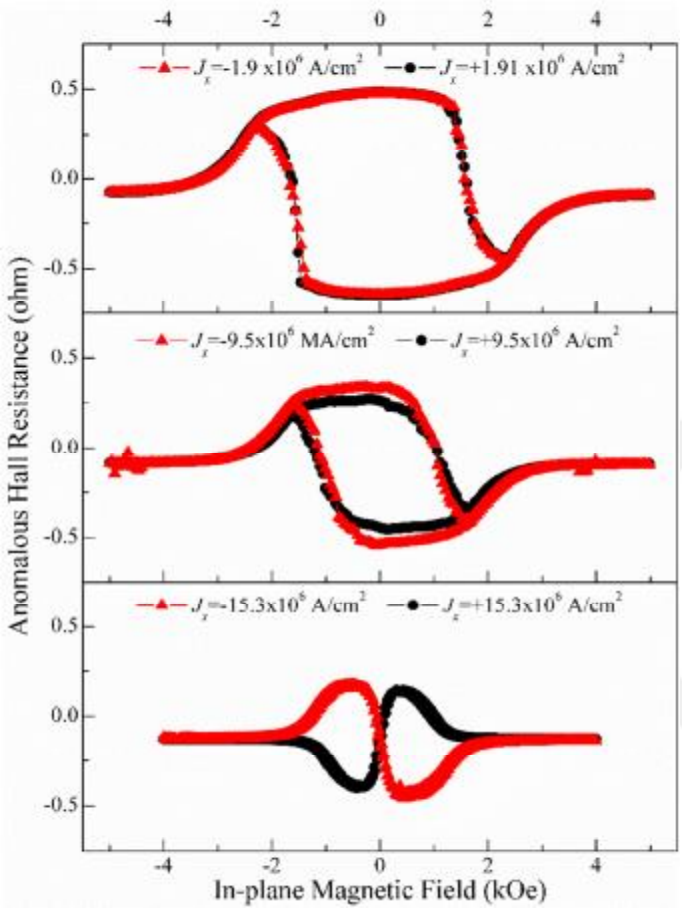


Figure 4.28. The anomalous Hall resistance as a function of in-plane magnetic field under several current density in Hf(10.0)|CoFeB(1.1)|MgO|Ta(2.0) multilayer structure.

4.1.6. Hf Layer Thickness Dependence on Damping-Like Spin-Orbit Torque in Hf(*t*)|CoFeB|MgO|Ta Multilayer Structures

To quantify the effect of the heavy metal layer thickness on damping-like spin–orbit torque, vector measurements were done, where we used a small amplitude sinusoidal a.c. with a frequency of 154 Hz through the Hall bars (along $\pm x$) of each device. More information on the vector measurement can be found in Chapter 3.

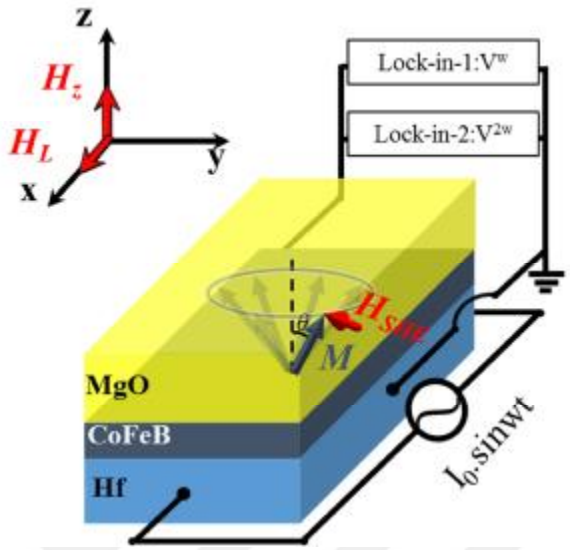


Figure 4.29. The schematic illustration of the multilayer structure and vector measurement configuration under sinusoidal bias current.

The current-induced magnetization switching is enabled by the damping-like SOT. The normalized first, V^w and second harmonic voltage, V^{2w} as a function of the longitudinal magnetic field (same direction with current), are shown in Figure 4.30 for different thicknesses of the heavy metal layer. The dip and peak points in the second harmonic signals correspond to the effective fields of the torque on the magnetization. The V^{2w} in Figure 4.30, the peak (dip) points are at the positive (negative) magnetic fields for the thickness of Hf up to 7.0 nm. However, an unexpected behavior is observed in the t_{Hf}=8.5 nm sample, where multiple dip and peak points are seen for both positive and negative fields. Once the thickness of Hf reaches 10.0 nm, the peak (dip) point changes from the positive (negative) to the negative (positive) magnetic field axis.

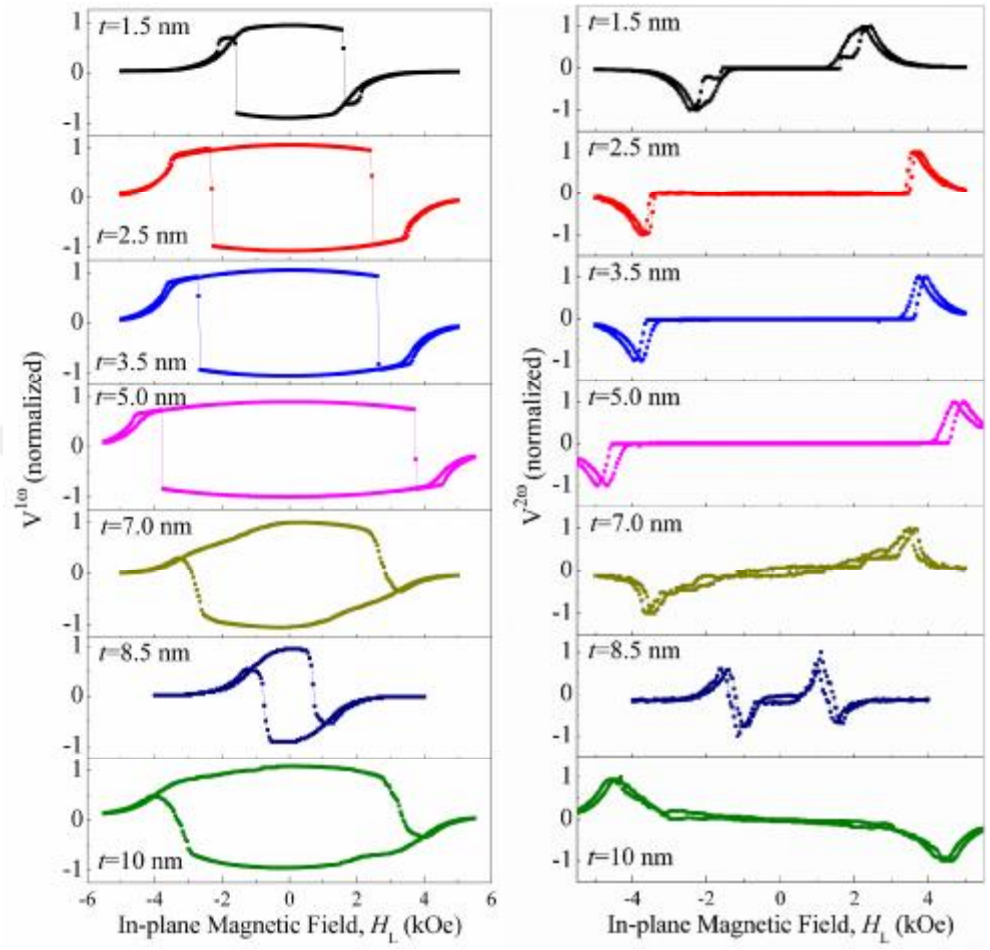


Figure 4.30. The first and second harmonic voltage as a function of in-plane longitudinal magnetic field for various Hf layer thickness in Hf(t)|CoFeB|MgO|Ta multilayer structure (t_{Hf} = 1.5, 2.5, 3.5, 5.0, 7.0, 8.5 and 10 nm).

The polarization of V^{2w} shows that the sign of the damping-like SOT is changed when the thickness of the Hf layer is increased. This may be understood in terms of a competition between the damping-like SOT and an unknown mechanism with an opposite sign. Based on the experimental data, we calculated the strength of the damping-like SOT-induced effective magnetic field expressed as β_{DL} =

$\Delta H_{DL}/J_x$ where J_x is the current density and ΔH_{DL} is the damping-like SOT-induced magnetic field found for both magnetization states (M_z^{Up} and M_z^{Down}). The calculation method of ΔH_{DL} was explained in Chapter 3. The Hf layer thickness dependence of β_{DL} is shown in Figure 4.31, where the β_{DL} increases first with the thickness of Hf, as expected. However, at a critical Hf thickness, it starts to reduce with increasing thickness of Hf. Finally, the sign of DL-SOT changes once the thickness of Hf is increased above 7.0 nm. A similar reduction in the DL-SOT was observed by *Torrejon et al* where the thickness of Hf was increased up to 6.0 nm; however, the change of the torque sign was not observed within the thickness range of that work (Torrejon et al., 2014).

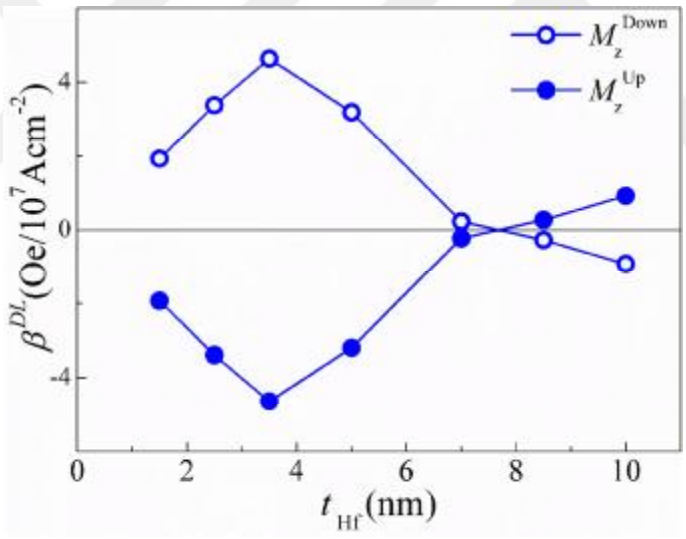


Figure 4.31. The damping-like spin-orbit torque dependence Hf layer thickness for both M_z^{Up} and M_z^{Down} states in Hf(t)|CoFeB|MgO multilayer structure (t_{Hf} = 1.5, 2.5, 3.5, 5.0, 7.0, 8.5 and 10 nm).

It is believed that while the thickness of the heavy metal as a source of creating spin-current by bulk spin-Hall effect contribution cannot change the sign of damping-like SOT due to the linear dependence of spin current on the thickness

of the heavy metal, $J_s(t) \approx 1 - sech\left({}^{t_{HM}}/_{\lambda_{sd}}\right)$ where t_{HM} is the thickness of heavy-metal and λ_{sd} is the spin-diffusion length, the magnitude of SOT can be affected by changing the thickness of the heavy metal, ferromagnets, and insulating layer. Figure 4.32 indicates a modelling of polarization of spin current as a function of heavy metal layer thickness. As seen from the figure that the polarized spin-currents increases with the increasing heavy-metal layer thickness and then saturated after the critical thickness of heavy metal which is limited to the spin-diffusion length. But, there are limited number of studies which show sign reversal behavior in damping-like SOT(Yu et al., 2014; Kim et al., 2013; Qiu et al., 2015).

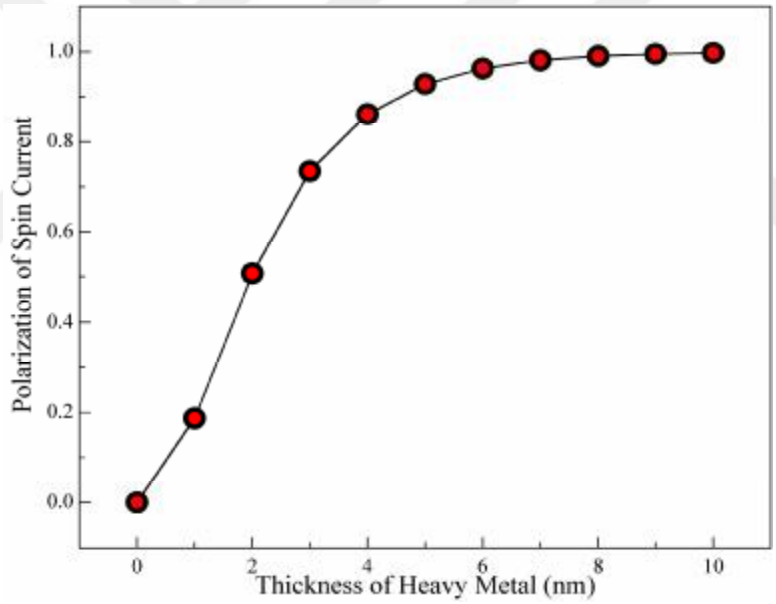


Figure 4.32. The modelling of polarization of spin current as a function of heavy metal layer thickness.

In addition to interfacial and bulk contributions from the HM, recent experimental and theoretical studies have shown that oxygen content in ferromagnetic layer, the oxide layer, ferromagnetic layer thickness, and surface

roughness can contribute to the SHE (Kim et al., 2013; Qiu et al., 2015; Akyol et al., 2015; Zhou et al., 2015; Fan et al., 2014). If the interfacial SOC has an opposite sign to the bulk spin-Hall contribution, the effective damping-like SOT can be changed by the interfacial SOC contribution. Therefore, the competition of these two terms in the multilayer system can determine the sign of the effective damping-like SOT. In the light of these possible scenarios, we evaluate each as outlined below.

Among the possible contributions to the SOT, in the present multilayer structures, the oxygen content of the interface, which is one possible reason of sign-reversal (Qiu et al., 2015), is expected to be the same in all samples. Another possible reason is interface scattering and interfacial spin-orbit coupling previously studied at the surface of a non-heavy metal thin film, such as Cu (Zhou et al., 2015; Wang et al., 2013; Hayden et al., 2013). The spin-orbit coupling at a rough interface results in spin-Hall conductivity due to the potential gradient at the interface. Zhou et al. theoretically showed that Cu thin films with rough surface can create a spin-Hall effect itself, and the spin-Hall angle (%0.35) is comparable with Au, which is known as a heavy metal (Zhou et al., 2015). In addition, they showed that the spin-Hall angle can be increased with increasing roughness. In the present case, we observed thickness dependent surface segregation by atomic force microscopy images, where the roughness increases with Hf thickness. This can contribute to interface spin-orbit coupling. The interface SOC thus drives a torque on the magnetization which is opposite in sign to the bulk SOC. The spin-Hall angle coming from the interface roughness is larger for rough surfaces. Since the back-scattering electrons from the uniform interface cannot be large as in a rough interface, the bulk-SOT contribution can be dominant in the whole system. The bulk-SOT can be enhanced by the increasing thickness of heavy-metal layer, limited to a couple of nanometers due to the low spin diffusion length of heavy-metals, as explained by the above relation. In a rough or asymmetric structure, the interface-SOT can be emerged because of interfacial effective electric field and

back-scattered electrons. The effective SOT of these bulk and interfacial torques can be either enhanced or weakened. One can thus presume that the observation of sign reversal in DL-SOT in thick Hf samples may in part be related to the larger surface roughness in those samples.

4.1.7. Current-Driven Magnetization Switching by Spin-Orbit Torques in Hf(*t*)|CoFeB|MgO|Ta Multilayer Structures

The effect of the sign reversal behavior was worked on current-driven magnetization switching in the presence of an in-plane magnetic field to break the symmetry (Liu et al., 2012; Yu et al., 2014; Liu et al., 2012; Garello et al., 2013; Akyol et al., 2015). Figure 4.33a-b show a schematic illustration of the damping-like spin-orbit torque on magnetization; a) without and b) with longitudinal external magnetic field. In the absence of longitudinal field case, the effective DL-SOT are same for all magnetization states means the effective torque is zero. Once the longitudinal field is applied to the device (see Figure 4.33b), the magnetization switching can be performed by breaking the symmetry. Therefore, the longitudinal external magnetic field is needed to switch the magnetization from up to down or vice versa.

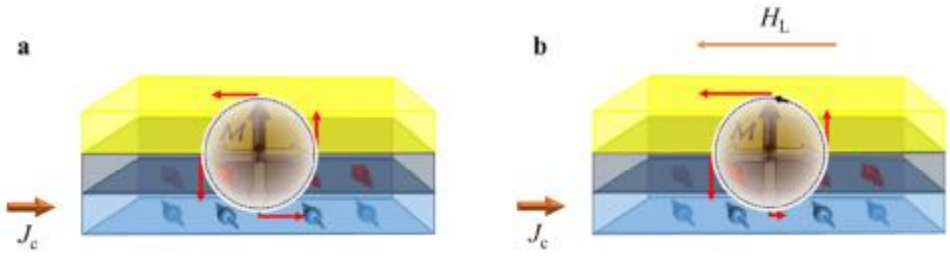


Figure 4.33. The damping-like spin-orbit torque on magnetization a) without and b) with longitudinal external magnetic field.

The anomalous Hall resistances, means out-of-plane magnetization, M_z because of direct relation between R_{AHE} and M_z, as a function of driven electric current density are shown in Figure 4.34a-b, Figure 4.35a-b, Figure 4.36a-b, Figure 4.37a-b and Figure 4.38a-b for t_{Hf}=1.5, 2.5, 3.5, 5.0 and 10.0 nm, respectively. The magnetic switching direction is in the clockwise (counter-clockwise) for the thickness of Hf up to 7.0 nm under positive (negative) external magnetic field. For t_{Hf}=7.0 and 8.5 nm, there is no full magnetization switching observed. However, an opposite switching behavior is observed for t_{Hf}=10.0 nm, as expected.

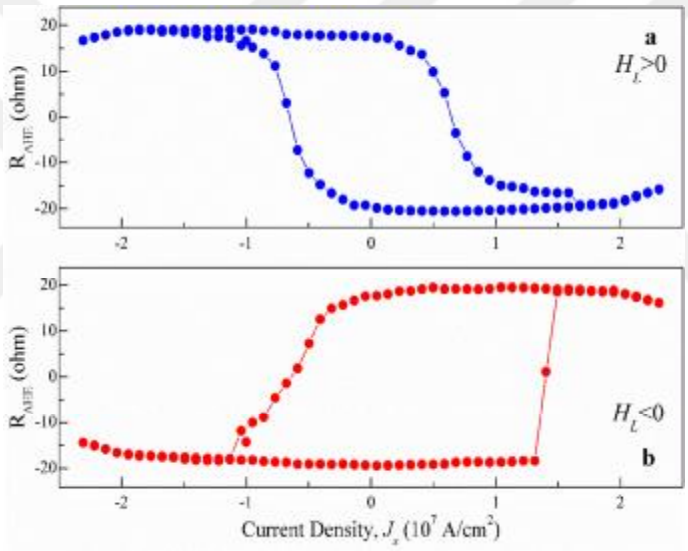


Figure 4.34. The current-driven magnetization switching by spin-orbit torques in Hf(1.5)|CoFeB(1.1)|MgO|Ta(2.0) multilayer structure by applying a) positive and b) negative longitudinal external field to break the symmetry.

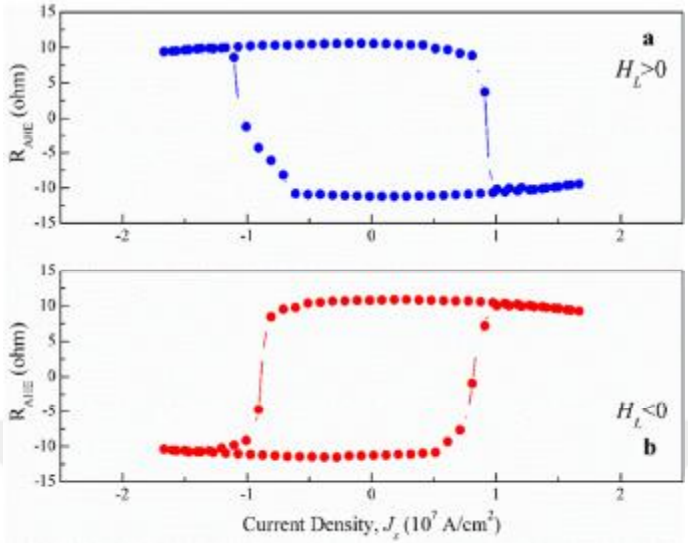


Figure 4.35. The current-driven magnetization switching by spin-orbit torques in Hf(2.5)|CoFeB(1.1)|MgO|Ta(2.0) multilayer structure by applying a) positive and b) negative longitudinal external field to break the symmetry.

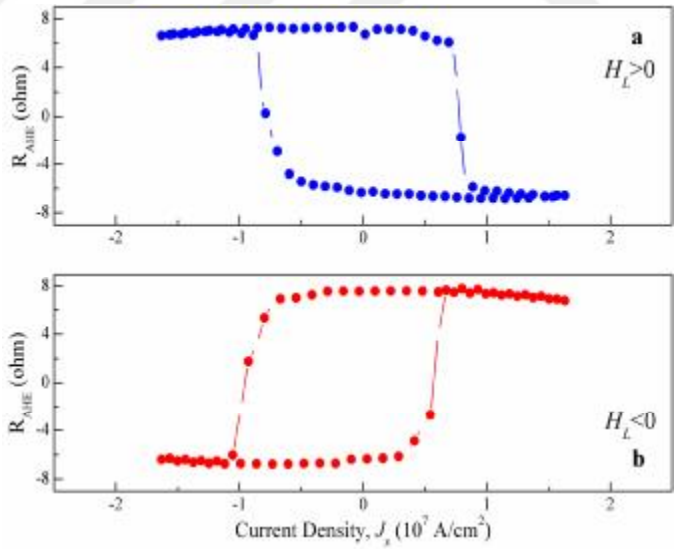


Figure 4.36. The current-driven magnetization switching by spin-orbit torques in Hf(3.5)|CoFeB(1.1)|MgO|Ta(2.0) multilayer structure by applying a) positive and b) negative longitudinal external field to break the symmetry.

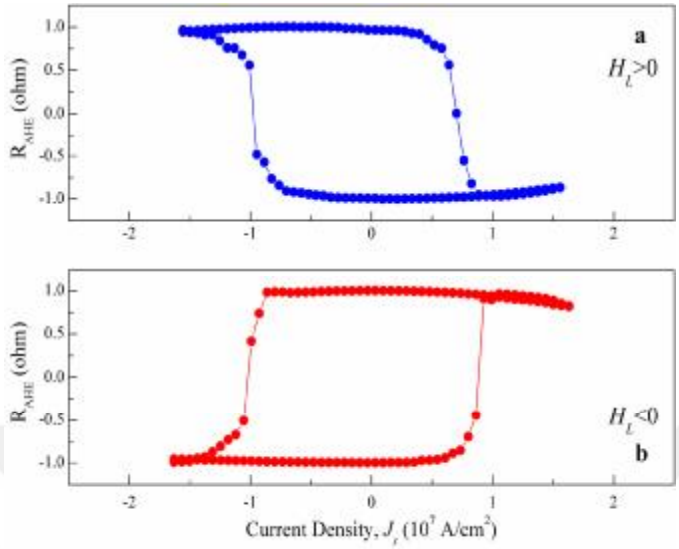


Figure 4.37. The current-driven magnetization switching by spin-orbit torques in Hf(5.0)|CoFeB(1.1)|MgO|Ta(2.0) multilayer structure by applying a) positive and b) negative longitudinal external field to break the symmetry.

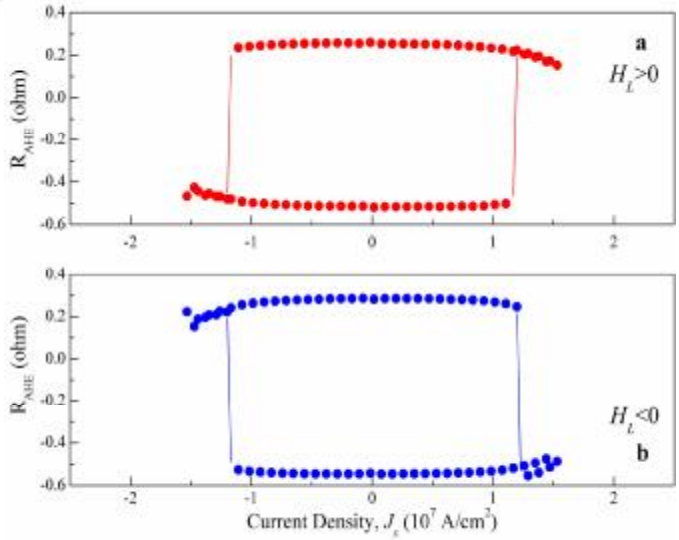


Figure 4.38. The current-driven magnetization switching by spin-orbit torques in Hf(10.0)|CoFeB(1.1)|MgO|Ta(2.0) multilayer structure by applying a) positive and b) negative longitudinal external field to break the symmetry.

In conclusion, we have systematically worked on the effect of heavy-metal layer thickness on structural, magnetic and spintronic properties in Hf(*t*)|CoFeB(1.1)|MgO(2.0)|Ta(2.0) (*t*=0.5, 0.75, 1.0, 1.5, 2.5, 3.5, 5.0, 7.0, 8.5 and 10.0 nm) multilayer structures. The experimental results show that the heavy-metal layer thickness is important for both structural and magnetic properties of the multilayer films, as well as spintronic properties of their device form. In the light of these experimental results, we continue to investigate the effect of other factors on spintronic parameters as following section.

4.2. Oxide Layer Effect on Magnetic, Transport and Spintronic Properties in Hf|CoFeB|MgO and Hf|CoFeB|TaO_x Multilayer Structures

The tunneling layer (insulator layer) in magnetic tunnel junctions has crucial roles in terms of energy consumption, density and sensitivity of the devices. In current-driven SOT-based memory devices, several works have addressed the effect of the heavy metal layer, ferromagnetic layer, and their interface on the resulting SOTs in such structures. Different heavy metal materials such as Ta, Pt, and W (Liu et al., 2012; Liu et al., 2012; Miron et al., 2011; Mihai Miron et al., 2010; Emori et al., 2013; Pai et al., 2012; Garello et al., 2013; Pai et al., 2014) and their thickness dependence, as well as ferromagnetic layers such as Co and CoFeB (Pai et al., 2012; Kim et al., 2013) or the effect of the interface between the heavy metal and the ferromagnetic layer have been worked intensively (Liu et al., 2012; Fan et al., 2013). So far, however, there has been little attention for studying the effect of the oxide layer (OX) on the SOTs in heavy-metal|ferromagnet|oxide (HM|FM|OX) multilayers (Yu et al., 2014; Liu et al., 2012). In this section, we investigate the oxide layer effect on current-driven SOTs in perpendicularly magnetized Hf|CoFeB|MgO and Hf|CoFeB|TaO_x multilayers. It is shown that the choice of the insulator material significantly affects both the field-like (FL) and damping-like (DL) SOT terms. The film stacks used in this section are labelled as

Sample I and Sample II for Hf(5.0)|$Co_{20}Fe_{60}B_{20}$(0.8)|MgO|TaO_x and Hf(5.0)|$Co_{20}Fe_{60}B_{20}$(0.8)|TaO_x (thickness in nanometers, and the composition of the CoFeB in atomic percent), respectively. The multilayer film deposition process as same as previous samples. The detail on growing process can be found in Chapter 3. Here, the oxidation of Ta on top of the CoFeB layer is different than the traditional deposition process. The TaO_x layer was formed by oxidizing a 1.5 nm Ta layer under an O_2/Ar plasma. In the case of MgO, a 5.0 nm MgO film was grown by rf-sputtering from an MgO target and a thin TaO_x layer was then grown on top of the MgO for protection. After the deposition process, we annealed both samples to improve crystallinity, which also enhanced the perpendicular magnetic anisotropy. The films were patterned into to 20 μm×130 μm Hall bar structures by photo-lithography and dry-etching techniques, as explained in Chapter 3.

4.2.1. Oxide Layer Effect on Magnetic Anisotropy and Transport Properties in Hf|CoFeB|MgO and Hf|CoFeB|TaO_x Multilayer Structures

Measurements of the dependence of the anomalous Hall effect resistance, R_{AHE} on out-of-plane applied magnetic field, H_z were used to identify the equilibrium magnetization direction of the devices, given the proportionality between R_{AHE} and the perpendicular component of magnetization, M_z in the CoFeB layer. For direct current measurements, we used the same experimental configuration in both samples, which is given in Figure 4.39a (also showing the device structure). Here, the bias current was applied along the *x*-axis and the voltage generated by the AHE was measured along the *y*-axis.

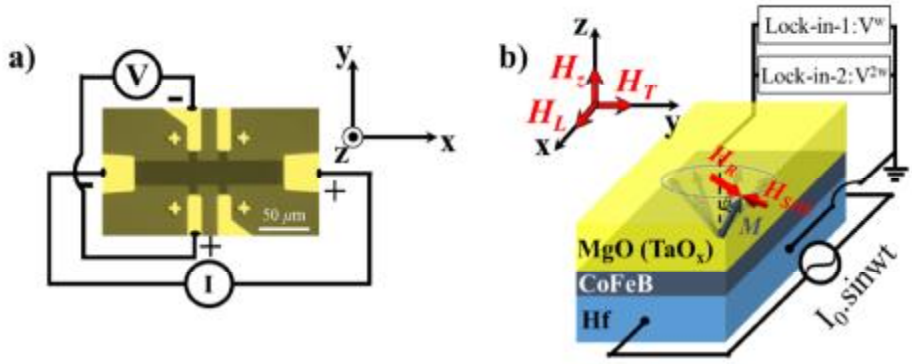


Figure 4.39. a) Optical graph of one device and the dc experimental configuration. b) The film structure of Hf|CoFeB|MgO(TaO_x) multilayer with ac electric current. H_R corresponds to the Rashba-field, H_{SHE} denotes the equivalent field due to the spin-Hall-effect, and M represents the magnetization direction of the CoFeB layer.

Figure 4.40a-b show R_{AHE} as a function of H_z under +1 mA bias current for Sample I and Sample II, respectively. The magnetization direction, M_z^{Up}(M_z^{Down}) is labeled by arrows corresponding to R_{AHE}<0 (R_{AHE}>0). As can be seen from these two figures, the magnetic anisotropy in both samples is perpendicular since the square shape of R_{AHE} versus H_z loop indicates the magnetization orientation in the out-of-plane is in easy-axis. The coercive fields in both cases seem to very similar that those are ~21 and ~22 Oe for Sample I and Sample II, respectively. Because the coercive field is related to the effective magnetic moments in ferromagnetic layer in the multilayer structure, we can result that the CoFeB layer in both films are formed similar. However, the magnetic dead layer thickness for the multilayer films was determined to be 0.17 and 0.24 nm for Sample I and Sample II, respectively. The way of determination dead layer thickness will be discussed detail in Section 4.3.1. This small difference in magnetic dead layer thickness may be attributed to a combination of the different oxidation process used for the MgO and TaO_x layers, as well as due to damage induced by the initial Ta deposition itself, in agreement with the previous reports on large magnetic dead layers (up to 0.5 nm) in Ta-capped CoFeB (Ikeda et al., 2010; Worledge et al., 2011). The

saturation magnetizations were found to be nearly identical at 1210 and 1170 emu/cm^3 for Sample I and Sample II, respectively.

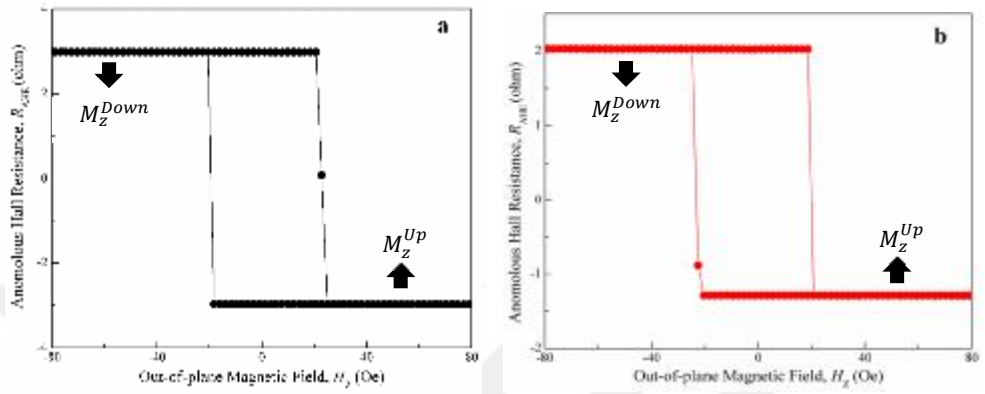


Figure 4.40. Anomalous Hall resistance, R_{AHE} as a function of the out-of-plane magnetic field, H_z in a) Hf|CoFeB|MgO and b) Hf|CoFeB|TaO_x multilayers.

Figure 4.41a-b show R_{AHE} as a function of longitudinal magnetic field, H_L under +1 mA bias current for Sample I and Sample II, respectively. As seen from the figures, whereas the magnetic anisotropy field can be found for Sample II because of the observing saturation in anomalous Hall resistance at high magnetic fields, it is not possible to found for Sample I because of the magnetic field limitation of our probe station. It can be concluded that the magnetic anisotropy in MgO-capped sample is higher than that of TaO_x-capped sample. More explanation and results on the CoFeB layer thickness dependence of magnetic property for MgO and TaO_x-capped structures will be discussed in Section 4.3.1.

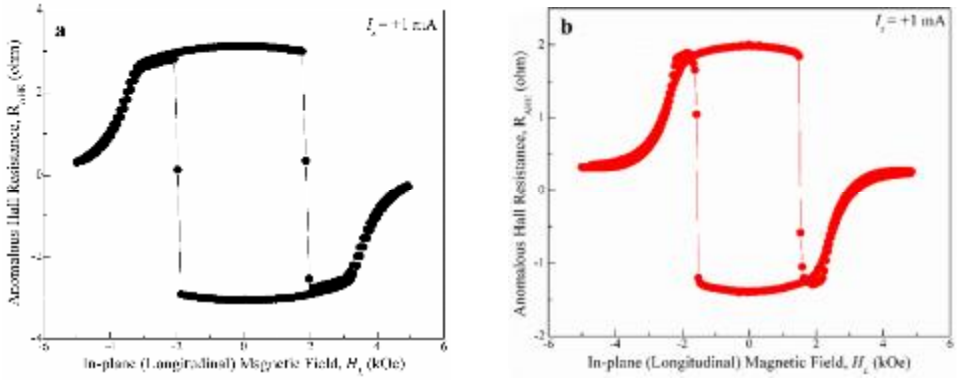


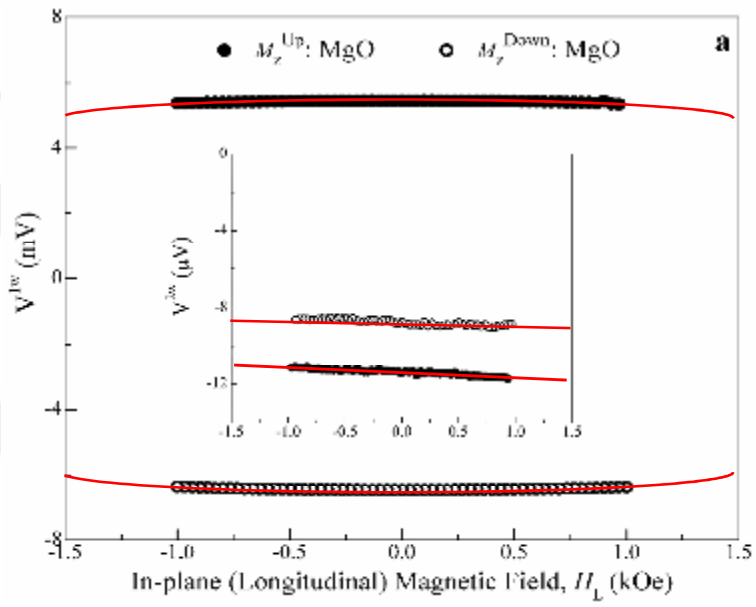
Figure 4.41. Anomalous Hall resistance, R_{AHE} as a function of the in-plane (longitudinal) magnetic field, H_L in a) Hf|CoFeB|MgO and b) Hf|CoFeB|TaO_x multilayers.

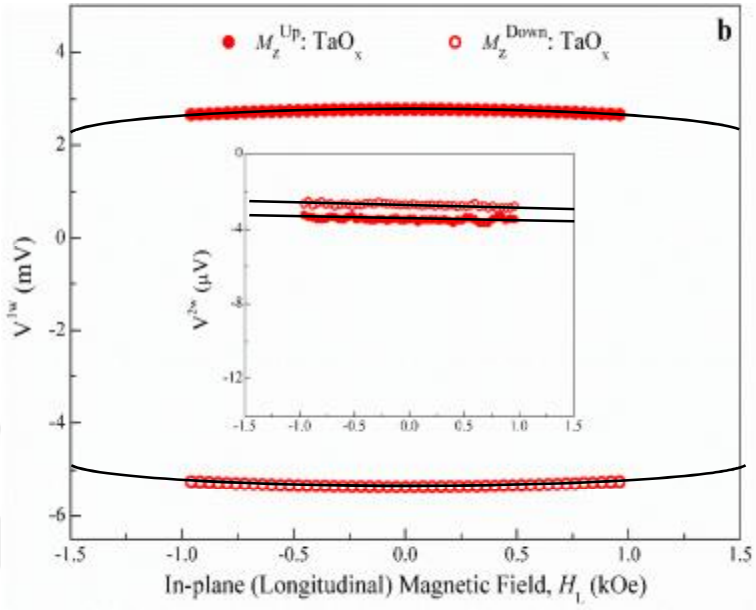
4.2.2. Oxide Layer Effect on Spin-Orbit Torques in Hf|CoFeB|MgO and Hf|CoFeB|TaO_x Multilayer Structures

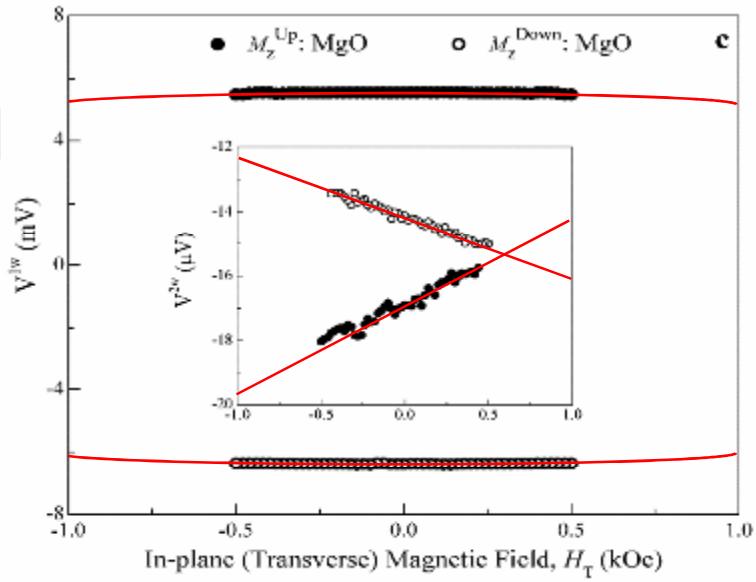
We used the vector measurement technique (Kim et al., 2013; Pi et al., 2010) to quantify the current-induced effective fields corresponding to the damping-like and field-like SOTs, using a sinusoidal current with a frequency of 100 Hz through the hall bars (along ±*x*), and measuring the Hall voltage (along ±*y*) using two lock-in amplifiers. The set-up of the vector measurement is illustrated in Figure 4.39.b. The first and second lock-in amplifiers were used to measure the first harmonic, V^{1w} and second harmonic voltage, V^{2w}, respectively. The in-plane magnetic field was applied along the *x* (longitudinal field, H_L) and *y* (transverse field, H_T) directions to quantify the longitudinal SOT-induced effective field (ΔH^{DL}), which is generally referred to as damping-like torque, and the SOT-induced transverse effective field (ΔH^{FL}), which is associated with the field-like torque, for both samples. First, we measured the V^{1w} and V^{2w}, sweeping the H_L and H_T fields at different bias currents to calculate ΔH^{DL} and ΔH^{FL} using the equation of (3.16).

The first-harmonic voltages, V^{1w}, as a function of the longitudinal, H_L (transverse, H_T) external magnetic field in Sample I and Sample II are shown in Figure 4.42a-b (Figure 4.42c-d), respectively. The insets of each figure correspond

to the second-harmonic voltage, V^{2w}, as a function of the external magnetic field for each device. First (second) harmonic curves were fitted using quadratic (linear) fitting curves to determine the SOT-induced effective magnetic fields using Eq. (3.16). The detail of the SOT effective field calculation has been given in Chapter 3.




b
M_z^{Up}: TaO_x
M_z^{Down}: TaO_x
V^{1w} (mV)
V^{2w} (μV)
In-plane (Longitudinal) Magnetic Field, H_L (kOe)


c
M_z^{Up}: MgO
M_z^{Down}: MgO
V^{1w} (mV)
V^{2w} (μV)
In-plane (Transverse) Magnetic Field, H_T (kOe)

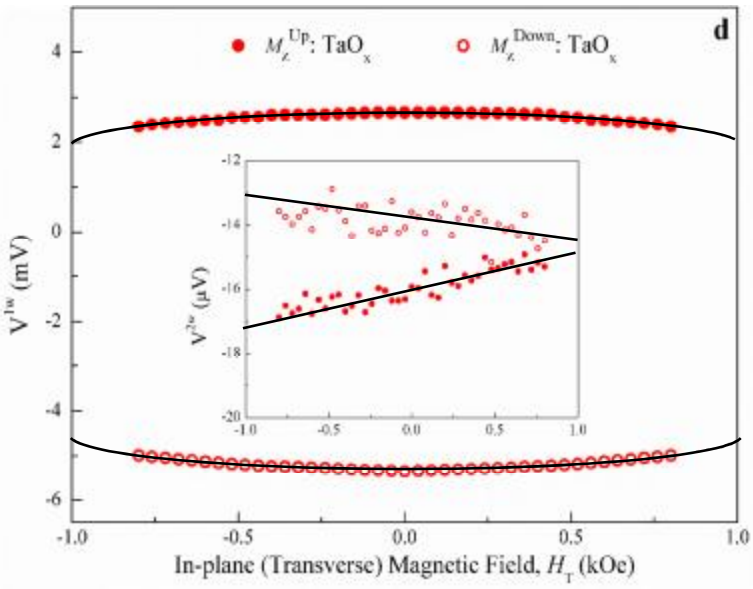
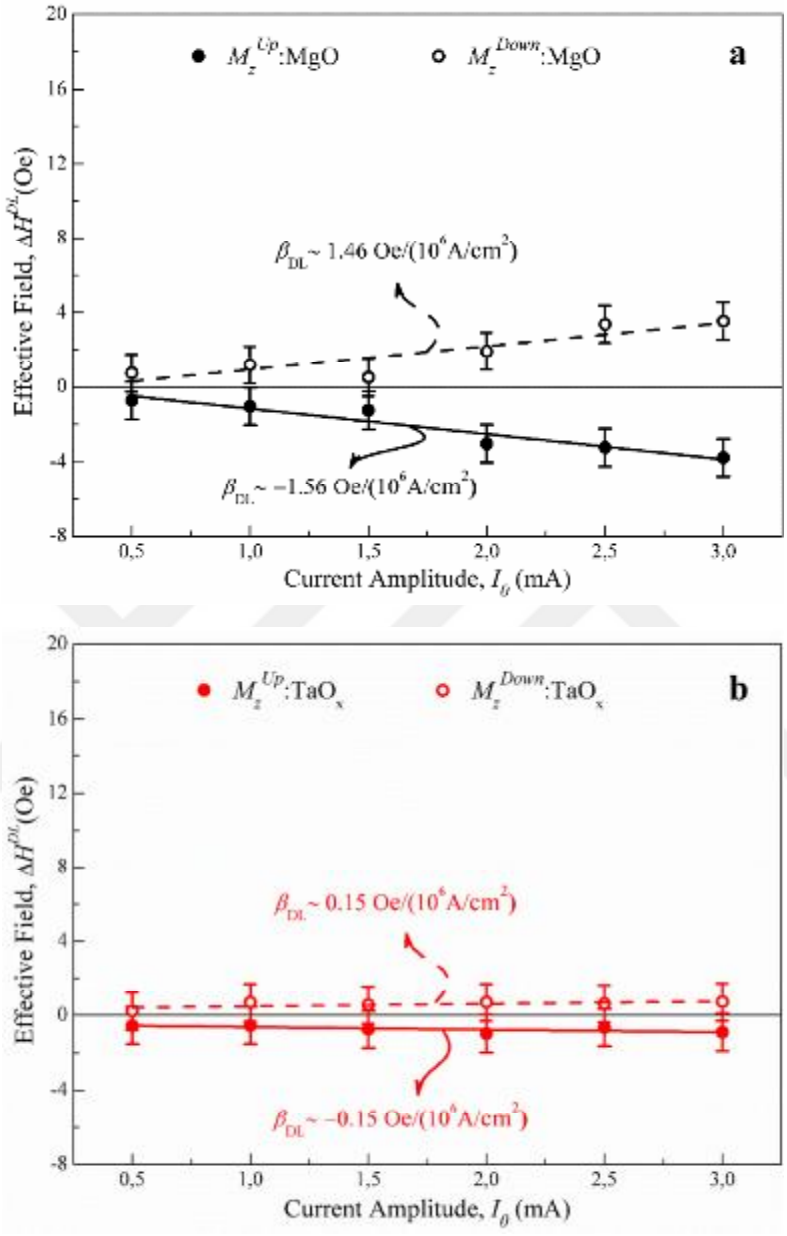


Figure 4.42. First-harmonic signals, V^w as a function of in-plane magnetic field applied to the device in longitudinal, H_L (transverse, H_T) a) (c) Sample I and b) (d) Sample II and transverse direction, H_T. Inset of each figure corresponds to the second-harmonic signal, V^{2w} as a function of applied field for each sample. Solid red (solid black) and open red (open black) symbols represent the signal coming from the magnetization states of M_z>0, up and M_z<0, down, respectively.

Next, we calculated the effective magnetic field corresponding to the damping-like SOT, which is plotted as a function of the input bias current amplitude (I_0) of the ac sinusoidal signal, for both devices in Figure 4.43a-b. We determined the SOT fields for both magnetization states separately, which are along the positive (negative) z direction, i.e. M_z^{Up} (M_z^{Down}). While the trend of ΔH^{DL} is linear with the bias current amplitude for both M_z^{Up} and M_z^{Down} cases, the sign is opposite for the different magnetization states, as expected. One can thus express the effective field as $\Delta H^{DL} = \beta_{DL} J_x$, where J_x is the applied current density. The parameter β_{DL} (i.e., the slope of the fitted curves) in Figure 4.43a-b measures the strength of the SOT-induced damping-like effective field per unit

current density. β_{DL} was found to be $-1.56\ Oe/10^6 Acm^{-2}$ ($1.46\ Oe/10^6 Acm^{-2}$) for M_z^{Up} (M_z^{Down}) in the Hf|CoFeB|MgO multilayer and $-0.15\ Oe/10^6 Acm^{-2}$ ($0.15\ Oe/10^6 Acm^{-2}$) for M_z^{Up} (M_z^{Down}) in the Hf|CoFeB|TaO_x multilayer. Hence, the effective field associated with the damping-like SOT in Hf|CoFeB|MgO is about one order of magnitude larger than that in Hf|CoFeB|TaO_x.

Similarly, the transverse SOT-induced effective field ΔH^{FL} was calculated using the experimental data in Figure 4.42 via Eq. (3.16) and then plotted as a function of I_0 for Sample I and Sample II, as shown in Figure 4.43c-d, respectively. As expected, we find that the sign of ΔH^{FL} does not depend on the magnetization state (unlike ΔH^{DL}). The dependence of ΔH^{FL} on the applied current is linear for both M_z^{Up} and M_z^{Down}, similar to the dependence of ΔH^{DL} discussed above. The experimental data were fitted using the linear relation $\Delta H^{FL} = \beta_{FL} J_x$, where the extracted β_{FL} values are found to be $6.23\ Oe/10^6 Acm^{-2}$ ($6.57\ Oe/10^6 Acm^{-2}$) for M_z^{Up} (M_z^{Down}) in the Hf|CoFeB|MgO multilayer and $1.02\ Oe/10^6 Acm^{-2}$ ($0.92\ Oe/10^6 Acm^{-2}$) for M_z^{Up} (M_z^{Down}) in the Hf|CoFeB|TaO_x multilayer. Hence, it is evident that the transverse effective field, which is associated with the field-like SOT, is almost 4× larger than damping-like SOT in both samples. Additionally, the β_{FL} parameter for the Hf|CoFeB|MgO stack is found to be about 6× larger than the one in Hf|CoFeB|TaO_x.


a
M_z^{Up}:MgO
M_z^{Down}:MgO
β_{DL} ~ 1.46 Oe/(10^{6}A/cm^2)
β_{DL} ~ −1.56 Oe/(10^{6}A/cm^2)
Effective Field, ΔH^{DL}(Oe)
Current Amplitude, I_0 (mA)
b
M_z^{Up}:TaO$_x$
M_z^{Down}:TaO$_x$
β_{DL} ~ 0.15 Oe/(10^{6}A/cm^2)
β_{DL} ~ −0.15 Oe/(10^{6}A/cm^2)
Effective Field, ΔH^{DL}(Oe)
Current Amplitude, I_0 (mA)

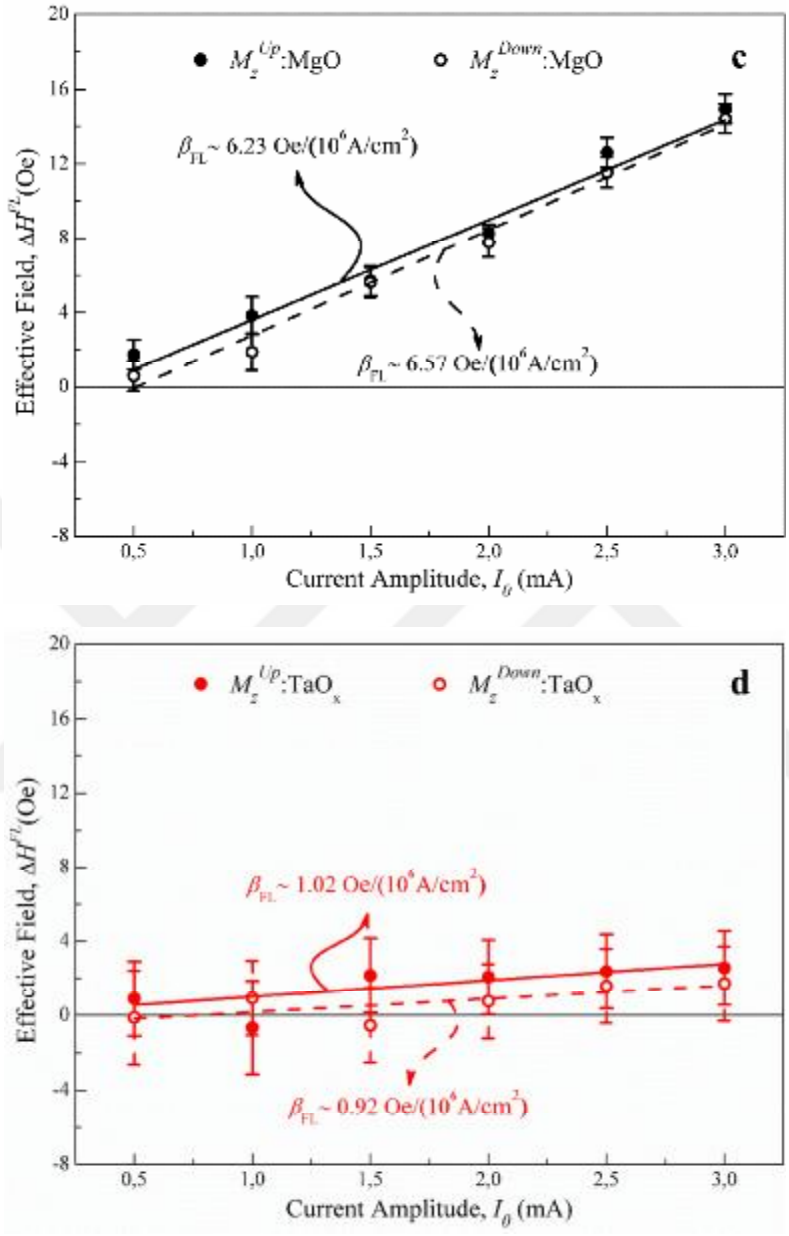


Figure 4.43. Longitudinal (transverse) SOT-induced effective field generated by in-plane electric current depends on the amplitude of the alternating current for a) (c) Sample I and b) (d)Sample II.

The schematic illustration of effective fields, *i.e.* field-like and damping-like, on the magnetization for up and down cases is shown in Figure 4.44.

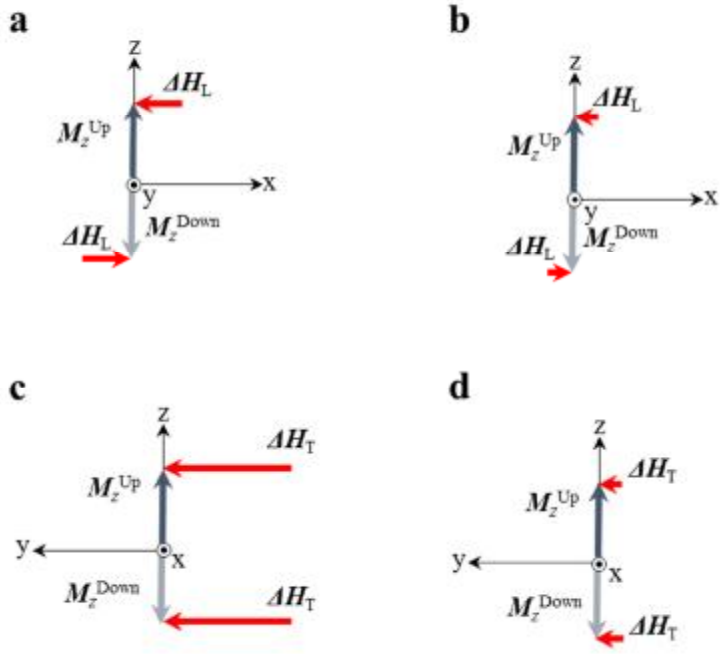


Figure 4.44. The illustration of a, b) DL and c, d) FL effective fields on M_z^{Up} and M_z^{Down} in Hf|CoFeB|MgO and Hf|CoFeB|TaO_x structures.

At least two possible mechanisms may contribute to the observed difference in SOTs for the two material stacks. First, the different preparation conditions of the two oxides (deposited by rf-sputtering of MgO and plasma oxidation of a dc-sputtered Ta layer, respectively) may have an effect on the crystallinity, oxygen content, and defect density of the underlying CoFeB and Hf layers, thereby affecting the resulting SOTs. To evaluate this possibility, we performed vibrating sample magnetometer experiments on the samples. As explained in the previous section that the small differences in magnetic dead layer thickness may be attributed to a combination of the different oxidation process used for the MgO and TaO_x layers, as well as due to damage induced by the initial Ta deposition itself.

Moreover, the interface anisotropy K_i values were also found to be comparable, with the anisotropy being slightly larger in the MgO-capped sample (1.56±0.3 ergs/cm^2) than in the TaO_x-capped case (1.26±0.3 ergs/cm^2). Hence, while there is a small difference in magnetic properties between MgO and TaO_x-capped samples, this likely cannot explain the significant difference in field-like and damping-like torques observed in this work. The detail magnetic property of the samples will be discussed in Section 4.4.1.

A second possible model to explain our experimental data is in terms of the different internal electric fields depending on the oxide cap layer in HM|FM|OX structures with different oxide films. In general, one needs to include contributions from both the interfaces between the ferromagnet and the oxide layer (e.g., FM|OX), and the heavy metal and the ferromagnetic layer (e.g., HM|FM), to the observed SOTs. In this case, the different interfacial electric fields in each structure, resulting from the different oxide capping work function, can also affect the observed SOTs via the Rashba effect. In particular, due to the different work functions of the layers in the studied stacks, internal electric fields E_{int}, perpendicular to the interfaces, will exist at each interface. The electric field is expected to decay mostly at the interface and its strength is expected to be proportional to the change in the work function between the two materials at each interface. This change is expected to be ~6.0eV between the MgO (~1.1 to ~1.4eV with a (001) crystallization (Butti et al., 2004; Giordano et al., 2006; Bieletzki et al., 2010; König et al., 2009) and CoFe (4.75 eV) (Jeon et al., 2011) layers, while only ~0.05eV is expected between CoFe and Ta_2O_5 (4.8 eV) (Greiner et al., 2012). The change in the work functions between Hf (3.6 eV) (Michaelson, 1977; Eastman, 1970) and CoFe is estimated to be ~1.15 eV, but this quantity remains constant for both material stacks. In the one-particle Hamiltonian, considering spin-orbit coupling in a ferromagnetic layer, the strength of the Rashba term is proportional to the effective local electric field, ∇V such that $\hat{H} \approx \left(\vec{\nabla} V \times \hat{p}\right).\hat{\sigma}$

where $\hat{p}$ is the momentum operator and $\hat{\sigma}$ is the operator of Pauli-spin matrices. Hence, the larger field-like SOT in Hf|CoFeB|MgO compared to Hf|CoFeB|TaO_x, may be phenomenologically explained in terms of the larger asymmetry in the band structure in the case of MgO capping. However, further structural analysis as well as first principles calculations may be needed to better understand and quantify the possible roles of band structure and structural effects on the SOTs. In Figure 4.45, we would like to model of our experimental results to explain the physical meaning behind of the devices.

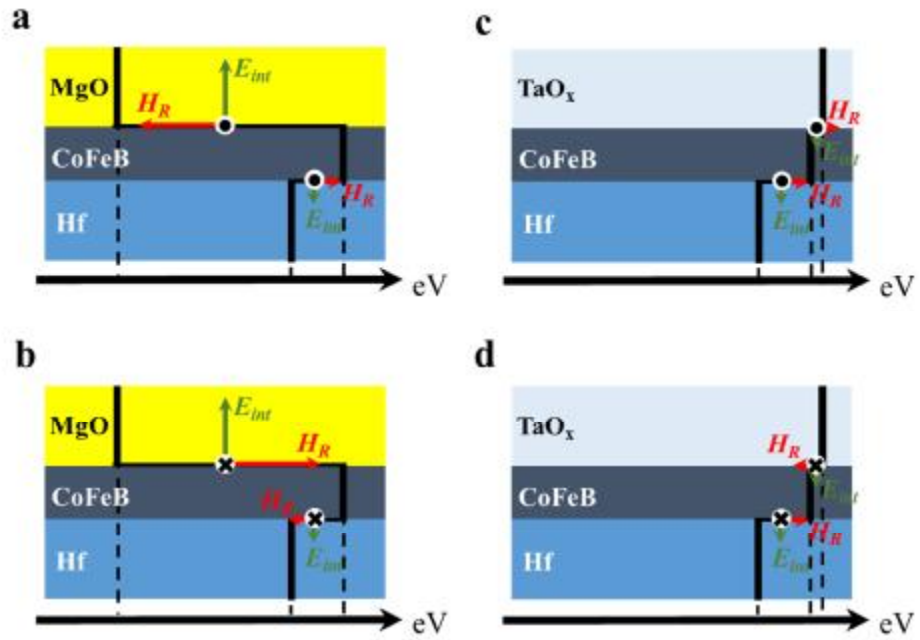


Figure 4.45. The schematically illustration of the Hf|CoFeB|MgO (TaO_x) film stacks with each interface effect on ferromagnetic layer under in-plane electric current. Current is flowing in the $+x$ direction a) (c) and $-x$ direction b) (d) for MgO (TaO_x) cap layer.

4.2.3. Current-Driven Magnetization Switching in Hf|CoFeB|MgO and Hf|CoFeB|TaO_x Multilayer Structures

The effect of MgO and TaO_x as capped layer in the structure on magnetization switching has been worked by current-driven magnetization switching in the presence of an in-plane magnetic field to break the symmetry. The anomalous Hall resistances, means out-of-plane magnetization, M_z as a function of driven electric current are shown in Figure 4.46a-b for Sample I and Sample II, respectively. In both samples, the magnetic switching direction is in the clockwise (counter-clockwise) direction under positive (negative) external magnetic field. Since the current-driven magnetization switching direction is related to the effective spin-orbit torques on the magnetization, it is expected that the sign of the switching is same for both capped samples. In addition, the minimum switching electric current, $I_s = (I_s^+ + I_s^-)/2$ where $I_s^+ (I_s^-)$ is the enough electric current to switch the magnetization at positive (negative) direction, in TaO_x-capped sample is higher (~6.2 mA) than the MgO-capped one (~2.3 mA). As the DL-SOT in MgO-capped sample is found one order larger than the TaO_x-capped sample, the switching current requirement is low for MgO-capped sample, as expected. This results show that the capped layer as an insulating barrier in free part of the magnetic tunnel junctions has a crucial role to create SOTs, and thus energy consumption.

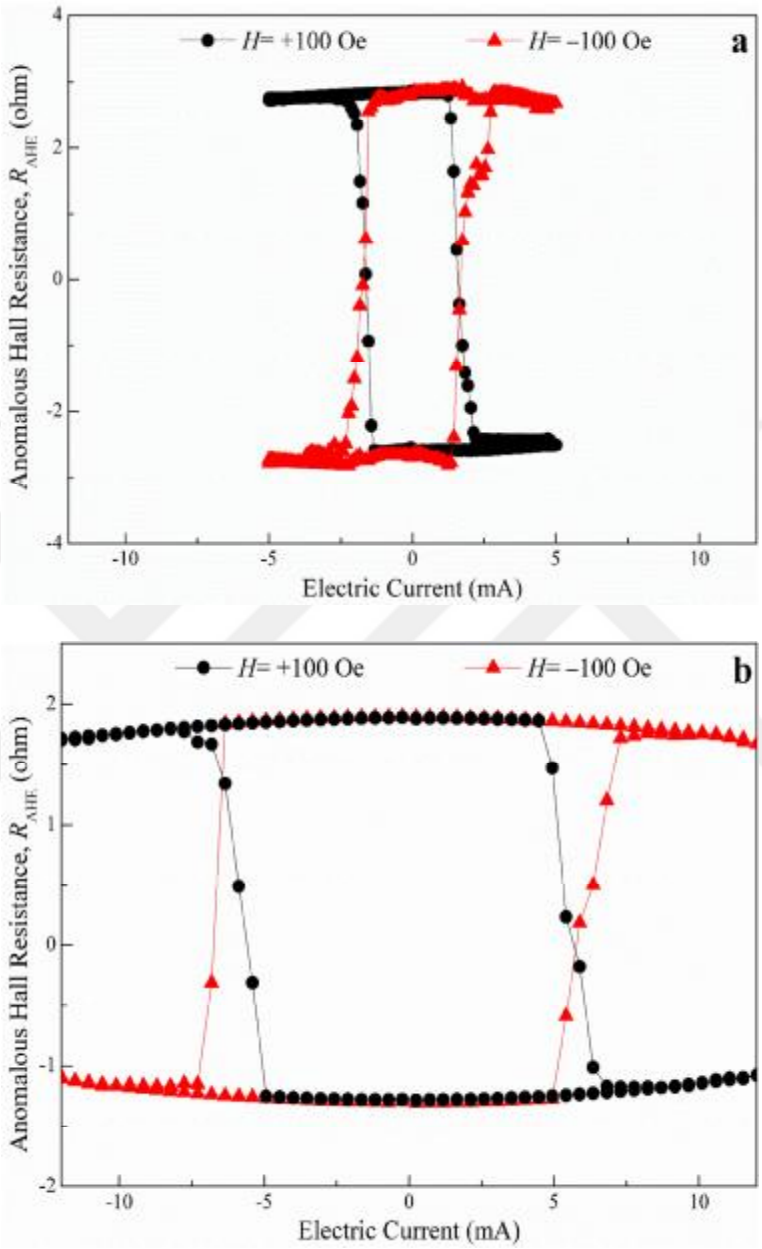


Figure 4.46. Current-driven magnetization switching for a) MgO and b) TaO_x capped devices under positive (black) and negative (red) longitudinal magnetic fields.

4.3. New Spin-Orbit Torque Engineering via Lateral Symmetry Breaking in both Hf|CoFeB(*wedge*)|MgO and Hf|CoFeB(*wedge*)|TaO_x Multilayer Structures

Structural symmetry breaking in nanomagnetic systems has attracted great attention to develop ultralow-power spintronic devices. The breaking of structural symmetry in magnetic heterostructures has been engineered to create an interaction between electric currents and magnetization. This interaction induces spin-orbit torques on the magnetization (Liu et al., 2012; Liu et al., 2012; Miron et al., 2011; Mihai Miron et al., 2010; Kim et al., 2013; Fan et al., 2013). The conventional SOTs (DL and FL) have been used to mediate current-induced magnetization switching and domain-wall motion in structural asymmetric nanomagnetic systems (Liu et al., 2012; Miron et al., 2011; Ryu et al., 2013; Emori et al., 2013; Pai et al., 2012; Haazen et al., 2013) where an ultra-thin ferromagnetic layer must be sandwiched between a heavy non-magnetic metal with strong spin-orbit coupling and an insulator.

As explained in Section 1.7, an external magnetic field in a SOT-based device is needed to switch the magnetization of ferromagnetic layer in such heterostructures. The external magnetic field allows to favor a particular orientation for the out-of-plane magnetization component. Thus, the magnetization can be controlled by electric current and external magnetic field. To overcome the requirement of external field, an internal in-plane magnetic field source may be integrated by engineering the device stack. However, this internal fixed field is not desirable for particle applications due to the reducing thermal stability of perpendicular bit by lowering energy barrier between the states. Since one of the main goals is to reduce the writing power in MRAM device, the current-driven magnetization switching without external magnetic fields is important for practical applications in SOT-based devices. In naturally, there are currently no solutions to overcome this requirement. But, it can be fabricated by engineering the symmetry

of the nanomagnetic stack in both growing and lateral directions. While the growing asymmetry in the structure can generate conventional SOTs on the magnetization, the lateral asymmetry replaces the role of the external in-plane magnetic field.

In this section, we investigate the symmetry-based study of SOT interactions and field-free switching coming from the lateral symmetry-breaking which creates a new field-like torque when an in-plane electric current is driven through the device. To break the lateral symmetry, the film structure has been engineered during the film deposition process. Figure 4.47 represents a schematic illustration indicating both growing asymmetry and lateral asymmetry.

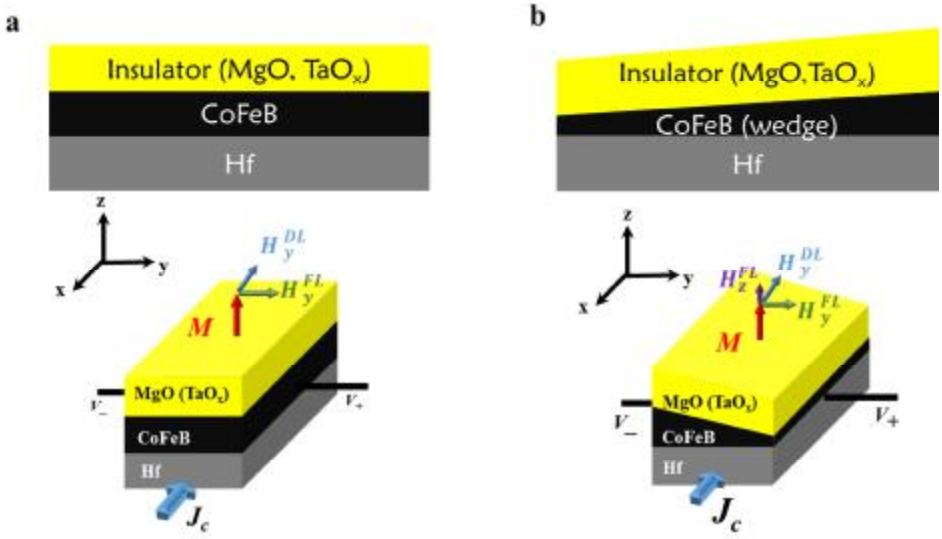


Figure 4.47. Schematics of symmetry breaking in a) *z*-direction and b) both *y* and *z*-directions.

Figure 4.47a indicates the case symmetry is broken only along the *x*-axis means growing asymmetry which results in current-induced conventional SOTs that consist of a field-like term $\vec{\tau}^{FL} = \gamma H_y^{FL} \vec{M} \times \hat{y}$ and a damping-like term $\vec{\tau}^{DL} = \gamma H_y^{DL} \vec{M} \times \vec{M} \times \hat{y}$ where γ is gyromagnetic ratio, $\vec{M}$ denotes a unit vector

along the magnetization, $\hat{y}$ is the unit vector which is in-plane and transverse to the electrical current. These torques can be expressed in terms of effective magnetic fields, $\vec{H}_y^{FL} = H_y^{FL}\hat{y}$ and $\vec{H}_y^{DL} = H_y^{DL}\vec{M} \times \hat{y}$ where H_y^{FL} and H_y^{DL} represent the current-dependent proportionality constants for each term. As explained in Section 1.7 and 4.1.7, such SOTs cannot switch the magnetization without external magnetic field due to the favoring same direction of magnetization for all axis under electric current.

The limitation of the conventional SOTs in the standard devices can be achieved by breaking the lateral symmetry (*y*-axis) in addition to the growing directions. A particular current direction can determine the magnetization components. Figure 4.47b indicates the structural asymmetry along the *y*-axis by varying thickness of CoFeB layer. The breaking lateral structure can replace the role of external magnetic field. If we use symmetry-based phenomenology (Hals et al., 2013), the SOT on the magnetization due to the asymmetry both the *y*- and *z*-axes can be written by;

$$\vec{\tau}_{SOT} = \gamma H_y^{FL}\vec{M} \times \hat{y} + \gamma H_y^{DL}\vec{M} \times \vec{M} \times \hat{y} + \gamma H_z^{FL}\vec{M} \times \hat{z} + \gamma H_z^{DL}\vec{M} \times \vec{M} \times \hat{z} \quad (4.1)$$

The last two terms (H_z^{FL} and H_z^{DL}) of the equation (4.1) are corresponding to the parameterize the strengths of the current-induced effective fields coming from the additional asymmetry for new FL and DL-SOT terms, respectively. This new FL term results in a current-induced effective field H_z^{FL} along the *z*-axis. Therefore, it can mediate the current-induced deterministic switching of perpendicular magnetization without external magnetic fields.

Here, the ferromagnetic CoFeB layer was grown in a wedge shape (i.e., with varying thickness from 0.4 to 1.6 nm across 50 mm along the wafer) along the *y*-axis. The wedge layer effect on current-driven SOTs in perpendicularly magnetized Hf|CoFeB(***wedge***)|MgO and Hf|CoFeB(***wedge***)|TaO_x multilayers has been

investigated in this section. As discussed in the previous section, the choice of the insulator material significantly affects both the field-like and damping-like SOT terms in such structures. Therefore, we used both MgO and TaO_x oxide layer in engineered ferromagnetic layer in multilayer structures which are Hf(5.0)|$Co_{20}Fe_{60}B_{20}$(*wedge*)|MgO(5.0)|TaO_x(1.0) and Hf(5.0)|$Co_{20}Fe_{60}B_{20}$(*wedge*)|TaO_x(5.0) (thickness in nanometers, and the composition of the CoFeB in atomic percent) deposited on Si substrates covered with a thermally oxidized SiO_2 (100 nm) layer using a magnetron sputtering system. The oxide layers have been deposited as explained in the previous section. The films were patterned into to 20 µm×130 µm Hall bar structures by photo-lithography and dry-etching techniques, as explained in Chapter 3.

4.3.1. Wedge Shape Effect on Perpendicular Magnetic Anisotropy in Hf|CoFeB(*wedge*)|MgO and Hf|CoFeB(*wedge*)|TaO_x Multilayer Structures

Since the CoFeB layer is in a wedge shape in both multilayer film structures, we first determine the moment per area of the films as a function of CoFeB layer thickness by VSM experiment. The films were cut in 10 pieces and their average thickness was considered. Figure 4.48 shows the moment per area of the measured pieces of the films as a function of CoFeB layer thickness in both Hf|CoFeB(wedge)|MgO and Hf|CoFeB(wedge)|TaO_x multilayer structures. As seen from the figure that the data points linearly increase with the CoFeB layer thickness in both samples, as expected. The slope of the data points were calculated by linear fitting to determine the saturation magnetization, M_s which are found as 1210 and 1180 emu/cm^3 for Hf|CoFeB(wedge)|MgO and Hf|CoFeB(wedge)|TaO_x samples, respectively.

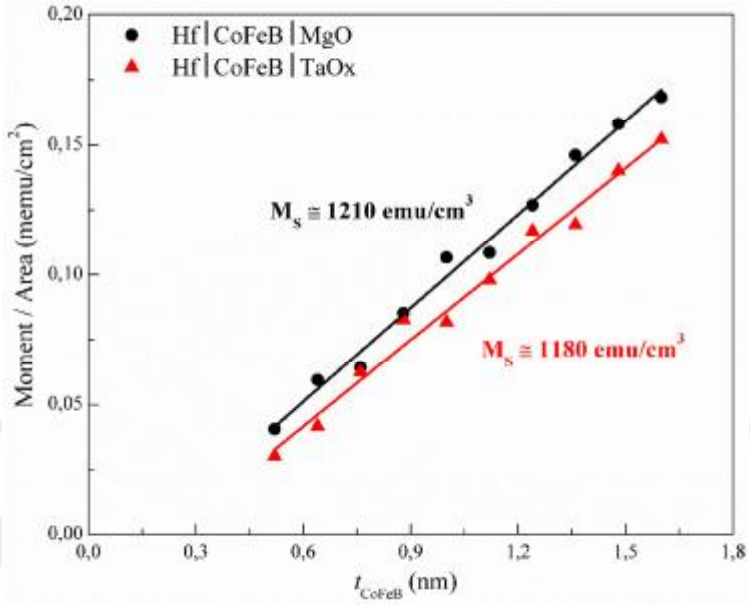


Figure 4.48. Moment per area as a function of CoFeB layer thickness in Hf|CoFeB(*wedge*)|MgO and Hf|CoFeB(*wedge*)|TaO_x structures.

The magnetic dead layer can be evaluated by linear fitting of moment versus ferromagnetic layer thickness in the structure. The linear fit curves cut the *y*-axis at zero point in *x*-axis means the magnetization is zero at the corresponding CoFeB layer thickness. The magnetic dead layer thickness for the samples was determined to be 0.17 and 0.24 nm for Hf|CoFeB(*wedge*)|MgO and Hf|CoFeB(*wedge*)|TaO_x multilayer structures, respectively. This small difference in magnetic dead layer thickness may be attributed to a combination of the different oxidation process used for the MgO and TaO_x layers, as well as due to damage induced by the initial Ta deposition itself, in agreement with the previous reports on large magnetic dead layers (up to 0.5 nm) in Ta-capped CoFeB (Ikeda et al., 2010; Worledge et al., 2011).

Next, we calculated the effective magnetic anisotropy energy to determine interfacial anisotropy energy for both samples from;

$$K_{eff} = K_b - 2\pi M_s^2 + {}^{K_i}/_{t} \quad (4.2)$$

where K_b is the bulk anisotropy energy density, K_i is the interfacial anisotropy energy density, and M_s is the saturation magnetization. Figure 4.49 shows the effective magnetic anisotropy energy, K_{eff}, multiplied by the thickness of the CoFeB layer, t_{CoFeB}, as a function of the CoFeB thickness in Hf|CoFeB(*wedge*)|MgO and Hf|CoFeB(*wedge*)|TaOx structures. Both samples exhibit out-of-plane anisotropy $K_{eff} > 0$ for the thickness of CoFeB ranging from ~0.5 to ~1.5 nm, while in-plane anisotropy $K_{eff} < 0$ was observed for thicker CoFeB films. Based on a linear fit of the data in Figure 4.49, we found the interfacial anisotropies to be $K_i = 1.5 \mp 0.3\ erg/cm^2$ in MgO-based and $K_i = 1.2 \mp 0.3\ erg/cm^2$ in TaO_x-based samples, respectively. It can be concluded that the perpendicular magnetic anisotropy in the MgO-based sample is stronger than that in TaO_x-based structures, as seen from Figure 4.49.

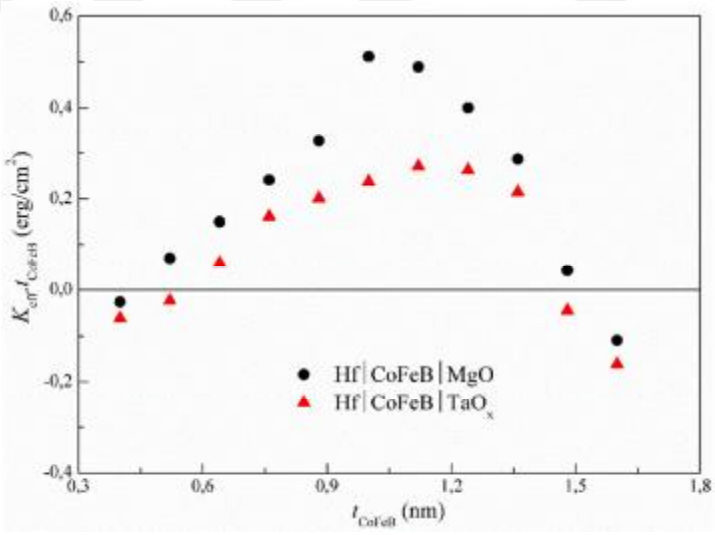


Figure 4.49. Effective magnetic anisotropy energy, K_{eff} multiplied by the thickness of the CoFeB film, t_{CoFeB}, as a function of the CoFeB thickness in Hf|CoFeB(*wedge*)|MgO and Hf|CoFeB(*wedge*)|TaO_x multilayer structures.

4.3.2. Transport Analysis of Symmetry Breaked Hf|CoFeB(*wedge*)|MgO and Hf|CoFeB(*wedge*)|TaO_x Multilayer Structures

Next, we performed transport measurements on both samples. The measurement set-up is the same with other dc transport measurements in this thesis. Due to the wedge shape of the sample, we have 42 devices through the wafer which is 1cm×5cm. In order to compare of these two structures' transport properties, we only introduce the eight of 42 devices in Figure 4.50. The anomalous Hall resistance as a function of out-of-plane magnetic field in Hf|CoFeB(*wedge*)|MgO and Hf|CoFeB(*wedge*)|TaO_x structures in Figure 4.50a-b, respectively. The right axis indicates the thickness of CoFeB layer in both multilayer structures. As seen from both figures, the magnetic anisotropy is weak for thin and thick CoFeB regions in both samples. The coercive field as a function of CoFeB layer thickness is shown in Figure 4.51. It is seen that the trend of H_c as a function of CoFeB layer thickness is similar in both structure. But, the H_c values are higher in MgO-capped structure than that of TaO_x-capped structure. The reason in the enhanced of coercive field might be the strong magnetic coupling at the interface between MgO and CoFeB layers.

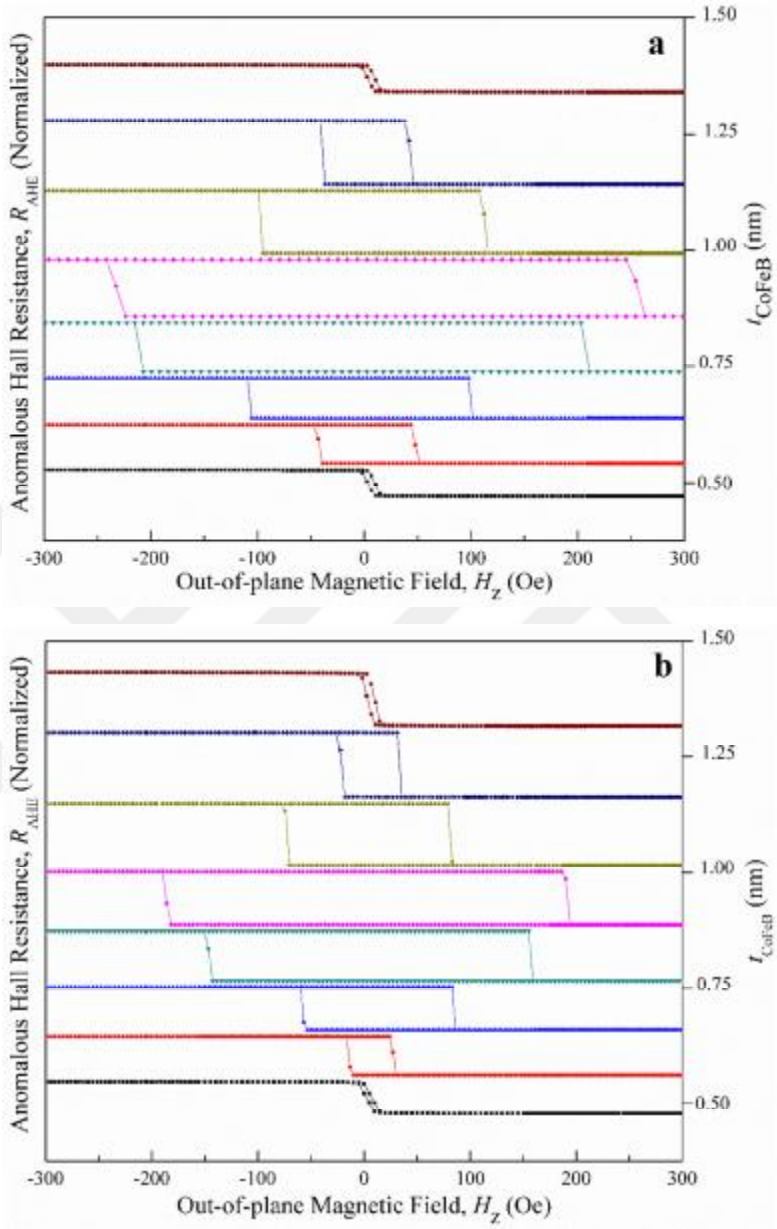


Figure 4.50. Anomalous Hall resistance as a function of out-of-plane magnetic field in a) Hf|CoFeB(wedge)|MgO and b) Hf|CoFeB(wedge)|TaO_x structures. The right axis indicates the thickness of CoFeB layer thickness in both multilayer structures.

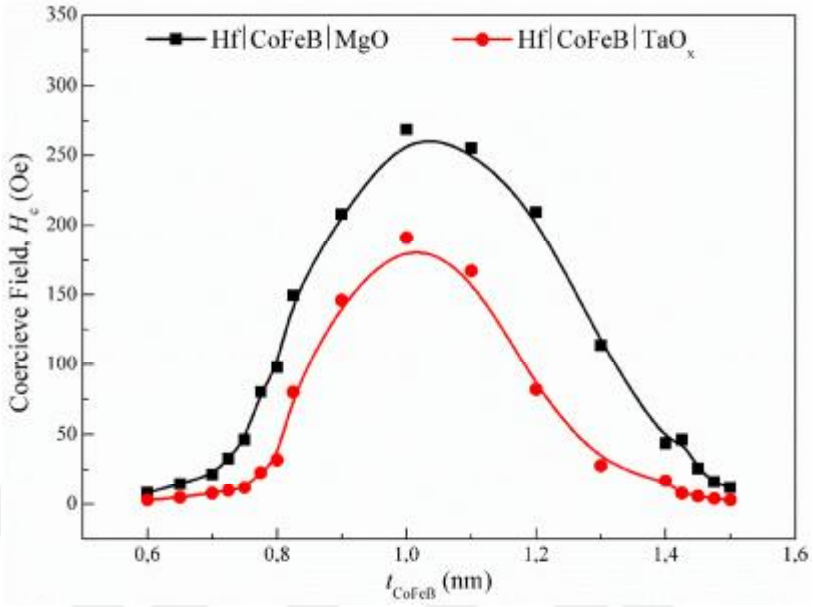


Figure 4.51. The coercive field, H_c as a function of the CoFeB layer thickness in Hf|CoFeB(*wedge*)|MgO and Hf|CoFeB(*wedge*)|TaO_x multilayer structures.

In addition, we also draw the anisotropy field, H_k determined from the VSM measurements, as a function of CoFeB layer thickness for both samples (see Figure 4.52). A similar trend is observed in H_k and H_c for both samples. It can be concluded that the magnetic anisotropy of the films is consisted in both transport and magnetic experiments. To make a fair comparison of the spin-orbit torques, we selected four devices from each sample in terms of the same CoFeB layer thickness. These eight devices are referred as Device I (Device II), Device III (Device IV), Device V (Device VI) and Device VII (Device VIII) which are based on the thickness of CoFeB layer as ~0.76, 0.9, 1.11 and 1.3 nm in the Hf|CoFeB|MgO (Hf|CoFeB|TaOx) material stack, respectively (see Figure 4.52).

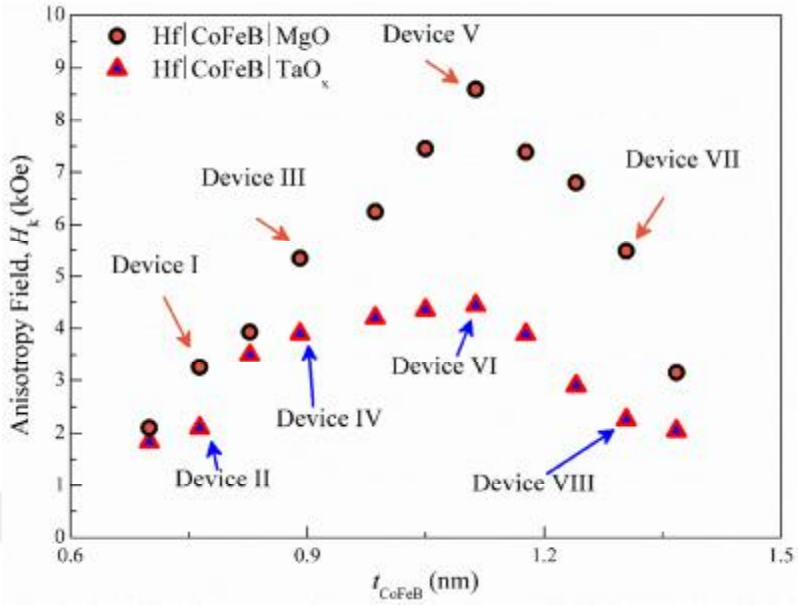


Figure 4.52. Anisotropy field, H_k as a function of CoFeB layer thickness in Hf|CoFeB(*wedge*)|MgO and Hf|CoFeB(*wedge*)|TaO_x structures.

Figure 4.53 shows the anomalous Hall resistance, R_{AHE} as a function of the out-of-plane magnetic field, H_z at ±1, ±5, and ±10 mA bias current for Device I. When the bias current value is increased from 1 to 10 mA, the coercivity is decreased as expected. However, it is observed that the centers of the hysteresis loops are shifted to the left (right) at positive (negative) currents for Device I (Hf|CoFeB|MgO). The shifting of the $R_{AHE} - H_z$ curves along the easy axis indicates that there is a current-induced effective field in the *z* direction, H^{FL} caused by the in-plane structural asymmetry due to the varying thickness of the CoFeB layer (Yu et al., 2014; Yu et al., 2014). As expected, this field depends on both the direction and magnitude of the applied current.

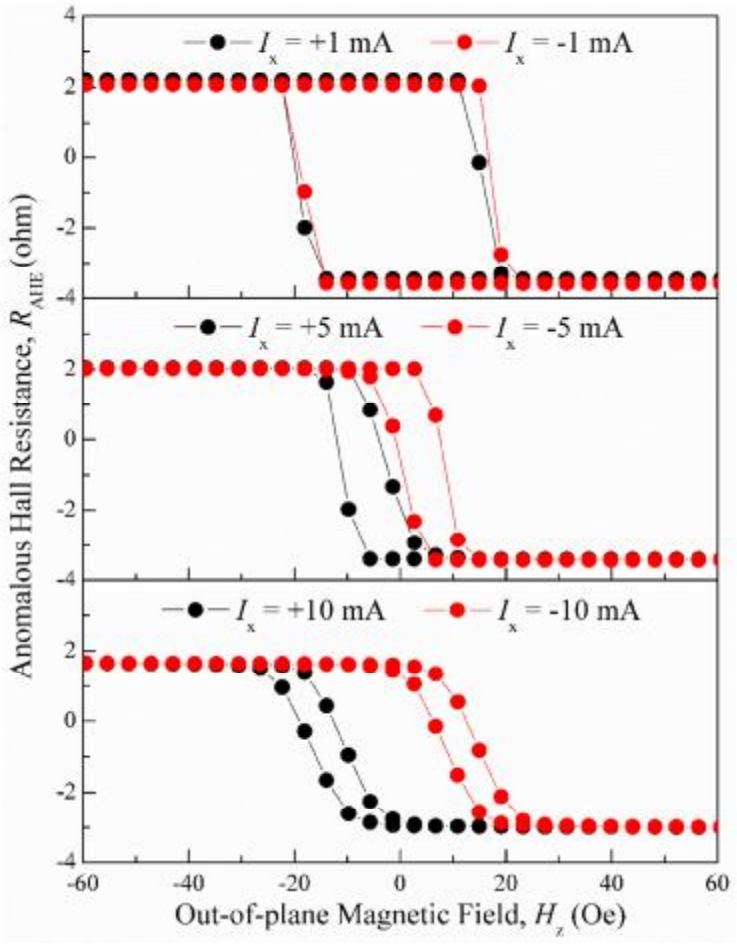


Figure 4.53. Anomalous Hall resistance as a function of out-of-plane magnetic field at various bias currents for Device I.

Next, we determined the offset field as a function of applied dc electric current by using $H_{offset} = (H^+ - H^-)/2$ where $H^+(H^-)$ is the positive (negative) switching field at each bias current value applied from ±1 to ±10 mA. Figure 4.54 show offset field as a function of the bias current density (along the *x*-axis) for Device I. It is observed that the offset field in Device I changes linearly with the bias current along the *x*-axis. From these results, one can then extract the

offset field magnitude per current density, i.e., $\beta_z = {\Delta H_{offset}}/{\Delta J_x}$. The resulting values of β_z for Devices I is found as -14.12 Oe/10^7 Acm^{-2}.

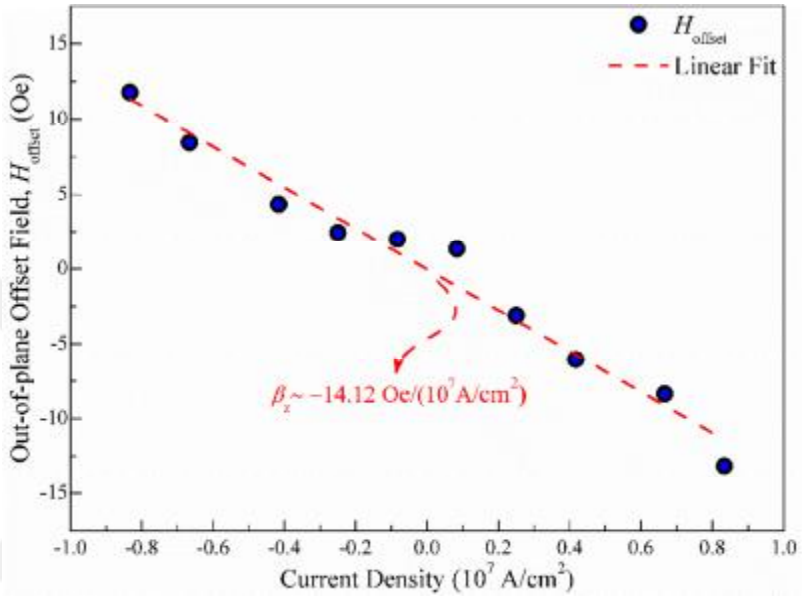


Figure 4.54. The offset field as a function of current density for Device I.

Figure 4.55 shows the anomalous Hall resistance, R_{AHE} as a function of the out-of-plane magnetic field, H_z at ±1, ±5, and ±10 mA bias current for Device II. When the bias current value is increased from 1 to 10 mA, the coercivity is decreased as expected. In contrast to the Device I, there is no shift in the centers of the hysteresis loops at both positive and negative currents for Device II (Hf|CoFeB|TaO_x).

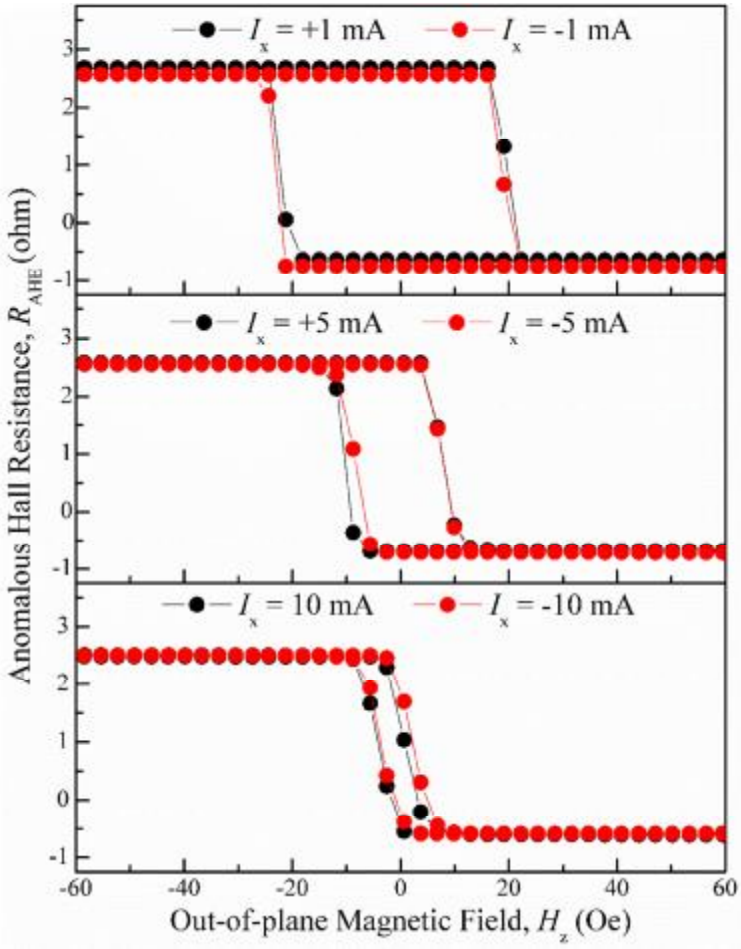


Figure 4.55. Anomalous Hall resistance as a function of out-of-plane magnetic field at various bias currents for Device II.

Next, even there is no strong shift in the hysteresis loops, we determined the offset field as a function of applied dc electric current as same as previous one. Figure 4.56 shows offset field as a function of the bias current (along the *x*-axis) for Device II. It is observed that the offset field in Device II changes linearly with the bias current along the *x*-axis. From these results, value of β_z for Devices II is found as -1.05 Oe/10^7 Acm^{-2}. The values of β_z for Device I and Device II which have same CoFeB thickness in Hf|CoFeB|MgO and Hf|CoFeB|TaO_x multilayer

structures, respectively, indicate that the effective field per current density in the Hf|CoFeB|MgO structure is ~13× larger than in the Hf|CoFeB|TaO_x case.

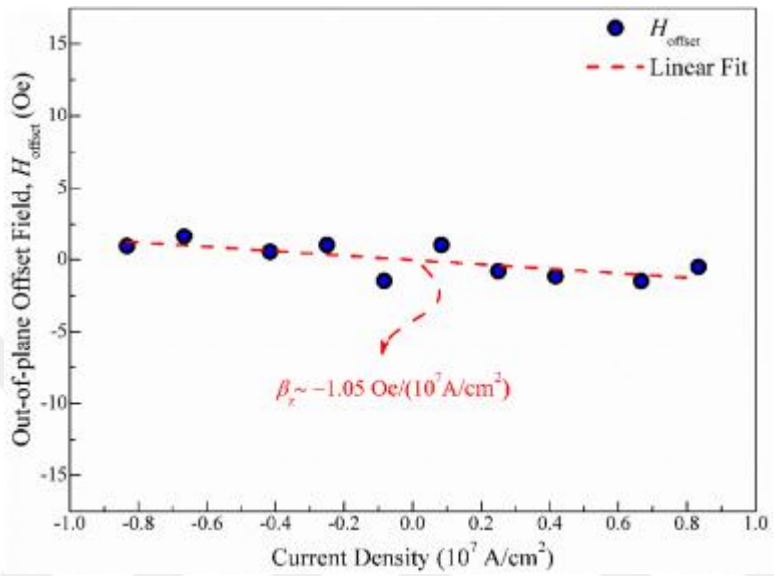


Figure 4.56. The offset field as a function of current density for Device II.

Figure 4.57 shows the anomalous Hall resistance, R_{AHE} as a function of the out-of-plane magnetic field, H_z at ±1, ±5, and ±10 mA bias current for Device III. When the bias current value is increased from 1 to 10 mA, the coercivity is decreased as expected. A similar behavior with the Device I that the centers of the hysteresis loops are shifted to the left (right) at positive (negative) currents for Device III (Hf|CoFeB|MgO), as well. However, the magnitude of the hysteresis shifting in Device III is weaker than Device I. To see clearly this shifting, we added an extended figure under ±10 mA for Device III as an inset figure in the bottom of Figure 4.57.

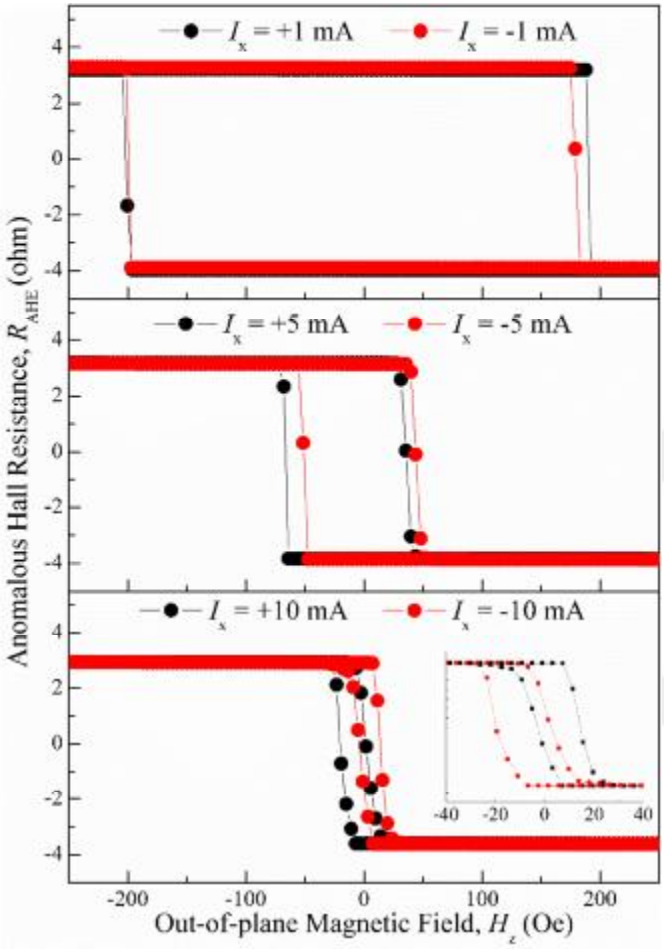


Figure 4.57. Anomalous Hall resistance as a function of out-of-plane magnetic field at various bias currents for Device III.

As same as previous calculation, we determined the offset field as a function of applied dc electric current. Figure 4.58 shows offset field as a function of the bias current (along the *x*-axis) for Device III. It is observed that the offset field in Device III changes linearly with the bias current along the *x*-axis. The value of β_z for Devices III is found as -8.45 Oe/10^7 Acm^{-2}. The values of β_z for Device I is found larger than Device III in Hf|CoFeB|MgO structure. The difference between

these two devices is the thickness of CoFeB where they are 0.76 and 0.9 nm for Device I and Device III, respectively.

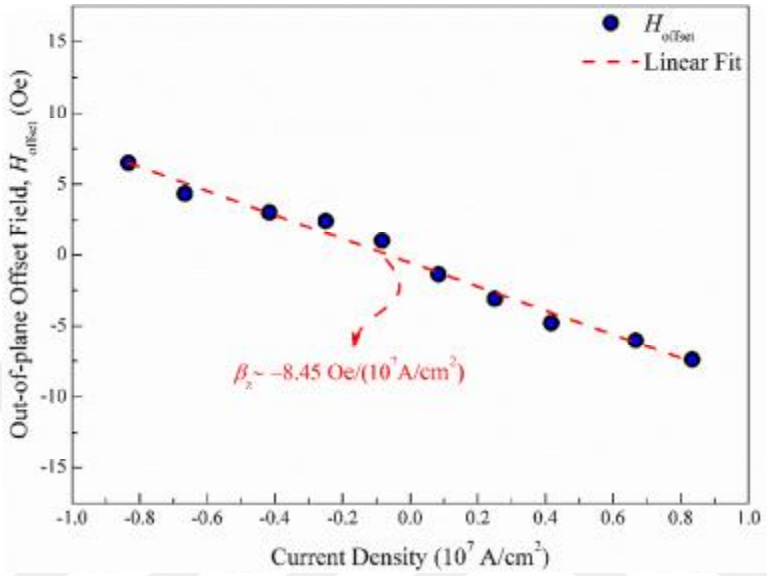


Figure 4.58. The offset field as a function of current density for Device III.

Figure 4.59 shows the anomalous Hall resistance, R_{AHE} as a function of the out-of-plane magnetic field, H_z at ±1, ±5, and ±10 mA bias current for Device IV. When the bias current value is increased from 1 to 10 mA, the coercivity is decreased as expected. However, we could not observe reasonable shifting in the hysteresis loops at both positive and negative current directions.

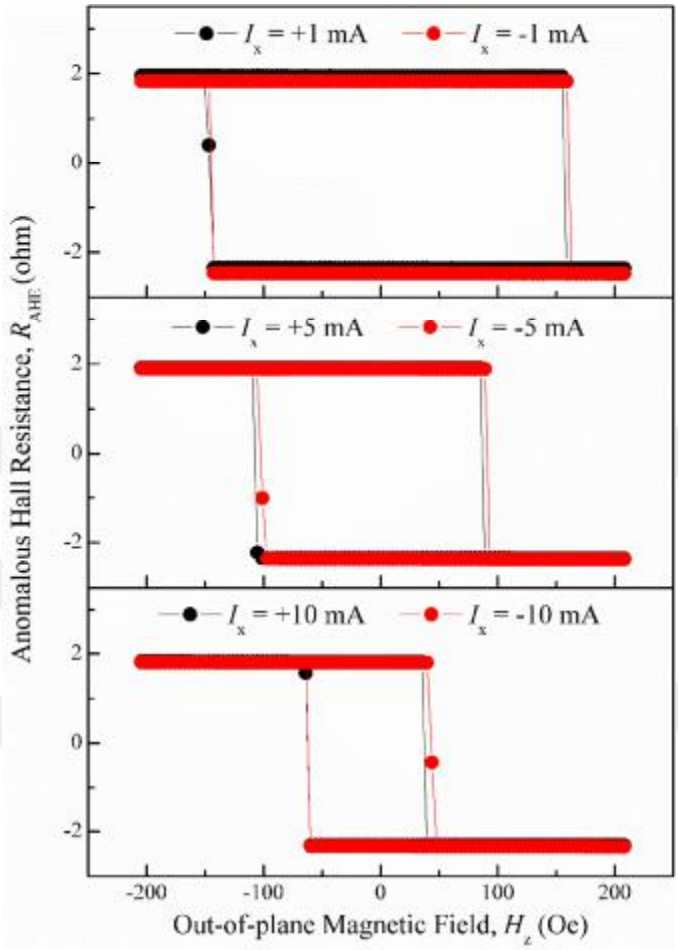


Figure 4.59. Anomalous Hall resistance as a function of out-of-plane magnetic field at various bias currents for Device IV.

As similarly, we determined the offset field as a function of applied dc electric current. Figure 4.60 shows offset field as a function of the bias current (along the *x*-axis) for Device IV. It is observed that although the value of the shifting field is not strong in Device IV, it changes linearly with the bias current along the *x*-axis. The value of β_z for Devices IV is found as -1.13 Oe/10^7 Acm^{-2}.

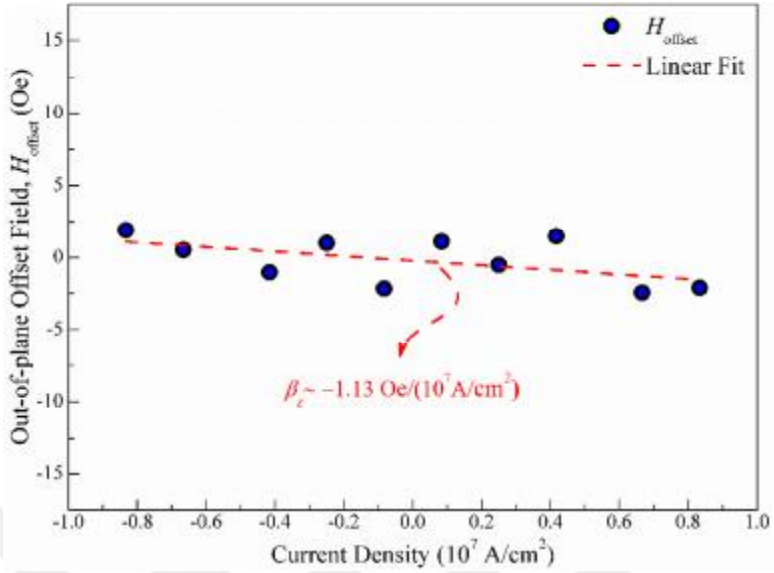


Figure 4.60. The offset field as a function of current density for Device IV.

Figure 4.61 shows the anomalous Hall resistance, R_{AHE} as a function of the out-of-plane magnetic field, H_z at ±1, ±5, and ±10 mA bias current for Device V. When the bias current value is increased from 1 to 10 mA, the coercivity is decreased as expected. In contrast to the Device I and Device III, we could not see any reasonable shift in the hysteresis loop at positive and negative electric currents.

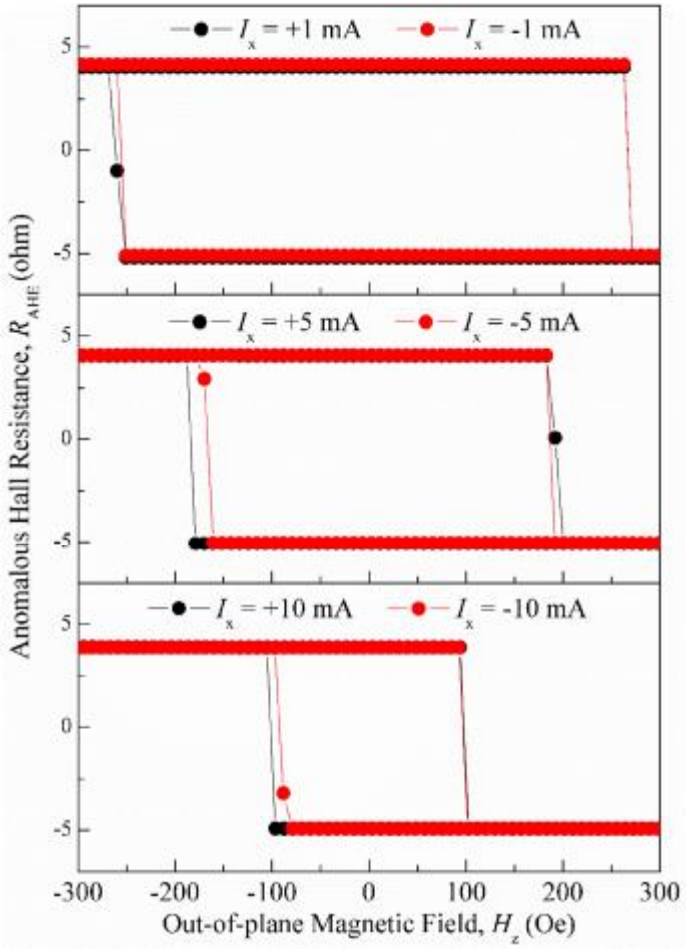


Figure 4.61. Anomalous Hall resistance as a function of out-of-plane magnetic field at various bias currents for Device V.

Similarly, we determined the offset field as a function of applied dc electric current. Figure 4.62 shows offset field as a function of the bias current (along the *x*-axis) for Device V. The offset field in Device V changes linearly with the bias current along the *x*-axis. The value of β_z for Devices V is found as -4.01 Oe/10^7 Acm^{-2}. The values of β_z for Device I (t_{CoFeB}=0.76 nm) is found larger than Device III (t_{CoFeB}=0.9 nm) and Device V (t_{CoFeB}=1.3 nm) in Hf|CoFeB|MgO structure. One can be concluded that the values of β_z inversely proportional to the thickness of

CoFeB layer in the structure. The more detail on the thickness dependence property will be discussed in Section 4.3.4.

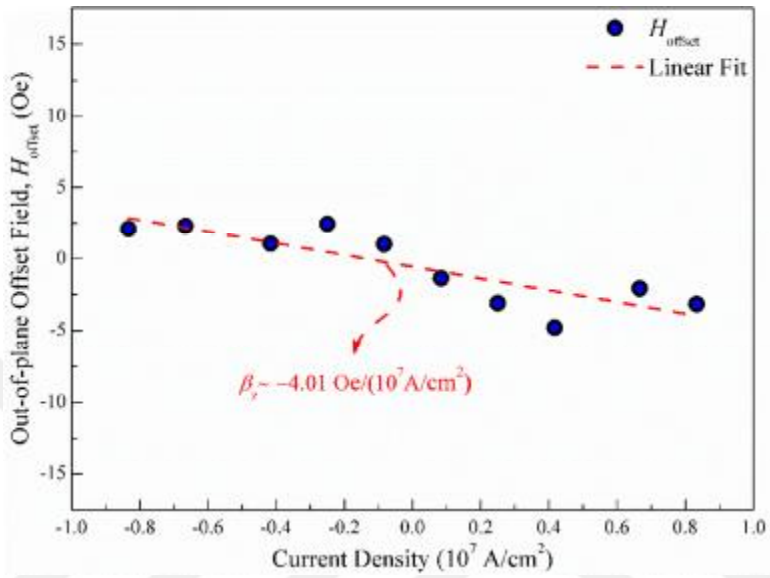


Figure 4.62. The offset field as a function of current density for Device V.

Figure 4.63 shows the anomalous Hall resistance, R_{AHE} as a function of the out-of-plane magnetic field, H_z at ±1, ±5, and ±10 mA bias current for Device VI. When the bias current value is increased from 1 to 10 mA, the coercivity is decreased as expected. Here, we also could not see any reasonable shift in the hysteresis loop at positive and negative electric currents.

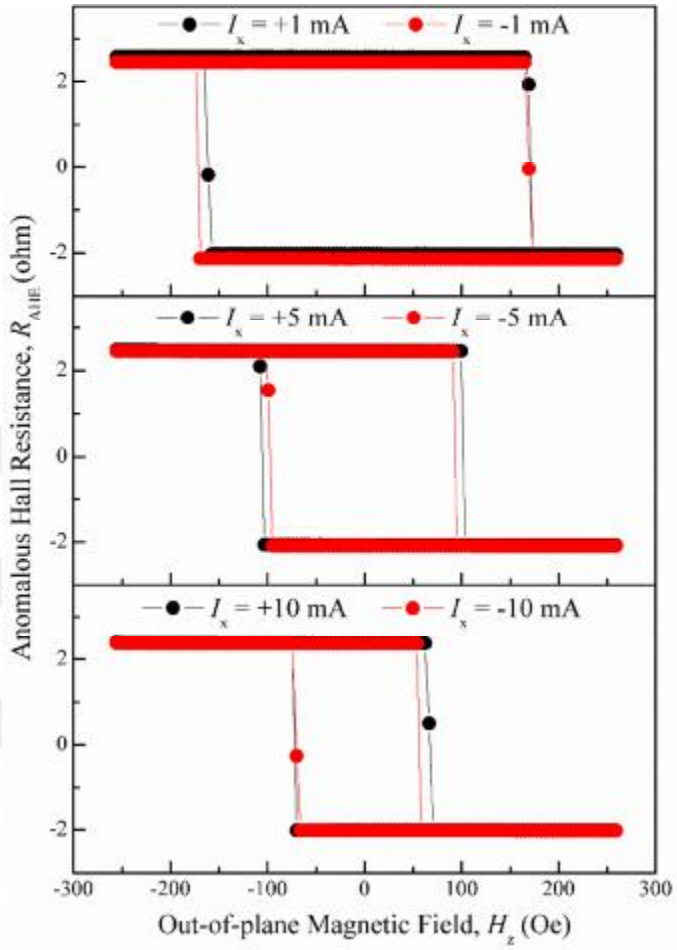


Figure 4.63. Anomalous Hall resistance as a function of out-of-plane magnetic field at various bias currents for Device VI.

We determined the offset field as a function of applied dc electric current. Figure 4.64 shows offset field as a function of the bias current (along the *x*-axis) for Device VI. Due to the low value of the offset field in Device VI, the trend of the points seems linear dependence with the bias current along the *x*-axis. The value of β_z for Devices VI is found as -0.46 Oe/10^7 Acm^{-2}.

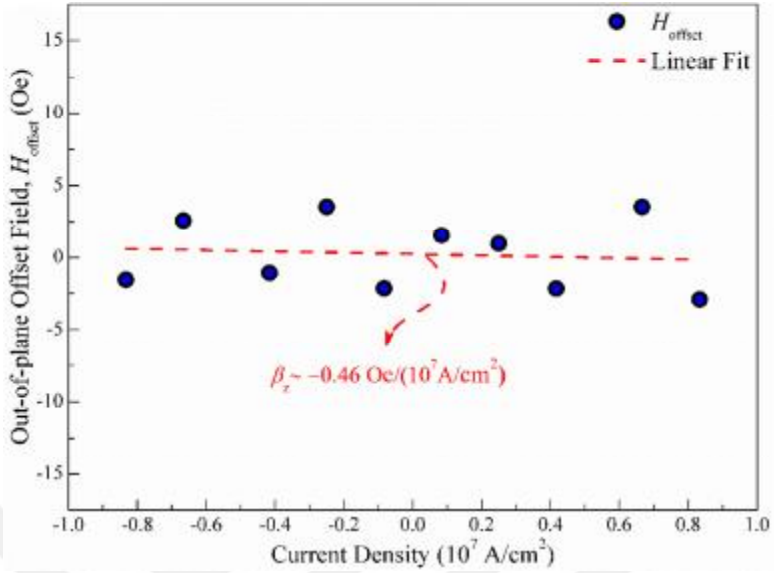


Figure 4.64. The offset field as a function of current density for Device VI.

Figure 4.65 shows the anomalous Hall resistance, R_{AHE} as a function of the out-of-plane magnetic field, H_z at ±1, ±5, and ±10 mA bias current for Device VII. When the bias current value is increased from 1 to 10 mA, the coercivity is decreased as expected. However, we could not see any reasonable shift in the hysteresis loop at positive and negative electric currents for this device as well.

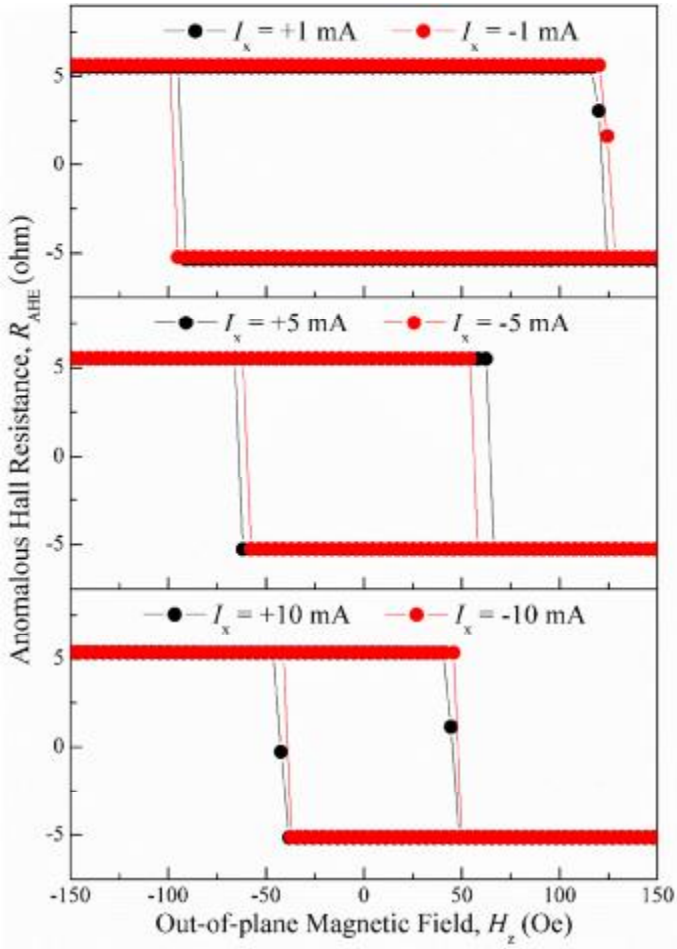


Figure 4.65. Anomalous Hall resistance as a function of out-of-plane magnetic field at various bias currents for Device VII.

The offset field as a function of applied dc electric current for Device VII is shown in Figure 4.66. As same as Device VI, value of the offset field in Device VI is in the error of the measurement. But, it can be seen the trend of the points which seems linear dependence with the bias current along the *x*-axis. The value of β_z for Devices VII is found as -2.31 Oe/10^7 Acm^{-2}.

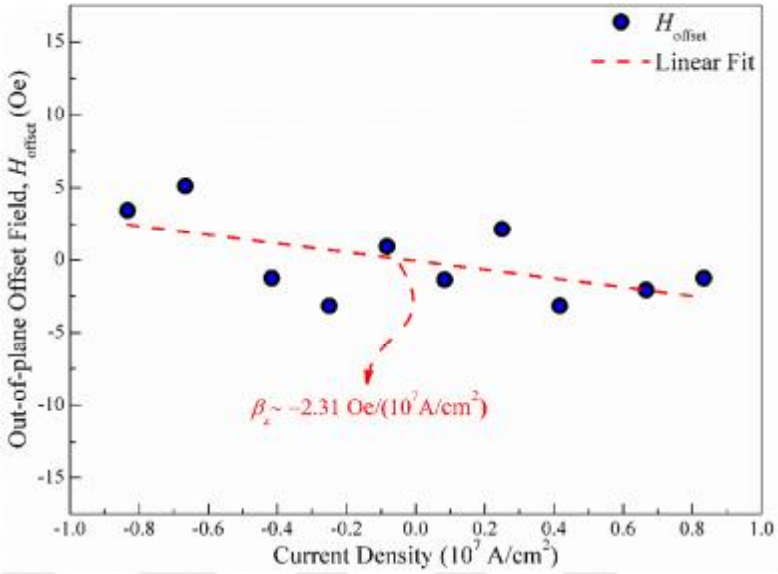


Figure 4.66. The offset field as a function of current density for Device VII.

Figure 4.67 shows the anomalous Hall resistance, R_{AHE} as a function of the out-of-plane magnetic field, H_z at ±1, ±5, and ±10 mA bias current for Device VIII. When the bias current value is increased from 1 to 10 mA, the coercivity is decreased as expected. In the hysteresis loops, we also could not see any reasonable shift at positive and negative electric currents.

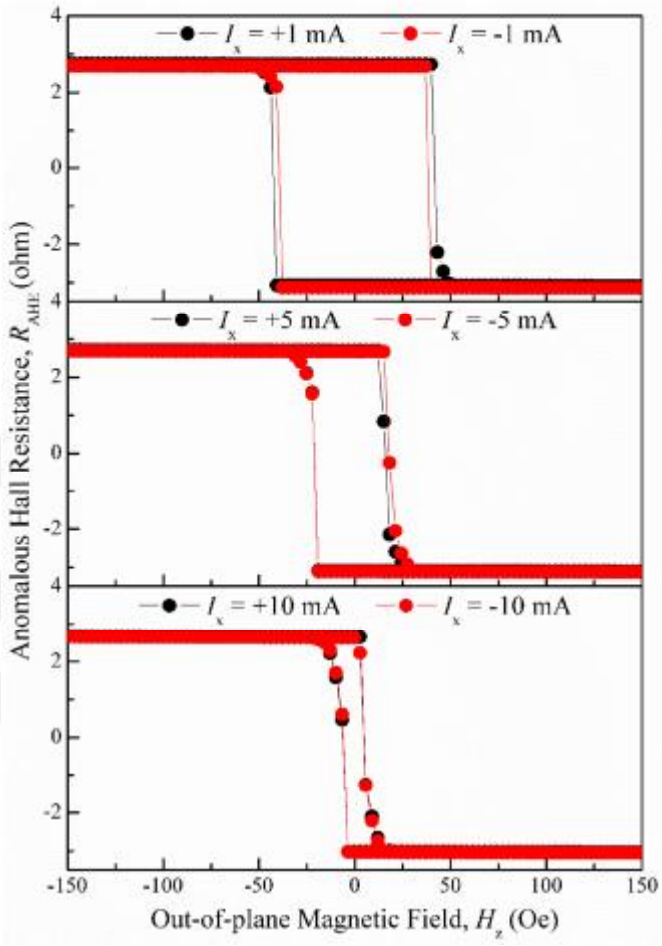


Figure 4.67. Anomalous Hall resistance as a function of out-of-plane magnetic field at various bias currents for Device VIII.

The offset field as a function of applied dc electric current for Device VIII is shown in Figure 4.68. As same as Device VI, value of the offset field in Device VIII is in the error of the measurement. The linear fit of the points is found as -0.49 Oe/10^7 Acm^{-2}.

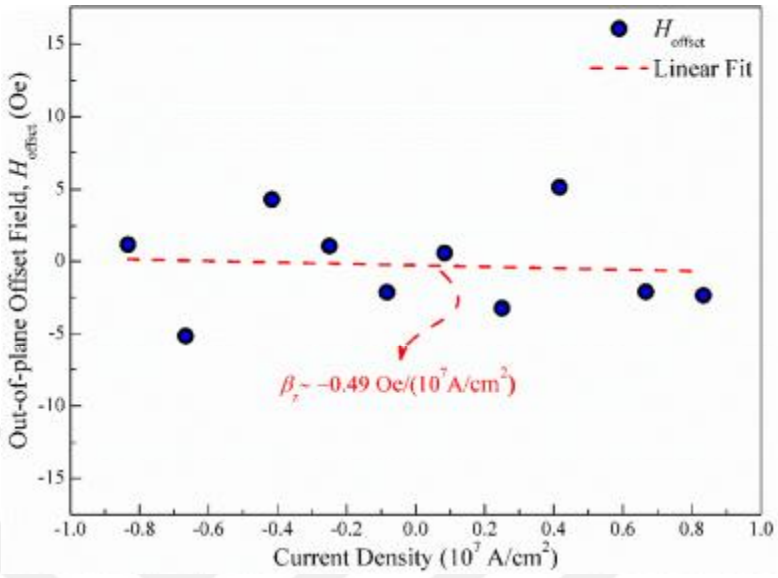


Figure 4.68. The offset field as a function of current density for Device VIII.

In conclusion, we have worked on the transport measurements in the lateral symmetry breaking in Hf|CoFeB(wedge)|MgO and Hf|CoFeB(wedge)|TaO_x multilayer structures. It is observed that the symmetry breaking in both lateral and growing directions generates a new field-like out-of-plane magnetic field, means a new torque on the magnetization, under bias electric current. This new term can help to switch of the magnetization without external magnetic field in such structure. This lateral breaking mechanism was first proposed by ***Yu et al*** in Ta|CoFeB|TaO_x(wedge) structure (Yu et al., 2014). Here, we showed both material in the seed layer and wedge of CoFeB layer as a ferromagnet can also create out-of-plane internal magnetic field by current-driven spin-orbit-torque. Therefore, Hf material can be used as a spin generator in the magnetic tunnel junctions, since it has both strong perpendicular magnetic anisotropy property and strong spin-orbit coupling as same order as Ta. The detail of the CoFeB layer thickness dependence will be discussed in Section 4.3.4.

4.3.3. Current-Driven Magnetization Switching by Spin-Orbit Torques in Hf|CoFeB(wedge)|MgO and Hf|CoFeB(wedge)|TaO_x Multilayer Structures

Current-driven magnetic switching in the perpendicularly magnetized devices with Hf|CoFeB|MgO and Hf|CoFeB|TaO_x stacks have been performed in terms of out-of-plane magnetization, M_z (normalized using the Anomalous Hall resistance values) as a function of the current density. It is observed that the perpendicular effective field, H_z^{FL} allows for deterministic switching of the perpendicularly magnetized CoFeB layer, using an in-plane electric current without an external magnetic field in Hf|CoFeB|MgO (Device I and III in Figure 4.69 and Figure 4.71, respectively). As the β_z decreases with increasing CoFeB layer thickness found in the transport measurement, the switching current density increases from Device I do Device III due to lower value of β_z in Device III. And finally, in Device V, the current-driven magnetization switching was hardly succeed under external magnetic field because the very low value of β_z (see Figure 4.73). But, in Device VII, we couldn't switch the magnetization within our system's limitation.

On the other hand, in TaO_x-capped devices which are Device II, IV, VI and VIII, an external magnetic field is necessary to switch the magnetization via in-plane currents due to their negligible β_z values. This field that serves to tilt the magnetization from the *z*-axis to enable deterministic switching of CoFeB, increases with increasing CoFeB layer thickness. Figure 4.70, Figure 4.72 and Figure 4.74 are representing the current-driven magnetization switching under both positive and negative external magnetic fields for Device II, Device IV and Device VI, respectively. As similar with Device VII in MgO-capped structure, we couldn't switch the magnetization within our system's limitation in Device VIII.

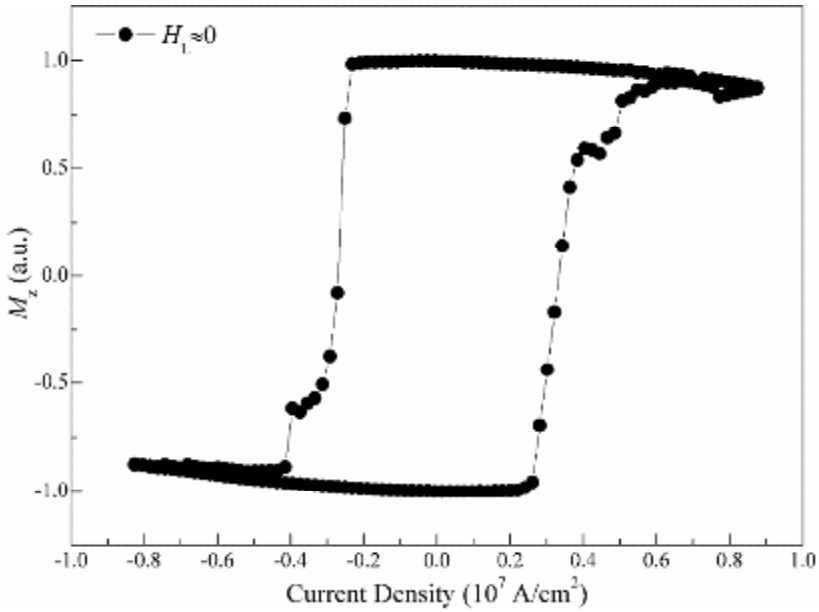


Figure 4.69. Current-induced out-of-plane magnetization, M_z as a function of the current density for Device I.

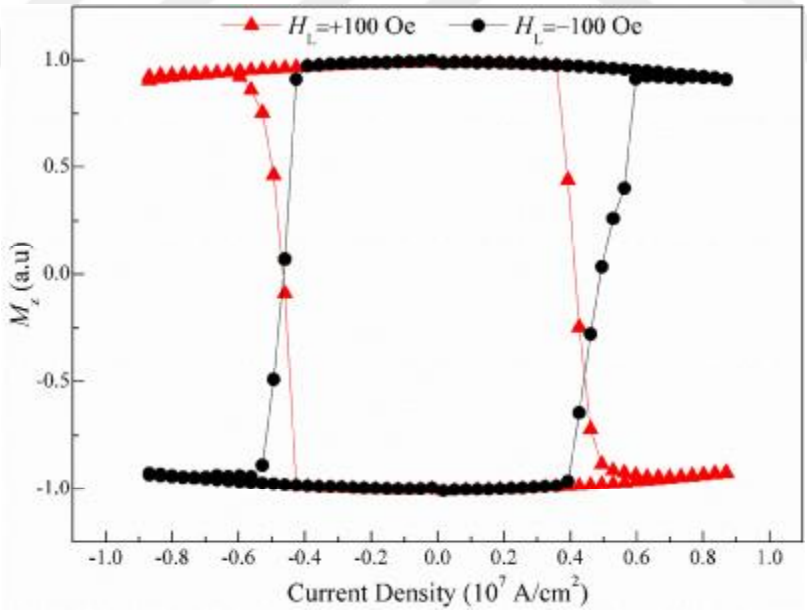


Figure 4.70. Current-induced out-of-plane magnetization, M_z as a function of the current density for Device II.

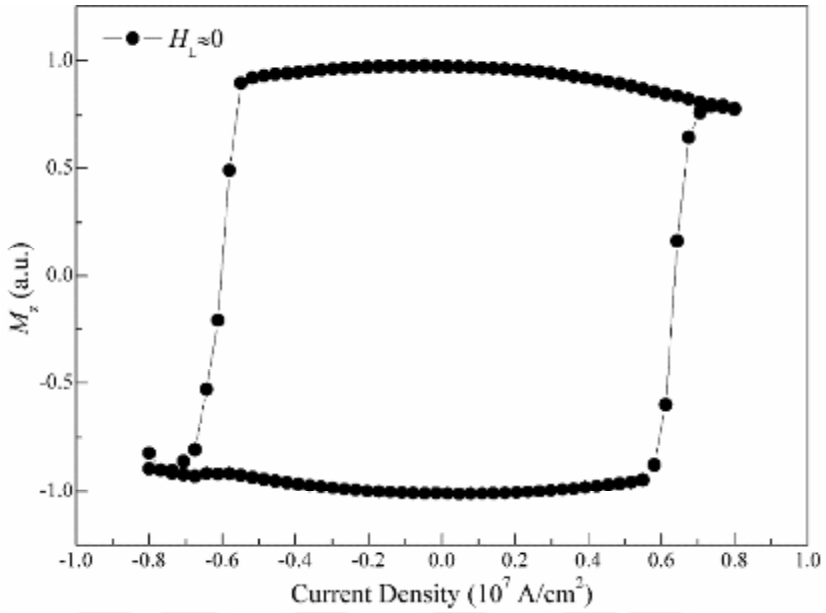


Figure 4.71. Current-induced out-of-plane magnetization, M_z as a function of the current density for Device III.

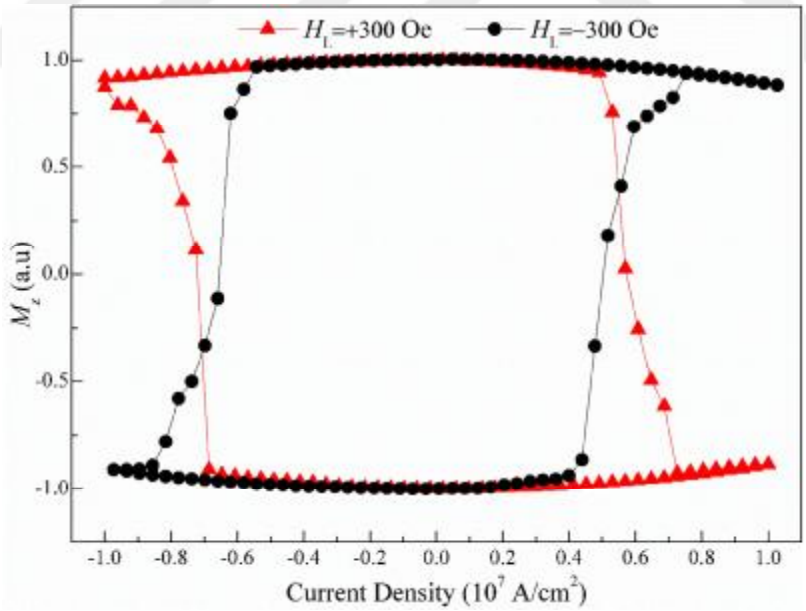


Figure 4.72. Current-induced out-of-plane magnetization, M_z as a function of the current density for Device IV.

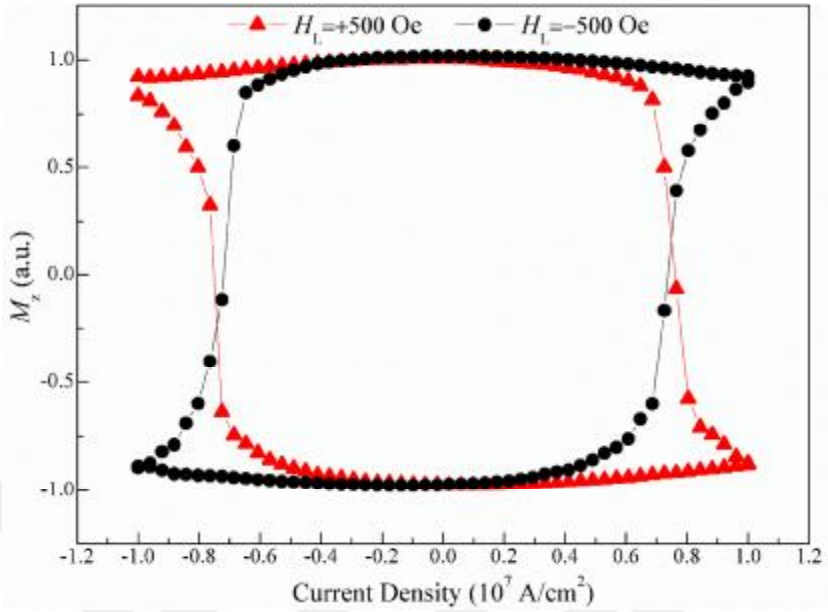


Figure 4.73. Current-induced out-of-plane magnetization, M_z as a function of the current density for Device V.

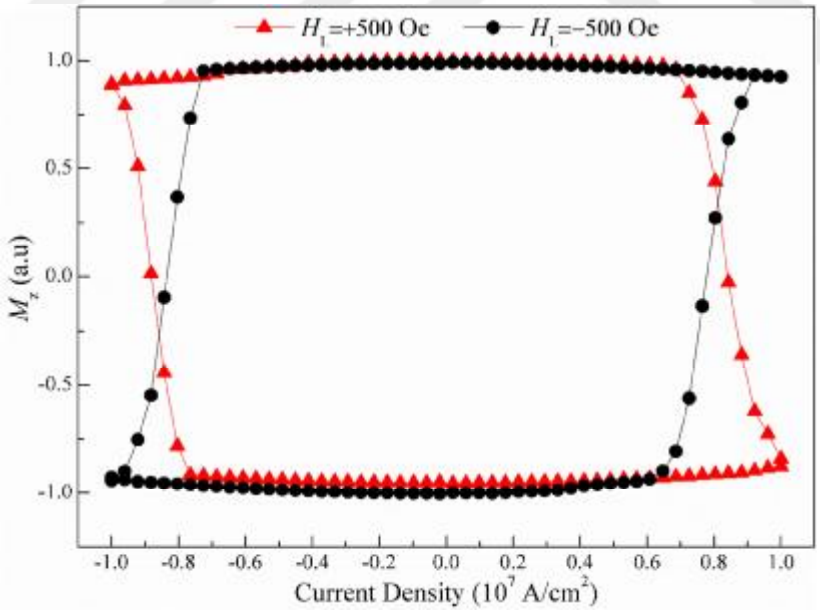


Figure 4.74. Current-induced out-of-plane magnetization, M_z as a function of the current density for Device VI.

In order to understand the switching mechanism of the ferromagnetic CoFeB layer in both Hf|CoFeB(wedge)|MgO and Hf|CoFeB(wedge)|TaO_x multilayer structures, we point out schematic illustration of the switching mechanism of magnetization under conventional spin-orbit-torque effective fields (FL and DL) and symmetry-break out-of-plane effective field in both structure. Figure 4.75a-b show the all effective fields contributed on the magnetization under positive and negative electric currents in Hf|CoFeB(wedge)|MgO multilayer structure, respectively. Figure 4.75c-d indicate the switching mechanism of CoFeB layer under positive and negative electric currents, respectively. As can be seen from these illustrations, the lateral symmetry breaking can switch the magnetization without external magnetic field in Hf|CoFeB(wedge)|MgO multilayer structure.

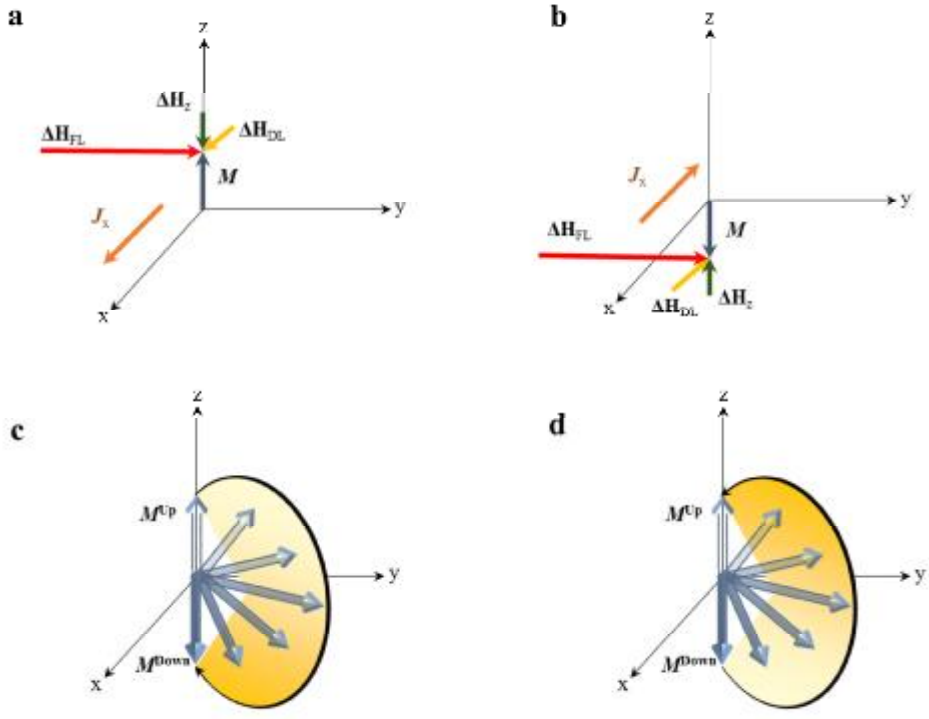


Figure 4.75. The switching mechanism of magnetization under DL, FL and out-of-plane effective fields in Hf|CoFeB(wedge)|MgO structure.

Figure 4.76a-b show all effective fields contributed on the magnetization under positive and negative electric currents in Hf|CoFeB(wedge)|TaO_x multilayer structure, respectively. As it is found from the transport measurements that the out-of-plane bias field under electric current is relatively weaker than MgO-capped sample structure. Therefore, in TaO_x-capped devices, we must apply external magnetic field to tilt the magnetization in a certain direction. Figure 4.76c-d indicate the schematic illustration of all effective field contributions to the magnetization when an external positive and negative magnetic field is applied to the devices. Figure 4.76e-f indicate the switching mechanism of CoFeB layer under positive and negative electric currents and magnetic fields, respectively. As can be seen from these illustrations, the magnetization can be only switched by electric current as well as applying external magnetic field in Hf|CoFeB(wedge)|TaO_x multilayer structure. These experimental results show that the lateral symmetry breaking mechanism cannot work in all structure. The physic behind of the symmetry breaking is related to the interfacial spin-transport mechanism. As we discussed in our previous results where we worked on the oxide layer effect on conventional spin-orbit-torque mechanism in Section 4.2, the work function difference at the interfaces can generate an internal electric field, thus it creates an internal magnetic field source. Therefore, we can conclude that when the designing of a full magnetic tunnel junction to use in magnetic random access memory, the oxide layer material and the thickness of CoFeB layer in a wedge structure must be selected mindfully.

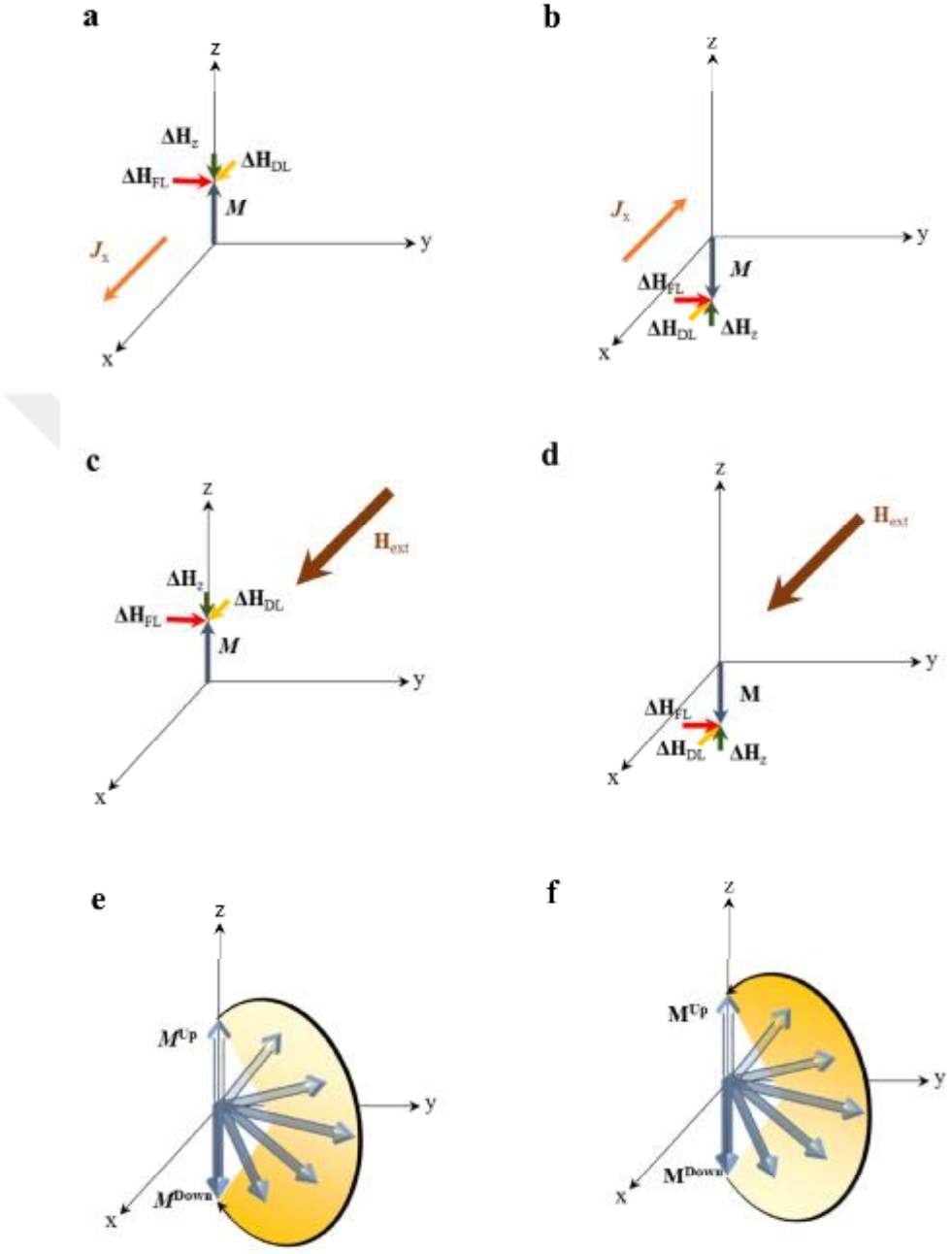


Figure 4.76. The switching mechanism of magnetization under DL, FL and out-of-plane-FL effective fields in Hf|CoFeB(wedge)|TaO_x structure.

4.3.4. CoFeB Layer Thickness Dependence on Field-Like Spin-Orbit Torque in Hf|CoFeB(*wedge*)|MgO and Hf|CoFeB(*wedge*)|TaO_x Multilayer Structures

Due to the breaking symmetry in both growing (*z*-axis) and transverse (*y*-axis) directions, the ferromagnetic layer thickness dependence on the field-like spin-orbit torque has been determined by vector measurements as similar with previous experiment given in Section 4.1.6. More information on the measurement can be found in Section 3.3.5 and 4.1.6. Figure 4.77 and Figure 4.78 show the FL-SOT expressed as $\beta_{FL} = \Delta H^{FL}/J_x$ as a function of CoFeB layer thickness in Hf|CoFeB(*wedge*)|MgO and Hf|CoFeB(*wedge*)|TaO_x, respectively. The β_{FL} gradually decreases with increasing CoFeB thickness, up to ~1.1 nm, in Hf|CoFeB(*wedge*)|MgO multilayer structure. And then, the values of β_{FL} reduce to near zero once the thickness of CoFeB goes above ~1.1 nm in the Hf|CoFeB(*wedge*)|MgO structure. The reason of decrement in FL-SOT in the thickness region of 0.6-1.1 nm can be related to the magnetic anisotropy which increases also in this thickness region. In the region of t_{CoFeB} > 1.1 nm, the PMA decreases with increasing CoFeB thickness (see Figure 4.49). In addition to the PMA, the interface source of FL-SOT might be weaker when the thickness increases. Since the origin of FL-SOT is coming from the Rashba-interface effects, the thicker films can be act as bulk material's property means the interface contribution is being weaker and bulk contribution is getting stronger.

On the other hand, for TaO_x-based devices, the values of β_{FL} were generally too small to observe a clear trend of the β_{FL} dependence on CoFeB thickness (see Figure 4.78). In section 4.2, the oxide layer effect on both DL and FL-SOTs has been discussed in detail. Here, we can conclude that the oxide layer has a crucial role to generate FL-SOT in heavy-metal|ferromagnet|oxide multilayer structure for various CoFeB layer thickness, as well.

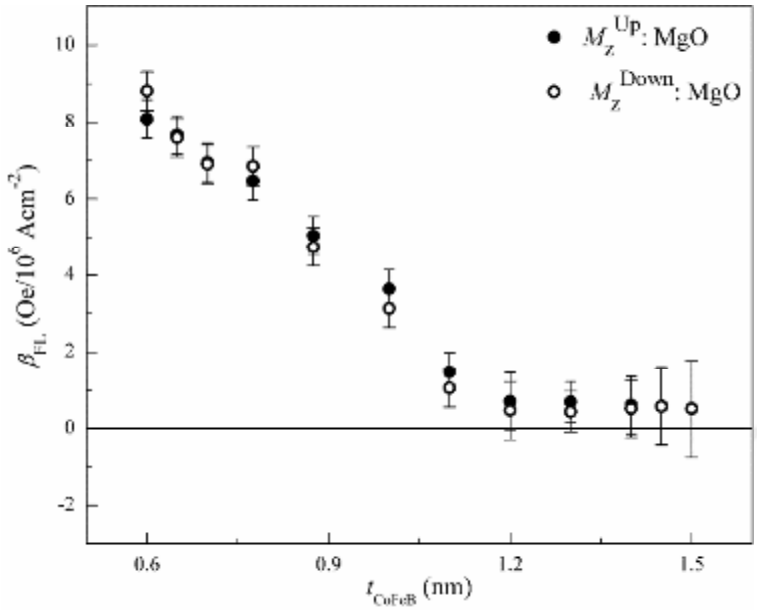


Figure 4.77. The β_{FL} values as a function of the CoFeB thickness in Hf|CoFeB(*wedge*)|MgO multilayer structure.

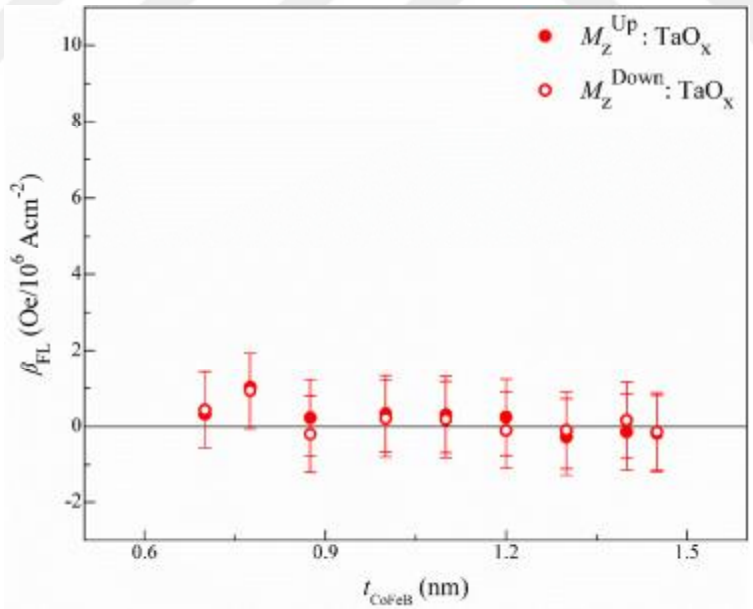


Figure 4.78. The β_{FL} values as a function of the CoFeB thickness in Hf|CoFeB(*wedge*)|TaO_x multilayer structure.

Figure 4.79 and Figure 4.80 show the dependence of β_z on the CoFeB thickness along the wedge for Hf|CoFeB(*wedge*)|MgO and Hf|CoFeB(*wedge*)|TaO_x multilayer structures, respectively. In Figure 4.79, the magnitude of β_z decreases with the increasing of CoFeB thickness up to ~1.0 nm. As mentioned before, the effective magnetic anisotropy energy increases with CoFeB thickness up to this same thickness (see Figure 4.49). In addition, the values of β_z reduce to zero once the thickness of CoFeB goes above ~1.0 nm in the Hf|CoFeB(*wedge*)|MgO structure. In this region (t_{CoFeB} > 1.0 nm), the PMA decreases with increasing CoFeB thickness (see Figure 4.49). This behavior is consistent with results of an earlier work (Yu et al., 2014) on Ta-seeded samples with a CoFeB wedge, where in the thicker CoFeB region, the lateral symmetry breaking due to variation of anisotropy does not result in the β_z torque on magnetic moments. On the other hand, for TaO_x-based devices, the values of β_z were generally too small to observe a clear trend of the β_z dependence on CoFeB thickness (see Figure 4.80). In addition to applying electric current along the *x*-axis, which means the current is perpendicular to the wedge direction, an electric current parallel to the wedge was also applied to verify the effect of the symmetry breaking on the effective out-of-plane magnetic field generated by electric current.

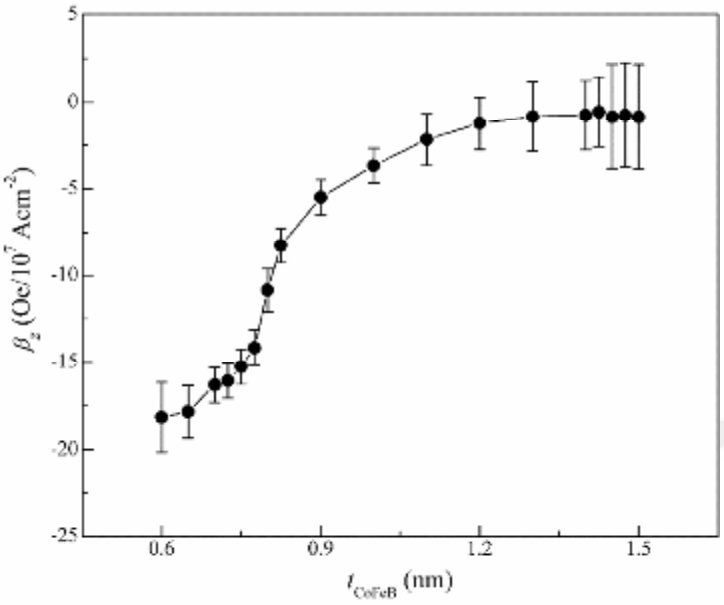


Figure 4.79. The β_z values as a function of the CoFeB thickness in Hf|CoFeB(*wedge*)|MgO multilayer structure.

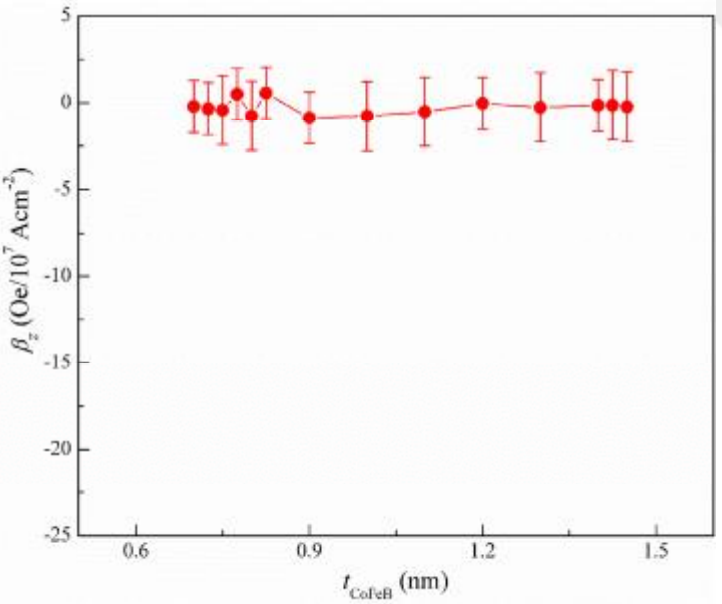


Figure 4.80. The β_z values as a function of the CoFeB thickness in Hf|CoFeB(*wedge*)|TaO_x multilayer structure.

4.3.5. CoFeB Layer Thickness Dependence on Current-Driven Magnetization Switching in Hf|CoFeB(*wedge*)|MgO and Hf|CoFeB(*wedge*)|TaO_x Multilayer Structures

Next, we performed current-induced magnetic switching measurements for devices with different CoFeB thickness along the wedge. Based on the data, one can construct a phase diagram for current-induced magnetic switching in these samples, which is given in Figure 4.81 and Figure 4.82 for Hf|CoFeB(*wedge*)|MgO and Hf|CoFeB(*wedge*)|TaO_x multilayer structures, respectively. In these figures, the switching current density was determined using $|J_{sw}| = |(J_{sw}^{+} + J_{sw}^{-})|/2$, where J_{sw}^{+} (J_{sw}^{-}) is the positive (negative) switching current density. The current-induced magnetic switching distributions are represented by color, which changes from blue ($|H_L| = 0\ Oe$) to red ($|H_L| = 500\ Oe$). The black color represents that there is no full magnetic switching within the applied range of current density (up to 10^7A/cm^2) and longitudinal magnetic field (up to 500 Oe). The dark blue area represents zero-field magnetic switching in Figure 4.81, indicating that below CoFeB thickness of ~0.9 nm, the perpendicularly magnetized CoFeB can be switched by current-induced torques at zero magnetic field. The switching current density increases with the CoFeB thickness as expected, because the PMA is increasing with the thickness in this range, while also the β_z magnitude is decreasing with increasing CoFeB thickness below 0.9 nm. On the other hand, in Figure 4.82, one does not observe any current-driven magnetic switching at zero magnetic field within the present range of currents, as expected due to the very small β_z for all devices on the Hf|CoFeB(*wedge*)|TaO_x sample.

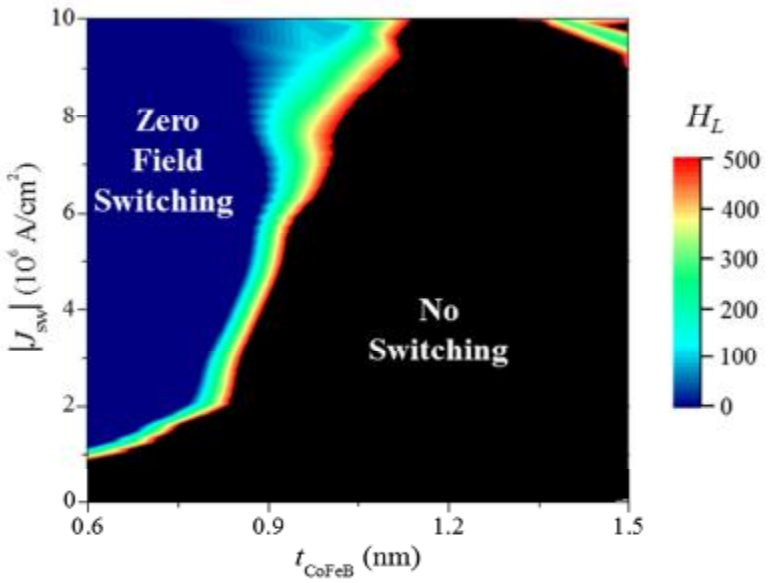


Figure 4.81. Current-induced perpendicular magnetic switching phase diagram in Hf|CoFeB(*wedge*)|MgO multilayer structure.

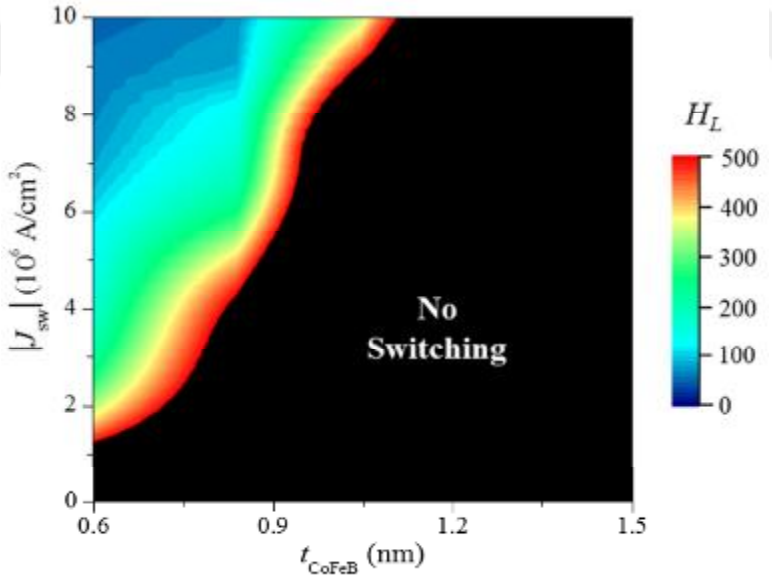


Figure 4.82. Current-induced perpendicular magnetic switching phase diagram in Hf|CoFeB(*wedge*)|TaO_x multilayer structure.

5. CONCLUSIONS

A systematic study of current-driven magnetization dynamics in metallic multilayer structures has been presented in this thesis. The multilayer films deposited by magnetron sputtering system and micron-scale Hall-bar shape devices fabricated by photolithography have been analyzed by performing structural, magnetic and transport measurements. The results of current research can help to understand and develop the magnetic tunnel junction by current-driven spin-orbit-torque on the way of improving the next generation magnetic random access memory technology. We have mainly focused on the current-driven perpendicular magnetization switching mechanism in free-part of magnetic tunnel junctions that comprises of seed-layer|ferromagnetic-free-layer|tunnel-barrier|capped-layer. In addition, the controlling of magnetization has been studied by engineering the multilayer structure to overcome the needed external magnetic field. We would like to highlights of the results found in this thesis as following;

- The seed layer in magnetic tunnel junctions has important roles in terms of quality of the film, perpendicular magnetic anisotropy, device fabrication and energy requirement. Various materials such as Ta, Ru, W, Pt, Hf have been used as a seed layer, i.e. they are also heavy-metals, in the magnetic tunnel junctions. Since these materials have different electronic configurations and interface coupling properties which affects the magnetic anisotropy and Rashba interface coupling, the materials become crucial to design high performance magnetic tunnel junction devices. Beyond the type of material in seed layer, it must be also considered its thickness, growing conditions and their effect on the transport and spintronic properties. Therefore, we worked on the heavy-metal layer thickness dependence on structural, magnetic, transport and spintronic properties in Hf(t)|CoFeB(1.1)|MgO(2.0)|Ta(2.0) multilayer structures films (t = 1.0, 1.5,

2.5, 3.5, 5.0, 7.0 and 10 nm). The structural properties of the multilayer films have been analyzed by performing atomic force microscope imaging and X-ray photoelectron spectroscopy techniques. The surface morphologies of the films are quiet smooth, and they show the uniform deposition of the films up to 5.0 nm. However, the morphology and the quality of the films is getting worse above t_{Hf} = 5.0 nm. The roughness of the films almost linearly increases with the Hf layer thickness in the multilayer structure and it was found in a range of 0.12 nm to 0.45 nm. In addition to the roughness, we observed some island formation above t_{Hf} = 5.0 nm. The crystal quality of the CoFe layer is reduced as the thickness of Hf is increased, and the effective perpendicular magnetic anisotropy is reduced as well. The XPS results indicate that the amount of bonding B-O increases when buffer layer thickness is decreased. The increment in B-O bonding reduces the Fe-O hybridization at the interface between CoFeB and MgO layers. Thus, interfacial magnetic anisotropy energy is weaker when buffer layer thickness (t_{Hf}) is below 1.0 nm in our multilayer structure. The presented transport results indicate that the sign of damping-like spin-orbit-torque can change with the thickness of the Hf heavy metal layer. The origin of the sign reversal is possibly related to interface SOC due to scattering at rough interfaces of the Hf and CoFeB layers. The results show that the thickness of the heavy metal layer, in addition to its spin Hall effect, is an important parameter when designing devices for applications in magnetic random access memory.

· The other important part of the magnetic tunnel junctions is the tunnel barrier. To separate two ferromagnetic layers and tunnel of polarized electrons in magnetic tunnel junctions, an insulator layer is used between the free and fixed ferromagnetic layer. As explained through the thesis that high tunneling magnetoresistance ratio is required for sensitive reading of data from the magnetic tunnel junctions. Thus, the materials used in tunnel

barrier is important for high TMR value. However, in the writing process, there is no work in the literature in terms of material based writing performance for current-driven magnetization switching. Here, we worked the effect of oxide (tunnel) layer on magnetic, transport and spintronic properties in Hf(5.0)|CoFeB(0.8)|MgO(5.0) and Hf(5.0)|CoFeB(0.8)TaO_x(5.0) multilayer structures films. Vector measurements in the longitudinal and transverse directions were performed to investigate the current-driven effective fields due to spin-orbit torques. The results show that both effective fields, i.e., the contributions from the damping-like and field-like SOT, can be significant and are both strongly affected by the cap oxide layer in Hf|CoFeB|MgO (TaO_x) multilayers. Based on our results, this may not entirely be attributed to the effect of the Hf layer, and the entire stack needs to be considered when analyzing the expected magnitude and type of the observed SOTs. The results demonstrate the critical role of the oxide capping layer in the current-induced spin-orbit torques and may help clarify the physics behind SOTs in such structures, especially in Hf|CoFeB|MgO multilayer, which could be considered as a candidate system for future MRAM applications driven by spin-orbit torques.

- For energy consumption, we have engineered the structure of the devices by breaking structure through lateral and growing directions. We have demonstrated the electric current-induced perpendicular magnetization switching, and its dependence on the choice of different oxide layers, in Hf|CoFeB(*wedge*)|MgO and Hf|CoFeB(*wedge*)|TaO_x structures. To break the structural symmetry in the sample plane, a CoFeB layer with varying thickness is used. While a large current-induced effective field in the *z*-direction is observed in Hf|CoFeB|MgO, this was not the case in Hf|CoFeB|TaO_x. It was also shown that the current-induced magnetic

switching phase diagram in Hf|CoFeB(*wedge*)|MgO and Hf|CoFeB(*wedge*)|TaO_x is in good agreement with the magnitude of β_z. Due to the high tunneling magneto-resistance ratio in MTJ devices with MgO barrier, a three-terminal MTJ device comprising Hf|CoFeB|MgO can potentially be used to manipulate the free layer in Magnetic Random Access Memory arrays, writing data using the current-induced SOT effect under zero magnetic field.

REFERENCES

Akyol, M., Alzate, J. G., Yu, G., Upadhyaya, P., Wong, K. L., Ekicibil, A., Khalili Amiri, P. and Wang, K. L., 2015. Effect of the oxide layer on current-induced spin-orbit torques in Hf|CoFeB|MgO and Hf|CoFeB|TaOx structures. Applied Physics Letters 106, 3 032406.

Akyol, M., Yu, G., Alzate, J. G., Upadhyaya, P., Li, X., Wong, K. L., Ekicibil, A., Khalili Amiri, P. and Wang, K. L., 2015. Current-induced spin-orbit torque switching of perpendicularly magnetized Hf|CoFeB|MgO and Hf|CoFeB|TaOx structures. Applied Physics Letters 106, 16 162409.

Althammer, M., Meyer, S., Nakayama, H., Schreier, M., Altmannshofer, S., Weiler, M., Huebl, H., Geprägs, S., Opel, M., Gross, R., Meier, D., Klewe, C., Kuschel, T., Schmalhorst, J.-M., Reiss, G., Shen, L., Gupta, A., Chen, Y.-T., Bauer, G. E. W., Saitoh, E. and Goennenwein, S. T. B., 2013. Quantitative study of the spin Hall magnetoresistance in ferromagnetic insulator/normal metal hybrids. Physical Review B 87, 22 224401.

Ando, K. and Saitoh, E., 2010. Inverse spin-Hall effect in palladium at room temperature. Journal of Applied Physics 108, 11 113925.

Ando, K., Takahashi, S., Harii, K., Sasage, K., Ieda, J., Maekawa, S. and Saitoh, E., 2008. Electric Manipulation of Spin Relaxation Using the Spin Hall Effect. Physical Review Letters 101, 3 036601.

Ando, K., Takahashi, S., Ieda, J., Kajiwara, Y., Nakayama, H., Yoshino, T., Harii, K., Fujikawa, Y., Matsuo, M., Maekawa, S. and Saitoh, E., 2011. Inverse spin-Hall effect induced by spin pumping in metallic system. Journal of Applied Physics 109, 10 103913.

Anikeeva, P., Beach, G. and Holten-Andersen, N., 2013. Electronic, Optical and Magnetic Properties of Materials. Spring.

Azevedo, A., Vilela-Leão, L. H., Rodríguez-Suárez, R. L., Lacerda Santos, A. F. and Rezende, S. M., 2011. Spin pumping and anisotropic magnetoresistance voltages in magnetic bilayers: Theory and experiment. Physical Review B 83, 14 144402.

Bae, J. Y., Lim, W. C., Kim, H. J., Lee, T. D., Kim, K. W. and Kim, T. W., 2006. Compositional change of MgO barrier and interface in CoFeB⁄MgO⁄CoFeB tunnel junction after annealing. Journal of Applied Physics 99, 8 08T316.

Baibich, M. N., Broto, J. M., Fert, A., Van Dau, F. N., Petroff, F., Etienne, P., Creuzet, G., Friederich, A. and Chazelas, J., 1988. Giant Magnetoresistance of (001)Fe/(001)Cr Magnetic Superlattices. Physical Review Letters 61, 21 2472-2475.

Berger, L., 1970. Side-Jump Mechanism for the Hall Effect of Ferromagnets. Physical Review B 2, 11 4559-4566.

Berger, L., 1996. Emission of spin waves by a magnetic multilayer traversed by a current. Physical Review B 54, 13 9353-9358.

Bieletzki, M., Hynninen, T., Soini, T. M., Pivetta, M., Henry, C. R., Foster, A. S., Esch, F., Barth, C. and Heiz, U., 2010. Topography and work function measurements of thin MgO(001) films on Ag(001) by nc-AFM and KPFM. Physical Chemistry Chemical Physics 12, 13 3203-3209.

Binasch, G., Grünberg, P., Saurenbach, F. and Zinn, W., 1989. Enhanced magnetoresistance in layered magnetic structures with antiferromagnetic interlayer exchange. Physical Review B 39, 7 4828-4830.

Butler, W. H., Zhang, X. G., Schulthess, T. C. and MacLaren, J. M., 2001. Spin-dependent tunneling conductance of Fe|MgO|Fe sandwiches. Physical Review B 63, 5 054416.

Butti, G., Trioni, M. I. and Ishida, H., 2004. Electronic properties calculation of MgO thin films adsorbed on semi-infinite Ag(001). Physical Review B 70, 19 195425.

Carvello, B., Ducruet, C., Rodmacq, B., Auffret, S., Gautier, E., Gaudin, G. and Dieny, B., 2008. Sizable room-temperature magnetoresistance in cobalt based magnetic tunnel junctions with out-of-plane anisotropy. Applied Physics Letters 92, 10 102508.

Coey, J. M. D.,2010. Magnetism and Magnetic Materials. Cambridge University Press.

Cui, B., Song, C., Wang, G. Y., Wang, Y. Y., Zeng, F. and Pan, F., 2013. Perpendicular magnetic anisotropy in CoFeB/X (X = MgO, Ta, W, Ti, and Pt) multilayers. Journal of Alloys and Compounds 559, 112-115.

Day, C., 2005. Two groups observe the spin hall effect in semiconductors. Physics Today 58, 2 17-19.

Dexin, W., Nordman, C., Daughton, J. M., Zhenghong, Q. and Fink, J., 2004. 70% TMR at room temperature for SDT sandwich junctions with CoFeB as free and reference Layers. IEEE Transactions on Magnetics 40, 4 2269-2271.

D'yakonov, M. I. and Perel', V. I., 1971. Possibility of Orienting Electron Spins with Current. JETP Letters 13, 11 467.

Eastman, D. E., 1970. Photoelectric Work Functions of Transition, Rare-Earth, and Noble Metals. Physical Review B 2, 1 1-2.

Eisberg, R. and Resnick, R., 1974. Quantum Physics of Atoms, Molecules, Solids, Nuclei and Particles. John Wiley & Sons.

Emori, S., Bauer, U., Ahn, S.-M., Martinez, E. and Beach, G. S. D., 2013. Current-driven dynamics of chiral ferromagnetic domain walls. Nat Mater 12, 7 611-616.

Fan, J. and Eom, J., 2008. Direct electrical observation of spin Hall effect in Bi film. Applied Physics Letters 92, 14 142101.

Fan, X., Celik, H., Wu, J., Ni, C., Lee, K.-J., Lorenz, V. O. and Xiao, J. Q., 2014. Quantifying interface and bulk contributions to spin–orbit torque in magnetic bilayers. Nat Commun 5,

Fan, X., Wu, J., Chen, Y., Jerry, M. J., Zhang, H. and Xiao, J. Q., 2013. Observation of the nonlocal spin-orbital effective field. Nat Commun 4, 1799.

Feng, Z., Hu, J., Sun, L., You, B., Wu, D., Du, J., Zhang, W., Hu, A., Yang, Y., Tang, D. M., Zhang, B. S. and Ding, H. F., 2012. Spin Hall angle quantification from spin pumping and microwave photoresistance. Physical Review B 85, 21 214423.

Garello, K., Miron, I. M., Avci, C. O., Freimuth, F., Mokrousov, Y., Blugel, S., Auffret, S., Boulle, O., Gaudin, G. and Gambardella, P., 2013. Symmetry and magnitude of spin-orbit torques in ferromagnetic heterostructures. Nat Nano 8, 8 587-593.

Getzlaff, M.,2008. Fundamentals of Magnetism. Springer

Gilbert, T., 1955. A Lagrangian formulation of gyromagnetic equation of the magnetization field. Phys. Rev. 100,

Giordano, L., Cinquini, F. and Pacchioni, G., 2006. Tuning the surface metal work function by deposition of ultrathin oxide films: Density functional calculations. Physical Review B 73, 4 045414.

Gradhand, M., Fedorov, D. V., Zahn, P. and Mertig, I., 2010. Extrinsic Spin Hall Effect from First Principles. Physical Review Letters 104, 18 186403.

Greer, A. A., Gray, A. X., Kanai, S., Kaiser, A. M., Ueda, S., Yamashita, Y., Bordel, C., Palsson, G., Maejima, N., Yang, S.-H., Conti, G., Kobayashi, K., Ikeda, S., Matsukura, F., Ohno, H., Schneider, C. M., Kortright, J. B., Hellman, F. and Fadley, C. S., 2012. Observation of boron diffusion in an annealed Ta/CoFeB/MgO magnetic tunnel junction with standing-wave hard x-ray photoemission. Applied Physics Letters 101, 20 202402.

Greiner, M. T., Chai, L., Helander, M. G., Tang, W.-M. and Lu, Z.-H., 2012. Transition Metal Oxide Work Functions: The Influence of Cation Oxidation State and Oxygen Vacancies. Advanced Functional Materials 22, 21 4557-4568.

Grundy, P. J., 1998. Thin film magnetic recording media. Journal of Physics D: Applied Physics 31, 21 2975.

Haazen, P. P. J., Murè, E., Franken, J. H., Lavrijsen, R., Swagten, H. J. M. and Koopmans, B., 2013. Domain wall depinning governed by the spin Hall effect. Nat Mater 12, 4 299-303.

Hahn, C., de Loubens, G., Klein, O., Viret, M., Naletov, V. V. and Ben Youssef, J., 2013. Comparative measurements of inverse spin Hall effects and magnetoresistance in YIG/Pt and YIG/Ta. Physical Review B 87, 17 174417.

Hall, E. H., 1879. On a New Action of the Magnet on Electric Currents. American Journal of Mathematics 2, 3 287-292.

Hall, E. H., 1881. On the "Rotational Coefficient" in nickel and cobalt. Philosophical Magazine Series 5 12, 74 157-172.

Hals, K. M. D. and Brataas, A., 2013. Phenomenology of current-induced spin-orbit torques. Physical Review B 88, 8 085423.

Hayden, L. X., Raimondi, R., Flatté, M. E. and Vignale, G., 2013. Intrinsic spin Hall effect at asymmetric oxide interfaces: Role of transverse wave functions. Physical Review B 88, 7 075405.

Hirsch, J. E., 1999. Spin Hall Effect. Physical Review Letters 83, 9 1834-1837.

Hoffmann, A., 2013. Spin Hall Effects in Metals. IEEE Transactions on Magnetics 49, 10 5172-5193.

Hung, H. Y., Luo, G. Y., Chiu, Y. C., Chang, P., Lee, W. C., Lin, J. G., Lee, S. F., Hong, M. and Kwo, J., 2013. Detection of inverse spin Hall effect in epitaxial ferromagnetic Fe3Si films with normal metals Au and Pt. Journal of Applied Physics 113, 17 17C507.

Ikeda, S., Hayakawa, J., Ashizawa, Y., Lee, Y. M., Miura, K., Hasegawa, H., Tsunoda, M., Matsukura, F. and Ohno, H., 2008. Tunnel magnetoresistance of 604% at 300K by suppression of Ta diffusion in CoFeB/MgO/CoFeB pseudo-spin-valves annealed at high temperature. Applied Physics Letters 93, 8 082508.

Ikeda, S., Miura, K., Yamamoto, H., Mizunuma, K., Gan, H. D., Endo, M., Kanai, S., Hayakawa, J., Matsukura, F. and Ohno, H., 2010. A perpendicular-anisotropy CoFeB–MgO magnetic tunnel junction. Nat Mater 9, 9 721-724.

Ikeda, S., Koizumi, R., Sato, H., Yamanouchi, M., Miura, K., Mizunuma, K., Gan, H., Matsukura, F. and Ohno, H., 2012. Boron Composition Dependence of Magnetic Anisotropy and Tunnel Magnetoresistance in MgO/CoFe(B) Based Stack Structures. IEEE Transactions on Magnetics 48, 11 3829-3832.

Iwasaki, S., 1980. Perpendicular magnetic recording. IEEE Transactions on Magnetics 16, 71-76.

Jeon, K.-R., Min, B.-C., Jo, Y.-H., Lee, H.-S., Shin, I.-J., Park, C.-Y., Park, S.-Y. and Shin, S.-C., 2011. Electrical spin injection and accumulation in CoFe/MgO/Ge contacts at room temperature. Physical Review B 84, 16 165315.

Jung, J. H., Lim, S. H. and Lee, S. R., 2010. Strong perpendicular magnetic anisotropy in thick CoFeB films sandwiched by Pd and MgO layers. Applied Physics Letters 96, 4 042503.

Kaidatzis, A., Bran, C., Psycharis, V., Vázquez, M., García-Martín, J. M. and Niarchos, D., 2015. Tailoring the magnetic anisotropy of CoFeB/MgO stacks onto W with a Ta buffer layer. Applied Physics Letters 106, 26 262401.

Karplus, R. and Luttinger, J. M., 1954. Hall Effect in Ferromagnetics. Physical Review 95, 5 1154-1160.

Kato, Y. K., Myers, R. C., Gossard, A. C. and Awschalom, D. D., 2004. Observation of the Spin Hall Effect in Semiconductors. Science 306, 5703 1910-1913.

Kay, Y., Kenji, N., Takeshi, S., Hitoshi, K., Akio, F., Taro, N., Shinji, Y. and Koji, A., 2010. High Magnetoresistance Ratio and Low Resistance–Area Product in Magnetic Tunnel Junctions with Perpendicularly Magnetized Electrodes. Applied Physics Express 3, 5 053003.

Khvalkovskiy, A. V., Cros, V., Apalkov, D., Nikitin, V., Krounbi, M., Zvezdin, K. A., Anane, A., Grollier, J. and Fert, A., 2013. Matching domain-wall configuration and spin-orbit torques for efficient domain-wall motion. Physical Review B 87, 2 020402.

Kim, H., Noh, J.-S., Roh, J. W., Chun, D. W., Kim, S., Jung, S. H., Kang, H. K., Jeong, W. Y. and Lee, W., 2011. Perpendicular Magnetic Anisotropy in FePt Patterned Media Employing a CrV Seed Layer. Nanoscale Research Letters 6, 1 13-13.

Kim, J., Sinha, J., Hayashi, M., Yamanouchi, M., Fukami, S., Suzuki, T., Mitani, S. and Ohno, H., 2013. Layer thickness dependence of the current-induced effective field vector in Ta|CoFeB|MgO. Nat Mater 12, 3 240-245.

Kim, G., Sakuraba, Y., Oogane, M., Ando, Y. and Miyazaki, T., 2008. Tunneling magnetoresistance of magnetic tunnel junctions using perpendicular magnetization L10-CoPt electrodes. Applied Physics Letters 92, 17 172502.

Kontani, H., Tanaka, T., Hirashima, D. S., Yamada, K. and Inoue, J., 2009. Giant Orbital Hall Effect in Transition Metals: Origin of Large Spin and Anomalous Hall Effects. Physical Review Letters 102, 1 016601.

Kondou, K., Sukegawa, H., Mitani, S., Tsukagoshi, K. and Kasai, S., 2012. Evaluation of Spin Hall Angle and Spin Diffusion Length by Using Spin Current-Induced Ferromagnetic Resonance. Applied Physics Express 5, 7 073002.

König, T., Simon, G. H., Rust, H. P. and Heyde, M., 2009. Work Function Measurements of Thin Oxide Films on Metals—MgO on Ag(001). The Journal of Physical Chemistry C 113, 26 11301-11305.

Landau, L. D. and Lifschitz, E. M.,1935. Theory of the dispersion of magnetic permeability in ferromagnetic bodies. Phys. Z. Sowietunion 8,

Landau, L. D. and Lifschitz, E.,1965. Quantum Mechanics. Pergamon

Lee, Y. M., Hayakawa, J., Ikeda, S., Matsukura, F. and Ohno, H., 2007. Effect of electrode composition on the tunnel magnetoresistance of pseudo-spin-valve magnetic tunnel junction with a MgO tunnel barrier. Applied Physics Letters 90, 21 212507.

Liu, L., Moriyama, T., Ralph, D. C. and Buhrman, R. A., 2011. Spin-Torque Ferromagnetic Resonance Induced by the Spin Hall Effect. Physical Review Letters 106, 3 036601.

Liu, L., Pai, C.-F., Li, Y., Tseng, H. W., Ralph, D. C. and Buhrman, R. A., 2012. Spin-Torque Switching with the Giant Spin Hall Effect of Tantalum. Science 336, 6081 555-558.

Liu, L., Lee, O. J., Gudmundsen, T. J., Ralph, D. C. and Buhrman, R. A., 2012. Current-Induced Switching of Perpendicularly Magnetized Magnetic Layers Using Spin Torque from the Spin Hall Effect. Physical Review Letters 109, 9 096602.

Liu, T., Cai, J. W. and Sun, L., 2012. Large enhanced perpendicular magnetic anisotropy in CoFeB/MgO system with the typical Ta buffer replaced by an Hf layer. AIP Advances 2, 3 032151.

Mathon, J. and Umerski, A., 2001. Theory of tunneling magnetoresistance of an epitaxial Fe/MgO/Fe(001) junction. Physical Review B 63, 22 220403.

Meng, H., Lum, W. H., Sbiaa, R., Lua, S. Y. H. and Tan, H. K., 2011. Annealing effects on CoFeB-MgO magnetic tunnel junctions with perpendicular anisotropy. Journal of Applied Physics 110, 3 033904.

Michaelson, H. B., 1977. The work function of the elements and its periodicity. J. Appl. Phys. 48, 4729

Mihai Miron, I., Gaudin, G., Auffret, S., Rodmacq, B., Schuhl, A., Pizzini, S., Vogel, J. and Gambardella, P., 2010. Current-driven spin torque induced by the Rashba effect in a ferromagnetic metal layer. Nat Mater 9, 3 230-234.

Mihajlović, G., Pearson, J. E., Garcia, M. A., Bader, S. D. and Hoffmann, A., 2009. Negative Nonlocal Resistance in Mesoscopic Gold Hall Bars: Absence of the Giant Spin Hall Effect. Physical Review Letters 103, 16 166601.

Miron, I. M., Garello, K., Gaudin, G., Zermatten, P.-J., Costache, M. V., Auffret, S., Bandiera, S., Rodmacq, B., Schuhl, A. and Gambardella, P., 2011. Perpendicular switching of a single ferromagnetic layer induced by in-plane current injection. Nature 476, 7359 189-193.

Morota, M., Niimi, Y., Ohnishi, K., Wei, D. H., Tanaka, T., Kontani, H., Kimura, T. and Otani, Y., 2011. Indication of intrinsic spin Hall effect in $4d$ and $5d$ transition metals. Physical Review B 83, 17 174405.

Mosendz, O., Vlaminck, V., Pearson, J. E., Fradin, F. Y., Bauer, G. E. W., Bader, S. D. and Hoffmann, A., 2010. Detection and quantification of inverse spin Hall effect from spin pumping in permalloy/normal metal bilayers. Physical Review B 82, 21 214403.

Mott, N. F. and Massey, H. S.,1965. The Theory of Atomic Collisions. Clarenda Press

Mott, N. F., 1929. The Scattering of Fast Electrons by Atomic Nuclei. Proceedings of the Royal Society of London A: Mathematical, Physical and Engineering Sciences 124, 794 425-442.

Nakayama, H., Althammer, M., Chen, Y. T., Uchida, K., Kajiwara, Y., Kikuchi, D., Ohtani, T., Geprägs, S., Opel, M., Takahashi, S., Gross, R., Bauer, G. E. W., Goennenwein, S. T. B. and Saitoh, E., 2013. Spin Hall Magnetoresistance Induced by a Nonequilibrium Proximity Effect. Physical Review Letters 110, 20 206601

Niimi, Y., Morota, M., Wei, D. H., Deranlot, C., Basletic, M., Hamzic, A., Fert, A. and Otani, Y., 2011. Extrinsic Spin Hall Effect Induced by Iridium Impurities in Copper. Physical Review Letters 106, 12 126601.

Niimi, Y., Kawanishi, Y., Wei, D. H., Deranlot, C., Yang, H. X., Chshiev, M., Valet, T., Fert, A. and Otani, Y., 2012. Giant Spin Hall Effect Induced by Skew Scattering from Bismuth Impurities inside Thin Film CuBi Alloys. Physical Review Letters 109, 15 156602.

Nishimura, N., Hirai, T., Koganei, A., Ikeda, T., Okano, K., Sekiguchi, Y. and Osada, Y., 2002. Magnetic tunnel junction device with perpendicular magnetization films for high-density magnetic random access memory. Journal of Applied Physics 91, 8 5246-5249.

Nistor, L. E., Rodmacq, B., Auffret, S. and Dieny, B., 2009. Pt/Co/oxide and oxide/Co/Pt electrodes for perpendicular magnetic tunnel junctions. Applied Physics Letters 94, 1 012512.

Ohmori, H., Hatori, T. and Nakagawa, S., 2008. Perpendicular magnetic tunnel junction with tunneling magnetoresistance ratio of 64% using MgO (100) barrier layer prepared at room temperature. Journal of Applied Physics 103, 7 07A911.

Onoda, S., Sugimoto, N. and Nagaosa, N., 2008. Quantum transport theory of anomalous electric, thermoelectric, and thermal Hall effects in ferromagnets. Physical Review B 77, 16 165103.

Pai, C.-F., Nguyen, M.-H., Belvin, C., Vilela-Leão, L. H., Ralph, D. C. and Buhrman, R. A., 2014. Enhancement of perpendicular magnetic anisotropy and transmission of spin-Hall-effect-induced spin currents by a Hf spacer layer in W/Hf/CoFeB/MgO layer structures. Appl. Phys. Lett. 104, 082407

Pai, C.-F., Liu, L., Li, Y., Tseng, H. W., Ralph, D. C. and Buhrman, R. A., 2012. Spin transfer torque devices utilizing the giant spin Hall effect of tungsten Appl. Phys. Lett. 101, 122404

Park, J.-H., Park, C., Jeong, T., Moneck, M. T., Nufer, N. T. and Zhu, J.-G., 2008. Co⁄Pt multilayer based magnetic tunnel junctions using perpendicular magnetic anisotropy. Journal of Applied Physics 103, 7 07A917.

Parkin, S. S. P., Kaiser, C., Panchula, A., Rice, P. M., Hughes, B., Samant, M. and Yang, S.-H., 2004. Giant tunnelling magnetoresistance at room temperature with MgO (100) tunnel barriers. Nat Mater 3, 12 862-867.

Peng, S., Wang, M., Yang, H., Zeng, L., Nan, J., Zhou, J., Zhang, Y., Hallal, A., Chshiev, M., Wang, K. L., Zhang, Q. and Zhao, W., 2015. Origin of interfacial perpendicular magnetic anisotropy in MgO/CoFe/metallic capping layer structures. Scientific Reports 5, 18173.

Pi, U. H., Kim, K. W., Bae, J. Y., Lee, S. C., Cho, Y. J., Kim, K. S. and Seo, S., 2010. Tilting of the spin orientation induced by Rashba effect in ferromagnetic metal layer Appl. Phys. Lett. 97, 162507

Read, J. C., Mather, P. G. and Buhrman, R. A., 2007. X-ray photoemission study of CoFeB⁄MgO thin film bilayers. Applied Physics Letters 90, 13 132503.

Ryu, K.-S., Thomas, L., Yang, S.-H. and Parkin, S., 2013. Chiral spin torque at magnetic domain walls. Nat Nano 8, 7 527-533.

Sakurai, J. J., 1967. Advanced Quantum Mechanics Addison-Wesley Publishing Company

Sakurai, J. J., 1967. Advanced Quantum Mechanics Addison-Wesley Publishing Company

Seki, T., Hasegawa, Y., Mitani, S., Takahashi, S., Imamura, H., Maekawa, S., Nitta, J. and Takanashi, K., 2008. Giant spin Hall effect in perpendicularly spin-polarized FePt/Au devices. Nat Mater 7, 2 125-129.

Shankar, R., 1994. Principles of Quantum Mechanics. Plenum Press-New York and London 2nd Edition,

Sinova, J., Valenzuela, S. O., Wunderlich, J., Back, C. H. and Jungwirth, T., 2015. Spin Hall effects. Reviews of Modern Physics 87, 4 1213-1260.

Slater, J. C., 1960. Quantum Theory of Atomic Structure. McGraw-Hill Vol-2, 493.

Slonczewski, J. C., 1996. Current-driven excitation of magnetic multilayers. Journal of Magnetism and Magnetic Materials 159, 1 L1-L7.

Smit, J., 1958. The spontaneous hall effect in ferromagnetics II. Physica 24, 1 39-51.

Tanaka, T., Kontani, H., Naito, M., Naito, T., Hirashima, D. S., Yamada, K. and Inoue, J., 2008. Intrinsic spin Hall effect and orbital Hall effect in $4d$ and $5d$ transition metals. Physical Review B 77, 16 165117.

Thomson, W., 1856. On the Electro-Dynamic Qualities of Metals:--Effects of Magnetization on the Electric Conductivity of Nickel and of Iron. Proceedings of the Royal Society of London 8, 546-550.

Torrejon, J., Kim, J., Sinha, J., Mitani, S., Hayashi, M., Yamanouchi, M. and Ohno, H., 2014. Interface control of the magnetic chirality in CoFeB/MgO heterostructures with heavy-metal underlayers. Nat Commun 5,

Tsoi, M., Jansen, A. G. M., Bass, J., Chiang, W. C., Seck, M., Tsoi, V. and Wyder, P., 1998. Excitation of a Magnetic Multilayer by an Electric Current. Physical Review Letters 80, 19 4281-4284.

Qiu, X., Narayanapillai, K., Wu, Y., Deorani, P., Yang, D.-H., Noh, W.-S., Park, J.-H., Lee, K.-J., Lee, H.-W. and Yang, H., 2015. Spin–orbit-torque engineering via oxygen manipulation. Nat Nano 10, 4 333-338.

Wang, K. L., Alzate, J. G. and Khalili Amiri, P., 2013. Low-power non-volatile spintronic memory: STT-RAM and beyond. J. Phys. D: Appl. Phys. 46, 7 074003.

Wang, X., Xiao, J., Manchon, A. and Maekawa, S., 2013. Spin-Hall conductivity and electric polarization in metallic thin films. Physical Review B 87, 8 081407.

Wanger, C. D., Riggs, W. M., Davis, L. E., Moulder, J. F. and Muilenberg, G. E., 1979. Handbook of X-ray Photoelectron Spectroscopy. Perkin-Elmer Corp. Physical Electronic Division.

Weischenberg, J., Freimuth, F., Sinova, J., Blügel, S. and Mokrousov, Y., 2011. Ab Initio Theory of the Scattering-Independent Anomalous Hall Effect. Physical Review Letters 107, 10 106601.

Wolf, S. A., Awschalom, D. D., Buhrman, R. A., Daughton, J. M., von Molnár, S., Roukes, M. L., Chtchelkanova, A. Y. and Treger, D. M., 2001. Spintronics: A Spin-Based Electronics Vision for the Future. Science 294, 5546 1488-1495.

Wunderlich, J., Kaestner, B., Sinova, J. and Jungwirth, T., 2005. Experimental Observation of the Spin-Hall Effect in a Two-Dimensional Spin-Orbit Coupled Semiconductor System. Physical Review Letters 94, 4 047204.

Worledge, D. C., Hu, G., Abraham, D. W., Sun, J. Z., Trouilloud, P. L., Nowak, J., Brown, S., Gaidis, M. C., O'Sullivan, E. J. and Robertazzi, R. P., 2011. Spin torque switching of perpendicular Ta|CoFeB|MgO-based magnetic tunnel junctions. Applied Physics Letters 98, 2 022501.

Valenzuela, S. O. and Tinkham, M., 2006. Direct electronic measurement of the spin Hall effect. Nature 442, 7099 176-179.

Vlaminck, V., Pearson, J. E., Bader, S. D. and Hoffmann, A., 2013. Dependence of spin-pumping spin Hall effect measurements on layer thicknesses and stacking order. Physical Review B 88, 6 064414.

Yang, H. X., Chshiev, M., Dieny, B., Lee, J. H., Manchon, A. and Shin, K. H., 2011. First-principles investigation of the very large perpendicular magnetic anisotropy at Fe/MgO and Co/MgO interfaces. Physical Review B 84, 5 054401.

Yang, S., Lee, J., An, G., Kim, J., Chung, W. and Hong, J., 2015. Ta thickness-dependent perpendicular magnetic anisotropy features in Ta/CoFeB/MgO/W free layer stacks. Thin Solid Films 587, 39-42.

Yakushiji, K., Saruya, T., Kubota, H., Fukushima, A., Nagahama, T., Yuasa, S. and Ando, K., 2010. Ultrathin Co/Pt and Co/Pd superlattice films for MgO-based perpendicular magnetic tunnel junctions. Applied Physics Letters 97, 23 232508.

Yoshikawa, M., Kitagawa, E., Nagase, T., Daibou, T., Nagamine, M., Nishiyama, K., Kishi, T. and Yoda, H., 2008. Tunnel Magnetoresistance Over 100% in MgO-Based Magnetic Tunnel Junction Films With Perpendicular Magnetic L10-FePt Electrodes. IEEE Transactions on Magnetics 44, 11 2573-2576.

Yu, G., Upadhyaya, P., Fan, Y., Alzate, J. G., Jiang, W., Wong, K. L., Takei, S., Bender, S. A., Chang, L.-T., Jiang, Y., Lang, M., Tang, J., Wang, Y., Tserkovnyak, Y., Amiri, P. K. and Wang, K. L., 2014. Switching of perpendicular magnetization by spin-orbit torques in the absence of external magnetic fields. Nat Nano 9, 7 548-554.

Yu, G., Chang, L.-T., Akyol, M., He, C., Li, X., Upadhyaya, P., Wong, K. L., Amiri, P. K. and Wang, K. L., 2014. Current-driven perpendicular magnetization switching in Ta/CoFeB/[TaOx or MgO/TaOx] films with lateral structural asymmetry Appl. Phys. Lett. 105, 102411.

Yu, G., Upadhyaya, P., Wong, K. L., Jiang, W., Alzate, J. G., Tang, J., Amiri, P. K. and Wang, K. L., 2014. Magnetization switching through spin-Hall-effect-induced chiral domain wall propagation. Physical Review B 89, 10 104421.

Yuasa, S., Nagahama, T., Fukushima, A., Suzuki, Y. and Ando, K., 2004. Giant room-temperature magnetoresistance in single-crystal Fe/MgO/Fe magnetic tunnel junctions. Nat Mater 3, 12 868-871.

Zhou, L., Grigoryan, V. L., Maekawa, S., Wang, X. and Xiao, J., 2015. Spin Hall effect by surface roughness. Physical Review B 91, 4 045407.

CURRICULUM VITAE

Mustafa AKYOL was born in Adana, Turkey in 1986. He received his B.S. degree by receiving 1st ranked in the Department of Physics Department from the Çukurova University in 2008. He graduated from MSc in the Department of Physics Department from the Çukurova University in 2011. After his MSc graduation, he started to work as a research assistant in the same department in 2011. He has working as a research assistant in Physics Department in Çukurova University since 2011. He joined the Device Research Laboratory (DRL) research group in 2013 to pursue his Ph.D. dissertation research in Electrical and Electronics Engineering in the University of California, Los Angeles (UCLA). He has worked in several research projects supported by Scientific and Technological Council of Turkey and Scientific Research Project Unit of Çukurova University. His research areas are nano-magnetism, nano-technology, spin-based electronics (spintronics), diluted magnetic semiconductors and metal/semiconductor based devices. In particularly, he is working on non-volatile magnetic memory and logic, magnetic tunnel junctions, electric-field and electric-current control of magnetism in perpendicularly magnetized magnetic tunnel junctions.